

UNIVERSITY OF CALIFORNIA, SAN DIEGO

Combining EEG Source Dynamics Results across Subjects, Studies and Cognitive

Events

A dissertation submitted in partial satisfaction of the requirements for the degree

Doctor of Philosophy

in

Electrical and Computer Engineering (Intelligent Systems, Robotics, and Control)

by

Nima Bigdely-Shamlo

Committee in charge:

Professor Kenneth Kreutz-Delgado, Chair

Professor Virginia De Sa

Professor Gert Lanckriet

Professor Scott Makeig

Professor Nuno Vasconcelos

2014

Copyright

Nima Bigdely-Shamlo, 2014

All rights reserved.

The Dissertation of Nima Bigdely-Shamlo is approved, and it is acceptable in quality
and form for publication on microfilm and electronically:

Chair

UNIVERSITY OF CALIFORNIA, SAN DIEGO

2014

DEDICATION

To Audrey Buss, as without her encouragement and kind support this journey would not be possible.

TABLE OF CONTENTS

Signature Page.....	iii
Dedication.....	iv
Table of Contents.....	v
List of Figures.....	xiv
List of Tables.....	xix
Acknowledgements.....	xx
Vita.....	xxiii
Abstract.....	xxv
Chapter 1 Introduction	1
Chapter 2 EEGLAB Workflow.....	7
2.1 Introduction.....	7
2.2 Application of ICA in EEG Analysis	7
2.3 Equivalent Dipole Model for ICs.....	8
2.4 EEGLAB Workflow	10
2.5 Acknowledgments	13
2.6 Figures	15
Chapter 3 EEG Independent Component Polarity Normalization by Two-way Partitioning	17
3.1 Abstract.....	17
3.2 Introduction.....	18
3.3 Methods	20

3.3.1	Problem Description	21
3.3.2	Convex solution.....	22
3.3.3	Monte Carlo solution.....	23
3.4	Results.....	25
3.5	Discussion and Conclusion.....	30
3.6	Acknowledgments	32
3.7	Figures	32
Chapter 4	Detecting Eye Activity Related ICs (EyeCatch)	38
4.1	Abstract.....	38
4.2	Introduction.....	39
4.3	Methods	40
4.3.1	Scalp maps Database Preprocessing.....	40
4.3.2	Eye-related template scalp map dataset.....	40
4.4	Results.....	42
4.5	Conclusions.....	43
4.6	Acknowledgments	44
4.7	Figures	45
Chapter 5	Imaging half a million ICA-component scalp maps reveals EEG source hotspots	49
5.1	Introduction.....	49
5.2	Methods	50
5.2.1	Data Preprocessing	50

5.2.2	Dipole Density Calculation	51
5.2.3	Calculating Average Dipole Residual Variance.....	52
5.2.4	Calculating Average Dipole Orientation.....	53
5.2.5	Defining the radial vector direction for each voxel.....	55
5.3	Results.....	56
5.4	Discussion.....	57
5.5	Acknowledgements.....	59
5.6	Figures	60
	Chapter 6 Measure Projection Analysis: A Probabilistic Approach to EEG Source Comparison and Multi-Subject Inference	78
6.1	Abstract.....	78
6.2	Introduction.....	80
6.3	Methods	86
6.3.1	Experimental data.....	87
6.3.2	Subject task.....	87
6.3.3	Data preprocessing.	87
6.3.4	ERSP measure projection	88
6.3.5	ERSP domain clustering.....	91
6.3.6	PCA-based IC clustering	92
6.3.7	PCA-based ERSP measure clustering	94
6.4	Results.....	95
6.4.1	ERSP measures for PCA-based IC clusters.....	95

6.4.2	ERSP measure projection results.....	96
6.4.3	Comparison of MPA and PCA-based clustering methods	97
6.4.4	Simulation.....	100
6.5	Discussion.....	103
6.5.1	Relative Parsimony.....	104
6.5.2	Source Measure Consistency.....	106
6.5.3	Source Clustering Coherency	107
6.5.4	Cluster membership.....	108
6.5.5	Cluster shape	109
6.5.6	Cluster equivalence across measures.....	110
6.5.7	Subject comparisons	111
6.5.8	Group-Level ICA decomposition	112
6.6	Conclusion	116
6.7	Acknowledgements.....	116
6.8	Figures	118
6.9	Appendix A - Measure Projection Analysis (MPA) Method Description...	128
6.10	Appendix B - Threshold-based Clustering and Outlier Rejection using Affinity Propagation	135
Chapter 7	Subject Space Analysis	144
7.1	Introduction.....	144
7.2	Methods	144
7.3	Results and Discussion	146

7.4	Figures	148
Chapter 8	Classification feature analysis of oscillatory EEG dynamics accompanying auditory/visual attention switching	150
8.1	Introduction.....	150
8.2	Methods	152
8.2.1	Experimental Task.....	152
8.2.2	Data Analysis.....	154
8.2.3	Regularized Spatial-Spectral Dynamics (RSSD)	155
8.2.4	Data Preprocessing for RSSD	155
8.2.5	Adaptive Mixture ICA.....	157
8.2.6	Regularization.....	158
8.2.7	Spatial source restriction	160
8.2.8	Optimization and performance estimation	161
8.2.9	Measure Projection Analysis	162
8.3	Results.....	165
8.3.1	RSSD results.....	165
8.3.2	Measure Projection Analysis	167
8.4	Discussion.....	168
8.5	Conclusion	169
8.6	Acknowledgements.....	169
8.7	Figures	170
Chapter 9	Network Projection	176

9.1	Introduction.....	176
9.2	Methods	177
9.3	Results.....	180
9.4	Discussion.....	182
9.5	Figures	183
Chapter 10	Optimal Low pass Filtering	189
10.1	Introduction.....	189
10.2	Methods	189
10.3	Results.....	191
10.4	Discussion.....	193
10.5	Acknowledgements.....	193
10.6	Figures	193
Chapter 11	Collaborative Averaging.....	200
11.1	Introduction.....	200
11.2	Methods	200
11.3	Results.....	203
11.4	Discussion.....	206
11.5	Acknowledgements.....	208
11.6	Figures	209
Chapter 12	Comparison of Averaging and Regression Techniques for Estimating Event Related Potentials.....	220
12.1	Abstract.....	220

12.2	Introduction.....	221
12.3	Background.....	222
12.3.1	A Problem With Averaging.....	222
12.3.2	Data.....	222
12.4	Methods	223
12.4.1	Preprocessing.....	223
12.4.2	Regression Framework.....	224
12.4.3	Performance Metrics	225
12.5	Results.....	227
12.5.1	ERP Estimates (Figure 2)	227
12.5.2	Performance as Measured by ROV (Figure 3).....	227
12.6	Discussion.....	228
12.7	Conclusion	230
12.8	Figures	230
Chapter 13	Hierarchical Event Descriptor (HED) Tags for Analysis of Event-Related EEG Studies	234
13.1	Abstract.....	234
13.2	Introduction.....	235
13.3	Hierarchical Event Descriptors	236
13.3.1	Example Tagging for RSVP	238
13.3.2	HED Grammar.....	240
13.4	HED Tools and Resources	241

13.4.1	Community HED Tagging	241
13.4.2	Real-time HED Tagging of Experimental Conditions	241
13.4.3	Extended Use of HED Tags for Study Meta-Data	243
13.5	Discussion.....	244
13.6	Acknowledgement	244
13.7	Figures	245
13.8	Appendix I, HED Node Hierarchy (1.31).....	248
13.8.1	Time-Locked Event [default]	248
13.8.2	State	257
13.8.3	Participant.....	259
13.8.4	Context	259
13.8.5	Experiment Control	260
13.8.6	Custom.....	261
13.8.7	Paradigm.....	261
13.8.8	Label	266
13.8.9	Description	266
13.8.10	Group ID.....	267
13.8.11	HED	267
13.8.12	Restrictions on HED Identifier Names.....	267
13.8.13	Color Names	268
Chapter 14	Towards an EEG Search Engine	269
14.1	Abstract.....	269

14.2	Introduction.....	270
14.3	Methods	271
14.4	Results.....	273
14.5	Discussion.....	274
14.6	Acknowledgements.....	276
14.7	Figures	276
	References	280

LIST OF FIGURES

Figure 2.1. EEGLAB single session and group analysis workflows.....	15
Figure 2.2. EEGLAB single session analysis workflow.	16
Figure 3.1. Sample study-A IC scalp maps before polarity normalization.	33
Figure 3.2. (Left) Matrix X obtained from convex relaxation	33
Figure 3.3. Sample study-A IC scalp maps after polarity normalization using convex relaxation.	34
Figure 3.4. A comparison of execution times for the convex relaxation and Monte Carlo methods.....	35
Figure 3.5. Equivalent dipole models for the 64 ICs in Study A located within 10 mm of the occipital brain region as per the LONI cortical atlas [52].....	36
Figure 3.6. Average ERP of 64 occipital ICs of study A after polarity normalization.	37
Figure 4.1. A sample 96 template component scalp maps	46
Figure 4.2. Correlations between eye-activity related component scalp map	47
Figure 4.3. Receiver Operator Characteristic (ROC) curve for EyeCatch	48
Figure 5.1. Histogram of equivalent dipole scalp map residual variances of brain dipoles.....	60
Figure 5.2. Over 130k EEG independent component (IC) brain source equivalent dipole locations, plotted as counts in 8-mm ³ MNI template brain voxels.....	61
Figure 5.3. (top) Axial view of computed dipole source density across the datasets. (bottom) Sagittal view.	62
Figure 5.4. (top) Axial distribution of brain areas with higher than random equivalent dipole density.....	63
Figure 5.5. Average residual variance (two-tailed p<0.01).....	64
Figure 5.6. Fractional Anisotropy at different brain locations (p<0.01).	65

Figure 5.7. Average dipole orientations colored by fractional anisotropy at different brain locations.	66
Figure 5.8. (a) Sample 2D slice of anatomical (MNI) brain volume mask	66
Figure 5.9. Three views of radial orientations for MNI brain volume.	67
Figure 5.10. Angle (in degrees) between average dipole orientation and the radial vector at each location ($p < 0.01$).	68
Figure 5.11. Histogram of the angle between radial orientation and the average dipole orientation at each brain voxel. Most IC equivalent dipole orientations have a < 30 degree angle with the radial orientation.	69
Figure 6.1. Timeline of each RSVP burst.....	118
Figure 6.2. Finding equivalent IC processes across subjects and/or session.....	119
Figure 6.3. IC-pair ERP and ERSP similarities.....	120
Figure 6.4. Dipole locations and cluster-mean ERSPs for 6 of 15 IC clusters obtained from PCA-based clustering	121
Figure 6.5. Dipole locations and mean Target ERSPs for a subset of clusters with weak ERSP values.....	122
Figure 6.6. Measure Projection Analysis	123
Figure 6.7. Alternative visualization of ERSP domains projected onto the template MNI cortical surface.....	124
Figure 6.8. (A) ERSP Domain 2 dipoles with probability of membership in the domain above 0.05.....	125
Figure 6.9. (A) Simulated ground-truth domain set consisting of four anatomical regions	126
Figure 6.10. (A) Simulated sample points to illustrate Threshold-based clustering. .	127
Figure 7.1. (A and B, C and D right) Subject space visualizations using 2-D multi-dimensional scaling	149
Figure 8.1. Time line of the task.....	170

Figure 8.2. Best-classifying component scalp maps and their time/frequency weights ..	171
Figure 8.3. Frontal source features were highly weighted in many though not in all subjects ..	172
Figure 8.4. Spatial distributions and exemplar voxel time-frequency weight maps ..	173
Figure 9.1. Sample ordered ROI pair ..	184
Figure 9.2. A schematic and description of two-back experiment paradigm, reproduced from [133] ..	185
Figure 9.3. Total ordered dipole pair density in each ordered ROI pair. Relatively few ROI pairs contain the majority of the density. ..	186
Figure 9.4. ROI-pairs with significant ($p < 0.05$, FDR corrected) effective time-varying theta band (5-7 Hz).....	187
Figure 9.5. Reproduced from [129]: “Time-varying theta-band (3-7 Hz) dDTF group-level inferences with 99% confidence intervals.	188
Figure 10.1. Sum of leave-one-out cross-validation ROVs at different low-pass frequencies for three ICs.	194
Figure 10.2. Original ERP (thin black) and optimal low-passed filtered ERP (at 7 Hz, thicker magenta) for an IC from the RSVP experiment.	195
Figure 10.3. ROV comparison between optimal and 20 Hz low-pass filtering of ERPs	196
Figure 10.4. Optimal low-pass frequencies for the top 30 high variance 30 ICs	197
Figure 10.5. (top) Areas with significant ($p < 0.05$, FDR corrected) MPA convergence values using ERPs low-passed at 20-Hz.	198
Figure 10.6. Areas with significant ($p < 0.05$, FDR corrected) ERSP convergence in green and areas with significant ERP convergence in red for 20-Hz low-passed.....	199
Figure 11.1. sample IC and its equivalent dipole in the right occipital region.....	210
Figure 11.2. Optimally low-passed ERP of the sample IC in red and the projected ERP from all other study sessions, scaled to equal L-2 norm, in green.	211

Figure 11.3. Correlations between the average ERP from all (118) trials and ERPs calculated by averaging	212
Figure 11.4. Percent ROV improvement using collaborative averaging compared to regular averaging for different number of trials.	213
Figure 11.5. Shows how many more trials, compared to using collaborative averaging, are needed to achieve the same level of correlation with the ERP calculated from all 118 trials.	214
Figure 11.6. Optimal weight for the average of other subjects, obtained by collaborative averaging for different number of trials.	215
Figure 11.7. Target ERP of the select IC from all trials (gray), the first 30 trials (blue) and collaborative averaging using the first 30 trials of the subject and individually weighted patterns from other subjects.	216
Figure 11.8. Correlations between the average ERP from all (118) trials and ERPs from a subset of trials calculated by regular averaging (black).....	217
Figure 11.9. Cross-validation reduction of variance (ROV) values for different numbers of trials and different pattern estimation methods.	218
Figure 11.10. Cross-validation reduction of variance (ROV) values for different numbers of trials and different pattern estimation methods.	219
Figure 12.1. Illustrating how averaging can produce an incorrect ERP estimate in the presence of overlapping activity due to closely spaced cognitive events.	231
Figure 12.2. Comparison of ERP estimates by averaging (<i>red</i>) and regression (<i>blue</i>)	232
Figure 12.3. Comparison between averaging and regression ROV for EEG channels and ICA components.	233
Figure 13.1. Trial schematic for an RSVP experiment [6].....	245
Figure 13.2. A system for real-time HED tagging and synchronous recording of EEG data and events.	246
Figure 13.3. Hierarchical representation of HED-tagged event types from 18 archived studies.	247

Figure 14.1. Flowchart of the proposed HeadIT Measure Search Engine.....	277
Figure 14.2. Flowchart of event-related measure comparison using measure projection.....	278
Figure 14.3. (top) input query, and (bottom) top-ranked ERSP measure search results	279

LIST OF TABLES

Table 5.1. Anatomical regions with high dipole density.....	70
Table 5.2. Average residual variance (RV) of anatomical regions with significantly low or high RV	74
Table 6.1. Anatomical locations, Brodmann areas, and nearby clusters associated with each ERSP domain.	140
Table 6.2. MPA performance scores for simulation results with a voxel significance p-value threshold of 0.05 and varying noise levels.	143
Table 8.1. Anatomical locations associated with domains in Figure 8.4.	174

ACKNOWLEDGEMENTS

I would like to acknowledge Professor Ken Kreutz-Delgado for his kind support as the chair of my committee and teaching me about signal processing and machine learning tools. I would also like to thank Professor Scott Makeig for teaching me about data collection, application of ICA to EEG, source localization techniques and basically 'almost everything I know about EEG analysis' in the last eight years. Lastly, I would like to thank Swartz Center for Computational Neuroscience for offering me a generous scholarship that supported my doctoral education.

Chapter 2, in part, is a reprint of the material as it appears in N. Bigdely-Shamlo, T. Mullen, K. Kreutz-Delgado, and S. Makeig, "Measure projection analysis: a probabilistic approach to EEG source comparison and multi-subject inference," NeuroImage, vol. 72, pp. 287-303, May 15 2013. The dissertation author was the primary investigator and author of this paper.

Chapter 3, in full is currently being prepared for submission for publication of the material. N. Bigdely-Shamlo, K. Kreutz-Delgado and S. Makeig. The dissertation author was the primary investigator and author of this material.

Chapter 4, in full, is a reprint of the material as it appears in N. Bigdely-Shamlo, K. Kreutz-Delgado, C. Kothe, S. Makeig, "EyeCatch: Data-mining over half a million EEG independent components to construct a fully-automated eye-component detector," Engineering in Medicine and Biology Society (EMBC), 2013 35th Annual

International Conference of the IEEE , vol., no., pp.5845,5848, 3-7 July 2013, doi: 10.1109/EMBC.2013.6610881. The dissertation author was the primary investigator and author of this paper.

Chapter 6, in full, is a reprint of the material as it appears in N. Bigdely-Shamlo, T. Mullen, K. Kreutz-Delgado, and S. Makeig, "Measure projection analysis: a probabilistic approach to EEG source comparison and multi-subject inference," NeuroImage, vol. 72, pp. 287-303, May 15 2013. The dissertation author was the primary investigator and author of this paper.

Chapter 8, in full is currently being prepared for submission for publication of the material. C. Kothe, N. Bigdely-Shamlo, M. Westerfield, J. Townsend, S. Makeig. The dissertation author was the secondary investigator and author of this paper.

Chapter 12, in full, is a reprint of the material as it appears in M. D. Burns, N. Bigdely-Shamlo, N. J. Smith, K. Kreutz-Delgado, S. Makeig, "Comparison of averaging and regression techniques for estimating Event Related Potentials," Engineering in Medicine and Biology Society (EMBC), 2013 35th Annual International Conference of the IEEE , vol., no., pp.1680,1683, 3-7 July 2013 doi: 10.1109/EMBC.2013.6609841. The dissertation author was the secondary investigator and author of this paper.

Chapter 13, in full, is a reprint of the material as has been submitted for publication and will appear in N. Bigdely-Shamlo, K. Kreutz-Delgado, K. Robbins, M.

Miyakoshi, M. Westerfield, T. Bel-Bahar, C. Kothe, J. Hsi, and S. Makeig, "Hierarchical Event Descriptor (HED) Tags for Analysis of Event-Related EEG Studies," IEEE GlobalSIP, Austin, TX, 2013. The dissertation author was the primary investigator and author of this paper.

Chapter 14 , in full, is a reprint of the material as has been submitted for publication and will appear in N. Bigdely-Shamlo, K. Kreutz-Delgado, C. Kothe, S. Makeig, "Towards an EEG Search Engine," IEEE GlobalSIP Conference, Austin, TX, 2013. The dissertation author was the primary investigator and author of this paper.

VITA

2003	Bachelor of Science in Physics, Sharif University of Technology
2005	Master of Science in Computational Science, San Diego State University
2005-2013	Programmer/Analyst, Swartz Center for Computational Neuroscience, Institute for Neural Computation, University of California, San Diego
2014	Doctor of Philosophy, University of California, San Diego

PUBLICATIONS

N. Bigdely-Shamlo, T. Mullen, K. Kreutz-Delgado, and S. Makeig, "Measure projection analysis: a probabilistic approach to EEG source comparison and multi-subject inference," *NeuroImage*, vol. 72, pp. 287-303, May 15 2013.

N. Bigdely-Shamlo, K. Kreutz-Delgado, C. Kothe, S. Makeig, "EyeCatch: Data-mining over half a million EEG independent components to construct a fully-automated eye-component detector," *Engineering in Medicine and Biology Society (EMBC)*, 2013 35th Annual International Conference of the IEEE , vol., no., pp.5845,5848, 3-7 July 2013, doi: 10.1109/EMBC.2013.6610881.

N. Bigdely-Shamlo, K. Kreutz-Delgado, K. Robbins, M. Miyakoshi, M. Westerfield, T. Bel-Bahar, C. Kothe, J. Hsi, and S. Makeig, "Hierarchical Event Descriptor (HED) Tags for Analysis of Event-Related EEG Studies," *IEEE GlobalSIP*, Austin, TX, 2013.

N. Bigdely-Shamlo, K. Kreutz-Delgado, C. Kothe, S. Makeig, "Towards an EEG Search Engine," *IEEE GlobalSIP Conference*, Austin, TX, 2013.

N. Bigdely-Shamlo, A. Vankov, R. Ramirez, S. Makeig, "Brain Activity-Based Image Classification From Rapid Serial visual Presentation," *IEEE Transactions on Neural Systems and Rehabilitation Engineering*, 2008, vol. 16, no 4.

- N. Bigdely-Shamlo, S. Makeig, "Mind-Mirror: EEG-Guided Image Evolution", Proceedings of the 13th inter. Conf. on Human-Computer interaction, Lecture Notes In Computer Science, vol. 5611. Springer-Verlag, Berlin, Heidelberg, 569-578, 2009.
- M. D. Burns, N. Bigdely-Shamlo, N. J. Smith, K. Kreutz-Delgado, S. Makeig, "Comparison of averaging and regression techniques for estimating Event Related Potentials," Engineering in Medicine and Biology Society (EMBC), 2013 35th Annual International Conference of the IEEE , vol., no., pp.1680,1683, 3-7 July 2013 doi: 10.1109/EMBC.2013.6609841.
- T. Rognon, R. Strautman, L. Jett, N. Bigdely-Shamlo, S. Makeig, T. Johnson, K. Robbins, "CTAGGER: Semi-structured Community Tagging for Annotation and Data-mining in Event-rich Contexts," IEEE GlobalSIP Conference, Austin, TX, 2013.
- C. Kothe, T. Mullen, N. Bigdely-Shamlo, Z. Zhilin, K. Kreutz-Delgado, "Evolving Signal Processing for Brain–Computer Interfaces," Proceedings of the IEEE, 2012, vol. 100, pp. 1567 - 1584, DOI: 10.1109/JPROC.2012.2185009.
- K. Gramann, J.T. Gwin, N. Bigdely-Shamlo, D.P. Ferris, S. Makeig, "Visual evoked responses during standing and walking," Frontiers in Human Neuroscience, 2010, vol. 3, p. 202.
- A. Mueen, E. Keogh, N. Bigdely-Shamlo, "Finding Time Series Motifs in Disk-Resident Data", IEEE International Conference on Data Mining series (ICDM), 2009.
- E. A. Edelstein, K. Gramann, J. Schulze, N. Bigdely-Shamlo, E., van Erp, A. Vankov, S. Makeig, E. Macagno, "Neural responses during navigation and wayfinding in the virtual aided design laboratory - Brain dynamics of re-orientation in architecturally ambiguous space", Report series of the Transregional Collaborative Research Center SFB/TR8 Spatial Cognition, University Bremen, University Freiburg, 2008,
- A. Delorme, T. Mullen, C. Kothe, Z. A. Acar, N. Bigdely-Shamlo, A. Vankov, S. Makeig, "EEGLAB, SIFT, NFT, BCILAB, and ERICA: New Tools for Advanced EEG Processing," Computational Intelligence and Neuroscience, vol. 2011, Article ID 130714, 12 pages, 2011. doi:10.1155/2011/130714.

ABSTRACT OF THE DISSERTATION

Combining EEG Source Dynamics Results across Subjects, Studies and Cognitive

Events

by

Nima Bigdely-Shamlo

Doctor of Philosophy in Electrical and Computer Engineering (Intelligent Systems,
Robotics, and Control)

University of California, San Diego, 2014

Professor Kenneth Kreutz-Delgado, Chair

This dissertation contains several projects, each providing a solution contributing to an aspect of group-level source-level EEG analysis. I explore different methods to extract better EEG measures from individual subjects: regression to reduce confounds originated from temporal proximity of cognitive events, optimal low-pass filtering to calculate better ERPs and collaborative averaging to obtain better measures from small numbers of trials. I introduce two methods for combining source-based EEG information, calculated with ICA and equivalent dipole localization, across subjects in a study: Measure Projection Analysis (MPA) allows study-level analysis for measures, such as ERP and ERSP, that are associated with single brain areas while

Network Projection Analysis enables combining network measures, such as effective connectivity, associated with an ordered pair of brain area.

The last two chapters of the dissertation are dedicated to discussing meta-analysis, i.e. combining information across multiple studies. This is a subject that is well developed in the fMRI field but is new in the field of source-based EEG analysis. I introduce a user-friendly schema (Hierarchical Event Descriptors, or HED), based on established cognitive ontologies, to describe cognitive event and states in a hierarchical and machine readable manner. HED facilitates automated meta-analysis and can benefit researchers by simplifying statistical designs and streamlining event information handling.

The current EEG analysis-publication workflow mostly documents qualitative descriptions of event-related EEG dynamics. This makes it difficult to look for comparable results in the literature since search options are limited to textual descriptions and/or similar-appearing results depicted in the paper figures. In the final chapter I demonstrate a method for quantitative comparison of source-resolved results (e.g., ERPs, ERSPs) across different EEG studies. The proposed *source-resolved EEG measure search engine* receives search queries composed of event-related EEG measures, each associated with an estimated brain source location to be compared using Measure Projection Analysis (MPA) to all records in the search engine database accumulated by automated data analysis workflows applied to data of multiple studies. A similarity-ranked list of events from other studies that have elicited similar EEG

dynamics in nearby source-locations is then returned to the user along with their experiment and event metadata.

Chapter 1

Introduction

In this dissertation I present a set of methods that enable the calculation of EEG source dynamics at the subject level and analyses of this information in and across studies. This is a worthwhile goal for three reasons (a) to further our understanding of human brain we need to be able to make statements that apply to more than a single participant, or small group of participants; (b) A large portion of the knowledge produced in EEG analysis field starts from digital data but is ultimately presented and published as natural text or figures, and hence is not accessible to meta-analysis and ‘big data’ analytics. Developing methods to facilitate automated knowledge generation from multiple studies and schemas to make collected data understandable to computer algorithms will significantly impact the pace of progress in cognitive neuroscience and brain computer interface (BCI) fields, (c) Collaborative filtering [1-3] and other newly proposed advanced methods for BCI design can benefit from priors obtained from large number of participants. Future commercial applications of BCI technology are likely to depend on the success of these methods in increasing the accuracy and robustness of BCI classifier while shortening the calibration time [4].

Each of the chapters in this dissertation is focused on providing a solution contributing to an aspect of group-level source-level EEG analysis:

In Chapter 2, I introduce the EEGLAB workflow. It forms the basis of the EEG analysis discussed in other chapters. The presented workflow is based on ICA and dipole representation of sources. Other methods of source reconstruction and representation (e.g. Loreta variants [5-8] or 2-D cortical patch presentation [9, 10]) may be used in conjunction with the methods proposed in this dissertation with minor changes in notation, e.g. 3-D Gaussian densities representing dipoles in chapters of this dissertation may be replaced by current density estimates, obtained from Loreta variants, over 2-D (cortical) or 3-D brain locations.

In Chapter 3, I discuss the issue of polarity normalization for group-level analysis of ERPs from ICA sources. This is an issue that is rarely discussed yet has important statistical implications if not handled properly. We see that an intuitive and practical solution exists to tackle this problem.

In Chapter 4, I show how an Eye-related IC detection algorithm based on data from a very large number of studies can perform as well as a method that requires human intervention. As we see in Chapter 5 an automated method for this task is necessary for separating out and processing brain-related ICs in large-scale analyses.

Chapter 5 is a window into the potential of source-based EEG meta-analysis methods. It shows how much can be learned from a large number of brain source

represented by dipoles even when only their location and orientation information are used.

In Chapter 6, the Measure Projection Analysis (MPA) method is presented. It is a natural extension of the Gaussian smoothing process introduced in Chapter 5 from scalar values into vectors representing EEG measures (ERP, ERSP). MPA is one of the major contributions of this dissertation.

Investigating individual variability is an active area of research with practical applications in medicine and performance training. In Chapter 7, I discuss how subjects and recording sessions, each associated with a discrete set of equivalent dipoles, can be compared in MPA framework.

Chapter 8 shows an example of using BCI features in MPA and how it can lead to results that are compatible with the neuroscience literature and may contribute to our understanding of human brain.

In Chapter 9, I extend the MPA methodology introduced in Chapter 6 to pairs of brain regions. The proposed method, called Network Projection Analysis or NPA, allows combining effective connectivity measures (e.g. dDTF [11, 12]) across subjects to study brain network dynamics.

Estimation of accurate EEG measures is necessary for obtaining statistically significant results at group level. I show in Chapter 10 that a proposed method for

adaptive low-pass filtering of ERPs can have a sizable effect on study-level results obtained from MPA.

The concept of ‘optimally predictive pattern’, introduced in Chapter 10, is exploited Chapter 11 and an algorithm for increasing the accuracy of measure estimation from a small number (<30) of single trials is presented. The results show that single subject EEG analysis could benefit from the group-level estimates.

In Chapter 12, I continue to explore ways to improve the estimation of EEG measures. Making conclusions based on results from a single EEG study requires careful attention to potential confounds and a major portion of these are caused by temporal proximity of cognitive events. This proximity is often inevitable in experimental paradigms, e.g. feedback request stimuli are often shortly followed by button press or other types of response. I show how the assumption that time-locked EEG dynamics from nearby events are linearly added together at each time point leads to the use linear regression for EEG measure estimation. The results in this chapter indicate that regression can provide significantly better estimates compared to averaging. By automating the removal of a large portion of confounds, temporal regression can also improve meta-analysis.

The last two chapters of my thesis are dedicated to discussing meta-analysis, i.e. combining information across multiple studies. This is a subject that is well developed in the fMRI field ([13-18]) but is new in the field of source-based EEG

analysis. In Chapter 13 I introduce a user-friendly schema (Hierarchical Event Descriptors, or HED), based on established cognitive ontologies, to describe cognitive event and states in a hierarchical and machine readable manner. HED facilitates automated meta-analysis and can benefit researchers by simplifying statistical designs and streamlining event information handling.

Lastly, in Chapter 14, I propose an EEG Search Engine that receives EEG measures, sets of brain regions of interest (ROIs), and HED tags as input queries and returns patterns from different studies that are most similar to these queries. The proposed search engine is built on MPA and uses a database of source-resolved EEG measures obtained from multiple studies.

Such a database can benefit from the various algorithms proposed in this dissertation: HED tags will be needed to describe events so they may be matched to input queries, temporal regression may be used to remove confound, optimal low-pass filtering may be employed to adaptively remove high-frequency noise, or collaborative averaging may be applied to better estimate measure from few trials. It is also possible to extend the engine and search across patterns of network connectivity with NPA.

The vision of enabling and exploiting comprehensive multi-study measure databases is one of the main motivations behind my dissertation. Such databases in fMRI, such as BrainMap [13-16] have greatly impacted the field (over 118 publication

in 2012 cited BrainMap papers) and it is time for EEG analysis to benefit from similar resources.

Chapter 2

EEGLAB Workflow

2.1 Introduction

EEGLAB is one of the most popular EEG analysis software toolkits used in laboratories around the world (based on a recent survey of 687 research respondents [19]). I was involved in the development of functions and toolboxes for EEGLAB during the eight year period of 2005-2013. Many of signal processing steps used in EEGLAB are common to other EEG analysis environments. However EEGLAB offers the most options for processing data separated into independent sources using ICA algorithm [20, 21].

2.2 Application of ICA in EEG Analysis

ICA [20] has become a method of widespread interest for analysis of EEG data [22], [23], [24], [25], [26]. In this approach to EEG source analysis, unaveraged continuous or epoched EEG data from multiple scalp channels are decomposed into independent component (IC) processes by learning a set of spatial filters that have fixed relative projections to the recording electrodes and produce maximally

independent individual time courses from the data. ICA thus learns *what* independent processes (information sources) contribute to the data and also reveals their individual scalp projection patterns (scalp maps), thereby simplifying the EEG inverse source localization problem to that of estimating *where* each source is generated, a much simpler problem than estimating the source distributions of their ever-varying linear mixtures as recorded by the scalp electrodes themselves.

The IC filters linearly transform the representational basis of EEG data from a channel matrix (scalp channels by time points) to a sum of independent component processes with maximally independent time courses and fixed scalp projections (scalp maps, with often strongly overlapping topographies). Many ICs predominately account for the contributions to the channel data from a non-brain ('artifactual') source process -- for example potentials arising from eye movements, scalp muscle activity, the electrocardiogram, line noise, etc., while many other ICs are compatible with a source within the brain itself, in particular within its convoluted cortical shell in which most of the spatially organized potentials reaching the scalp are generated [27].

2.3 Equivalent Dipole Model for ICs

Many of the brain-based ('non-artifactual') IC scalp topographies may be modeled as the projection of a single equivalent dipole inside the brain volume [26]. ICA algorithms return many such 'dipolar' IC data sources (those for which most of the spatial variance of the electric field pattern they produce on the scalp is accounted

for by the projection of a single ‘equivalent’ dipole). On average, the more independent the resulting ICs returned by an linear ICA decomposition method, the more near-dipolar ICs are returned [28]. Such dipolar ICs are compatible with an origin in locally-synchronous cortical field activity within a single cortical patch, which by biophysics must be located near to and oriented predominantly perpendicular to the equivalent dipole [29] (A few clearly brain-based ICs may have scalp maps very closely resembling the summed projection of two bilateral cortical patches that contribute synchronous activity to the scalp signals).

Finding the actual cortical patch (or patches) generating a given dipolar IC may be difficult [10], as it requires (at least) a good quality MR head image for the subject and accurately recorded scalp electrode positions [30]. Given a good estimate of where the scalp electrodes were placed on the head, and a near-dipolar IC scalp map, the location of the equivalent dipole may be found reliably, in many cases with less than a centimeter error when 3-D electrode positions are recorded (Akalin Acar, submitted) and an accurate skull conductance value is used in the analysis. Biophysical simulations also show that the equivalent dipole for a cm^2 -scale cortical patch source is, on average, less than 2 mm from the center of the generating patch (Akalin Acar, unpublished). Thus, a unique advantage of ICA applied to EEG is that localizing sources from its single-source IC scalp maps avoids uncertainties associated with multiple local minima that limit the accuracy of estimates of the more complex source distributions computed from scalp maps that sum projections of multiple

sources -- for example nearly all raw EEG scalp maps or maps for later peak latencies in ERP waveforms. Of course this level of spatial accuracy is only possible using single-subject head models, which are possible only when an MRI head image is available (as it was not for our subjects).

2.4 EEGLAB Workflow

Figure 2.1 shows EEGLAB single session and group analysis workflows. The preprocessing step often involves the following operations in this order:

1. **High-pass filtering:** The main reason for this step is to remove DC and very low frequency (<0.1Hz) drifts due to capacitance coupling and other factors as these are often much larger in amplitude than the EEG signal. Also, since the dynamics of EEG in low frequencies EEG (<1 Hz) are significantly different from higher frequency [31], and lower frequencies contain significantly more power, ICA results on data high-passed at 1 Hz often better relate to dipolar brain sources. It is suggested then to perform ICA on data high-passed at 1 Hz.
2. **Removal of electrical power line noise (optional):** 60 Hz (or 50 Hz in other countries) electrical power line noisy is often strongly present in raw EEG. ICA is often able to separate line noise into a subspace of a few scalpmaps, but if an experiment involves a significant head rotation or other movement that changes the relative position of electrodes to external power lines ICA may fail to properly remove the line noise, or ICA results may be degraded by this

noise. It is then recommended to remove this noise either by application of a notch filter, or using the more advanced ‘CleanLine’ method [32].

3. **Noisy channel detection:** EEG sensors may lose their electrical connection with the scalp during an experiment, e.g. due to subject movement, drying of the conductive gel, etc.. This loss of connection may be intermittent, e.g. a few seconds, or may continue for most of the experiment. Such poorly affixed electrodes often pick up a significant amount of noise and their inclusion in subsequent analysis may significantly degrade the quality of results. These noisy channels are often detected by visual inspection or with automated methods that examine the statistics of their activations (e.g. via correlation to neighboring channels, amplitude statistics), and then excluded from the analysis.
4. **Re-referencing:** The goal of referencing is to remove any so-called ‘common noise’ from all channels. This is performed by estimating the time course of common noise and then removing it, at each time point, from all channels. The three most popular ways to estimate the common noise are (a) merely sensing right or left mastoid signal (detected by the electrode below the ear). This is based on the assumption that this channel receives the least amount of EEG and hence it should be dominated by the common noise. (b) Measuring the average of left and right mastoid EEG channels (this provides less lateralized bias). (c) Computing the average of all channels: This offers the least amount of spatial bias. It is important to remember that re-referencing reduces the rank of the EEG data by one (1), and

that proper care (e.g. by computing PCA up to the rank of the new data) should be taken when applying ICA to the resulting rank-deficient data.

5. **Data Exclusion:** It is usually necessary to exclude portions of the data that contain artifacts before applying ICA as they often have significantly higher amplitude and degrade ICA decomposition quality for uncontaminated portions of the data. This ‘data cleaning’ step may be performed visually or by automated methods that examine the statistics (e.g. unusual amplitudes) of small windows of the data. Recently an advanced artifact correction method, called Artifact Subspace Reconstruction (ASR) [33] is proposed that eliminates high amplitude noise from data segments while maintaining and their full-rank.

After these preprocessing steps have been performed, the ICA algorithms can be applied to the whole data, or to the segments of interest (e.g. excluding segments between experiment blocks when participants were resting and not engaged in the experiment). Also, ICA may be applied to data high-passed over 1-Hz and the ICA unmixing matrix then be applied to data that includes lower, e.g. 0.1 – 1 Hz frequencies. This is sub-optimal in terms of mutual information reduction expected from ICA but may allow for the analysis of low-frequency dynamics of brain sources found by ICA.

The next step is to find single or a bilaterally symmetric pair of, equivalent dipoles that explain a large portion (e.g. over 85%) of the variance of scalp maps obtained from ICA (see section 6.2 for a more detailed discussion). After identifying

time markers associated with cognitive events of interest, segments of EEG, or *epochs*, surrounding these markers are extracted to form an ‘epoched dataset’. EEG measures (such as ERP, ERSP, etc.) are then calculated for ICs of interest from epochs that are deemed to be relatively free of noise (either by visual inspection or via the use of automated methods). These calculated measures are then aggregated across all recording session in a study and used for group analysis. Figure 2.2 shows a flowchart of this workflow.

Before the introduction of the Measure Projection Toolbox (MPT, see Chapter 6), IC clustering with PCA and *k*-means (see section 6.3.6) was the recommended method for group analysis in EEGLAB. Due to the large number of tunable parameters in this method (e.g. number of clusters and the relative weights for different measures), the practical application of IC clustering often involves an iterative process (see Group Study Analysis in Figure 2.1) of selecting a set of parameters, which is typically done by visually inspecting the results for (subjectively) ‘nice looking’ clusters and changing the parameters to obtain ‘better looking’ results (e.g. more compact clusters or more clusters with significant differences across conditions). A detailed analysis of IC clustering and its drawbacks is provided section 6.5.

2.5 Acknowledgments

Chapter 2, in part, is a reprint of the material as it appears in N. Bigdely-Shamlo, T. Mullen, K. Kreutz-Delgado, and S. Makeig, "Measure projection analysis: a probabilistic approach to EEG source comparison and multi-subject inference," NeuroImage, vol. 72, pp. 287-303, May 15 2013. The dissertation author was the primary investigator and author of this paper.

2.6 Figures

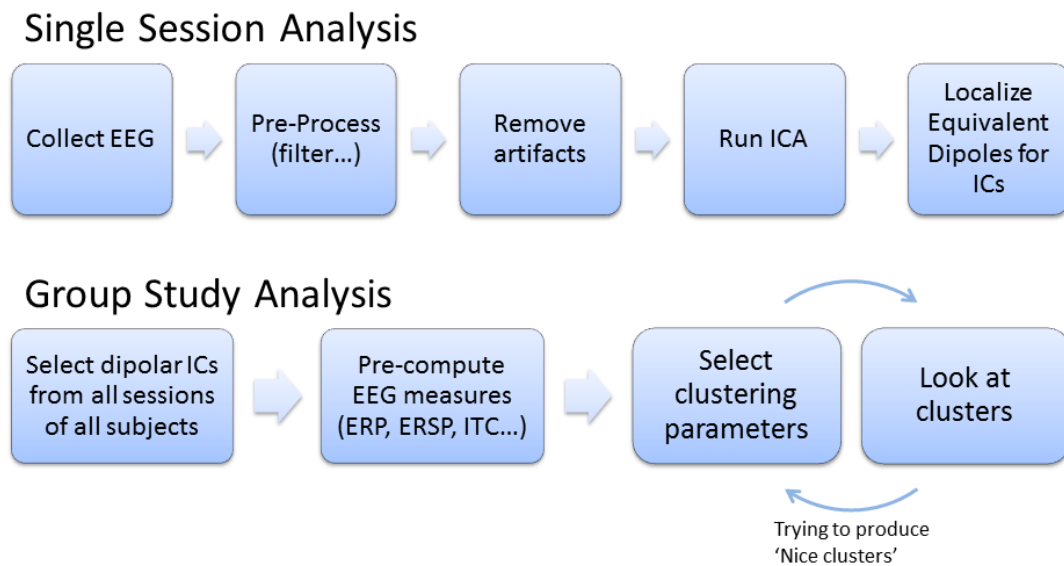


Figure 2.1. EEGLAB single session and group analysis workflows.

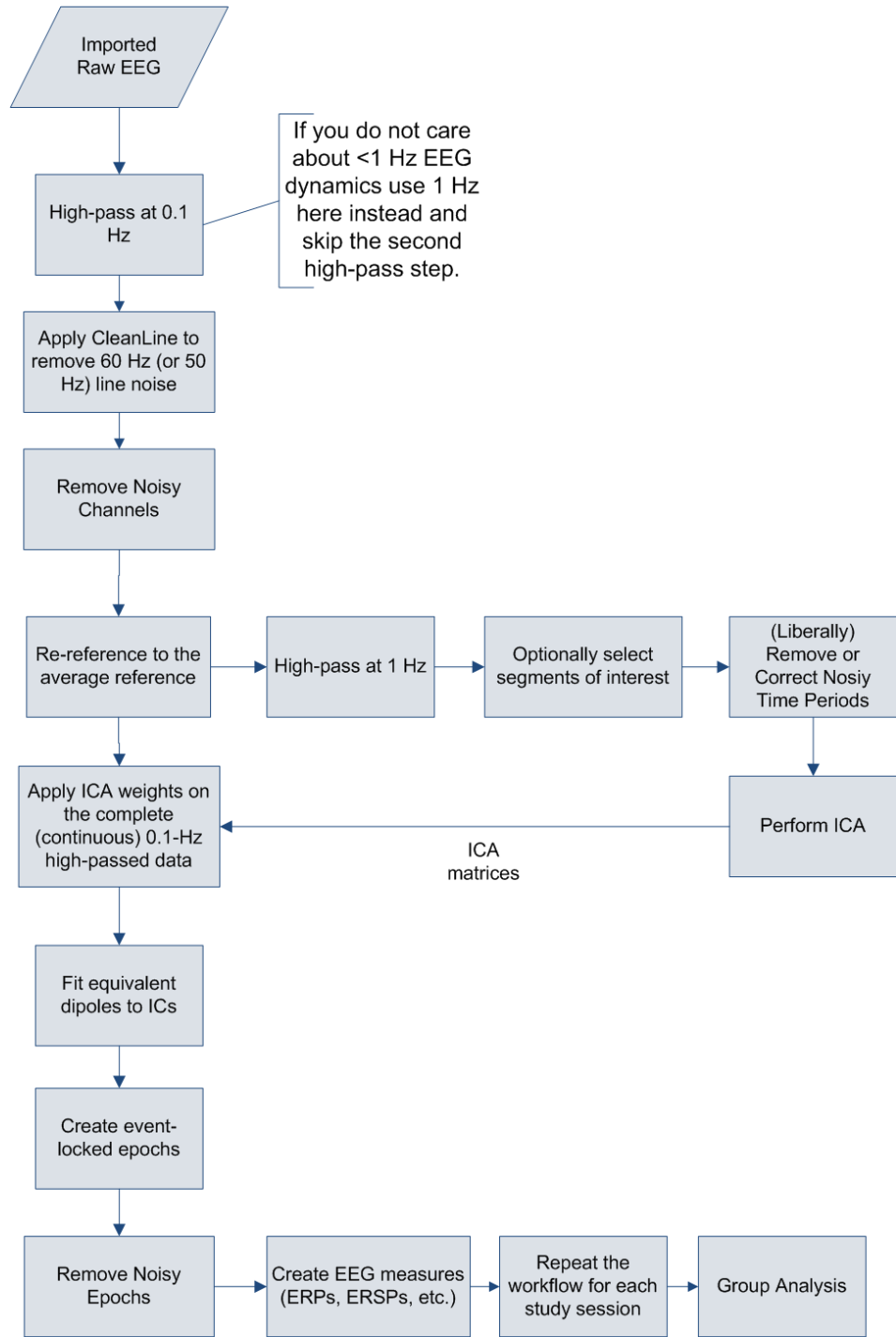


Figure 2.2. EEGLAB single session analysis workflow.

Chapter 3

EEG Independent Component

Polarity Normalization by Two-way Partitioning

3.1 Abstract

Independent Component Analysis (ICA) is a popular method for finding independent brain and artifact sources in EEG data. But there exists an inherent indeterminacy in the polarity of the scalp map and activation associated with each Independent Component (IC), when considered separately from its associated time course, that can interfere with the comparison and interpretation of the learned IC topographies from multiple subjects. These polarities need to be assigned in a consistent manner to allow IC activations to be used in multi-subject inference or in training Brain Computer Interface (BCI) models based on IC activations from more than one subject or recording session. Here we propose two IC map polarity normalization methods, both based on solving a Two-way Partitioning problem. The

first method uses convex relaxation while the second employs a Monte-Carlo approach. We test these methods on two sample studies and show that both generate reliable and equally well-formed solutions. However, the Monte-Carlo approach can be up to 89 times faster and is applicable to larger problems.

3.2 Introduction

Independent Component Analysis (ICA) is a popular method for finding maximally distinct brain and artifact sources in EEG data [20, 22, 25, 34]. The effectiveness of ICA in EEG analysis is rooted in the linear mixing of electrical potentials generated by brain and artifact sources at scalp recording electrodes, and in the ability of ICA algorithms to undo this mixing by exploiting statistical properties of the signals (e.g., by assuming spatial stationarity of the source projections to the scalp channels and statistical independence among the source activities). In particular, the input EEG channel data matrix $D \in R^{n \times m}$ (n channels by m samples) can be factorized into two matrices:

$$D = S A \quad (1)$$

where:

$S \in R^{n \times n}$ is the Source projection matrix: each column of this matrix contains the spatial (topographical) pattern of electrical potential produced by a single ICA source (IC) at the scalp channels.

$A \in R^{n \times m}$ is the Source activation matrix: each row of this matrix contains the temporal dynamics of source activity.

Because this is a blind source separation problem (i.e., both of the multiplicative matrix factors are unknown), there are two inherent indeterminacies, one is the ordering of the ICs (i.e., of the columns of S , which is irrelevant for EEG analysis); the other is the scaling, which is by Equation (1) split across the component activations and topographic source projections (scalp maps) [35]. The only observable quantity for each source is its projected potential at the scalp electrodes, which remains the same if both scalp map factor and activation vectors are multiplied by, respectively, any non-zero scaling factor and its inverse. Normalization of the component scalp maps to give them a unit L2 norm (in the appropriate physical units, e.g., microvolts) partially fixes this problem, but an ambiguity in the joint scalp map and activation time course polarities (i.e., of the +1 signs) still remains for each IC separately (i.e., for each column of S). To perform multi-subject analyses and online classifier learning, it is desirable to make the IC scalp map polarities from nearby and potentially equivalent sources across subjects and/or sessions maximally coherent.

Otherwise, when calculating averages over IC activities, polarity reversals may result in erroneous signal cancellation.

Although joint decomposition methods such as group-ICA [36], [37], [38], [39] [40], multi-set canonical correlation analysis [41] [42], and J-BSS [43] [44] have been proposed to solve this problem, these methods are often based on one of two assumptions (see [45] for detailed discussion): (a) subjects share common group-level scalp maps. This is not accurate since cortical folding is different across subjects [27]; (b) there are linear dependencies across activations of different subjects resulting in shared event-locked group IC component measure features. The latter could be only true if these activities are time-locked to certain experimental events and these events produce salient ERPs with significant similarities across subjects. This assumption may not be valid when there are no time-locked events (e.g., for resting EEG), in time periods further than a few seconds from events of interest, or in the case of many EEG phenomena that occur in time-frequency domain (ERSP) in such a way as to contribute few or no features to average ERPs (e.g., changes in alertness level [46]). Alternatively, the path we follow is to achieve polarity normalization by forcing ICs with similar scalp maps to have similar polarities (i.e., when signals are real, making the inner product of their scalp map vectors positive). Here we first show how this can be achieved using convex relaxation of a two-way partitioning problem.

3.3 Methods

3.3.1 Problem Description

We want to find a vector of scalp map polarities $x \in R^n, x_i \in \{-1, 1\}, i = 1..n$ in a study with n ICs that minimizes the negative sum of normalized scalp map inner products

$$W_{i,j} = \frac{-s_j^T s_i}{\|s_i\| \|s_j\|} \quad (2)$$

where the inner products comprise the components of a matrix W and S_i is the i th column of the study source projection matrix S . This matrix is created by concatenating select columns of ICA source projections matrices from different sessions and/or subjects in the study. The IC selection criterion is a low residual variance in fitting the IC scalp map with an equivalent dipole model associated with a cortical source. The scalar quantity $x^T W x$, subject to the constraint that the components of x are either +1 or -1, provides an aggregate measure of total dissimilarity across scalp maps in the study, the quantity we desire to minimize with respect to the x -component signs. This is because

$$x^T W x = \sum_{i=1..n} x_i \sum_{j=1..n} W_{i,j} x_j = \sum_{i,j=1..n} x_i x_j W_{i,j} \quad (3)$$

gives the sum of scalp map inner products after changing their polarities according to the signs of the components of the x vector. We can formulate this as the following optimization problem, also called a Two-way Partitioning problem [47]:

$$\text{minimize } f_0 = x^T Wx, \text{ subject to } x_i \in \{-1, 1\}. \quad (4)$$

Note that this problem is not convex since the domain of $x_i \in \{-1, 1\}$ is not convex. A possible convex relaxation candidate for this problem could be to allow $x_i \in [-1, 1]$, but our experiments show that this does not produce useful results since the continuous scaling permitted by this relaxation dominates the solution, so that using $\text{sign}(x)$ for x allowed to vary in value continuously on the interval does not effectively minimize the objective function in Equation (4).

3.3.2 Convex solution

An alternative convex formulation which is effective in finding approximation solutions to Equation (4) can be derived by re-writing it in the equivalent form

$$\begin{aligned} & \text{minimize } \text{tr}(WX), \\ & \text{subject to } X \succeq 0, \\ & \quad \text{rank}(X) = 1, \\ & \quad X_{ii} = 1, \quad i = 1, \dots, n \end{aligned} \quad (5)$$

with symmetric positive semi-definite variable $X \in \mathbb{S}^n$, $X = xx^t$ (since $\text{tr}(WX) = \sum_{i,j=1..n} X_{ij}W_{ij}$ and $X_{ij} = x_i x_j$). We then employ convex relaxation, a popular method in optimization [47], and drop the $\text{rank}(X) = 1$ constraint to obtain the convex optimization problem

$$\text{minimize } \text{tr}(WX),$$

$$\text{subject to } X \geq 0, X_{ii} = 1, i = 1, \dots, n \quad (6)$$

Since this new problem is less constrained, its optimal value will provide a lower bound on the optimal value of the original problem (Equation (4)). After solving problem Equation (4), we are able to obtain the vector of polarities x from $X = x^t x$ using the real Schur decomposition $X = U Q U^T$ where U is a unitary matrix ($U^{-1} = U^T$) and Q is an upper triangular (in this symmetric case, diagonal) matrix. If X is low rank (recall that we have relaxed the problem by allowing it to have a rank larger than one), we can ignore all elements of this matrix except the highest value on the diagonal, located at $Q_{n,n}$. Equation 7 below shows how to obtain x (the polarity vector) from the last column of U :

$$X = U Q U^T, Q \sim \begin{bmatrix} 0 & \cdots & 0 \\ \vdots & \ddots & \vdots \\ 0 & \cdots & \sigma \end{bmatrix} \xrightarrow{X \sim x x^t} x = \text{sign}(U_n). \quad (7)$$

3.3.3 Monte Carlo solution

Another way to solve Equation (4) is to use a Monte Carlo approach and at each step calculate the cost function f_0 for a change in the polarity of a subset of scalp maps. If the new cost value is lower, the polarity change is accepted. Given enough (\rightarrow infinite) time, iterative execution of the above algorithm, using subsets of random size, can find the best solution to Equation (4). The number of subsets of size k selected from n scalp maps is

$$\binom{n}{k} = \frac{n!}{k!(n-k)!} \quad (8)$$

and grows quickly with k . We empirically found that as k increases the performance of Monte Carlo algorithm (total f_0 reduction in a few thousand iterations) is significant reduced. This is due to a reduction, at larger k values, in the proportion of subsets whose polarity reversal produces a lower cost function relative to the total number of possible subsets.

We chose $k=1$ (change the polarity of only one scalp map in each iteration) since the performance of the Monte-Carlo method on the polarity normalization problem was best for this value. We also accelerated the Monte Carlo algorithm by calculating, at each iteration, the change in the cost function

$$\Delta f_0^i = -2 \sum_{j=1..n, j \neq i} x_j W_{ij} \quad (9)$$

for a polarity x_i reversal in each scalp map and only selecting a single random scalp map from the subset of maps with $\Delta f_0^i < 0$. In this implementation, iterations continued until either a maximum number of iterations (5000) was reached or no new polarity reversals were found to give a better solution. Since the Monte Carlo is stochastic and can thus produce a different solution for each execution, we used the best solution (lowest f_o) across three runs, each starting from the original polarity vector and using a different random generator seed value.

3.4 Results

We used data from two studies. Study A consisted of data from 15 sessions in which 8 subjects performed a Rapid Serial Visual Presentation (RSVP) task [48] (the raw data are available at <ftp://sccn.ucsd.edu/pub/headit/RSVP>, the EEGLAB Study files at ftp://sccn.ucsd.edu/pub/measure_projection/rsvp_study). Each session comprised 504 4.9-s image bursts of 49 oval image clips from a large satellite image of London presented at a rate of 12/s. Some (60%) of these bursts contained one image in which a target white airplane shape was introduced at a random position and orientation. Following each burst, subjects were asked to press one of two buttons to indicate whether or not they had detected a target airplane in the burst. For further details see [48].

After preprocessing each subject data set using EEGLAB (sccn.ucsd.edu/eeglab) and custom Matlab functions to re-reference the active-reference Biosemi EEG data to an electrode over the right mastoid, we performed high-pass filtering above 2 Hz, and rejected channels and data containing non-stereotypical artifacts. An ICA decomposition was then performed for each recording session using extended Infomax ICA [20]. To focus the analysis on cortical source [28], the subset of ICs that could be represented by an equivalent dipole model with low error was selected for analysis (here, this was defined as more than 85% of channel variance in the IC scalp map being accounted for by a single equivalent dipole

or, in a few cases, a bilaterally symmetric equivalent dipole pair). ICs with equivalent dipoles located outside the MNI brain volume (e.g., those with a minimum distance to the MNI brain surface larger than 1 mm) were removed as non-brain artifact processes, leaving 266 IC scalp maps.

Figure 3.1 shows a number of these scalp maps with rectangles enclosing sample IC pairs with a similar pattern but reversed polarities. Our goal is to minimize such occurrences by changing the polarity of some of these scalp maps.

Study B consisted of data from 119 ADHD and control subjects in a “Rotated Head” P-300 study [49-51]. A similar workflow as Study A, except with high-pass filtering above 1 Hz instead of 2 Hz, was used to obtain 4,345 IC scalp maps.

We used the CVX Matlab library to solve the convex relaxation of the two-way partitioning problem (Equation (6)) associated with the polarity normalization of scalp maps in Study A and obtained matrix X . A Schur decomposition (Equation (7)) was used to find polarity vector x .

Figure 3.2 (left) shows the matrix X and the rank = 1 approximation of it, $X^1 = x^T x$, for scalp maps from Study A is displayed in

Figure 3.2 (right). The visual similarity of these plots together suggests that that the answer to the convex relaxation problem (Equation (6)) should be close to the answer of the original non-convex problem (Equation (5)).

We then applied the learned (optimized) polarity vector x to normalize scalp maps by multiplying appropriate columns of the ICA mixing (scalp map) matrix:

$$S_i^{\text{norm}} = x_i S_i, \quad i = 1, \dots, n \quad (10)$$

Figure 3.3 shows IC scalp maps of Study A from Figure 3.2. (Left) Matrix X obtained from convex relaxation with normalized polarities. Each IC pair indicated in Figure 3.2. (Left) Matrix X obtained from convex relaxation with a rectangle (IC-pairs with apparent reverse polarities) has a common polarity for the two ICs in Figure 3.3, indicating that at least in these cases our polarity optimization method has been successful.

We then performed three numerical tests: first we tested the reliability of the solutions obtained from convex relaxation and Monte Carlo methods by randomly negating the polarities of some maps in Study A (with 50% probability) in 100 trials and calculating the solutions from both methods in each trial. We then compared these solutions, both in terms of the cost function f_o , and the calculated polarity vector x . We observed that in 100% of trials the solutions from the two methods were identical and the final cost function was close to (less than 3% different than) the lower bound that may be obtained by solving the Lagrange dual problem [5] for Equation (4):

$$L(x, v) = x^T W x + \sum_{i=1}^n v_i (x_i^2 - 1) = x^T (W + \text{diag}(v)) x - 1^T v$$

$$g(v) = \inf_x x^T (W + \text{diag}(v))x - 1^T v = \begin{cases} -1^T v & W + \text{diag}(v) \geq 0 \\ -\infty & \text{otherwise,} \end{cases}$$

maximize $g(v) = -1^T v$

subject to $W + \text{diag}(v) \geq 0$ (11)

This suggests that our relaxed solution is close or equal to the solution of Equation (4). We also observed that both methods perfectly compensated for the random negation of polarities in each trial and produced a normalization vector that, when multiplied element-wise by random trial polarity reversals, resulted in effectively the same unique set of final scalp map polarities (up to a trivial global sign flip of all the maps). This implies that both polarity normalization methods produce reliable solutions.

In the next two tests we compared the two polarity normalization methods by applying them to groups of random subsets of scalp maps with different sizes. Each group contained a fixed number of random subsets with equal number of scalp maps (each subset was drawn independently from all study scalp maps and contained no duplicates). The polarities of scalp maps in each subset were randomly negated (with 50% probability) and then both normalization methods were applied to each subset (both methods were applied to the same data).

In a second test, we used Study A IC scalp maps. Subsets of study IC scalp maps were created in groups associated with 11 subset sizes linearly distributed between 50 and 260. Each group contained 50 subsets of equal size. In the third test

we used Study B scalp maps. Here, 20 groups were created for subset sizes logarithmically distributed between 50 and 524. Each of these groups contained 10 subsets, again, with equal numbers of scalp maps.

Paired *t*-test statistical comparisons between cost function f_o values of the two normalization methods showed no significant performance difference. In the second test, the significance of the difference was $p < 0.1$, and for the third test, $p < 0.13$. In combination, the statistical significance of this difference, combining data from both tests, was $p < 0.16$.

Figure 3.4 shows average execution times versus subset size for data from second and third tests on a powerful PC (Dual AMD Opteron 6238 2.6GHz twelve-core processors, 128GB RAM). Because of the high memory requirement and long execution time required, we did not try the convex optimization method on subsets with more than 524 scalp maps. As Figure 3.4 shows, the execution time of the convex method is significantly ($p < 3 \times 10^{-27}$) longer. The average speed up using the Monte Carlo method was 31 ± 0.6 times for all subset size groups and 89 ± 4.5 times for groups of subsets containing 524 IC scalp maps.

To demonstrate the application of our polarity normalization method in analyzing real data, we applied this method to 64 ICs of Study A with equivalent dipoles located in or near (distance < 10 mm) occipital areas (from LONI Atlas [52]). Figure 3.5 shows these dipoles. We calculated the average of target – non-target ERPs

of all these ICs and compared it to averages calculated from 10,000 bootstrap permutations with random polarities. Figure 3.6 shows these results with significant ($p < 0.05$) peaks at 340 and 570 ms in agreement with reported visual target (versus non-target) detection ERPs in the literature [53, 54].

3.5 Discussion and Conclusion

We showed that ICA scalp map polarities can be normalized by solving a two-way partitioning problem created from their pairwise inner products. We also introduced two methods to solve the resulting problem and compared their performance in terms of solution quality and execution speed. Our implementation of Monte Carlo method performed as well as convex optimization but ran significantly faster. It also had lower memory usage and could be scaled to larger problem sizes.

Time-domain analysis of multi-subject source activity often depends on scalp map polarities. For example, scalp map polarities affect ERP polarities that are used as input features to both Measure Projection Analysis [15] and IC clustering [27-30] as implemented in the EEGLAB environment [31, 32]. Training of source-based cross-subject brain computer interface (BCI) classifiers may also depend on scalp map polarity consistency and benefit from normalization methods demonstrated here. Matlab code implementing both these methods is included in the free, open source Measure Projection Toolbox (MPT) [15]. MPT automatically performs polarity normalization when importing ERP data.

There has been some work [33, 34] to assign correct IC scalp map polarities in channels where these polarities are inverted due to noise in ICA calculations. This noise is assumed to originate from having insufficient data, or from limitations of the ICA algorithm leading to it finding a ‘local’ instead of a global ICA solution. This problem is fully separate from the polarity normalization concept discussed here as the indeterminacy in scalp maps that we address is an inherent feature of the ICA algorithm and exists even if a global (true) solution is found by ICA.

Here we used pairwise inner product of normalized scalp maps for polarity normalization but alternative measures such as inner product of ERP time courses may also be used for this purpose. A drawback of the latter is that it could complicate the calculation of statistical significance of ERP averages since IC polarities would be normalized in a manner that encourages non-zero averages.

A comparison between ERP results obtained from group-ICA and subject-specific ICA component map polarity normalization is out of scope of this chapter, especially since such comparison would also depend on the type of group-level analysis performed on subject-specific ICA equivalent dipoles (e.g., PCA-based clustering or Measure Projection analysis).

A future direction is to take advantage of brain source location information and to incorporate this information as well as scalp map and/or ERP time course inner products in the pairwise IC matrix. This will highly weight polarity conflicts in nearby

sources and prefer solutions that result in higher spatial consistency values across time-domain measures such as ERPs.

3.6 Acknowledgments

The research described in Chapter 3 of this thesis was sponsored by the Army Research Laboratory and was accomplished under Cooperative Agreement Number W911NF-10-2-0022 and NIH grant 1R01MH084819-03. The views and the conclusions contained in this document are those of the authors and should not be interpreted as representing the official policies, either expressed or implied, of the Army Research Laboratory or the U.S Government. The U.S Government is authorized to reproduce and distribute reprints for Government purposes notwithstanding any copyright notation herein. The authors thank an anonymous reviewer for suggesting use of the Monte Carlo approach.

Chapter 3, in full is currently being prepared for submission for publication of the material by N. Bigdely-Shamlo, K. Kreutz-Delgado and S. Makeig. The dissertation author was the primary investigator and author of this material.

3.7 Figures

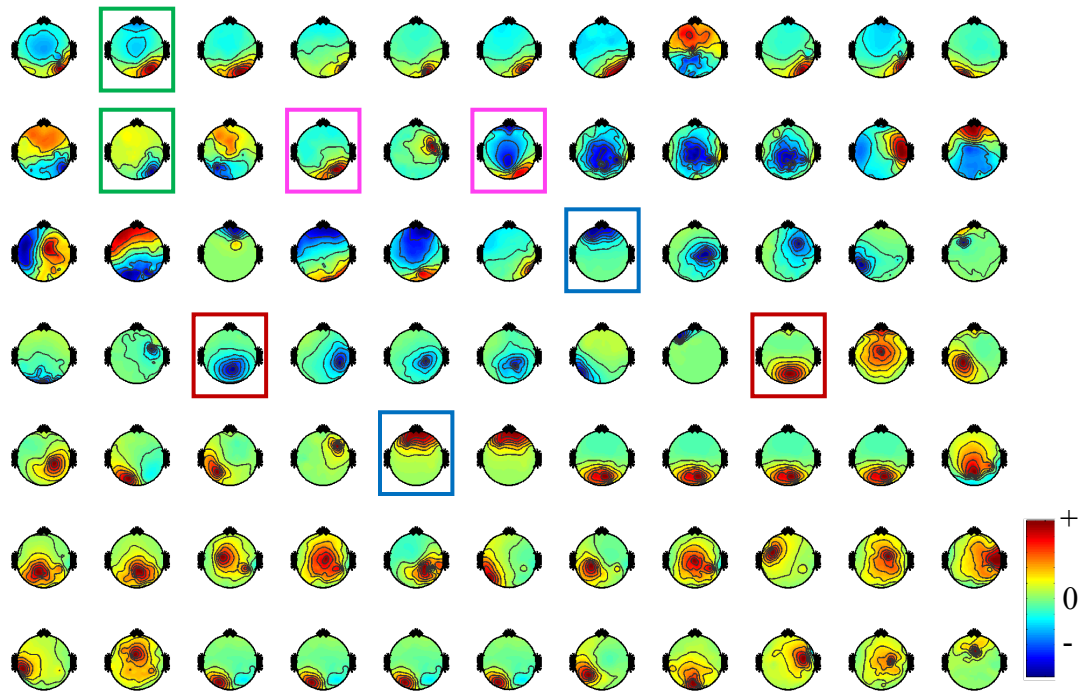


Figure 3.1. Sample study-A IC scalp maps before polarity normalization. IC pairs for which one IC is a candidate for polarity reversal are surrounded by colored rectangles.

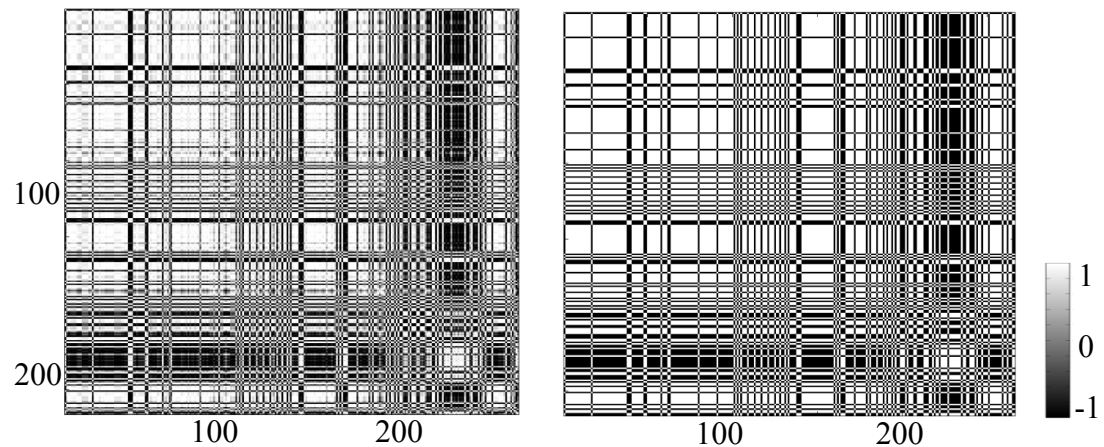


Figure 3.2. (Left) Matrix X obtained from convex relaxation (Equation (6)), (Right) Rank = 1 approximation of X from Equation (7).

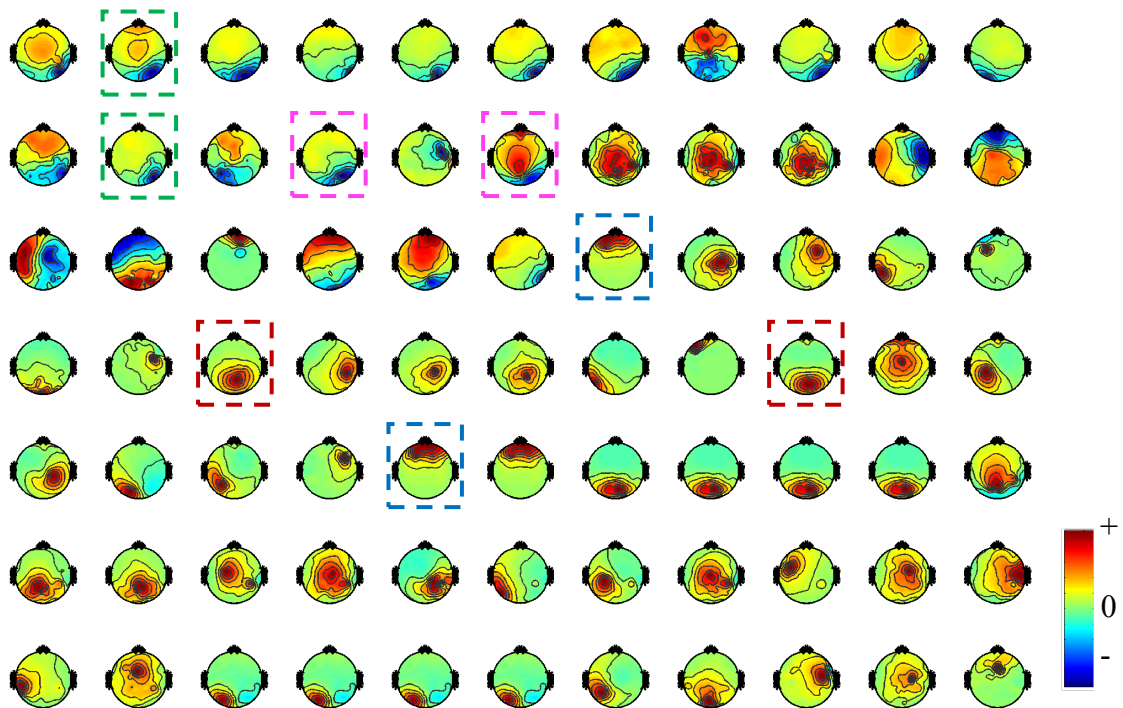


Figure 3.3. Sample study-A IC scalp maps after polarity normalization using convex relaxation. Dashed rectangles indicate the IC pairs highlighted in Figure 3.1 as candidates for polarity change. The polarities of all these pairs are changed after applying convex polarity normalization.

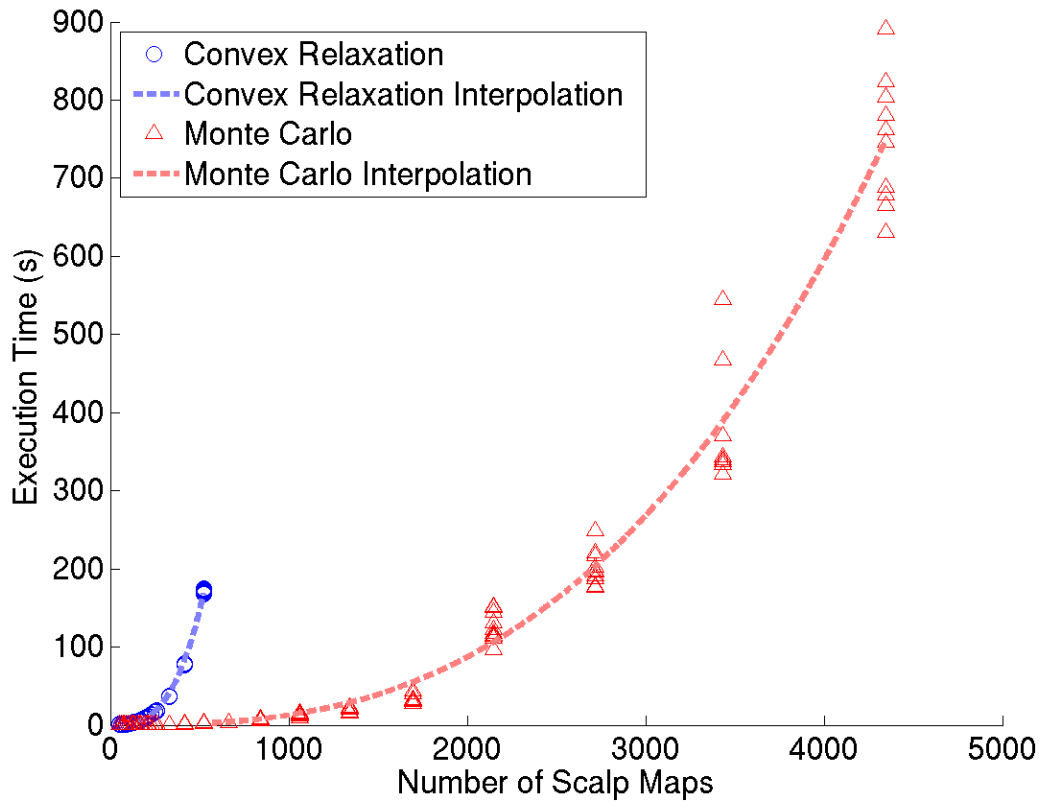


Figure 3.4. A comparison of execution times for the convex relaxation and Monte Carlo methods. Dashed lines show interpolated values using best fits to the formula $y = ax^b$.

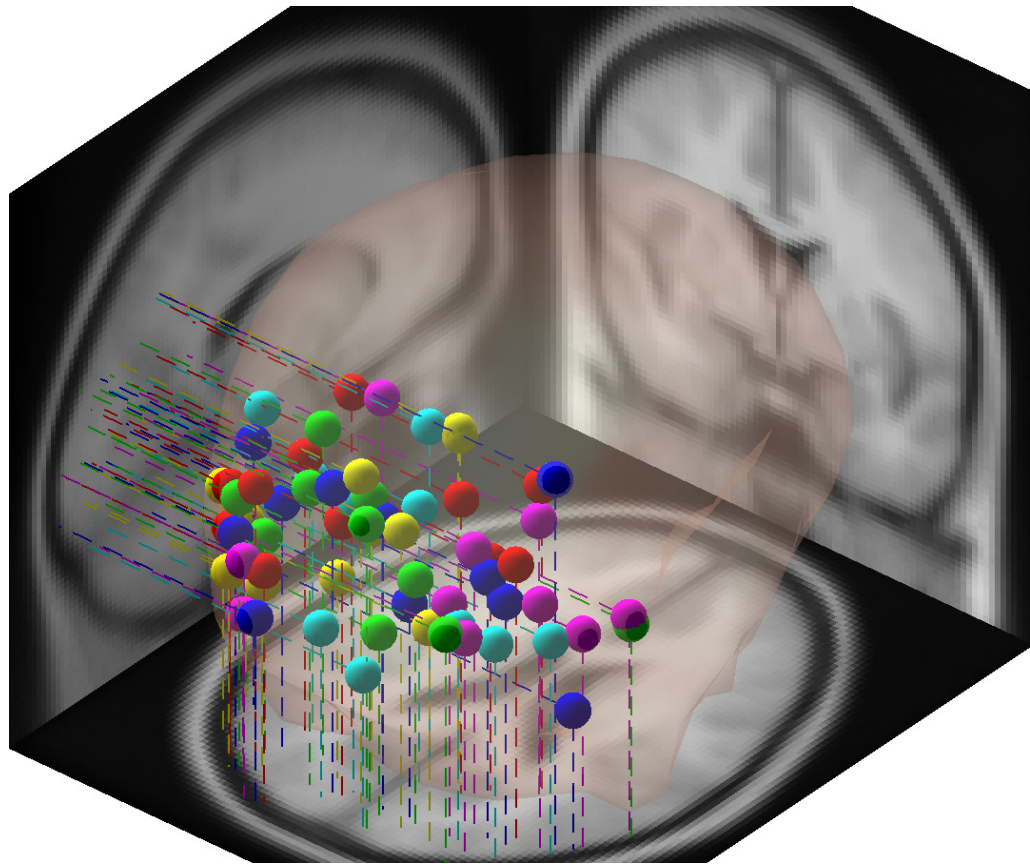


Figure 3.5. Equivalent dipole models for the 64 ICs in Study A located within 10 mm of the occipital brain region as per the LONI cortical atlas [52].

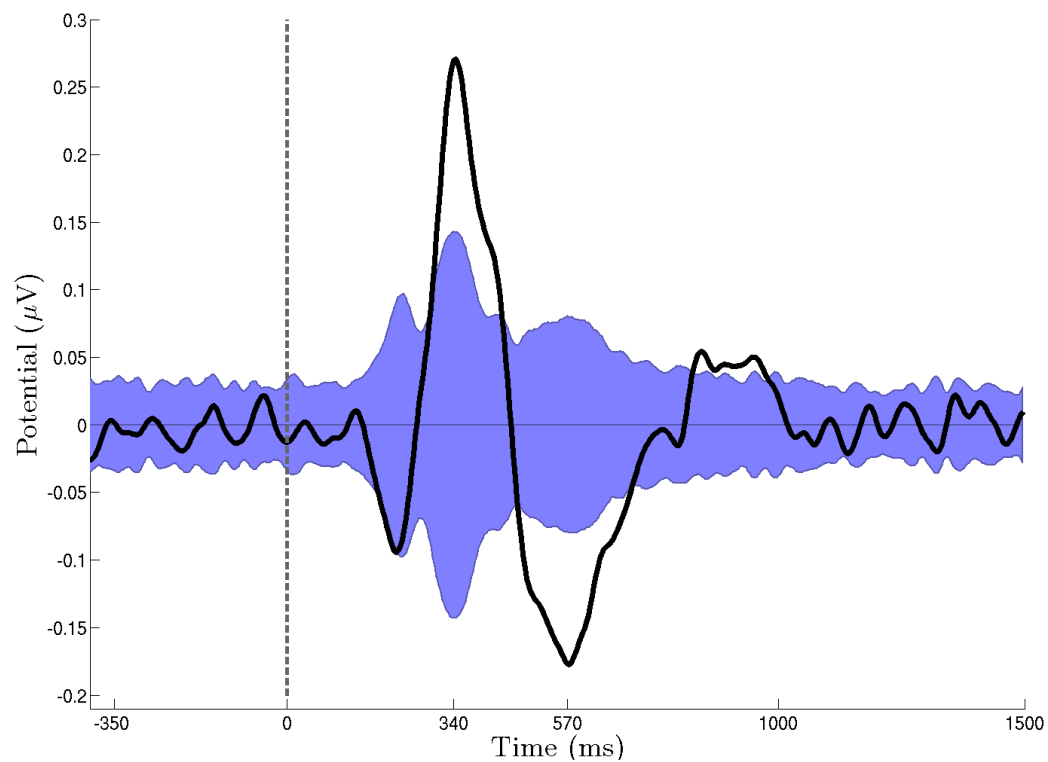


Figure 3.6. Average ERP of 64 occipital ICs of study A after polarity normalization. The blue area shows the $p > 0.05$ confidence bounds obtained from 10,000 bootstrap iterations with random IC polarities.

Chapter 4

Detecting Eye Activity Related ICs (EyeCatch)

4.1 Abstract

Independent component analysis (ICA) can find distinct sources of electroencephalographic (EEG) activity, both brain-based and artifactual, and has become a common pre-preprocessing step in analysis of EEG data. The highly non-Gaussian nature of the EEG signals is what makes them amenable to analysis via ICA techniques. Distinguishing between the brain and non-brain independent components (ICs) accounting for, e.g., eye or muscle activities is an important step in data analysis. Here we present a fully automated method to identify eye-movement related EEG components by analyzing the spatial distribution of their scalp projections (*scalp maps*). The *EyeCatch* method developed in this chapter compares each input scalp map to a database of eye-related IC scalp maps obtained by data-mining over half a million IC scalp maps obtained from 80,006 EEG datasets associated with a diverse set of EEG studies and paradigms. To our knowledge this is the largest sample of IC

scalp maps that has ever been analyzed. Our result show comparable performance to a previous state-of-art semi-automated method, CORRMAP [55], while eliminating the need for human intervention.

4.2 Introduction

Finding EEG sources through the application of ICA data decomposition has become a popular EEG analysis method [20-25]. An important aspect of ICA is it allows us to analyze EEG using ICA by separating brain source processes from the contributions to the scalp data from muscle and eye-movement related processes [56]. There are several algorithms proposed for this task: ADJUST [57] is a fully automatic algorithm that uses a combination of spatial and temporal features of independent components (ICs) to classify blinks, eye movements, and generic discontinuities. The method is based on a handful of spatial features (e.g., variance differences across groups of channels) manually constructed in a trial and error manner. When temporal information is not available, or when the EEG epochs are too short to obtain reliable statistics on temporal features, the performance of the ADJUST algorithm is unknown. CORRMAPP [55] is a semi-automated method that classifies eye-related ICs solely based on the correlation of their spatial projections (scalp maps) with one, or a few, templates. Each template is initially specified by the user and later refined by iterative clustering and averaging of detected eye components.

Here we present *EyeCatch*, a method that uses a large database of exemplar eye scalp maps instead of the single user-initiated template used in CORRMAP. The exemplar database is generated by analysis of a very large set of IC scalp maps from multiple studies to capture relevant eye component topographies while being robust to normal variations in subject anatomy, electrode locations, ICA decomposition quality, etc.

4.3 Methods

4.3.1 Scalp maps Database Preprocessing

We first gathered 106,749 single-subject EEG data sets from file servers of the UC San Diego Swartz Center for Computational Neuroscience (data collected during the period 2002-2012) and selected those with an ICA decomposition (nearly all determined by Extended Infomax [24] or AMICA [58, 59]) and unique dipolar IC source models computed using EEGLAB [21, 60]. From the selected 80,006 data sets we extracted 638,512 distinct IC scalp maps interpolated on a 67×67 2-D scalp grid using the *topoplot()* function in EEGLAB.

4.3.2 Eye-related template scalp map dataset

The eye-related scalp map template dataset was created in two stages. First we selected a single eye-movement related template scalp map from a well-studied Rapid Serial Visual Presentation (RSVP) experiment [48] and calculated its correlations with

the 265 scalp maps from three other laboratory studies. The ten IC scalp maps most highly correlated with the template were visually judged to be eye-activity related and added to the eye-related IC scalp map template database. Next, we sorted 499 IC scalp maps from an Attention-Shift study [61] by their maximum correlation to any of the scalp maps in the template database and visually selected 25 eye-activity related component scalp maps to add to the template database.

Next we calculated the highest absolute correlation between all 638,512 distinct IC scalp maps and any of the eye-related scalp maps in the template database. After sorting by this value and visual inspection, the scalp maps most highly correlated with any template map ($\max(|r|) > 0.994$) were clustered into 24 clusters using Affinity Propagation [62]. Sixteen of these clusters mostly contained scalp maps associated with a single type of eye-related activity (e.g., vertical or horizontal eye movements, or eye blinks). The rest were considered to be brain source ICs whose maps had some similarity to eye-activity related maps. We then visually inspected each of the sixteen eye-related scalp map clusters, and retained only scalp maps that were more similar than a visually appropriate correlation threshold to the cluster exemplar (cluster thresholds: $0.8 < |r| < 0.97$; median 0.94). After final visual adjustment (eliminating 13 ICs) we obtained a template database of 3,452 eye-activity related IC scalp maps.

The EyeCatch algorithm then simply calculates the maximum absolute correlation between an input scalp map and all 3,452 eye-activity related template

scalp maps in its database (i.e. by calculating the absolute correlation between an input scalp map and all template scalp maps and then take the maximum one). Cross validation results showed that this typically was more reliable than more complex nearest-neighbor distance weighted averaging methods.

4.4 Results

Figure 4.1 shows a sample 96 IC scalp maps in the EyeCatch template database. Many of these represent variations on a single type of template (e.g., accounting for EEG artifact produced by horizontal eye movements or eye blinks) arising from differences in subject anatomy, electrode locations, etc. Including this variability provides an advantage when using a simple similarity-based classification method and can be achieved only by processing data from a large sample of subjects and recording conditions.

We compared the performance of EyeCatch with the reported results of the semi-automatic CORMAP algorithm. The 4,256 IC scalp maps used in the CORRMAP paper [55] plus the ratings of these maps by eleven experts were kindly provided to us by the authors of [9]. We applied EyeCatch to these scalp maps using a range of decision correlation thresholds (between 0.95 and 0.99) and compared the results to the average of the [0|1] votes from the 11 experts who judged each given IC scalp map as either accounting for eye-movement activity (e.g., blinks or lateral eye movements) or not. Using Matlab (Mathworks, Inc.), 7.85 s were required to obtain

maximum correlation values for the 4,256 input maps (1.8 ms per map). Figure 4.2 shows the correlations between the EyeCatch output (length 4,256 vector of binary [0|1] values) and the expert vote averages (vector of range [0,1] values) for a range of EyeCatch maximum-correlation decision thresholds.

We also calculated the Receiver Operator Characteristic (ROC) curve [63] using the majority vote of the 11 experts as binary ground truth (thereby identifying 125 lateral eye movement or blink-related scalp maps) and the maximum absolute correlation similarity between each test scalp map and the 125 scalp maps in the EyeCatch template database as the detection variable.

Figure 4.3 displays this ROC curve. The area under the ROC curve is 0.993, demonstrating that EyeCatch has both high sensitivity and specificity.

4.5 Conclusions

As seen in Figure 4.2, for a range of decision correlation thresholds (from 95.5% to 98.3%) correlation to mean expert votes is above 0.8. This is highly comparable to the reported performance of CORRMAP, for which mean correlations with expert judgments for each study were 0.85-0.91 for lateral eye movements and 0.83-0.99 for blinks. However, once a database has been constructed, the EyeCatch algorithm is fully automated and does not involve the user interaction required by CORRMAP.

Our results show that high-performance eye-related IC classification can be achieved by using a large volume of data and relatively simple measures (here, scalp map correlation thresholding). This suggests that solving other problems in EEG analysis, from muscle-related component detection to robust Brain Computer Interface design, may also benefit from exploiting large databases spanning many EEG studies. This is consistent with current thinking in many application domains, that given enough data ("big data") even relatively simple algorithms can produce highly informative results.

However, still better performance for detecting both eye-activity and other non-brain ('artifact') IC types might be obtained by jointly considering IC scalps and time courses. For example, saccade and blink ICs have strong, fairly predictable time domain features; ICs accounting for scalp muscle (electromyographic, EMG) activity have characteristic spectral profiles, etc.

A freely available, open-source implementation of the EyeCatch algorithm running on Matlab is available in the Measure Projection Toolbox (MPT), an EEGLAB plug-in [64]. Documentation and stand-alone downloads are available at <http://sccn.ucsd.edu/wiki/EyeCatch>.

4.6 Acknowledgments

This research was sponsored by the Army Research Laboratory under Cooperative Agreement Number W911NF-10-2-0022 and by NIMH grant 1R01-MH084819-03. The views and the conclusions contained in this document are those of the authors and should not be interpreted as representing the official policies, either expressed or implied, of the Army Research Laboratory or the U.S Government. The U.S Government is authorized to reproduce and distribute reprints for Government purposes notwithstanding any copyright notation herein.

Chapter 4, in full, is a reprint of the material as it appears in N. Bigdely-Shamlo, K. Kreutz-Delgado, C. Kothe, S. Makeig, "EyeCatch: Data-mining over half a million EEG independent components to construct a fully-automated eye-component detector," Engineering in Medicine and Biology Society (EMBC), 2013 35th Annual International Conference of the IEEE , vol., no., pp.5845,5848, 3-7 July 2013, doi: 10.1109/EMBC.2013.6610881. The dissertation author was the primary investigator and author of this paper.

4.7 Figures

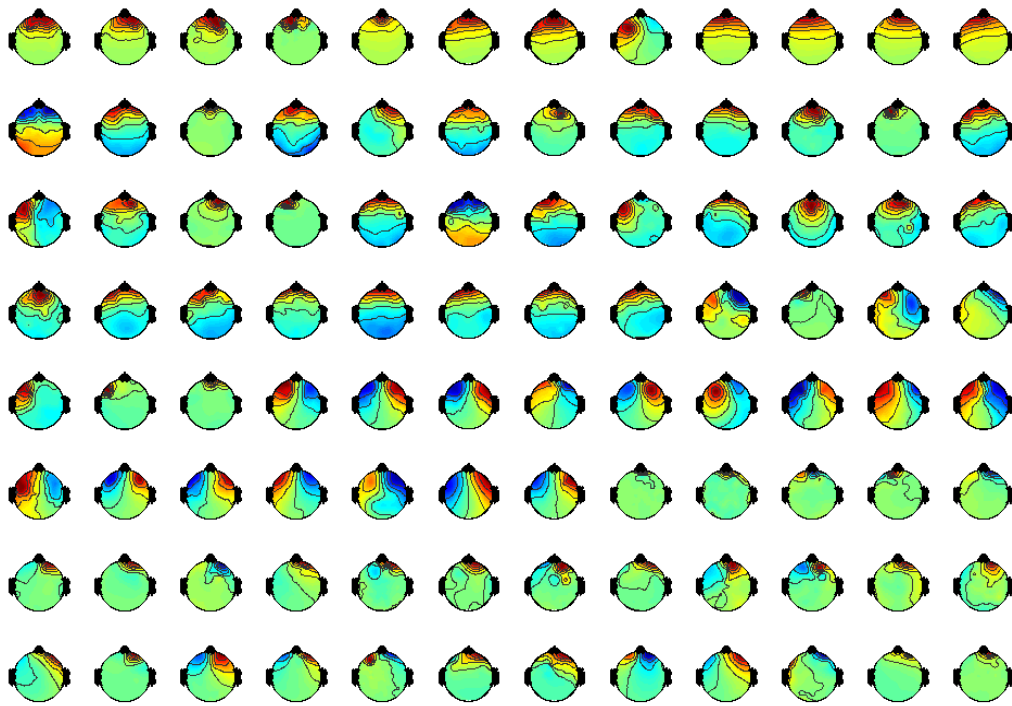


Figure 4.1. A sample 96 template component scalp maps (of 3,452) in the EyeCatch eye-related component template.

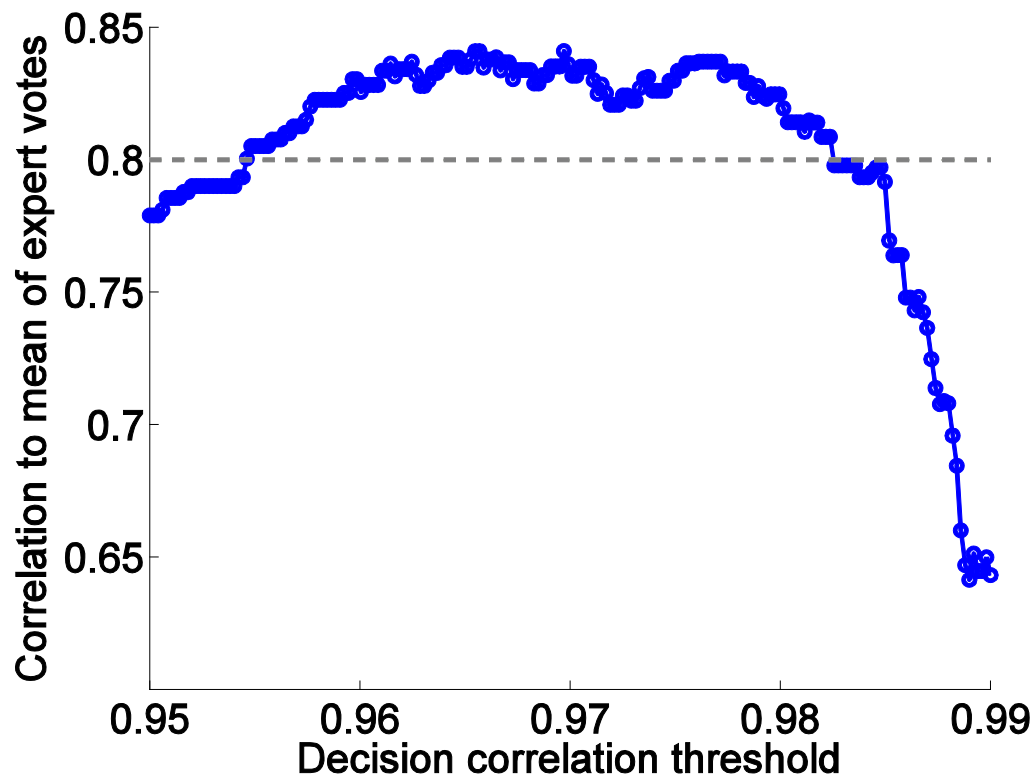


Figure 4.2. Correlations between eye-activity related component scalp map judgments by EyeCatch and the average votes (whether each component is eye activity related or not) from eleven experts as a function of the EyeCatch maximum-correlation decision threshold.

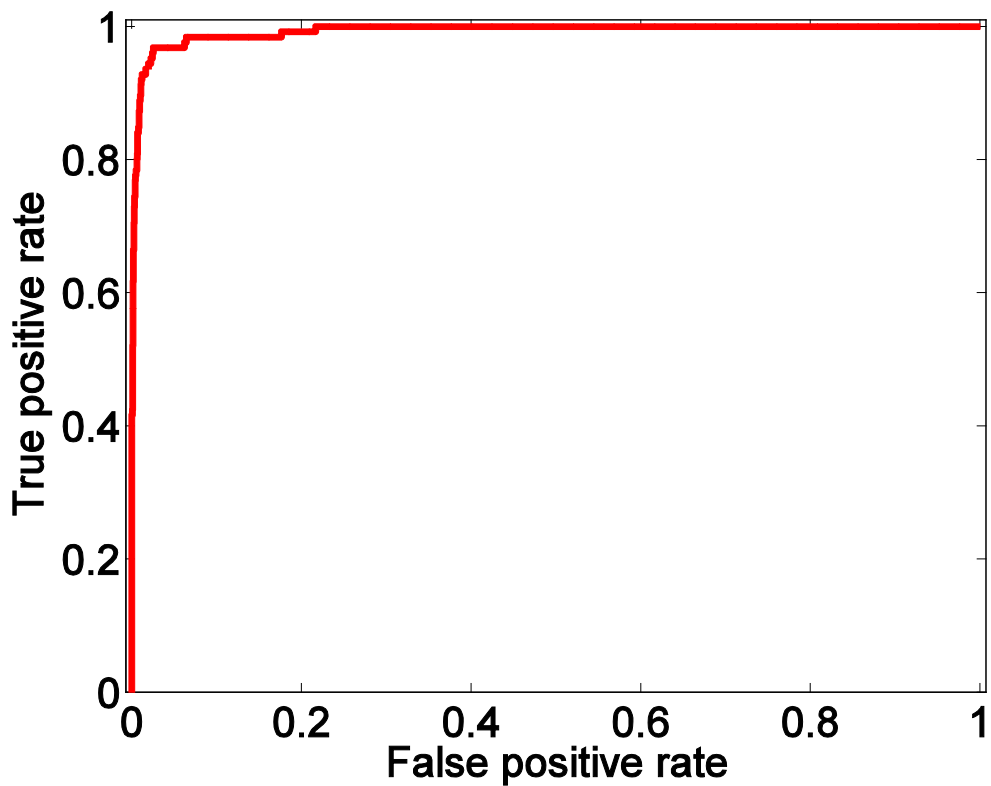


Figure 4.3. Receiver Operator Characteristic (ROC) curve for EyeCatch scalp map classification and expert majority voting on the CORRMAP paper component scalp map collection (area under the curve = 0.993).

Chapter 5

Imaging half a million ICA-component scalp maps reveals EEG source hotspots

5.1 Introduction

Finding EEG sources by applying ICA decomposition followed by single dipole fitting to each ICA component has become a popular and useful EEG source imaging approach [21, 28]. The probability of finding an independent component (IC) equivalent dipole in a brain area depends on two factors (a) The chance of finding the IC during the application of ICA to EEG. This depends, at least, on the relative session-average magnitude of IC contribution to channel data (since ICA gives higher priorities to separating sources with higher amplitudes) and is itself is a function of cortical electrophysiology and the task being performed by the subject. For example, [65] contrasted ICA source densities across groups of participants performing several stimulus response tasks. (b) The quality of forward electrical model available

associated with sources in the brain area (otherwise associated ICs cannot be modelled well enough by the equivalent dipole model and are hence ignored). Since in many cases a generic (not subject-specific) template forward electrical model is used, for each brain area the degree of anatomical variability across subjects, and hence deviation of the actual forward electrical field model from the template model, could influence the probability of observing an IC equivalent dipole. Here we present results of a large-scale analysis of ICA-derived EEG source locations and directions obtained from a diverse set EEG studies (including data from [65]).

5.2 Methods

5.2.1 Data Preprocessing

We first gathered 106,749 single-subject EEG data sets from file servers of the UCSD Swartz Center for Computational Neuroscience (2002-2012) and selected those that had an existing ICA decomposition (nearly all determined by extended infomax or AMICA) and localized dipolar sources computed from that decomposition. Of these, 80,006 had a unique equivalent dipole-fit solution (in terms of location and direction, obtained by use of the function *dipfit()* in EEGLAB), resulting in over 4 million (4,377,055) potentially dipolar sources (bilaterally symmetric component scalp maps were modeled using two bilaterally symmetrically located dipoles). Among these, 638,512 (15%) were unique (had distinct component scalp maps), from which 262,636 (41%) sources could be fit well by a one (or on occasion two) dipole model (e.g., with

> 85% of scalp-map variance accounted for). Lastly, we removed likely eye and muscle sources by only retaining sources inside the MNI modal brain volume (≥ 1 mm to CSF border) and then applying the EyeCatch algorithm (see Chapter 4) to remove remaining eye movement-related components. This resulted in 135,794 equivalent dipoles for brain EEG sources.

5.2.2 Dipole Density Calculation

To speed the computations, we represented the distribution of these source locations by calculating the numbers of dipoles in model brain voxels on a 3-D grid with 2-mm spacing. This voxel representation enabled the use of fast Matlab functions that act on data volumes. The maximum amount of spatial noise introduced during this process was $\sqrt{3} = 1.7\text{mm}$ which is not significant compared to the uncertainty in dipole location due to inaccuracies in the localization process (up to 20 mm).

To make sure that all dipoles contribute equally to the results, we multiplied the count value in each voxel $N_j, j = 1..m$ ($m = 249,686$ brain voxels) by a correction factor $f_j, j = 1..m$. This value was calculated at each location j by first placing a 3-D Gaussian with 19.5 mm std. (the value used in subsequent smoothing) at j and then setting f_j to the inverse of density mass that lays inside brain volume. This normalizes the total dipole mass inside brain volume to one (since after preprocessing the remaining dipoles are assumed to be of cortical origin).

We then applied spatial Gaussian (19.5-mm std.) smoothing to calculate the overall dipole density at each location while taking into account uncertainties in dipole localization (e.g., from errors in forward and inverse head modeling). To do this, we performed 15 iterations of 3-D smoothing, using the *smooth3()* Matlab function, by , at each iteration, convolving the corrected dipole count values $N_j^{corrected} = N_j f_j, i = 1..m$ with a 1.3 mm Gaussian. This resulted in an overall $1.3*15=19.5$ mm Gaussian smoothing.

To calculate the probability that the calculated dipole density in each voxel was higher than what would most likely be observed by chance, we performed bootstrap dipole density calculations using 200 permutations of placing the same number of dipoles in random voxel locations. Significance P value at each location was calculated as the ratio of random permutation with equal or more density at the location.

5.2.3 Calculating Average Dipole Residual Variance

Residual variance (RV) is a ratio of scalp map variance that can be explained by a dipole source model and defined as follows. For each scalp map $S_i, i = 1..n$ modeled by a dipole scalp map $S_i^{Dipole}, i = 1..n$, the residual variance is defined as:

$$RV_i = \frac{Var(S_i - S_i^{Dipole})}{Var(S_i)}. \quad (5.1)$$

We then calculate the average residual variance RV_j at brain voxel $j = 1..m$ using the formula

$$\overline{RV_j} = \frac{\sum_{i=1}^n RV_i P_{i,j}}{\sum_{i=1}^n P_{i,j}} \quad (5.2)$$

where $P_{i,j}$ is the dipole $D_i, i = 1..n$ density at voxel $j = 1..m$ and RV_i is the residual variance of this dipole.

5.2.4 Calculating Average Dipole Orientation

The uncertainty in the polarity of ICA scalp maps results in an uncertainty in the direction (but not the orientation) of associated equivalent dipoles (when such maps are well represented by such a model).

One way to calculate the average orientation of a number of dipoles is to remove direction information by representing each dipole orientation by a tensor. For dipole $D_i, i = 1..n$ ($n = 135,794$ dipoles) with dipole vector v_i , matrix $V_i = v_i * v_i^T$ represent the orientation but not the direction of the dipole. To calculate the average orientations, we can use the (unweighted) covariance formula:

$$C = Cov(D) = \sum_{i=1}^n v_i * v_i^T = \sum_{i=1}^n V_i \quad (5.3)$$

Matrix C represents an ellipsoid whose first principal direction (the eigenvector of C associated with its largest eigenvalue) points to the dominant orientation of dipoles $D_{i=1..n}$.

To include dipole location information in our averaging we have to calculate a weighted average at each location, emphasizing the orientations of nearby dipoles. Let α_i be the weight of dipole D_i , obtained from a probability density representation of the dipole (here we use a 19.5 std. Gaussian normalized to have unit total density in brain volume). The formula for calculating the weighted covariance matrix is

$$C = Cov(D) = k \sum_{i=1}^n \alpha_i v_i * v_i^T = k \sum_{i=1}^n \alpha_i V_i \quad (5.4)$$

where k is a scalar constant and can be ignored since it does not affect the eigenvector structure of C .

We represented each dipole orientation by a covariance matrix and performed Gaussian smoothing with 19.5 mm std. independently for each matrix element in the same way we calculated dipole densities in 5.2.1. This resulted in m covariance matrices $C_j, i = 1..m$, each associated with a different voxel.

The shape of the ellipsoid represented by C_j indicates the degree of dipole orientation preference or anisotropy. Fractional Anisotropy (FA) is a scalar value between zero and one that quantifies this orientation preference. FA is extensively

used in Diffusion Tensor Imaging (DTI) [66] and is calculated from the eigenvalues ($\lambda_1, \lambda_2, \lambda_3$) of the weighted covariance matrix C_j as

$$FA = \sqrt{\frac{1}{2} \frac{\sqrt{(\lambda_1 - \lambda_2)^2 + (\lambda_1 - \lambda_3)^2 + (\lambda_2 - \lambda_3)^2}}{\sqrt{\lambda_1^2 + \lambda_2^2 + \lambda_3^2}}}. \quad (5.5)$$

Note than if all the eigenvalue are equal (the isotropic or spherical) the FA is 0. If all dipole orientations are the same, the FA is 1.

We calculated FA values for $C_j, i = 1..m$ and obtained their significance P values by performing 200 bootstrap iterations. In each iteration the directions of the original n dipoles was replaced by the directions of n randomly selected dipoles from the original dipoles (allowing repetitions for a more conservative statistical estimate). Weighted covariance and FA calculations were then repeated for each iterations and significance P value of FA at each location was calculated as the ratio of FA values among all bootstrap iteration that were higher than the original FA value for the voxel.

5.2.5 Defining the radial vector direction for each voxel

Source orientations are often investigated in terms of principal radial and tangential axis relative to the boundary of the cortex, i.e. Cerebrospinal fluid (CSF) [67]. To compare our computed average dipole orientations to the radial orientation we first need to define this orientation for each brain location.

It is intuitive to define the radial direction for points near the boundary of the cortex (i.e. CSF) as the perpendicular direction to this boundary. In other words, this direction can be found by connecting the each point to the closest point of outer cortical surface (e.g. CSF). It is then only logical to extend this definition of radial direction to all voxels in the brain.

To accelerate the calculation of radial direction for brain voxels, instead of finding the closest point for each voxel we can use a highly efficient distance transform algorithm implemented in the *bwdist()* Matlab function. The input to this function is a binary mask and the output is the distance from each voxel to the closest point with a non-zero (true) in the input mask (Figure 5.8a) and the output is the distance from each voxel to the closest out-of-brain location (Figure 5.8b). The radial orientation for each voxel may be obtained by calculating the gradient of this distance (Figure 5.8c). Figure 5.9 shows radial orientation field for MNI [68] brain volume.

Once radial orientations are calculated, the angle between each orientation r_j at location j and the average dipole orientation (the first eigenvector of C , w_j) may be calculated as

$$\theta = \cos^{-1}\left(\frac{|r_j^T w_j|}{\|r_j\| \cdot \|w_j\|}\right). \quad (5.6)$$

5.3 Results

Figure 5.1 shows the histogram of remaining scalp-map variance not accounted for by dipole model (a single dipole or dual symmetric dipole). It suggests that most sources are well modeled by the dipole model (median residual variance = 5.8%).

Figure 5.2 shows calculated brain source equivalent dipole locations, plotted as counts in 8-mm³ voxels in the MNI template cortex [68]. In Figure 5.3 dipole density in this image (following Gaussian smoothing and partial volume effect correction) is displayed. Figure 5.4 shows areas with unexpectedly high dipole density ($p < 0.05$, FDR [69] corrected of multiple comparisons). Table 5.1 shows anatomical regions (based on the LONI project Probabilistic Atlas [52] and the Talairach Atlas [70], respectively) with highest dipole densities, along with the ratios of average dipole density in each region to mean dipole density through the brain volume.

Figure 5.6 shows Fractional Anisotropy (FA) at different brain locations. FA values for locations where FA is not significant ($p \geq 0.01$) are set to zero. Figure 5.7 shows average dipole orientations for different areas colored by FA. Figure 5.9 shows radial orientation field for MNI brain volume and Figure 5.10 shows the angle (in degrees) between average dipole orientation and the radial vector at each location with significant ($p < 0.01$) FA.

5.4 Discussion

Our dipole density results show the activation of anatomic areas involved in executive function, particularly response planning (e.g., mid-cingulate gyrus), resting periods (e.g., default network-related activity in precuneus [71]), visual response areas (e.g., lateral occipital), and hand sensorimotor cortex (e.g., parietal gyrus, hand-area mu rhythms during finger movement inhibition). This is consistent with the type of tasks commonly used in this collection of psychophysical EEG experiments in which participants performed quick visual perceptual decisions leading to finger press responses. To our knowledge, this is the first large-scale EEG analysis that combines ICA-derived source location information across a diverse set of studies and paradigms. The compactness of the ‘hotspots’ in the density image suggests that despite differences in tasks, head models and electrode numbers, placements, and registration methods, several compact component process clusters appear in the ICA decompositions of many or most typical experiment sessions.

Our results in Figure 5.5 and Table 5.1 indicate that there are significant differences in how well cortical sources at different regions can be modeled by dipoles using template forward models (e.g. MNI). Certain areas such as frontal and temporal regions have a significantly higher residual variance than average, while others such as occipital, precuneus and cuneus have a lower than average residual variance (RV) (FDR-corrected $p < 0.05$). The increase in RV in frontal areas may be partially due to the increased inaccuracy of forward models caused by the less spherical, more convoluted shape of scalp in these areas.

As shown in Figure 5.6, Fractional Anisotropy of EEG dipole orientation values is high for most brain areas (median FA = 0.73). This could be mostly due to the anatomical similarity in cortical orientation across subjects. Also, the angle between the average dipole orientation and the radial direction in 53% of voxels is less than 30 degrees (see Figure 5.10 and Figure 5.11), a fact that may have contributed to high FA values. Our results are not adequate to resolve the relationship between these factors together and the distributions of cortical sources as detected by EEG. In fact our results encourage further research to explain the preponderance of radial EEG dipole sources.

Source orientation coherence across individuals modulates the strength of group-level event-related potentials (ERPs) calculated at channel locations. This is because similarly oriented sources contribute similarity to each channel, strengthening the group-level ERP. It is expected then that areas with low FA in Figure 5.6 to produce less prominent ERPs of this type. On the other hand, ICA-based group-level ERPs, for example obtained from Measure Projection Analysis (see Chapter 6), should be relatively unaffected by low FA since they average ERP of different participants from dipoles at particular brain areas regardless of dipole orientations.

5.5 Acknowledgements

This work was supported by the Office of Naval Research.

5.6 Figures

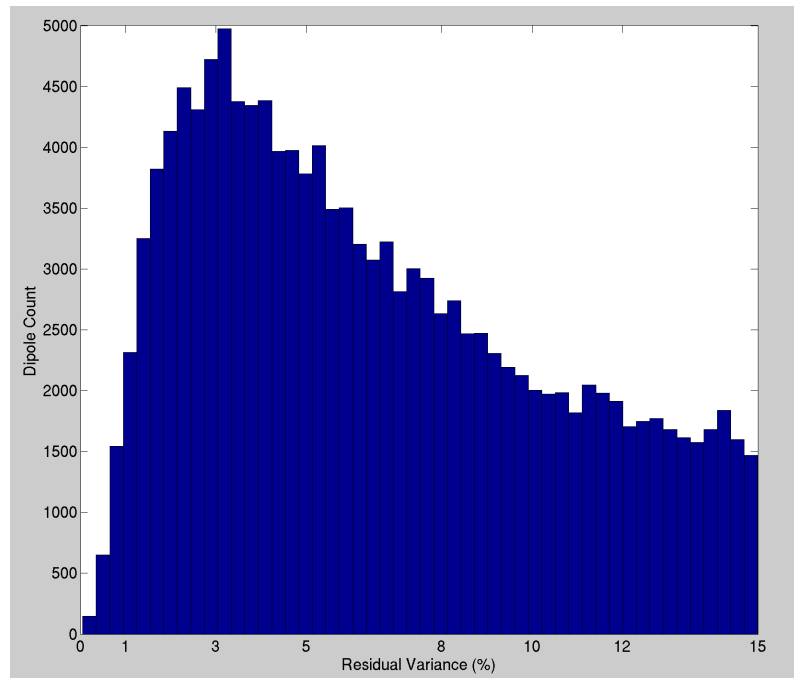


Figure 5.1. Histogram of equivalent dipole scalp map residual variances of brain dipoles (median = 5.8%).

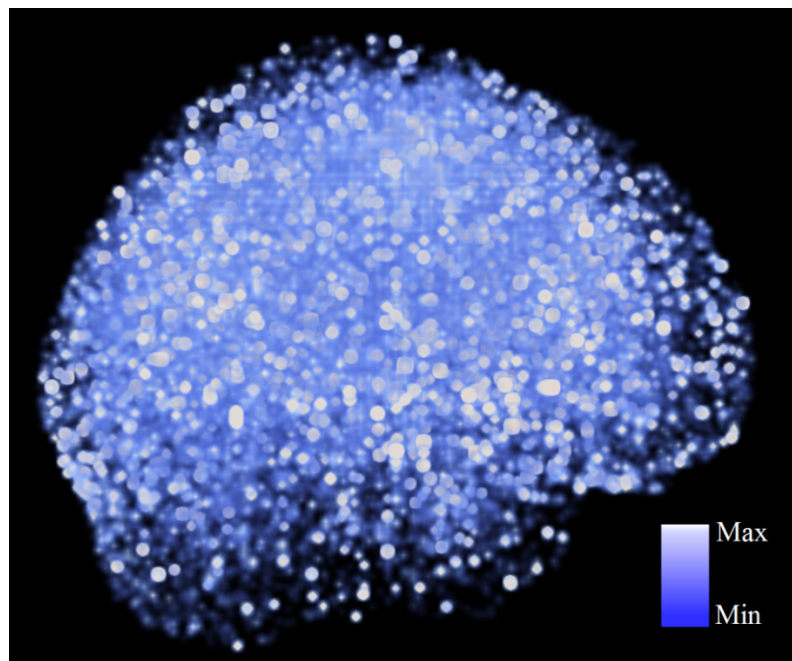


Figure 5.2. Over 130k EEG independent component (IC) brain source equivalent dipole locations, plotted as counts in 8-mm³ MNI template brain voxels.

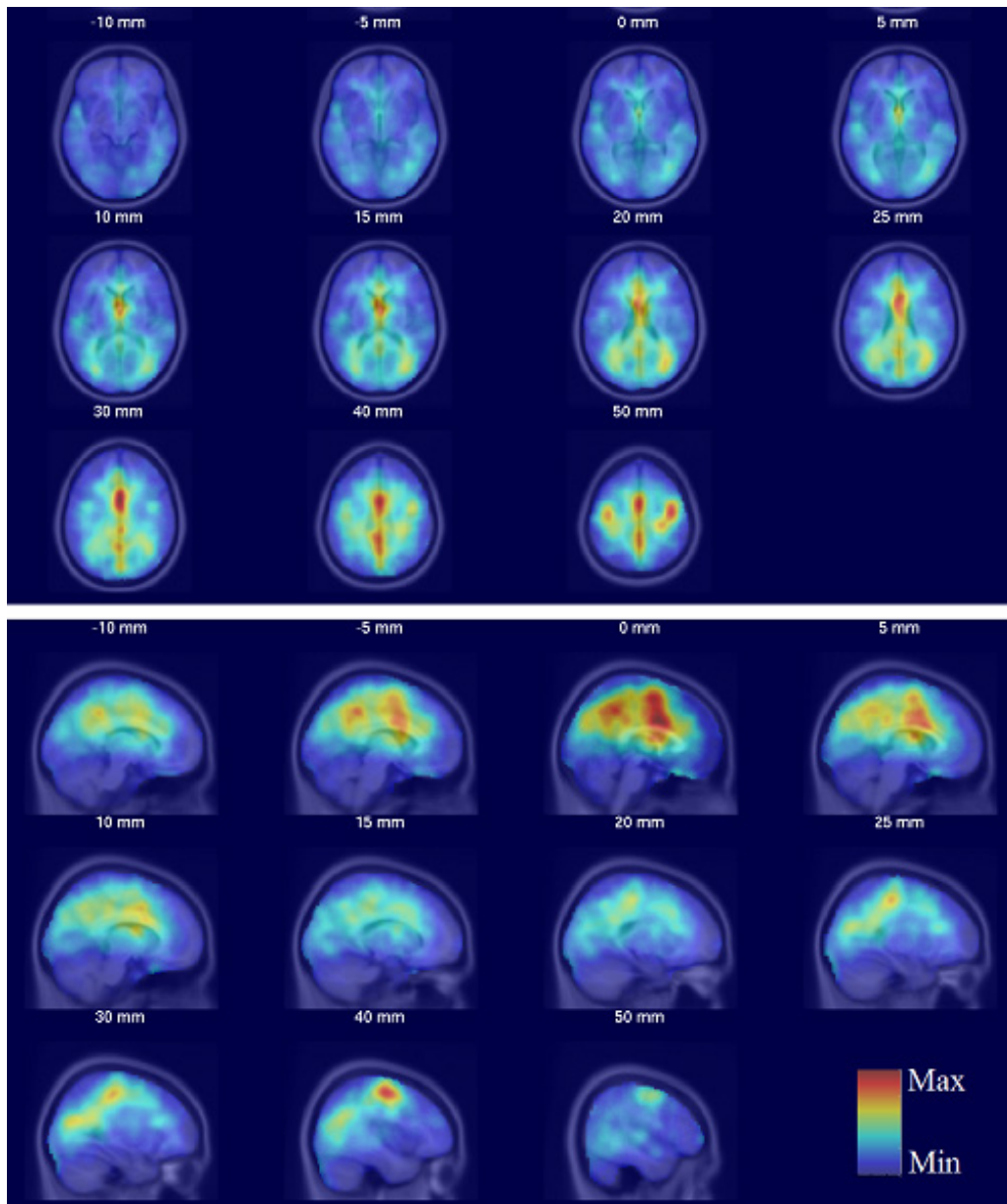


Figure 5.3. (top) Axial view of computed dipole source density across the datasets.
(bottom) Sagittal view.

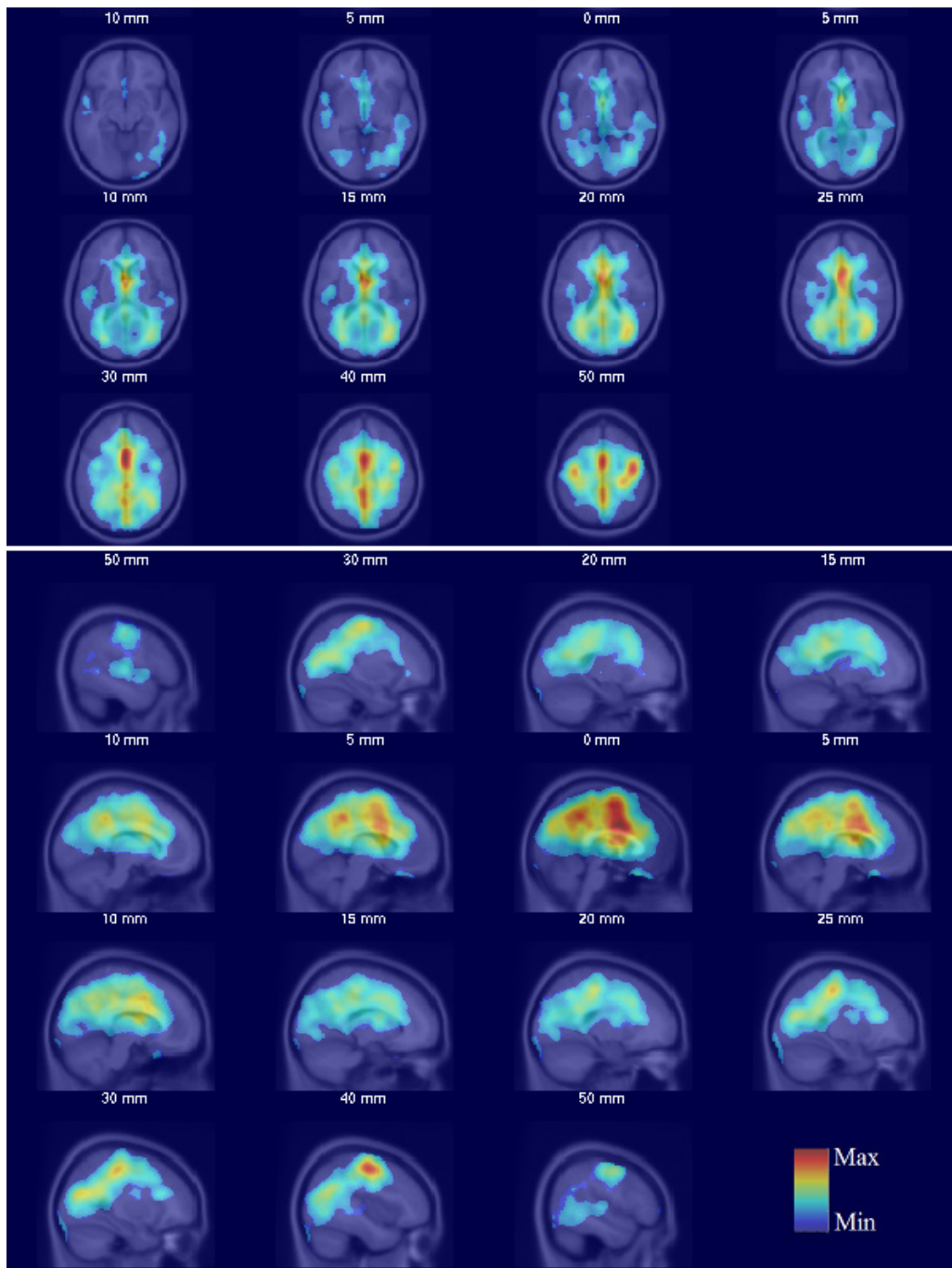


Figure 5.4. (top) Axial distribution of brain areas with higher than random equivalent dipole density ($p < .05$, FDR corrected). (bottom) Sagittal density.

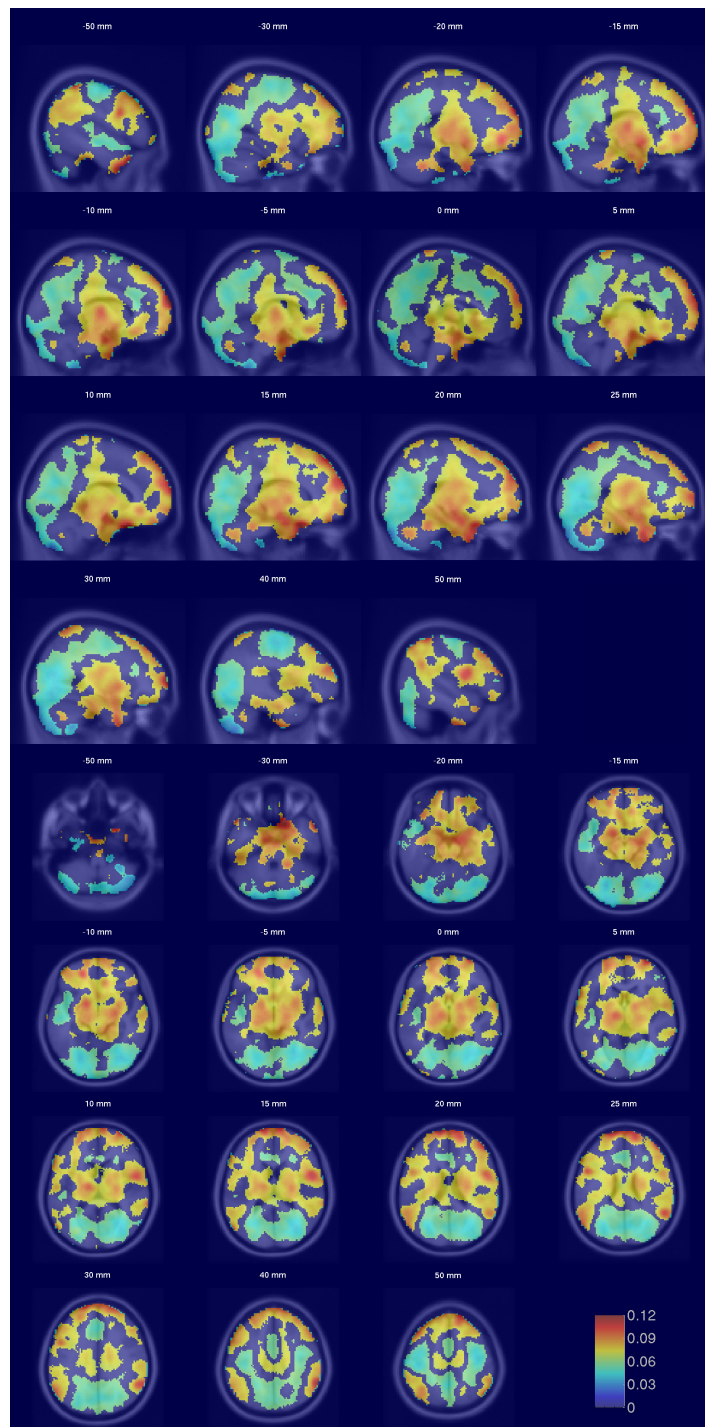


Figure 5.5. Average residual variance (two-tailed $p < 0.01$).

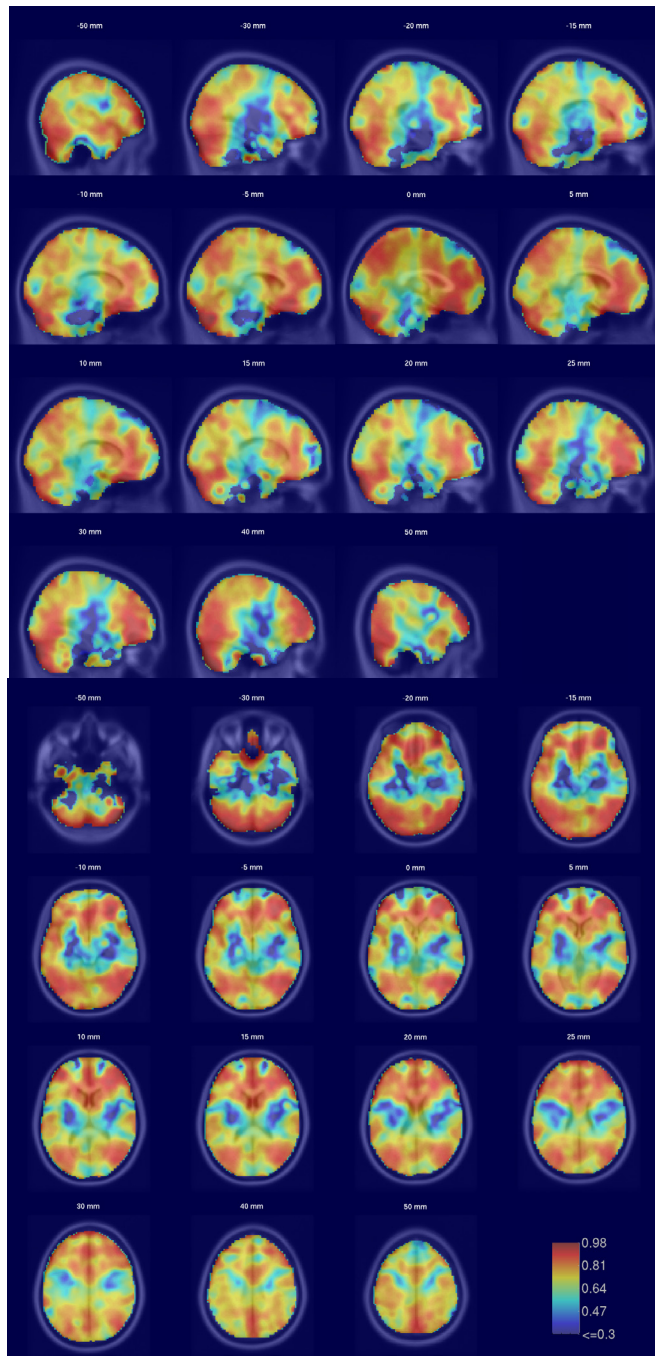


Figure 5.6. Fractional Anisotropy at different brain locations ($p<0.01$).

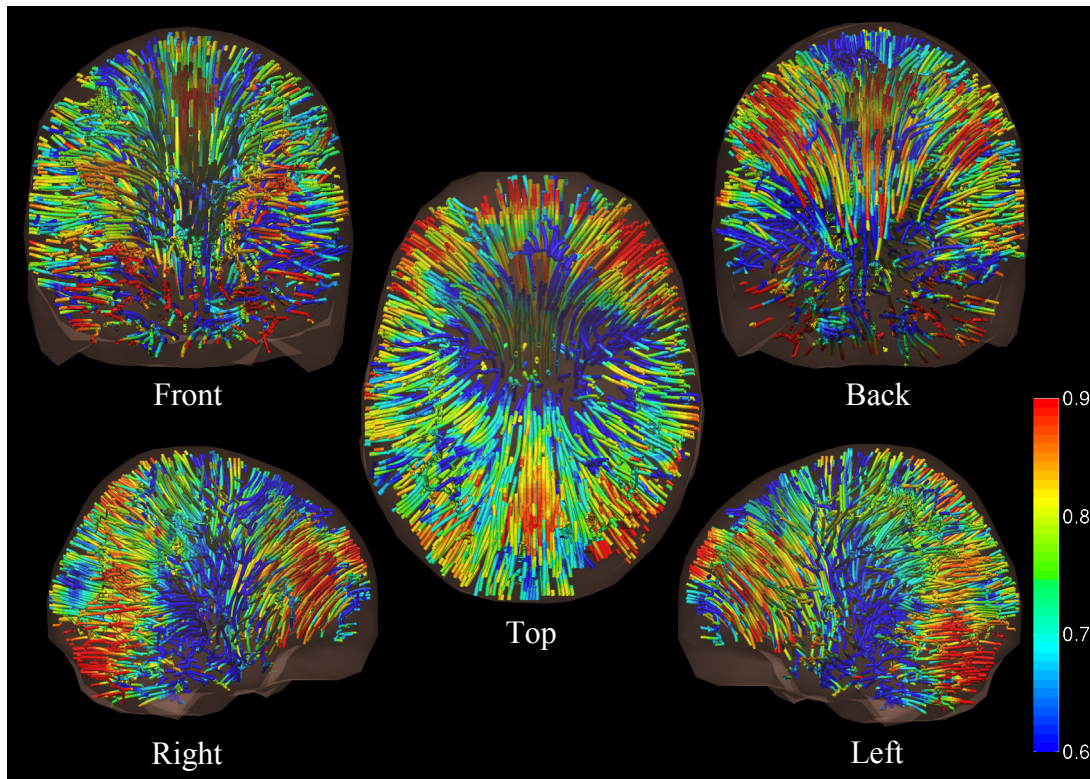


Figure 5.7. Average dipole orientations colored by fractional anisotropy at different brain locations.

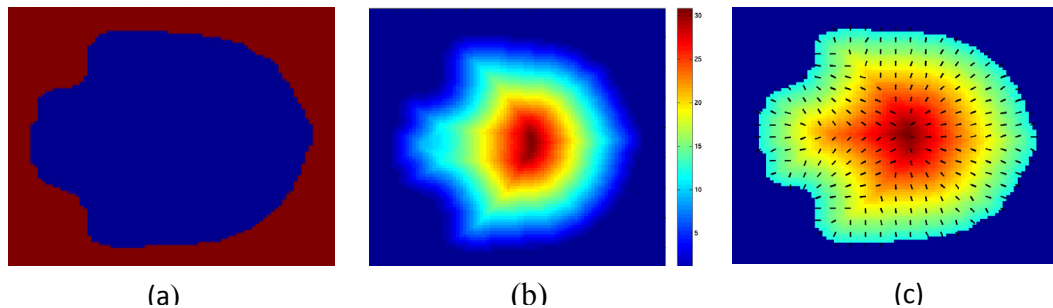


Figure 5.8. (a) Sample 2D slice of anatomical (MNI) brain volume mask. (b) Distance transform of image (a). (c) Radial vectors calculated from the gradient of (b).

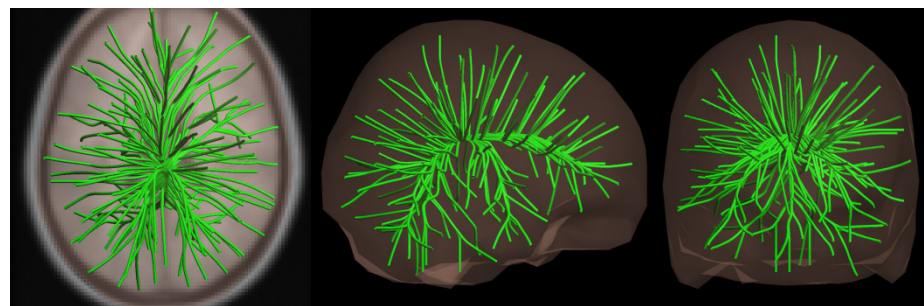


Figure 5.9. Three views of radial orientations for MNI brain volume.

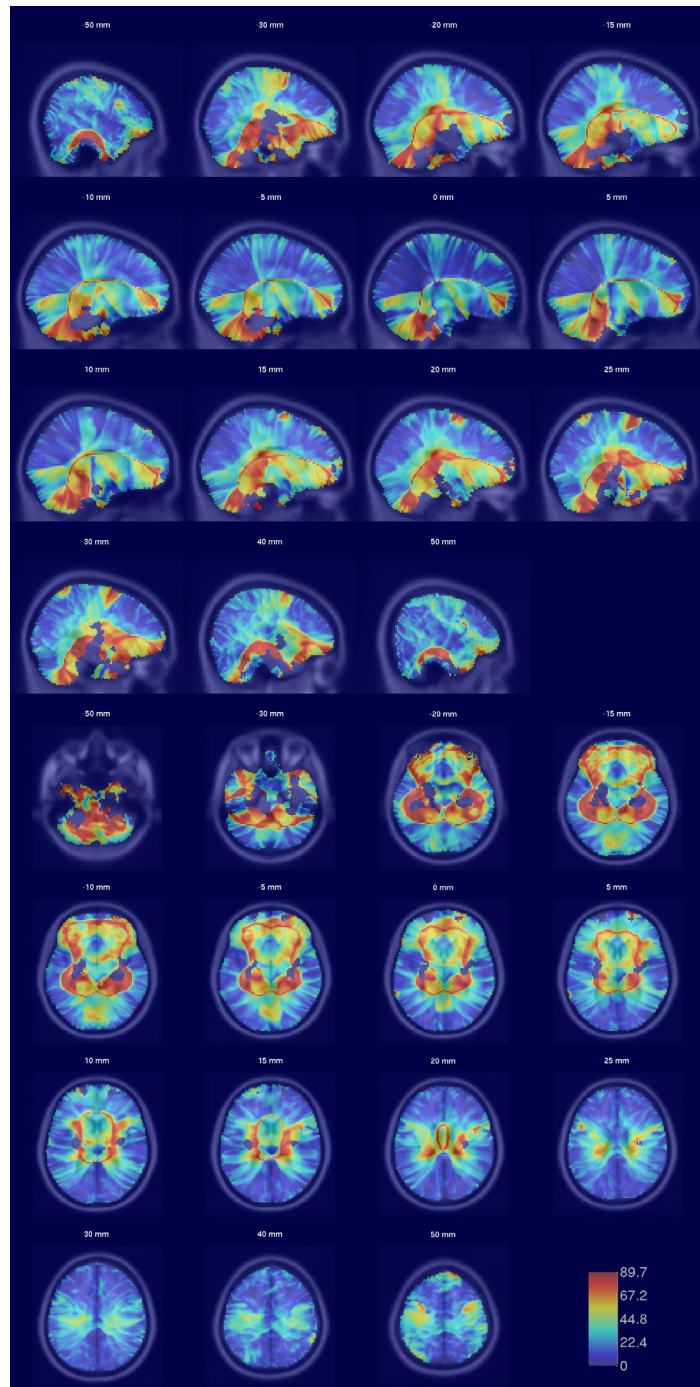


Figure 5.10. Angle (in degrees) between average dipole orientation and the radial vector at each location ($p < 0.01$).

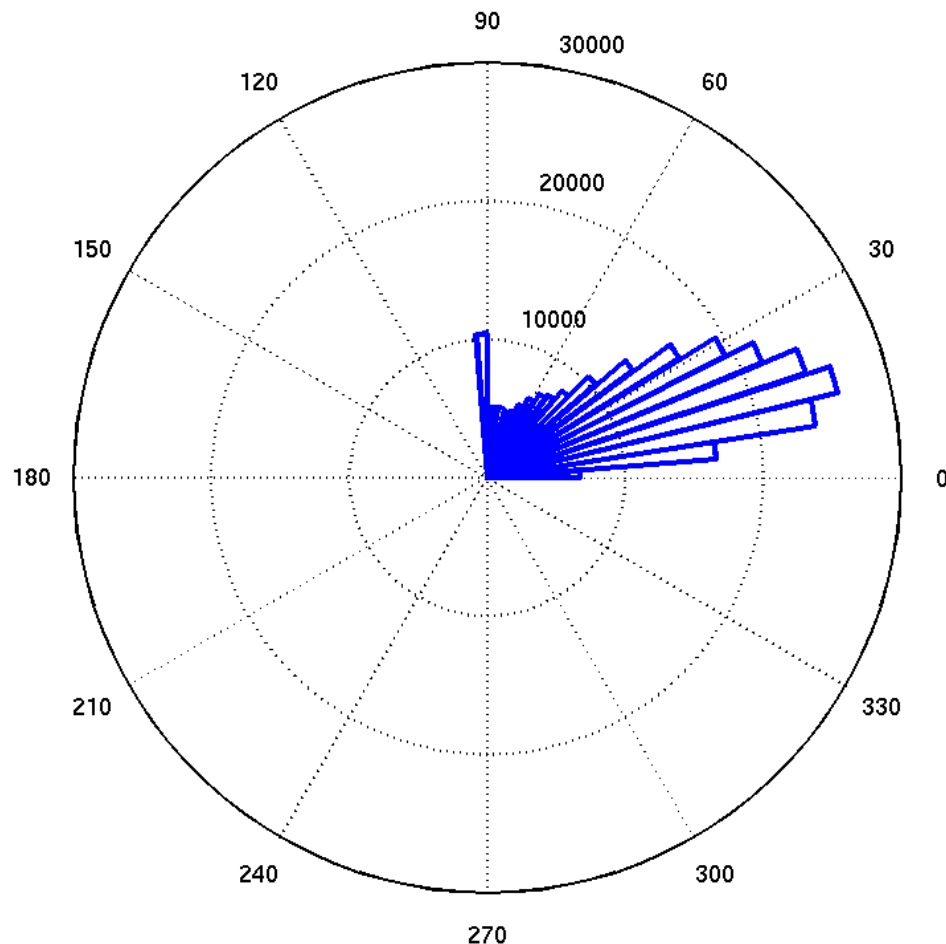


Figure 5.11. Histogram of the angle between radial orientation and the average dipole orientation at each brain voxel. Most IC equivalent dipole orientations have a <30 degree angle with the radial orientation.

Table 5.1. Anatomical regions with high dipole density.

Anatomical Region	Dipole Density Ratio	Anatomical Region	Dipole Density Ratio
R Cingulate Gyrus	2.62	L Inferior Frontal Gyrus	0.65
R Precuneus	2.49	L Putamen	0.64
L Cingulate Gyrus	2.47	R Parahippocampal Gyrus	0.58
L Precuneus	2.32	L Fusiform Gyrus	0.51
R Caudate	1.88	R Fusiform Gyrus	0.5
R Cuneus	1.73	R Inferior Temporal Gyrus	0.5
L Caudate	1.66	L Parahippocampal Gyrus	0.48
R Precentral Gyrus	1.66	R Hippocampus	0.46
L Precentral Gyrus	1.55	R Middle Orbitofrontal Gyrus	0.44
R Postcentral Gyrus	1.54	R Lateral Orbitofrontal Gyrus	0.44
R Superior Occipital Gyrus	1.52	L Inferior Temporal Gyrus	0.43
L Cuneus	1.44	L Hippocampus	0.4

Table 5.1., continued.

Anatomical Region	Dipole Density Ratio	Anatomical Region	Dipole Density Ratio
L Postcentral Gyrus	1.42	L Lateral Orbitofrontal Gyrus	0.4
R Superior Parietal Gyrus	1.27	L Middle Orbitofrontal Gyrus	0.36
L Superior Occipital Gyrus	1.26	Cerebellum	0.32
L Superior Frontal Gyrus	1.23	Brodmann Area 24	2.73
R Superior Frontal Gyrus	1.22	Brodmann Area 33	2.71
L Superior Parietal Gyrus	1.19	Brodmann Area 23	2.61
R Lingual Gyrus	1.14	Brodmann Area 31	2.54
R Inferior Occipital Gyrus	1.09	Brodmann Area 29	2.05
R Angular Gyrus	1.06	Brodmann Area 3 Primary Somatosensory	1.82
L Lingual Gyrus	1.04	Brodmann Area 4 Primary Motor	1.81
L Middle Occipital Gyrus	1.01	Brodmann Area 30	1.62
L Angular Gyrus	0.98	Brodmann Area 5	1.59

Table 5.1., continued.

Anatomical Region	Dipole Density Ratio	Anatomical Region	Dipole Density Ratio
R Gyrus Rectus	0.91	Brodmann Area 6 Premotor and Supplementary Motor	1.43
L Inferior Occipital Gyrus	0.9	Brodmann Area 7 Somatosensory Association	1.31
R Middle Frontal Gyrus	0.87	Brodmann Area 18 Secondary visual (V2)	1.24
R Putamen	0.84	Brodmann Area 2 Primary Somatosensory	1.22
L Supramarginal Gyrus	0.83	Brodmann Area 41 Primary and Association Auditory	1.2
L Insular Cortex	0.81	Brodmann Area 17 Primary visual (V1)	1.17
L Superior Temporal Gyrus	0.8	Brodmann Area 27	0.95
L Gyrus Rectus	0.79	Brodmann Area 19 Associative visual (V3)	0.94

Table 5.1., continued.

Anatomical Region	Dipole Density Ratio	Anatomical Region	Dipole Density Ratio
R Superior Temporal Gyrus	0.73	Brodmann Area 22	0.92
L Middle Frontal Gyrus	0.73	Auditory processing	
R Insular Cortex	0.7		
L Middle Temporal Gyrus	0.7		
R Inferior Frontal Gyrus	0.66		

Table 5.2. Average residual variance (RV) of anatomical regions with significantly low or high RV (FDR-corrected two-tailed p value < 0.05). Each area is marked as ‘High’ or ‘Low’ in the table as ‘type of significance’ depending on whether the average RV was higher or lower than what would be observed if the distribution of RVs was random.

Anatomica l Region	Average Residual Variance (%)	Type of significance	Anatomical Region	Average Residual Variance (%)	Type of significance
R Inferior Occipital Gyrus	4.9	Low	R Inferior Temporal Gyrus	7.4	High
L Inferior Occipital Gyrus	5	Low	L Supramargi nal Gyrus	7.4	High
R Middle Occipital Gyrus	5.5	Low	L Inferior Frontal Gyrus	7.4	High
R Superior Occipital Gyrus	5.5	Low	R Superior Frontal Gyrus	7.4	High
R Cuneus	5.6	Low	R Superior Temporal Gyrus	7.5	High

Table 5.2., continued.

Anatomica l Region	Average Residual Variance (%)	Type of significance	Anatomical Region	Average Residual Variance (%)	Type of significance
L Precuneus	5.7	Low	R Supramargi nal Gyrus	7.5	High
R Lingual Gyrus	5.7	Low	L Parahippocoa mpal Gyrus	7.5	High
L Superior Occipital Gyrus	5.8	Low	R Angular Gyrus	7.5	High
L Lingual Gyrus	5.8	Low	L Gyrus Rectus	7.6	High
L Cuneus	6	Low	R Middle Frontal Gyrus	7.6	High
L Middle Occipital Gyrus	6	Low	L Middle Frontal Gyrus	7.6	High
Cerebellum	6	Low	R Caudate	7.6	High

Table 5.2., continued.

Anatomical Region	Average Residual Variance (%)	Type of significance	Anatomical Region	Average Residual Variance (%)	Type of significance
L Postcentral Gyrus	6.2	Low	L Angular Gyrus	7.7	High
L Precentral Gyrus	6.4	Low	R Gyrus Rectus	7.8	High
L Middle Temporal Gyrus	6.7	High	R Insular Cortex	7.8	High
R Cingulate Gyrus	6.7	High	Brainstem	7.8	High
L Cingulate Gyrus	6.8	High	L Middle Orbitofrontal Gyrus	7.8	High
L Lateral Orbitofrontal Gyrus	7	High	R Middle Orbitofrontal Gyrus	7.9	High

Table 5.2., continued.

Anatomica l Region	Average Residua l Varianc e (%)	Type of significance	Anatomical Region	Average Residual Variance (%)	Type of significance
L Inferior Temporal Gyrus	7	High	L Hippocamp us	8	High
R Middle Temporal Gyrus	7.1	High	R Putamen	8.2	High
R Fusiform Gyrus	7.1	High	R Parahippoca mpal Gyrus	8.3	High
L Superior Frontal Gyrus	7.2	High	R Hippocamp us	8.8	High

Chapter 6

Measure Projection Analysis: A Probabilistic Approach to EEG Source Comparison and Multi-Subject Inference

6.1 Abstract

A crucial question for the analysis of multi-subject and/or multi-session electroencephalographic (EEG) data is how to combine information across multiple recordings from different subjects and/or sessions, each associated with its own set of source processes and scalp projections. Here we introduce a novel statistical method for characterizing the spatial consistency of EEG dynamics across a set of data records. *Measure Projection Analysis* (MPA) first finds voxels in a common template brain space at which a given dynamic measure is consistent across nearby source locations, then computes local-mean EEG measure values for this voxel subspace

using a statistical model of source localization error and between-subject anatomical variation. Finally, clustering the mean measure voxel values in this locally consistent brain subspace finds brain spatial domains exhibiting distinguishable measure features and provides 3-D maps plus statistical significance estimates for each EEG measure of interest. Applied to sufficient high-quality data, the scalp projections of many maximally independent component (IC) processes contributing to recorded high-density EEG data closely match the projection of a single equivalent dipole located in or near brain cortex. We demonstrate the application of MPA to a multi-subject EEG study decomposed using independent component analysis (ICA), compare the results to k-means IC clustering in EEGLAB (sccn.ucsd.edu/eeglab), and use surrogate data to test MPA robustness. A Measure Projection Toolbox (MPT) plug-in for EEGLAB is available for download (sccn.ucsd.edu/wiki/MPT). Together, MPA and ICA allow use of EEG as a 3-D cortical imaging modality with near-cm scale spatial resolution.

6.2 Introduction

Because of the very broad biophysical point-spread function governing volume conduction of areal potentials generated in the human brain to scalp electrodes measuring their summed electroencephalographic (EEG) activity, proper analysis of event-related or ongoing EEG dynamics should best focus on EEG source activities and corresponding (3-D) brain source locations rather than on scalp channel activity records and (2-D) channel locations. Comparing 3-D source locations and source dynamics across subjects and sessions of an EEG study is, however, more difficult than simply equating scalp channel locations across subject and sessions, as is typical in EEG studies that analyze the scalp channel signals directly.

Here we introduce a probabilistic approach, Measure Projection Analysis (MPA), for population-level inference from source-resolved EEG signals. This approach provides, for each EEG measure of interest, 3-D maps of separable brain domains with separable source measures plus statistical estimates of measure differences across group and/or conditions. Although source-level locations and dynamics used in MPA might be derived from any EEG source discovery method, e.g., beamforming or trial-averaged event-related potential (ERP) source analysis, we here demonstrate its application to an example EEG study decomposed using independent component analysis (ICA) and compare its results to those of the PCA-

based independent component (IC) clustering available in EEGLAB (Delorme & Makeig, 2004).

ICA [20] has become a method of widespread interest for analysis of EEG data [22], [23], [24], [25], [26]. In this approach to EEG source analysis, unaveraged continuous or epoched EEG data from multiple scalp channels are decomposed into independent component (IC) processes by learning a set of spatial filters that have fixed relative projections to the recording electrodes and produce maximally independent individual time courses from the data. ICA thus learns *what* independent processes (information sources) contribute to the data and also reveals their individual scalp projection patterns (scalp maps), thereby simplifying the EEG inverse source localization problem to that of estimating *where* each source is generated, a much simpler problem than estimating the source distributions of their ever-varying linear mixtures as recorded by the scalp electrodes themselves.

The IC filters linearly transform the representational basis of EEG data from a channel matrix (scalp channels by time points) to a sum of independent component processes with maximally independent time courses and fixed scalp projections (scalp maps, with often strongly overlapping topographies). Many ICs predominately account for the contributions to the channel data from a non-brain ('artifactual') source process -- for example potentials arising from eye movements, scalp muscle activity, the electrocardiogram, line noise, etc., while many other ICs are compatible

with a source within the brain itself, in particular within its convoluted cortical shell in which most of the spatially organized potentials reaching the scalp are generated [27].

Many of the brain-based ('non-artifactual') IC scalp topographies may be modeled as the projection of a single equivalent dipole inside the brain volume [26]. ICA algorithms return many such 'dipolar' IC data sources (those for which most of the spatial variance of the electric field pattern they produce on the scalp is accounted for by the projection of a single 'equivalent' dipole). On average, the more independent the resulting ICs returned by an linear ICA decomposition method, the more near-dipolar ICs are returned [28]. Such dipolar ICs are compatible with an origin in locally-synchronous cortical field activity within a single cortical patch, which by biophysics must be located near to and oriented predominantly perpendicular to the equivalent dipole [29] (A few clearly brain-based ICs may have scalp maps very closely resembling the summed projection of two bilateral cortical patches that contribute synchronous activity to the scalp signals).

Finding the actual cortical patch (or patches) generating a given dipolar IC may be difficult [10], as it requires (at least) a good quality MR head image for the subject and accurately recorded scalp electrode positions [30]. Given a good estimate of where the scalp electrodes were placed on the head, and a near-dipolar IC scalp map, the location of the equivalent dipole may be found reliably, in many cases with less than a centimeter error when 3-D electrode positions are recorded (Akalin Acar, submitted) and an accurate skull conductance value is used in the analysis.

Biophysical simulations also show that the equivalent dipole for a cm²-scale cortical patch source is, on average, less than 2 mm from the center of the generating patch (Akalin Acar, unpublished). Thus, a unique advantage of ICA applied to EEG is that localizing sources from its single-source IC scalp maps avoids uncertainties associated with multiple local minima that limit the accuracy of estimates of the more complex source distributions computed from scalp maps that sum projections of multiple sources -- for example nearly all raw EEG scalp maps or maps for later peak latencies in ERP waveforms. Of course this level of spatial accuracy is only possible using single-subject head models, which are possible only when an MRI head image is available (as it was not for our subjects). Using individual head models for localization will make it necessary to warp the cortical locations of the multiple subjects into a common head model to allow group Measure Projection. Results calculated, as here, using IC locations in a common head model may well have somewhat less spatial accuracy, though their accuracy might be improved in subject-level analysis by translating them back to associated locations in individual subject head models, including models constructed by warping a common template model to the recorded 3-D positions of the scalp electrodes (Acar and Makeig, 2010). However, unless subjects are highly ethnographically diverse (infants and adults, for example) the choice of head model is unlikely to have much effect on the topology of the MPA results -- more anterior source domains will remain more anterior, etc.

Since ICA uses waveform differences to separate independent sources, which depend both on the exact placements of the scalp electrodes and the individual subject cortical geography, optimal separation is achieved when it is applied to data channels recorded simultaneously from a single subject with a single scalp montage. The length of the training data must be sufficient for the number of recording channels. Since both EEG channel locations and conductance values slightly differ across subjects and sessions, and positions and orientations of corresponding cortical source areas differ across subjects, ICA decompositions are best applied separately to each recorded session or smaller data set from a single recording session.

A standard way to analyze EEG data is to first conduct an experiment in which a number of (outwardly) similar events occur, typically stimulus (e.g., image) presentation and behavioral events (e.g., impulsive button presses). Sets of EEG activity epochs recorded in some latency window around these events (experimental trial epochs) are extracted, averaged, and compared. A number of mean measures of event-related EEG trial data have been developed in recent years and incorporated into freely available software toolboxes including EEGLAB [21], Fieldtrip [72], the SPM toolkit [73], and ICALAB [74]. These measures, including average ERP time series and event-related spectral perturbation (ERSP) [75] and inter-trial coherence (ITC) time/frequency transforms, may equally be computed for single ICs as well as for single scalp channels. For each subject session and associated ICA decomposition, each IC has a unique scalp map and EEG time course. To support group-level

inferences about EEG measure differences across task trial conditions, subject groups, recording sessions, etc., IC location and EEG measure information must be integrated across subjects and sessions

In contrast to the common approach to obtaining group inferences from channel data, i.e. by assuming equivalence across subjects of electrode derivations from standardized scalp locations [76] [77], combining results across different ICA decompositions is non-trivial. Several methods have been proposed for this task. These typically fit into two categories: IC clustering [26], [78], [79] , [80] and joint decomposition methods such as group-ICA [36], [37], [38], [39], multi-set canonical correlation analysis [41] and J-BSS [43] [44] .

Although the IC clustering method uses a potentially larger subspace of the signal (involving less dimensionality reduction than most joint decomposition methods) and poses fewer restrictive assumptions regarding the relationship between signal sources at subject and group level, it often involves tuning multiple parameters (relative measure weights, number of cluster, etc..), potentially reducing the objectivity of the analysis and reproducibility of the results; for a recent approach to tackling this problem see [80]. Also, it is often impractical to calculate the significance of IC clusters themselves, whose averages are often used in subsequent statistical tests for measure differences across conditions or groups.

MPA aims to solve the problem of comparing EEG source locations and dynamics across subjects and sessions in 3-D brain space using a probabilistic approach that treats the source-resolved data as samples drawn from the distribution of source locations and dynamics. By performing statistical comparisons on a grid of brain locations instead of individual sources, and focusing on a single dynamic measure of interest at a time, MPA reduces the number of parameters assumed in the analysis, and delivers estimates of the statistical reliability of the results. Here we demonstrate the application of MPA by applying MPT tools to an example EEG study, comparing its results to standard PCA-based IC clustering, and studying the robustness of the MPA results using surrogate data.

6.3 Methods

The Measure Projection Analysis (MPA) approach introduced here comprises four steps: 1) After decomposition of the unaveraged EEG data by ICA into brain source processes (ICs), the location of each source signal used in the analysis is computed within a common brain template model, here in the form of a IC source equivalent dipole. 2) Spatial smoothing of a given dynamic measure for the equivalent dipole-localized ICs is performed using a truncated 3-D Gaussian spatial kernel; 3) A subspace of brain voxel locations with significant local IC measure similarity are identified (see Appendix A for a detailed description); 4) Spatial brain voxel domains

within the measure similarity subspace that exhibit sufficient measure differences are identified using affinity clustering (details in Appendix B).

6.3.1 Experimental data

EEG data were collected from 128 scalp locations at a sampling rate of 256 Hz using a Biosemi (Amsterdam) Active View 2 system and a whole-head elastic electrode cap (E-Cap, Inc.) forming a custom, near-uniform montage across the scalp, neck, and bony parts of the upper face.

6.3.2 Subject task

Our sample study consisted of data from 15 sessions recorded from 8 subjects performing a Rapid Serial Visual Presentation (RSVP) task [48] (the raw data are available at <ftp://sccn.ucsd.edu/pub/headit/RSVP>, the EEGLAB Study files at ftp://sccn.ucsd.edu/pub/measure_projection/rsvp_study). Each session comprised 504 4.9-s image bursts of 49 oval image clips from a large satellite image of London presented at a rate of 12/s. Some (60%) of these bursts contained one image in which a target white airplane shape was introduced at a random position and orientation. Following each burst, subjects were asked to press one of two buttons to indicate whether or not they had detected a target airplane in the burst. Figure 6.1 shows a time-line of each RSVP burst. For further details see [48].

6.3.3 Data preprocessing.

After preprocessing each subject data set using EEGLAB (sccn.ucsd.edu/eeglab) and custom Matlab functions for re-referencing, from the active-reference Biosemi EEG data to an electrode over the right mastoid, high-pass filtering above 2 Hz, and rejection of channels and data containing non-stereotypical artifact, an ICA decomposition was performed for each recording session. The subset of ICs that could be represented by an equivalent dipole model with low error (here defined as more than 85% of channel variance in the IC scalp map being accounted for by a single equivalent dipole or in a few cases a bilaterally symmetric equivalent dipole pair) were selected for analysis. ICs with equivalent dipoles located outside the MNI brain volume (e.g., those with a minimum distance to the MNI brain surface larger than 1 mm) were removed as artifactual, and mean event-related power spectral perturbations (ERSPs) to target and Nontarget images were computed for the remaining 260 ICs (per session mean 18, standard deviation ± 8).

6.3.4 ERSP measure projection

Figure 6.2A represents the processing pipeline schematically. To apply MPA to the RSVP study we used a Measure Projection Toolbox (MPT) for MATLAB (The Mathworks, Inc.) implementing MPA and operating as an EEGLAB plug-in (freely available for download at sccn.ucsd.edu/wiki/MPT). To compare MPA results to those of IC clustering as implemented in EEGLAB, we set the standard deviation of the three-dimensional Gaussian representing each equivalent dipole location probability density to 12 mm. This parameter reflected a heuristic estimation of the combined

ambiguity in equivalent dipole locations arising from a) numerical inaccuracies in the IC component maps, b) errors in co-registering the measured channel locations with the standard brain model, c) inaccuracies in the forward head model, d) particularly in assumed conductances of skull and brain tissues, and e) difference across subjects in brain locations of functionally equivalent brain areas. This standard deviation value was also chosen in part to produce smoother spatial distributions for this rather small EEG study: for larger studies it might be usefully reduced. We truncated each Gaussian to a radius of 3 standard deviations (36 mm) to prevent spurious influences from distant dipoles in sparsely filled source regions.

Brain model: A cubic dipole source space grid with 8-mm spacing (3,908 vertices) was situated in the brain volume in MNI (Montreal Neurological Institute and Hospital, [68]) space . Voxels outside the MNI brain volume were excluded. Local convergence values (see Appendix A for definition) were calculated using equation (A.2), A pairwise IC similarity matrix was constructed by estimating the signed mutual information between IC-pair ERSP measure vectors using a Gaussian distribution assumption [81]:

$$\text{Mutual Information} = \frac{1}{2} \text{sign}(\text{correlation}) \log_2 \left(\frac{1}{1 - \text{correlation}^2} \right) \text{(bits/sample)}$$

The reason for using an estimate of signed mutual information instead of correlation itself was because equal correlation intervals may reflect unequal information differences. For example, the difference in mutual information values

associated with IC measure correlation values of 0.8 and 0.9 is far greater than mutual information difference associated with IC correlations of 0.1 and 0.2. In addition, mutual information values (in bits/sample) may be meaningfully averaged. In switching to use of signed estimated mutual information instead of linear correlation, we also observed an improvement in the spatial smoothness of the obtained MPA significance values.

A significance threshold for convergence values at each brain grid location was obtained by bootstrap statistics. We permuted the similarity matrix (with substitution), in effect removing the correspondence between each IC and its associated ERSP, and calculated 2,000 surrogate convergence values at each voxel associated with the null hypothesis of no stable association between brain region and ERSP. Probability values were calculated by finding the percentage of bootstrap convergence values larger than the original convergence value (right-tail comparison).

A group-wise $p < 0.05$ threshold, corrected for multiple comparisons using False Discovery Rate (FDR) testing [69], gave a raw voxel significance threshold of $p < 0.0075$. Voxels with convergence probabilities lower than this threshold defined the ERSP ‘measure convergence subspace’ of brain voxel locations at which the local similarity of IC ERSPs was significantly higher than what could be expected by chance in these data.

Condition difference tests: For each identified study domain d and subject session s , statistical significance of differences between the Target and Non-Target condition ERSPs was computed by first projecting the ERSP associated with each condition c to each voxel i in the domain, producing projected measure $M(c,i,d)$. We then calculated a weighted-mean measure $W(d,s,c)$ across all v domain voxels, each weighted by $D(i,s)$, the dipole density of voxel i in session s , and then normalized by total domain voxel density.

$$W(d,s,c) = \frac{\sum_{i=1}^v M(c,i,d) D(i,s)}{\sum_{i=1}^v D(i,s)}$$

Where

$$D(i,s) = \sum_{j=1}^n P_j(i)$$

Above, n is the number of component dipoles in the session and $P_j(i)$ is the model probability that dipole j is actually at domain voxel i (see Appendix A).

Next, a two-tailed Student-T test was applied to the collection of session-mean projected measures in the two conditions to test for reliable domain-ERSP condition differences. For visualization, non-significant ($p \geq 0.05$) values in each domain condition-ERSP difference were masked by replacing them with 0s.

6.3.5 ERSP domain clustering

To simplify the analysis of projected source measure values in the measure convergence subspace, we separated them into several distinguishable spatial *domains* by threshold-based Affinity Propagation clustering (described in Appendix B) based on a similarity matrix of pair-wise correlations between the projected measure values at each voxel position. Affinity propagation automatically finds an appropriate number of clusters (below referred to as spatial domains) based on the maximum allowed correlation between cluster exemplars, automatically increasing the number of clusters until any other potential cluster exemplar becomes too similar to one of the existing exemplars. Here, maximal exemplar-pair similarity (forcing creation of additional clusters) was set to a correlation value of 0.8, and the outlier detection similarity threshold to a correlation value of 0.7. The method did not find any outlier voxels since all of the projected measures in each domain had a correlation with their domain exemplar higher than 0.7. The minimum correlation value is in fact an optional parameter: one could decide to not exclude any significant voxel from domain analysis by setting the minimum correlation threshold to negative infinity. Note that the voxel clustering procedure does not force the voxels within a single domain to be contiguous; for example near-identical ERSPs may be produced in bilaterally symmetric cortical regions, which may then be identified by affinity clustering as a single measure domain. Figure 6.2A summarizes the MPA steps used to create distinguishable spatial source domains for each EEG measure.

6.3.6 PCA-based IC clustering

In the PCA-based IC clustering approach implemented in EEGLAB (Makeig et al., 2002; Onton & Makeig, 2006), cross-session IC equivalence classes are typically defined by applying a clustering algorithm such as k-means to an L2-weighted combination of EEG measures of interest (e.g., IC equivalent dipole locations, scalp-map topographies, mean power spectra, average ERPs, etc.) so as to produce a desired number of IC clusters (10-30). Cluster-level mean EEG measure values may then be calculated by averaging across the members of each IC cluster, and may then be used for group-level inference and event or task condition comparison. The default IC clustering options create a *pre-clustering array* that represents each IC as positioned in a joint-measure feature space by the following operations:

- (1) *Mean EEG measure computation:* For each IC, each set of experimental trials (experimental ‘condition’) and each EEG measure of interest (ERP, mean power spectrum, ERSP, and/or Inter-Trial Coherence (ITC)), subject-mean IC measure values are computed and then concatenated across conditions.
- (2) *Measure dimensionality reduction:* Next, the dimensionality of the concatenated condition measures for each IC is reduced by PCA to a principal subspace. The subspace dimensionality is heuristically determined based on the amount of trial data available. Measure values associated with each IC in the PCA-reduced coordinates are normalized by dividing them by the standard deviation of the first principal component.

(3) *Equivalent dipole locations:* Dipole (x,y,z) location values in the adult template MNI brain space are normalized and then multiplied by a user-specified scalar weight to determine their relative influence in the subsequent clustering.

(4) *Joint-measure IC-space representation:* Dimensions associated with each EEG measure (after preprocessing steps describe above) are concatenated to represent each IC in a joint space. For example, ERSP information represented by 10 PCA dimensions may be concatenated with 5 PCA dimensions representing ERP information and 3 (MNI x,y,z) location dimensions representing dipole position to form a joint $10+5+3 = 18$ dimensional space in which each IC is located.

(5) *IC clustering:* ICs in this joint-measure IC space are then clustered using k -means or some other clustering method. The number of clusters is user supplied.

All ICs, represented by features in the resulting pre-clustering array, are then clustered using the k-means method implemented in the Matlab Statistics Toolbox (The Mathworks, Inc.). Figure 6.2B shows a flowchart of this clustering method. For more details and a sample application of this procedure, see [79].

6.3.7 PCA-based ERSP measure clustering

EEGLAB default (PCA) clustering was used to create 15 clusters using ERSP and dipole location measures. ERSP values for Target and Nontarget conditions were concatenated across the time dimension for each IC and were reduced to 10 principal

dimensions by PCA. After default normalization, equivalent dipole location values were weighted by the default factor 10. The MATLAB implementation of the *k*-means method was then used to form IC clusters.

Clustering results for different numbers of clusters were first examined by eye and the number of clusters was thereby adjusted such that (a) dipoles assigned to a given cluster formed a single, relatively focal cluster, in anatomical (MNI) space (although it is possible for multiple distal brain regions to display similar EEG dynamics, resulting in clusters with dipoles localized to multiple brain regions, we have found that such clusters usually appear as a consequence of cluster merging when the number of clusters is set too low); and (b) clusters are maximally non-overlapping and contain a reasonable number of dipoles (overlapping and/or small-size clusters may occur when the number of clusters is either too low or too high). These criteria did not take into account the similarity structure of other measures (e.g., ERPs) which would ideally further influence the choice of cluster number.

6.4 Results

6.4.1 ERSP measures for PCA-based IC clusters

Figure 6.3 shows a scatter-plot of computed IC-pair ERP and ERSP similarities. Because of the inherent ambiguity in the polarity of IC activations, absolute-value correlations of ERPs for each IC pair was used as an upper bound on their ERP similarity. As can be seen in this figure, as the correlation between these

two sets of values is low (0.26), the similarity structures of (absolute) ERP and ERSP measures are far from identical. This affirms our decision here to not include ERP measure data in ERSP clustering.

Figure 6.4 and Figure 6.5 show cluster dipole locations and Target ERSP values averaged over ICs belonging to each cluster. Figure 6.4 shows a subset of clusters with large (more than 1.7-dB) mean Target ERSP values, while Figure 6.5 shows clusters with mean Target ERSP values below 1.3 dB. Although most eye movement-related components were rejected as they were localized outside MNI brain volume, due to localization errors some of these IC were assigned to locations inside brain; these were concentrated in Cluster 11.

Nontarget ERSP values were lower ($p < 0.05$) or close to zero for all these clusters. Statistical significance analysis of differences between Target and Nontarget ERSPs was performed by bootstrap statistics permuting Target and Nontarget conditions across ICs belonging to each cluster. This statistical test was performed for each cluster separately.

6.4.2 ERSP measure projection results

Figure 6.6A shows the significant voxels ($p < 0.0075$; group-wise $p < 0.05$ under FDR). The voxels were colored by first applying non-metric multi-dimensional scaling (MDS, as implemented in Matlab *mdscale* function with stress normalized by the sum of squares of the interpoint distances and other parameters set to their default

values) to the projected (concatenated Target and Nontarget) ERSP measures, by this means mapping them to a single dimension. These 1-D MDS values were then mapped to the [.00, .69] hue interval in the MATLAB hue color scale (from red to blue) so as to display brain locations with similar projected measures in similar colors. Figure 6.6B shows four measure-consistent IC domains obtained from the Affinity Propagation method implemented as threshold-based clustering (Appendix B). These are colored by one-dimensional MDS of the projected measure associated with their most representative member (the domain exemplar, using a similar MDS procedure as in Figure 6.6A). By comparing Figure 6.6A and Figure 6.6B we can see how these four domains summarize the projected measure values: Figure 6.6A shows roughly four colored regions that map into the four identified measure domains shown in Figure 6.6B.

Figure 6.7 shows an alternative visualization of ERSP Domains: exemplar MNI cortical surface is colored by domain color, weighted by dipole density, from brain-grid positions radially below each cortical location.

6.4.3 Comparison of MPA and PCA-based clustering methods

Next, we compared the results obtained from PCA-based IC clustering to those obtained using measure projection analysis (MPA). Table 6.1 gives the cluster number(s) located in or near each domain. Average ERSPs for these clusters are highly similar to those of respective domain exemplars, indicating that here measure

projection analysis produced results in close agreement with IC clustering in locations with statistically significant ERSP similarity across subjects.

Our PCA-based clustering, on the other hand, gave 15 clusters, many not associated with any significantly convergent MPA region. For example, Clusters 2 and 3 in Figure 6.5 are relatively far from brain areas with significant ERSP convergence shown in Figure 6.6A. Since MPA showed that ICs associated with these PCA-based clusters have fairly dissimilar ERSP measures, there is not much statistical evidence in the data for MPA spatial convergence in these regions to support the validity of these clusters.

Table 6.1 also lists anatomical locations associated with each ERSP domain based on the LONI project probabilistic atlas [52] and Brodmann areas [82] from [70]. The listed functional associations of these areas are based on Brodmann's Interactive Atlas (fmriconsulting.com/brodmann/Introduction.html). On close inspection, because of errors in dipole localization related to insufficient electrical head modeling in the complex peri-orbital regions, many eye-artifact ICs (13 out of 16 highly contributing ICs) in this study were localized inside the brain volume and became the main contributors to ERSP Domain 1 and PCA Cluster 11. In measure projection analysis, brain and non-brain ICs should not be mixed. Performing an additional artifact IC rejection step, using methods for identifying eye artifact ICs from their activity profiles as well as their equivalent dipole locations such as CORRMAP [55] or

ADJUST [57] should be done before MPA to give meaningful results in frontal regions.

Of similar concern are ICs accounting for scalp muscle activity that, for EEG montages with sufficient scalp coverage, have scalp maps consistent with an equivalent dipole at the insertion of the muscle into the skull (as seen in[78]). These may be differentiated from brain ICs prior to measure projection by their dipole locations (outside the skull) and by their characteristic electromyographic (EMG) spectra with a minimum below 20 Hz and a high-level plateau at higher frequencies. Here we removed scalp/neck muscle ICs based on their dipole locations before applying measure projection.

Domains 2 and 3 are both associated with Secondary (V2), Associative (V3) and Primary (V1) visual cortex (BA 18,19 and 17) [83] [84]. Domain 3 is in or near BA 31 which has been reported to support high-demand visual processing and discrimination [85]. Domain 2 is in or near bilateral BA 37 and fusiform gyrus (with a right bias), areas reported in a fMRI study of a visual perceptual decision-making task [86]. Similar low-theta band activity occurring about 400 ms after visual target detection in these brain areas was reported in [87].

There is some evidence of mu rhythm desynchronization (suppression) in Domain 4, located in or near right-hand Primary Somatomotor, Primary Motor, and Somatosensory Association areas (BA 7,3,2,4), which may be related to mu rhythm

activity that appears in hand somatomotor cortex when subjects hold a button in their right hand [87]. Subjects were asked to wait until the end of RSVP image burst before pressing a response button. The mu rhythm activity in this area is thought to reflect cortical inhibitory (or ‘idling’) dynamics that may decrease the chance of prematurely pressing the button. Activation in or near BA40 and BA7 is also consistent with a preliminary FMRI study conducted by [54] in which BOLD activation was observed during rapid discrimination of visual objects accompanied by a motor response.

Since MPA represents each IC equivalent dipole location by a Gaussian density and computes MPA domains in brain regions exhibiting significant local measure convergence, we may expect that equivalent dipoles positioned in or near MPA domains will have EEG measures similar to the domain exemplar measure. To verify this prediction, in Figure 6.8A for one ERSP domain we plotted some such dipoles (e.g., those with total probability density within the domain above 0.05) and colored them by the correlation of their EEG measures with the domain exemplar. As expected, the majority of these dipoles have an ERSP similar to the domain exemplar. In Figure 6.8B, domain exemplar ERSPs for Target and Nontarget conditions and their statistically masked difference ($p < 0.05$) are plotted.

6.4.4 Simulation

To test and validate our MPA procedures, we conducted simulations to investigate the performance of the method across different noise levels and parameter choices.

We started by selecting four anatomical domains (Figure 6.9A: R Superior Parietal Gyrus, L Inferior Occipital Gyrus, L Lateral Orbitofrontal Gyrus and R Superior Temporal Gyrus, from LONI LPBA40 atlas [52]) in MNI space as ground truth and assigned to each the ERSP pattern from one of our RSVP-experiment domains. We then placed 31 dipoles by randomly selecting locations from the ground-truth domains and adding Gaussian spatial noise to the dipole locations using 12-mm std. dev. Gaussian noise to simulate localization error and subject variability in measured IC equivalent dipole positions. The number of dipoles per ground-truth domain (31) was selected to be the average number of dipoles for which more than 10% of their density, modeled by a truncated 3-D Gaussian, was located in an ERSP-measure domain of our RSVP experiment. We considered two simulation conditions: (1) assigning this ERSP patterns to simulated IC dipoles associated with each ground-truth domain (zero noise) (2) adding 0.2 dB RMS amplitude noise to the ERSP pattern associated with each IC dipole (simulating experiment noise).

We then sequentially added 142 other dipoles to the model, each placed at the brain volume location (in an 8-mm grid) farthest from all other existing dipoles. Pseudo-ERSP measures composed of random 0.2-dB white noise samples were assigned to these dipoles. The simulation thus contained the same number of brain

dipoles as our RSVP experiment, with spatially coherent measure values only in the four model domains.

MPA was then performed on this simulated collection of dipole locations and associated ERSP measures. The resulting domains were then compared to ground-truth domains for the two simulation noise conditions mentioned above (Figure 6.9B). We used two scoring methods to evaluate the performance of MPA method (a) Cohen's kappa [88], a measure of inter-rater agreement (b) the average percentage of ground-truth domain locations that were associated with the correct domain in the results. In both scoring methods we accounted for permutations in domain labels and included the locations which should not be associated with any ground-truth domain as an extra category (they should not be assigned to any domains in the results).

Table 6.2 shows MPA performance scores for simulation results with a voxel significance p-value threshold of 0.05, maximum exemplar correlation threshold of 0.8, and varying noise levels. To explore the sensitivity of MPA results to the choice of the location uncertainty parameter (the standard deviation of the Gaussian representing each dipole), we also tested different values of this parameter for two ERSP noise levels (noiseless and 0.2 dB). These simulation results show that MPA can recover brain domain locations with high accuracy ($> %80$) in the presence of noise, and that using inaccurate dipole density extent priors (e.g., using a 10-mm or a 14-mm instead of the ground-truth 12-mm std. dev. for the spatial-perturbation Gaussian) has relatively little effect on their locations.

6.5 Discussion

The localized EEG source estimates returned by ICA decomposition bring closer the promise of performing near cm-scale functional cortical imaging using non-invasive EEG while retaining its fine temporal resolution. However, applying ICA-based EEG imaging to studies involving multiple subjects and/or sessions requires a method for combining IC source location and activity measure information for ICs decomposed from multiple data sets. Here we demonstrate a first application of measure projection analysis (MPA) to EEG data sets collected in a visual RVSP task and decomposed separately using extended infomax ICA. We compare the results of MPA to results of applying k-means clustering jointly to the same IC source locations and EEG measures. Results of MPA were consistent with IC clustering but depended on fewer parameters and provided statistical significance values. MPA applied to surrogate data derived from the RVSP data demonstrated that MPA results are not highly sensitive to prior parameter choices.

While here we feature application of MPA to group and condition statistics for standard event-related mean measures (ERPs and ERSPs), MPA may equally well be applied to any other continuous or event-related EEG measure, or indeed to any measure at all. For example, MPA applied to recovered IC equivalent dipole locations from an EEG session and a measure of the subject's memory ability might reveal differences in IC dipole density associated with better or worse memory performance.

Reliable differences in dipole density might arise from difference either in brain structure or dynamics during the EEG data collection. MPA has several other attractive features:

6.5.1 Relative Parsimony

Since across-subject and -session variability both in estimated and actual source locations and in dynamic EEG measure estimates are expected in any study, any model of subject group and/or session mean measures for a high-density EEG study must be probabilistic and therefore controlled by model expectations and statistical thresholds used in the analysis (in this, MPA applied to EEG data is similar to group-level analyses for fMRI data). Among such methods, the principle of parsimony (Occam's Razor) prefers methods that characterize the data variability (here, across data sets) using a minimal number of free parameters. Applying MPA to a single- or multi-dimensional EEG measure computed for a number of EEG sources, each tagged with an estimated source location in a standard anatomic head model, requires 1) a width parameter for the Gaussian density representing each source location, 2) a (p-value) significance threshold that can affect the size of the measure convergence subspace, and 3) a maximum domain exemplar measure similarity threshold used in domain clustering (the outlier detection threshold is an optional parameter). These MPA parameters are neurophysiologically interpretable and may not require sensitive tuning in applications to different studies.

In comparison, the PCA-based multi-measure source clustering approach introduced in [26] and now available in EEGLAB [21] requires two parameters per dynamic EEG measure (the number of principal dimensions retained and the relative measure weighting value), plus a relative weight for equivalent dipole location and the number of clusters to create (e.g., four total independent parameters for one measure, six parameters for two measures, etc.). Since there is no statistically motivated method for choosing these parameters, they may in practice be set by the experimenter to produce most subjectively desirable results. Because of the relatively large number of such variables, and the sensitivity of final clustering results to their values, experimenter parameter settings may have profound effects on inferences at the group-level. This also introduces a significant and undesirable lack of objectivity in interpreting EEG data and hinders the calculating of significance statistics for group-level or session-level results. Even if well-justified methods were introduced to set the source clustering parameters, it would be still difficult to determine the statistical significance (including p-values) of cluster measure means because these statistical methods are often based on bootstrap null-hypothesis testing that is not easily and directly applicable to source clusters.

Recently an IC source clustering method called MAGMICK has been proposed by [80]. MAGMICK optimizes the relative weighting of different IC source measures so as to increase the mean silhouette value of IC clusters and selects the number of clusters found using modified K-Means clustering based on the constraint that two IC

sources from the same session should not be clustered together. Their results show that MAGMICK outperforms other direct IC source clustering methods applied to data from a sample MEG study.

However, the fact that session ICs are obtained by minimizing time-course independence over the whole experiment is not sufficient for the independence constraint conclusion made in MAGMICK. This is because ICA achieves maximal independence only for the whole time course of the experiment; ICs from the same decomposition may be transiently dependent, most likely in time periods in which EEG dynamics are non-stationary such as periods of significant ERP or ERSP activity. Lastly, MAGMICK does not provide statistical significance values for its clustering solution. Thus, a strength of MPA is that it provides a relatively parsimonious method for data driven identification of brain regions exhibiting statistically consistent measure values.

6.5.2 Source Measure Consistency

MPA provides a statistical characterization of the subspace of brain source locations that exhibit significant EEG measure homogeneity, and identifies, among such locations, spatial domains with distinctive measure features. By contrast, neither PCA-based multiple-measure clustering (as formulated in EEGLAB) nor Group ICA approaches (discussed below) provide such statistics (i.e., tests to determine whether within each identified cluster or factor the computed source measures are significantly

consistent with each other). For example, PCA-based clustering produced 15 clusters in our RSVP study, compared to only four MPA domains, but 9 of these clusters lacked significant measure homogeneity (measure convergence p-value, Eq. (A.3), at their centroid was higher than 0.05) and 8 of them did not have mean measures that were sufficiently distinct (correlation < 0.8) from other clusters.

6.5.3 Source Clustering Coherency

The MPA domain clustering procedure (used here to identify the four ERSP domains) is fundamentally different from the PCA-based clustering approach in that MPA, domain clustering is only employed to summarize projected results at significant brain locations and does not change the projected source measure values.

In contrast, cluster-mean values obtained by the PCA clustering method are highly dependent on the number of clusters and the specified relative measure weight parameters. Neither PCA-based source clustering nor Group ICA approaches use an explicit threshold for separating source clusters or factors based on measure differences. PCA clustering typically operates on a weighted combination of different measures, which prevents the use of meaningful similarity thresholds in threshold-based clustering (see Appendix B of this chapter). In contrast, MPA uses meaningful similarity thresholds (for example, here a maximum measure correlation of 0.8) to identify separate brain-voxel domains whose nearby source measures have separable features.

Using different maximum correlation thresholds only changes the granularity of the segmentation of brain regions exhibiting significant measure consistency into domains, and does not fundamentally affect the values assigned to domains. For example, in the MP analysis shown here, changing the maximum domain measure correlation to 0.9 might identify more measure domains, though the exemplar measures of the added (sub)domains would be quite similar. In general this value must be set based on the expected degree of measure noise and variability in the data which influences how similar two domain exemplar measures could be before they should be considered practically the same. Alternative clustering methods developed for identifying regions of similarly activated voxels in fMRI data, such as Cluster-Based Analysis (CBA) [89], might also be applied to MPA. The Affinity clustering approach used in the MPA toolbox (Appendix B) has the advantage of finding the appropriate number of clusters based on the given similarity threshold without having to specify a final number of clusters beforehand,

6.5.4 Cluster membership

PCA-based IC source clustering limits the types of group-level analysis methods that may be applied to EEG data. For example common clustering methods (e.g., k-means or linkage clustering) output a set of binary (“hard decision”) cluster membership values: each source either fully belongs to a certain cluster or not. As the formation of these clusters is often highly dependent on the multitude of clustering

parameters, it is difficult to separate the effect on the clustering results due to choosing these parameters from the contributions of group-level differences in source features.

As an example, a cluster of interest (e.g., having a particular target ERP feature) may mostly contain sources associated with a certain participant subgroup. At the same time, sources with similar features may exist in nearby clusters and may have been included if a lower number of clusters or slightly different weight parameters were applied to source measures during clustering. It then becomes unclear whether participants have meaningfully different measures (either in terms of source locations or ERP measure features) from a parent or alternate population, or whether the aggregation of sources from this subject group into a particular cluster is an artifact of selecting a particular set of clustering parameters. This problem could be alleviated if sources were given fractional (fuzzy) memberships and if noise were not introduced during the quantization of membership values by the clustering procedure. MPA allows such improvements by adopting a probabilistic spatial representation of source locations.

6.5.5 Cluster shape

MPA operates in brain source domain coordinates and thus gives source domains that are not restricted in shape and may even be discontinuous. For example, a single domain representing bilaterally symmetric source activations may account for synchronous activity within two non-contiguous (but perhaps highly connected)

cortical areas. PCA-based IC clustering, on the other hand, does not explicitly specify brain areas whose EEG-source signals are reactive within a class of experimental conditions. K-means clustering, in particular, is biased towards creating spherical clusters. Further, when an IC cluster is represented by the spatial centroid of its member IC equivalent dipole locations, the spatial extent of each cluster is not investigated statistically. Here MPA provides a statistically supported, data-driven model of cortical regions that exhibit consistent measure features, and the regions so identified may be readily compared to results of other functional imaging experiments, for example reported results of fMRI studies.

6.5.6 Cluster equivalence across measures

Here we propose that MPA should be applied to only one dynamic measure at a time. Another problem associated with PCA-based IC clustering stems from the fundamental assumption of IC cluster equivalence across all EEG measures. In this method it is assumed that those ICs that are similar in one respect (for example, in ERP time courses) are also similar in other aspects (say in their ERSPs or mean spectra), so that combining different measures before clustering (e.g. by concatenating them to form the IC pre-clustering array, Figure 6.2B) should produce better results (cluster distinctiveness is increased by combining measures). This rests on the assumption that the similarity structures of each measure of interest are dominated by an identical or at least compatible IC cluster structure. If this assumption is violated, as our results in Fig 3 indicate for the RSVP data, combining different IC measures may

actually degrade clustering results since they attempt to merge conflicting IC similarity structures.

For example, imagine a situation in which certain brain areas produce an ERP response to a stimulus event class (e.g., visual targets), but that significantly different, yet overlapping, brain areas produce transient mean (ERSP) changes in the IC power spectrum following events of this class. An IC clustering performed on a combination of these two measures (plus equivalent dipole locations) will at best find the spatial overlap between the two areas associated with ERP and ERSP measures, potentially a much smaller area than the areas associated with each EEG measure separately. If the goal of the analysis is, for example, to learn about ERP responses to visual targets, it would appear better to use only the ERP measures and equivalent dipole locations instead of including both ERP and ERSP measures, as we propose for MPA.

It may also be possible to subdivide multi-dimensional measures into sub-regions (for example, ERP latency ranges or time/frequency regions) and apply MPA to each measure region, a possibility that may deserve further examination.

6.5.7 Subject comparisons

When IC process clustering gives disjoint IC clusters, it is not always easy to compare the EEG dynamics of each subject to the group cluster solution. Some clusters may contain no ICs belonging to some subjects. Since so many variable parameters enter into a particular clustering solution, it may be difficult to argue that

the absence of a cluster IC from a given subject necessarily reflects the absence of equivalent EEG source activity for that subject. This issue worsens as the number of clusters increases and fewer subjects contribute ICs to each cluster. MPA overcomes this difficulty by probabilistic representation of dipole locations and abandoning the notion of discrete, disjoint IC clusters.

6.5.8 Group-Level ICA decomposition

ICA was initially applied at the group level as spatial ICA decomposition of group fMRI data [90], [91], [92] [93]. This method has also been applied to resting-state EEG [39] and to joint decomposition of concurrently recorded EEG-fMRI data [94], [36], [37], [38]. Group-ICA is implemented in the EEGIFT toolbox (<http://icatb.sourceforge.net/>) for EEG analysis. In this approach, data sets from multiple subjects are either, (a) concatenated in time, assuming common group IC scalp topographies, or (b) concatenated as separate channels, after some preprocessing (e.g., PCA-based dimensionality reduction), assuming shared event-locked group IC component measure features.

Each of these methods violates the physiological assumptions underlying ICA, arising from differences in brain anatomy and volume conduction [27]. Concatenating EEG recordings from different subjects along the time/latency dimension, and implicitly assuming that subject ICs share scalp maps, ignores significant differences across subjects in cortical anatomy, in particular differences in scalp projection

topography arising from differences in cortical folding, and in functional specificity of corresponding cortical areas [79]. Concatenating event-related response time series data from different subjects in the spatial (channel or PCA-reduced channel) dimension, on the other hand, assumes that ICs share strong feature similarities, in particular event-related response time courses. Thus, for example, for all but the very earliest (brainstem and primary cortical) ERP features a highly unrealistic degree of common event-related time-locking is assumed. Also, this ERP-oriented procedure is intrinsically unable to capture time-locked but not phase-locked dynamics, (as, e.g., captured by ERSPs).

In addition, during group-ICA preprocessing (as described in [95]), the channel data are usually strongly reduced in dimension using PCA (e.g., from 64 channels to 30 principal components) to keep the final number of dimensions after concatenation (across subjects) manageable for application of ICA. As the number of participants increases, even more aggressive PCA dimensionality reduction is necessary to keep the dimensionality of the concatenated data more or less constant (since the number of time points used in group-ICA remains constant and the final ICA requires a certain number of time-points for calculation of each weight in the unmixing matrix). But since PCA only takes into account second-order (correlation) dependencies across channel data, it has lower performance in terms of reducing mutual information compared to ICA, and therefore the remaining dimensions after PCA preprocessing

may potentially lack subspace information necessary for proper ICA separation at either the single subject or group levels.

Another issue with applying group ICA decomposition to event-related EEG data concatenated across channels is that it injects a bias towards finding patterns that are common across subjects. PCA-reduced activities from each subject are (to some degree) time-locked to the event, and subsequent group ICA processing tries to find components that are common across subjects. ERPs for a subset of these group ICs may then just be an artifact of the Group ICA decomposition process (since the common subspace across subjects is amplified and concentrated into a few Group ICs). This bias in data preparation makes calculating proper statistics difficult if not impossible. One would need to perform some type of bootstrap permutation test to estimate the significance of the common activity discovered by this approach, though performing a large number of Group-ICA decompositions on surrogate trial collections may prove computationally impractical.

There are two newer methods that improve on group-ICA for performing group-level joint decomposition: Multiset Canonical Correlation Analysis (M-CCA) [41], which uses an extension of Canonical Correlation analysis to maximize the correlation among the extracted source activations, and blind source separation by joint diagonalization of cumulant matrices [43] [44]. These algorithms avoid the PCA dimensionality reduction of group-ICA but they both also assume that significant linear correlations are present across source activations. EEG source activities across a

group of subjects can only be hypothesized to be similar or linearly correlated if they are all time-locked to a relevant event type (e.g., a rhythmic stimulus) and their duration are limited to data intervals that contain significant ERP features, often less than a second after (or in some cases before) the event. Outside of such time periods, no reliable correlation should exist that can be exploited by group-level decomposition methods. This limits the applicability of these methods for high-density EEG since the portion of data that can be assumed to contain group-level correlations is much shorter than the whole recording so there will be less data available to perform blind source separation (e.g., as compared to Infomax ICA decomposition of data from the entire session). This is likely to adversely affect the performance of the decomposition.

Also, many EEG phenomena occur in time-frequency domain in such a way as to contribute few or no features to average ERPs. In particular event-related spectral perturbations (ERSPs) such as those induced by changes in alertness level [46] measure event-related changes in spectral source power regardless of the level of event-locked phase coherence that produces the event-locked ERP. Since all group-level decomposition methods discussed above operate in the time domain, they are not amenable to time-domain Group ICA approaches.

Recently, [96] has suggested a method to test the inter-subject consistency of ICA solutions statistically based on scalp-map similarities. Because of the differences in dipole orientation arising from between-subject variations in cortical volumes and folding, ICs represented by dipoles in the same functional brain area may have

significantly different scalp maps. Hence this method is more suitable for different sessions of the same subject and should only provide a lower bound on inter-subject consistency (since similar scalp maps are typically associated with similar ICs but not necessarily *vice versa*). The same argument also applies to IC clusters obtained from this method, as they do not take into account equivalent dipole locations associated with ICs.

6.6 Conclusion

Here we have introduced measure projection analysis (MPA), a statistical method for combining source-localized EEG measure information across data sets. We also have presented empirical and simulated results and have discussed the advantages of measure projection relative to previously proposed independent component clustering methods. Measure projection puts results of EEG research into the same brain imaging framework and coordinate system as other brain imaging methods, thereby allowing EEG to be treated and used as a three-dimensional functional imaging modality.

6.7 Acknowledgements

Research was sponsored by the Army Research Laboratory and was accomplished under Cooperative Agreement Number W911NF-10-2-0022 and NIH grant 1R01MH084819-03. The views and the conclusions contained in this document

are those of the authors and should not be interpreted as representing the official policies, either expressed or implied, of the Army Research Laboratory or the U.S Government. The U.S Government is authorized to reproduce and distribute reprints for Government purposes notwithstanding any copyright notation herein.

Chapter 6, in full, is a reprint of the material as it appears in N. Bigdely-Shamlo, T. Mullen, K. Kreutz-Delgado, and S. Makeig, "Measure projection analysis: a probabilistic approach to EEG source comparison and multi-subject inference," NeuroImage, vol. 72, pp. 287-303, May 15 2013. The dissertation author was the primary investigator and author of this paper.

6.8 Figures

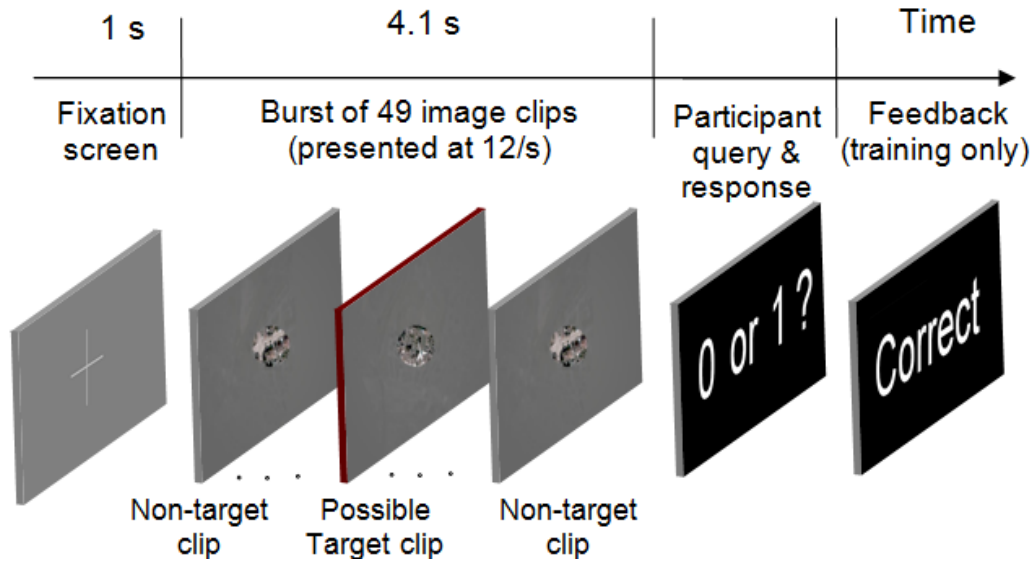


Figure 6.1. Timeline of each RSVP burst. Participant response feedback ('Correct' or 'Incorrect') was delivered only during Training sessions (rightmost panel).

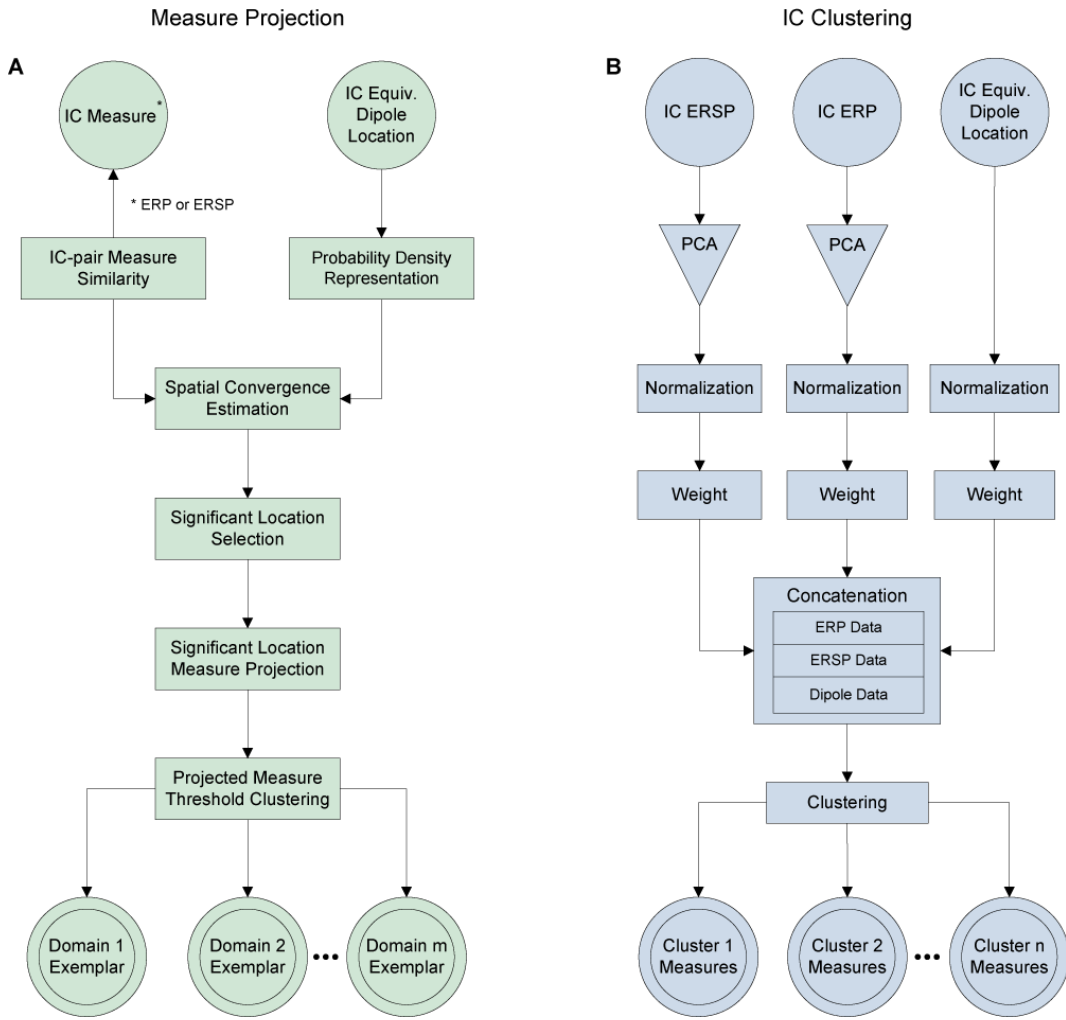


Figure 6.2. Finding equivalent IC processes across subjects and/or sessions: **(A)** Steps performed during measure projection analysis (MPA) to identify brain voxel domains associated with significantly different measures of independent component (IC) processes whose brain source locations are each tagged by the location of the IC equivalent dipole. **(B)** Steps performed during PCA-based clustering to find IC process clusters each composed of ICs with nearby equivalent dipole locations and similar measures. Whereas PCA-based clustering solutions may *simultaneously consider* multiple non-dipole EEG measures (for example, condition-mean ERPs and ERSPs), in MPA finding spatial domains supporting each condition-mean measure is performed *separately*.

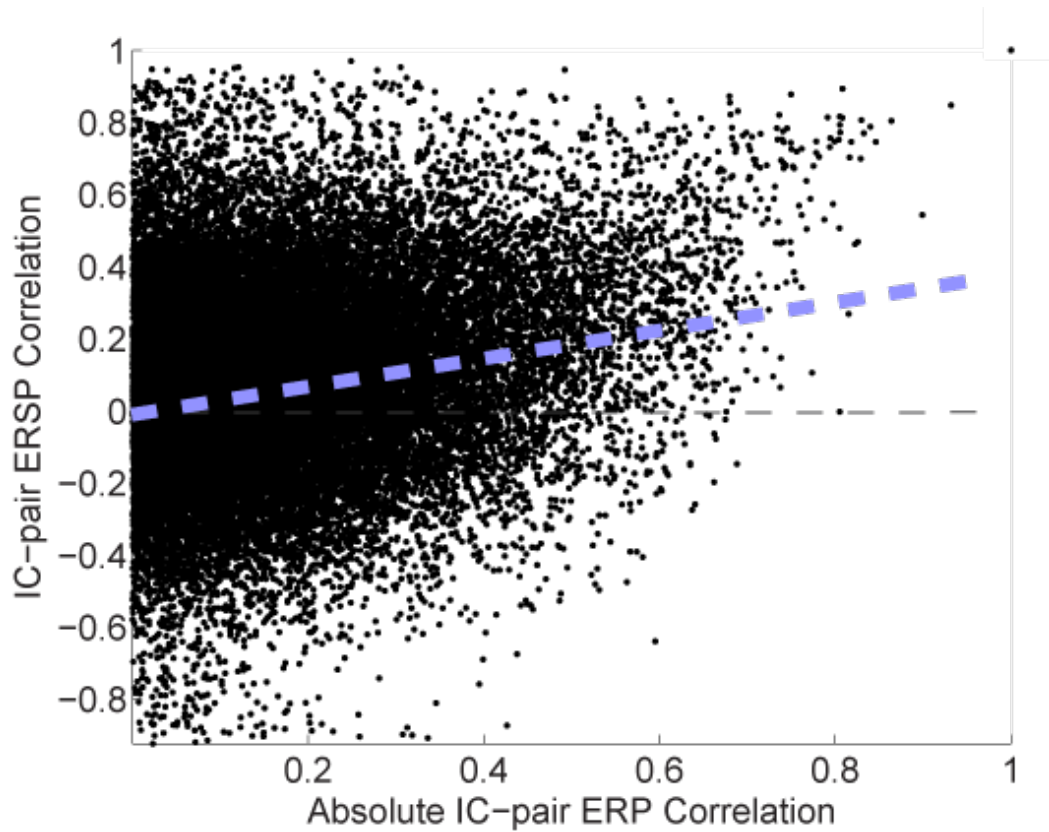


Figure 6.3. IC-pair ERP and ERSP similarities. Absolute-value ERP similarities are used to overcome the inherent ambiguity of the polarity of IC activations. Dashed line displays the best least-squares linear fit (Pearson correlation coefficient = 0.26).

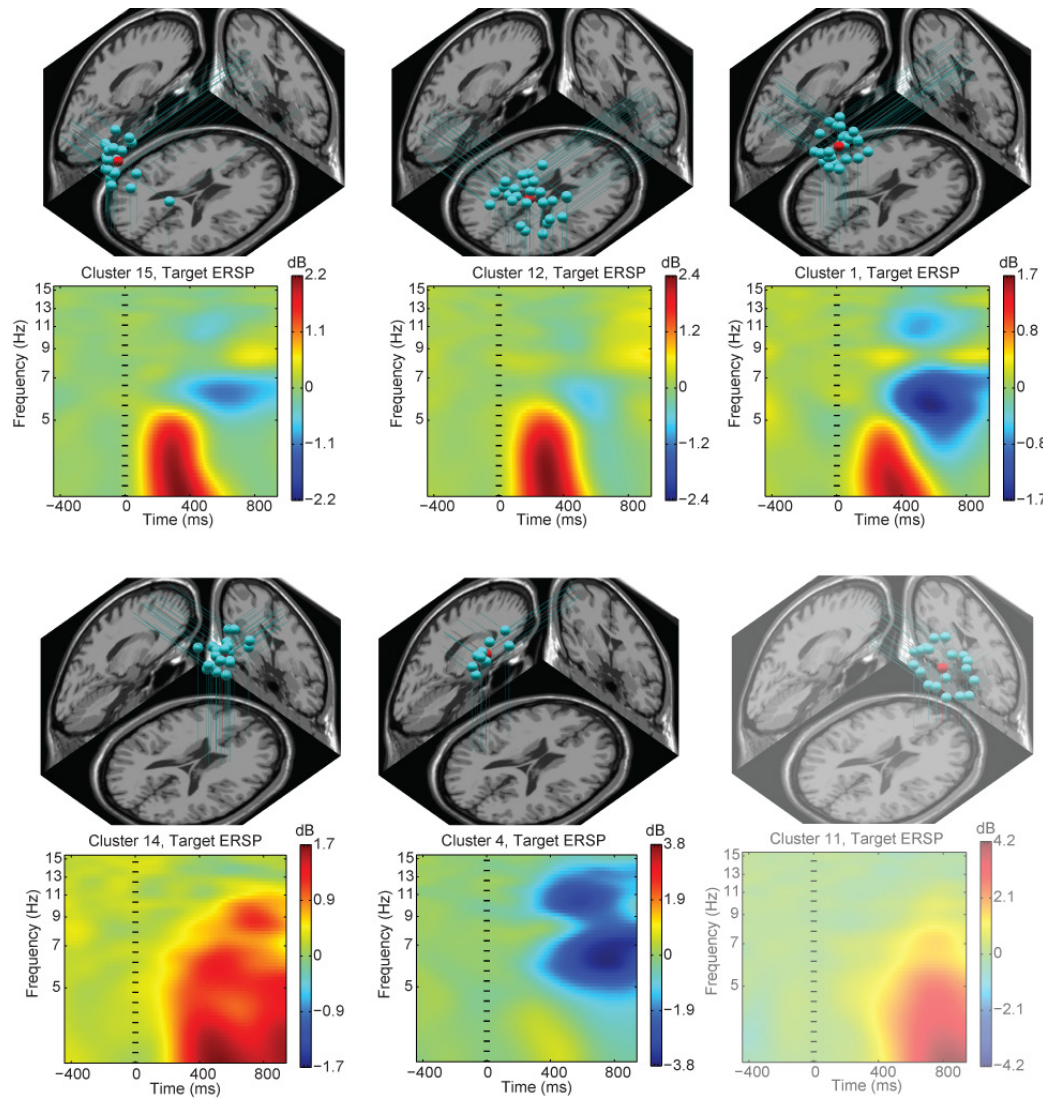


Figure 6.4. Dipole locations and cluster-mean ERSPs for 6 of 15 IC clusters obtained from PCA-based clustering (see Figure 6.2B) having relatively large Target event-related ERSP values, most in the low theta frequency band (each ERSP maxima equal or exceeding 1.7 dB). Cluster 11 is dominated by components accounting for eye movement artifacts.

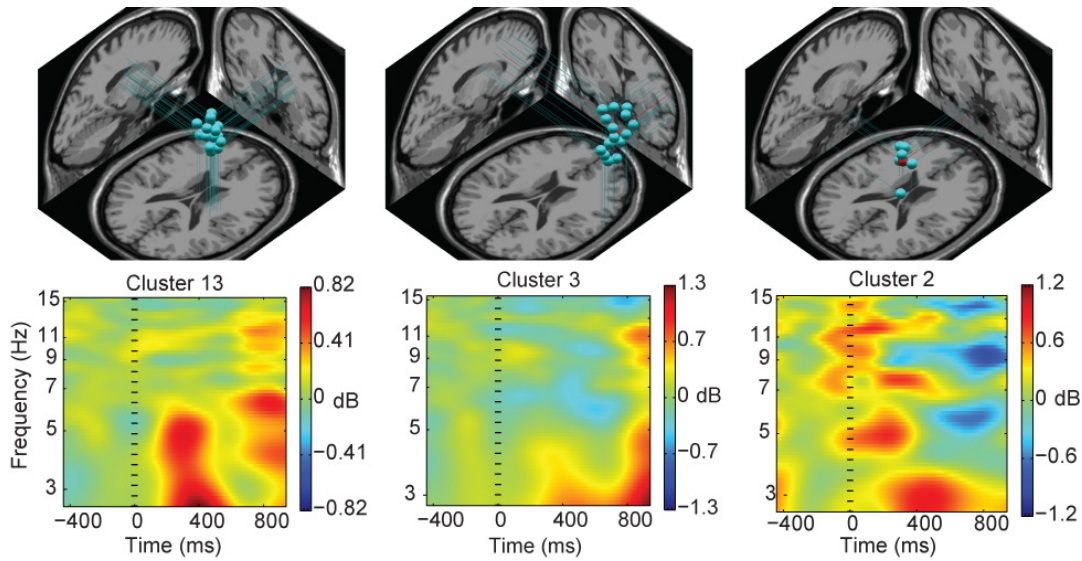


Figure 6.5. Dipole locations and mean Target ERSPs for a subset of clusters with weak ERSP values (each with absolute maxima lower than 1.3 dB; compare Figure 6.4).

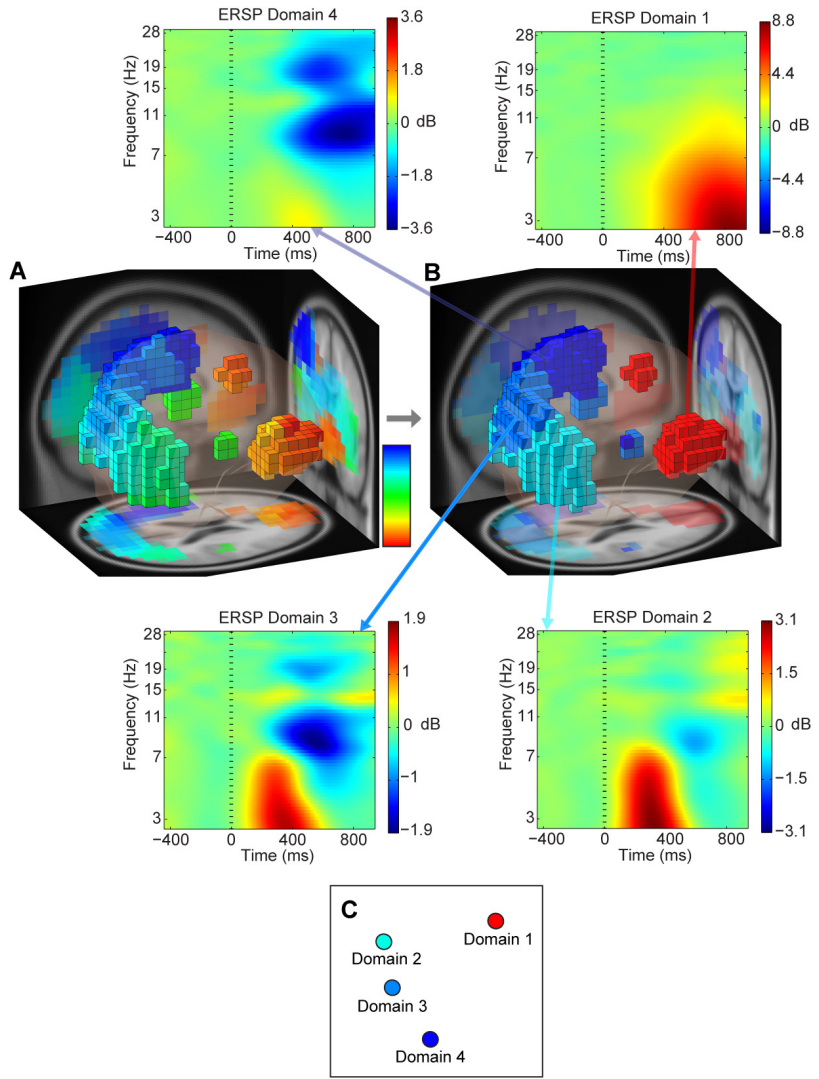


Figure 6.6. Measure Projection Analysis (MPA) of ERSP (see Figure 6.2A): (A) Voxels representing locations with significant convergence ($p < 0.075$) colored by multi-dimensional scaling (MDS) mapping of projected Target ERSP measures to hue (MATLAB ‘hue’ colormap values in the 0-0.69 interval, from red to blue). (B) Four domains identified in the projected measure values, colored by 1-D MDS of the projected measure at their exemplar voxel. (C) 2-D MDS image of exemplar similarities of the four domains. Note that Domain 1 (red, eye activities) is relatively distant from the other three Domains (blue, posterior cortex).

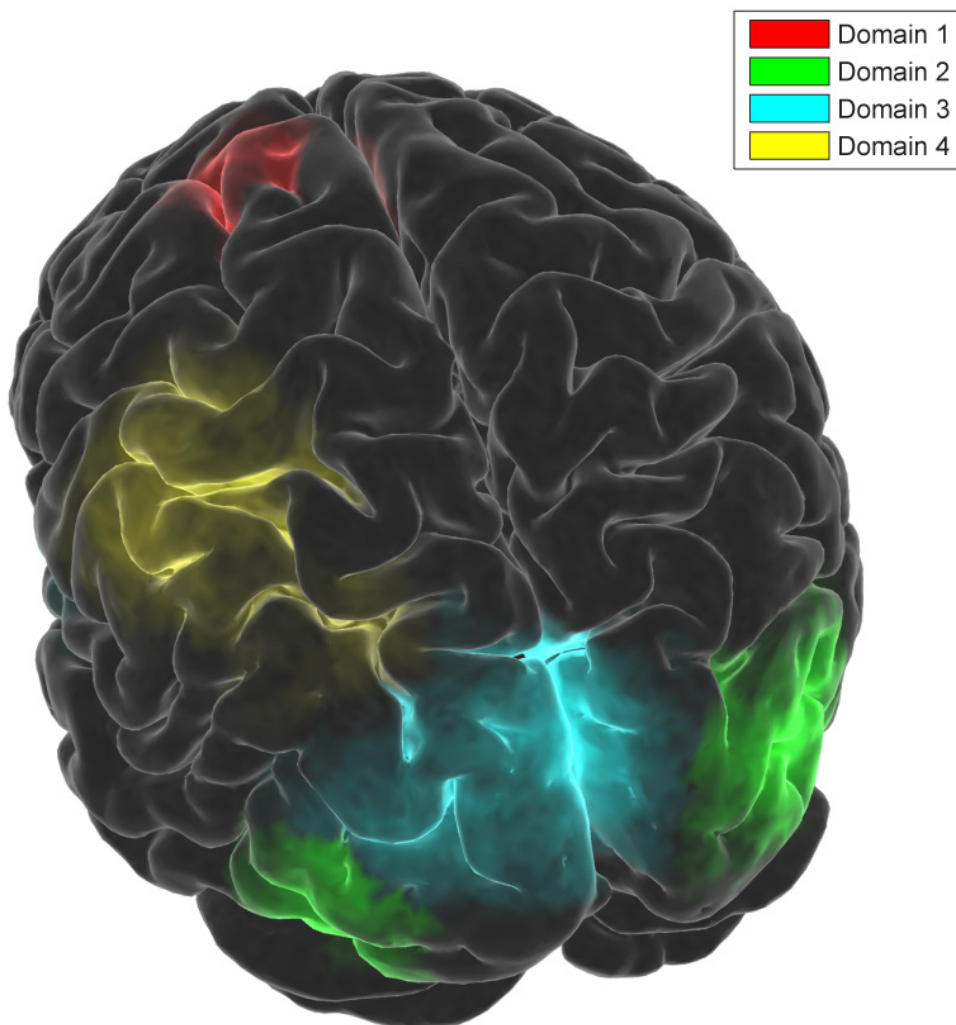


Figure 6.7. Alternative visualization of ERSP domains projected onto the template MNI cortical surface. Each cortical surface voxel is illuminated based on the domain color and total dipole density from brain-grid voxels located radially below the surface polygon.

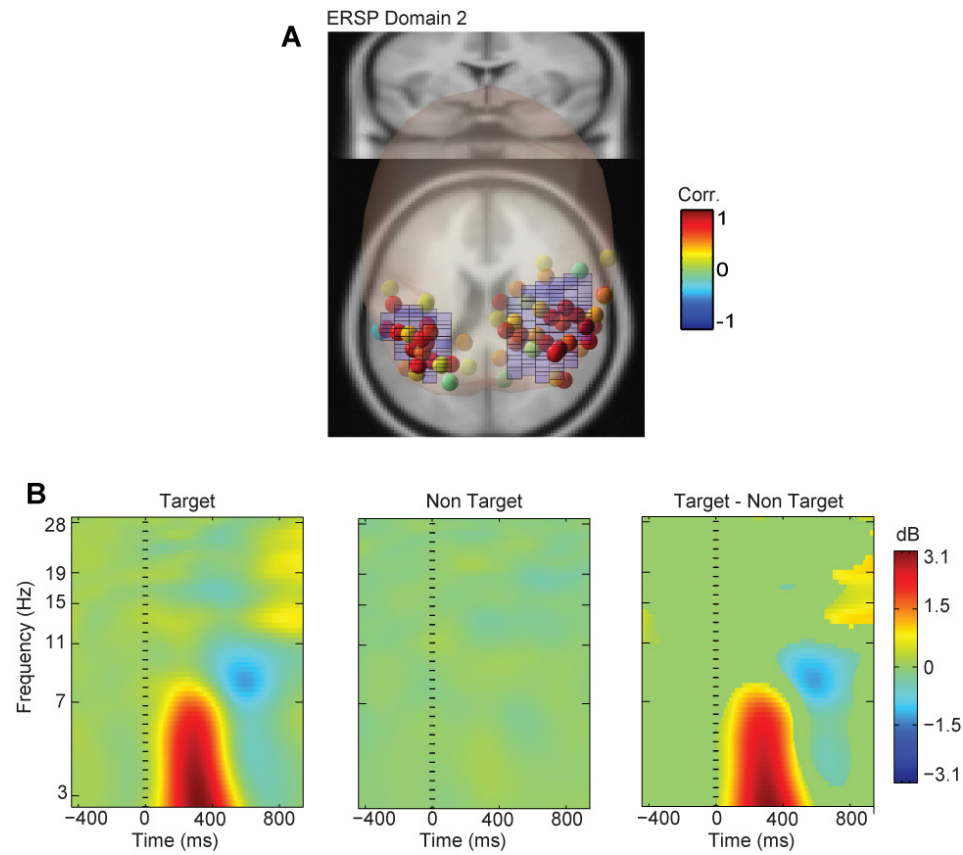


Figure 6.8. (A) ERSP Domain 2 dipoles with probability of membership in the domain above 0.05 are colored by the correlation of the dipole-associated measure with the domain exemplar. (B) (left and center) Projected Target and Non-Target condition ERSPs for ERSP Domain 2, and (right) their statistically masked difference ($p < 0.05$).

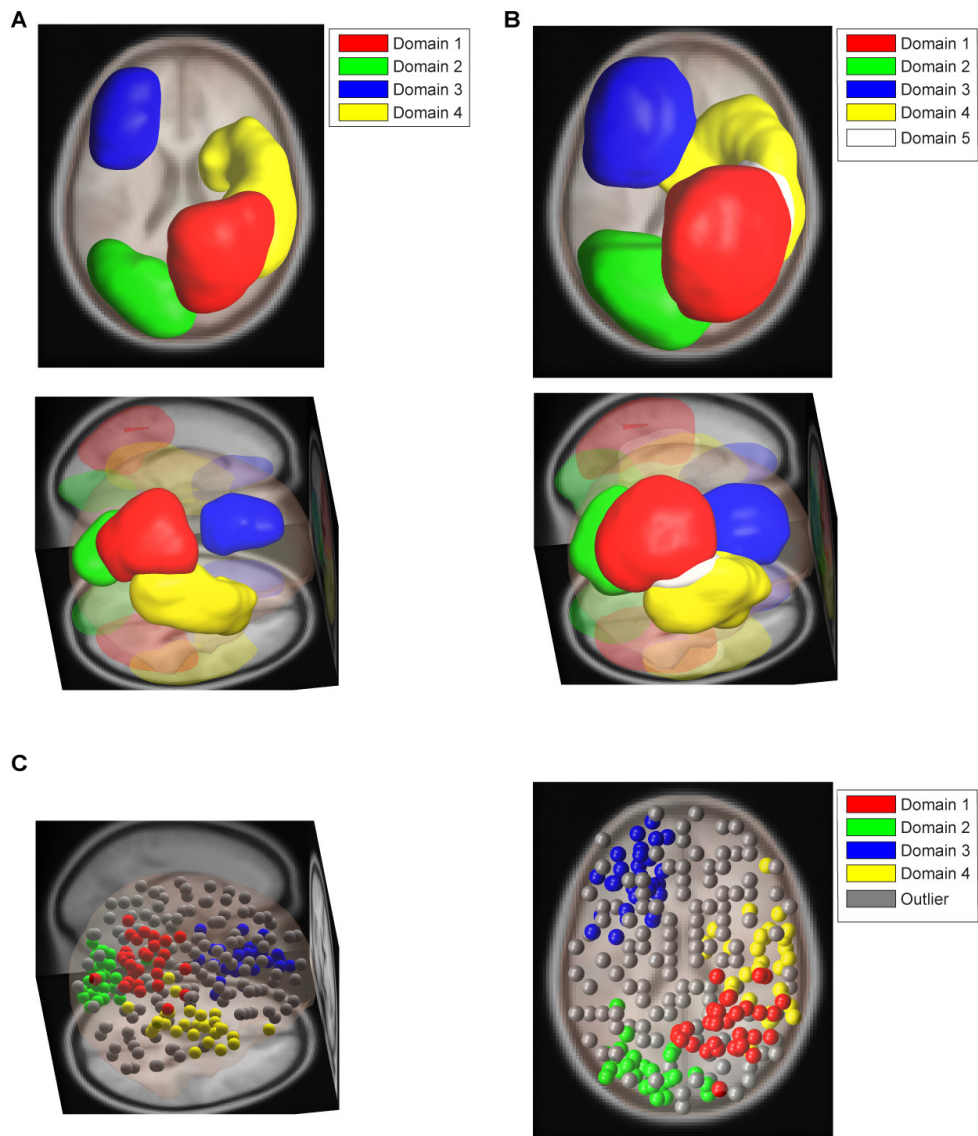


Figure 6.9. (A) Simulated ground-truth domain set consisting of four anatomical regions (B) MPA results based on using 12-mm Gaussian spatial noise blurring and an 0.88 ERSP Signal-to-Noise Ratio (SNR). (C) Simulated dipoles including subsets associated with each ground-truth ERSP domain plus randomly located outliers given random ERSP measures.

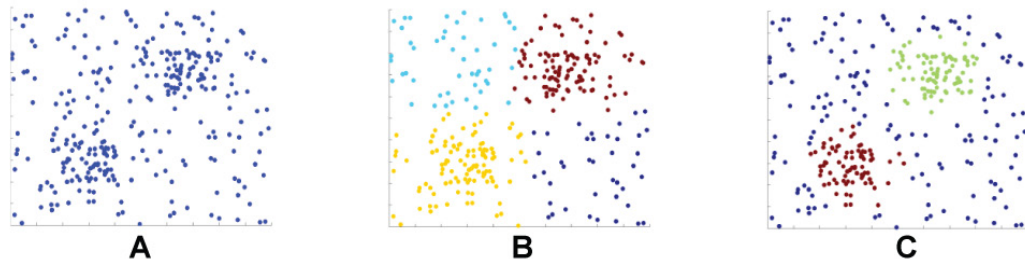


Figure 6.10. (A) Simulated sample points to illustrate Threshold-based clustering. (B) Points colored by cluster using $T_e = 0.2$ without outlier detection. (C) Points colored by cluster using $T_e = 0.2$ with outlier detection ($T_o = 0.2$).

6.9 Appendix A - Measure Projection Analysis (MPA)

Method Description

Problem. A subset of EEG independent component (IC) processes obtained by applying ICA decomposition to preprocessed channel activities from each recording session of a study consisting of multiple sessions and/or subjects may be accurately modeled by single (or in some cases bilaterally symmetrically located pairs of) equivalent dipoles located in the co-registered standard MNI brain coordinate system [28]. In this analysis we only consider equivalent dipoles within the MNI model brain volume (V), although the proposed method should also be separately applicable to equivalent dipoles located outside brain, such as in the eyes and at attachments of neck muscles to the scalp. Furthermore, we do not consider ICs that cannot be modeled using a single (or in some cases as dual symmetric) equivalent dipole model.

In practice, in any decomposition there may be an IC that can be accurately modeled by an equivalent dipole $D(x)$ located at any model brain location $x \in V \subset R^3$. Consider a measure vector $M(x)$, obtained by vectorizing ERP time-course or ERSP time-frequency image, associated with an IC with an equivalent dipole $D(x)$. Measure vectors typically estimate mean event-related changes in IC source activity, which are often monotonically related to the recorded scalp potential changes accounted for by the IC. Because of subject differences in skull thickness and brain dynamics, these

measure vectors may have dissimilar and unknown differences in scale and/or offset across subjects. For example, two subjects may show a similar (circa 10-Hz) central-lateral mu rhythm desynchronization pattern (reduction in power) during hand-motor imagery, but the maximum dB change for each subject may be quite different, as reflected in ERSP measures for one or more ICs from each subject's data.

During the set of experimental sessions in the study, up to n IC processes associated with n distinct equivalent dipoles $D_i \equiv D(x_i)$ (with indices $x_i, i = 1, \dots, n$) may be active. We desire to estimate an interpolated measure vector $M(y)$, defined across possible brain locations $y \in V$, and to estimate the statistical significance (p - value) of this assignment at each of these locations. These p-values are associated with the (null) hypothesis that the measure vectors have a random spatial distribution in the brain and there is no significant similarity between them within neighborhoods centered at brain locations $y \in V$.

Approach. Let σ be the standard deviation of a spherical 3-D multivariate Gaussian with covariance $\sigma^2 \cdot I$ centered at an estimated dipole location \hat{x}_j . We spherically truncate the density at a radial distance (to center) of $t\sigma$. After normalization to insure that densities both deep inside the brain volume and near the brain surface have unity mass within the brain volume, this truncated Gaussian is used to represent the probability density of the true equivalent dipole location given its estimated location. The parameter σ encapsulates errors in dipole localization arising

through errors in tissue conductivity estimates, head co-registration, numerical data decomposition, data noise, and between-subject variability in the locations (with respect to the head model) of equivalent functional cortical areas. We place a renormalized truncated Gaussian at each estimated dipole location. According to this model, the probability of estimated dipole D_j being truly located at position $y \in V$ is

$P_j(y) = TN(y; \hat{x}_j, \sigma^2 I, t)$, where \hat{x}_j is the estimated location of D_j (and TN is a normalized truncated Gaussian distribution). For an arbitrary location $y \in V$, the expected, or *projected*, value for the measure vector is

$$E\{M(y)\} = \langle M(y) \rangle = \frac{\sum_{i=1}^n P_i(y) M_i}{\sum_{i=1}^n P_i(y)} \quad (\text{A.1})$$

If an equivalent dipole were truly located at $y \in V$, it would have the measure projection $M(y)$ provided by (A.1). We want an estimate of $M(y)$ given by

$\langle M(y) \rangle = \sum_{i=1}^n \bar{P}(y) M_i$, where $\bar{P}(y)$ is the probability that $M_i(y) = M(y)$. Since the

probabilities have to sum to one ($\sum_{i=1}^n \bar{P}_i = 1$), it is natural to define $\bar{P}_i(y) \equiv \frac{P_i(y)}{\sum_{i=1}^n P_i(y)}$.

This gives (1) and shows that our estimate is given by a convex combination (weighted average) of measure values M_i that depends on equivalent dipole location $y \in V$.

Now that we have an estimate of the measure vector at each brain voxel location, we need to estimate the probability distribution of projected measures $M(y)$ under the null hypothesis that an estimated measure vector is actually produced by a random, set of measure vectors M_i in the spatial neighborhood. This is necessary to be able to assign any statistical meaning to the projected values. There are at least two ways to do so.

The first is to calculate p-values for each dimension of projected measure vector $M(y)$. There are, however, two drawbacks to this approach. Firstly, unknown scale and constant offset differences associated with measure values for different subjects may act as additional sources of variability (unless an effective measure normalization method is applied) reducing the power of statistical testing. Second, if measure vector $M(y)$ is high-dimensional, the issue of robustly correcting for multiple comparisons becomes critical, especially when a high-resolution spatial grid is placed in the brain volume. For example, an ERSP measure may typically consist of a matrix of 200 latencies by 100 frequencies giving 20,000 dimensions -- if brain voxels with 8-mm spacing are investigated, there will be about 4,000 locations examined, each associated with a 20,000-dimension vector. This would result in performing about 8×10^7 t-tests or some other type of null-hypothesis tests, which is undesirable: although methods for robust correction for multiple comparisons, including cluster-based techniques [97] and Gaussian random field theory [98] have been developed for high-dimensional data such as time-frequency images and fMRI

voxel maps, use of these methods require assumptions such as joint Gaussianity or smoothness. Thus, further investigation is needed to determine the applicability of these methods to MPA.

Measure convergence. An alternative method for obtaining significance values is to identify brain areas or *neighborhoods* that exhibit statistically significant similarities in one or more measures between IC equivalent dipoles within the neighborhood. To do so, we define the quantity $C(y)$ (measure convergence) at each brain location $y \in V$

$$C(y) = E\{S(y)\} = \frac{\sum_{i=1}^n \sum_{j=1, j \neq i}^n P_i(y)P_j(y)S_{i,j}}{\sum_{i=1}^n \sum_{j=1, j \neq i}^n P_i(y)P_j(y)} \quad (\text{A.2})$$

In this equation, $P_i(y)$ is the probability of dipole i being at location $y \in V$ and $S_{i,j}$ is the degree of similarity between measure vectors associated with dipoles i and j . Convergence $C(y)$ is the expected value of measure similarity at location $y \in V$ assuming that the joint probability of each dipole pair i and j being located at $y \in V$ can be factorized as $P_i(y)P_j(y)$ (based on the independence assumption). Problems caused by unknown scaling and offsets may be avoided by choosing a similarity matrix impervious to these distortions, such as normalized mutual information or linear correlation.

Calculated convergence $C(y)$ is a scalar and is larger for areas in which the measures associated with local ICs are homogeneous (similar). The probability of making an error of Type I may be obtained for each brain location by comparing $C(y)$ to a distribution of surrogate convergence values $C'(y), i = 1, \dots, k$ constructed from k randomized surrogates. Each surrogate convergence value is obtained by destroying the association between dipoles and their measure vectors by randomly selecting, with substitution, n surrogate measure vectors $M'_i, i = 1, \dots, n$ and associating them with dipoles $D_i, i = 1, \dots, n$. The surrogate similarity matrix $S'_{i,j}$ is obtained by calculating similarities between these surrogate measure vectors.

By repeating the process above k times, a distribution of surrogate convergence values $C'_i(y), i = 1, \dots, k$ at each brain location $y \in V$ is obtained and the significance of convergence $C(y)$ is obtained by comparing it to the right tail of this null distribution. This p-value is equal to the proportion of surrogate $C'(y)$ values higher than the actual convergence value $C(y)$

$$p\text{-value}\{C(y)\} = \frac{\#\{i : C'_i(y) > C(y); i \in 1, \dots, k\}}{k} \quad (\text{A.3})$$

After p-values are calculated for each brain voxel, they may be corrected for multiple comparisons across MNI brain grid locations and only those voxels with significant measure convergence (e.g., $p < 0.05$ after correction for multiple comparisons) selected for further analysis. Since $C(y)$ is a scalar value and often has a

much lower dimension than measure value $M(y)$, the multiple comparison problem is more manageable when dealing with convergence values.

Spatial domain clustering. Projected measure vectors associated with these locations may then be clustered to identify spatial *domains* exhibiting similar measure vectors in the data. Note that spatial domain clustering in MPA is different from IC clustering: in MPA, clustering is performed on the projected measure vectors $M(y), y \in V$ at each brain space voxel, so changes in domain clustering parameters do not change the voxel measures themselves. MPA operations such as subject or condition comparisons can act directly on these voxel measures and do not solely depend on domain exemplars. Mean measures of IC clusters, on the other hand, may take different values depending on the IC clustering parameters used, and only these mean measures are used in subject or group comparisons.

MPA toolbox. We have implemented the MPA method under MATLAB (The Mathworks, Inc.) as a plug-in for EEGLAB [21]. The Measure Projection Toolbox (MPT), freely available for download at <http://sccn.ucsd.edu/wiki/MPT>, includes high-level MATLAB software objects and methods that simplify the application of MPA to EEG studies. The toolbox also utilizes the probabilistic atlas of human cortical structures LPBA40, provided by the LONI project [52], to define anatomical regions of interest (ROIs) and find ratios of domain dipole masses for cortical structures of interest.

6.10 Appendix B - Threshold-based Clustering and Outlier Rejection using Affinity Propagation

Estimating the optimum number of clusters is an outstanding problem in the field of data clustering (Milligan & Cooper 1985, Gordon 1996). There have been several solutions proposed for this problem, each based on certain assumptions regarding noise and underlying cluster structure (Hardy 1996, Kryszczuk & Hurley 2010). On the other hand, in practice often the goodness of a clustering solution is evaluated by comparing a subset of its properties (e.g., the dissimilarity between cluster centers) with common domain or expert knowledge. For example, suppose that linear correlation is used as a similarity measure to obtain clusters using agglomerative hierarchical clustering (Hastie et al. 2009) and the clustering solution contains twenty clusters, two of which have exemplars (data points comprising cluster centers) more similar to each other than 0.95. Then additional domain knowledge such as assumed or expected noise level may allow us to infer that a better solution could be obtained with fewer clusters.

Another issue that arises in many practical clustering applications is the existence of outliers and their effect on the clustering solution. Outliers are defined as data points that are far from all cluster exemplars (centers) and should therefore not be assigned to any of them (in which case they can be grouped into a special ‘outlier cluster’). A common way to deal with this issue is to obtain a clustering solution

while treating outliers as any other data point, and then removing them *post hoc* in some principled manner. For example, a simple way to do this would be to remove all points that are further than a given distance threshold to any cluster center (such a method would be especially applicable if a distance or similarity threshold could be established based on domain or expert knowledge). A problem with this approach is that the clustering solution is affected by all data points, in particular the outliers which are removed in the second step. In cases in which the outliers in the total data set are significant in number, or are much more distant than regular points from cluster centers, the clustering solution may be visibly deteriorated by their presence.

Here we propose the use of Affinity Propagation clustering (Frey & Dueck, 2007) to address the abovementioned difficulties by incorporating two threshold values based on domain knowledge. Affinity propagation method finds exemplars by passing real-values messages between pairs of data points. The magnitude of these messages is based on the affinity of each point for choosing the other as its exemplar.

This algorithm is shown to be equal or better than K-means in minimizing clustering error on large datasets. It also only requires a pair-wise similarity matrix as input, a property exploited by our proposed method to find an appropriate number of clusters while ignoring outliers during the clustering process. Although our method is based on the use of Affinity Propagation clustering, it may, in principle, be combined with any clustering method that accepts a pairwise similarity matrix.

Let $S_{n \times n}$ be a pairwise similarity matrix for n input points $P_i, i = 1, \dots, n$ to be clustered. Our objective is to find a clustering solution in which:

- (a) Outliers, defined by points that are less similar than $T_o \in R$ to any cluster exemplar (centroid) E_k , are assigned to a special outlier cluster.
- (b) The data are clustered into the maximum number of clusters such that no cluster exemplar E_k is more similar to another than a given similarity threshold $T_e \in R$.

To achieve objective (a), we augment the original pairwise similarity matrix $S_{n \times n}$ to include a new *virtual point* P_{n+1} that has a constant similarity T_o to all original data points P_i :

$$S'_{n+1, n+1} = \left[\begin{array}{ccc|c} S_{1,1} & \dots & S_{1,n} & T_o \\ \vdots & & \vdots & T_o \\ S_{n,1} & \dots & S_{n,n} & T_o \\ \hline T_o & T_o & T_o & T_o \end{array} \right] \quad (B.1)$$

The augmented similarity matrix $S'_{n+1, n+1}$ is then used for clustering.

During the clustering process, points compete for becoming exemplars of others. These dynamically formed exemplars compete for assignment to data points and since the virtual point P_{n+1} has a constant similarity T_o to all other points, any

point which is less similar than T_o to all exemplars will be assigned to the cluster which contains the virtual point as its exemplar. This point hence becomes an exemplar for all outlier points in the data.

After the clustering process is finished, one of the following conditions will be met:

- (1) There are one or more outliers in the data, in which case they will be assigned to a cluster that includes the virtual point (see Figure 6.10C).
- (2) There are no outliers in the data and the virtual point is assigned as the exemplar of a cluster with only one member (itself).
- (3) There are no outliers in the data, but the virtual point is assigned to a cluster that is not an outlier cluster.

To distinguish between conditions 1 and 3 above, we can calculate the similarity between all exemplars and members of the cluster that includes the virtual point. If any similarity value is greater than T_o then condition 3 must be the case. Our use of an augmented similarity matrix thus achieves the first goal of separating outlier points during the clustering process.

To achieve objective (b) we begin by clustering $S'_{n+1,n+1}$ into a minimum number of clusters (1 or 2) and iteratively increase the number of clusters (if using Affinity Propagation, this is achieved by increasing the similarity value assigned

between each data point and itself in the similarity matrix, which indirectly controls the number of clusters). In each iteration we calculate the minimum similarity T_{\min} between cluster exemplars and compare it with T_e . If $T_{\min} > T_e$ then the procedure terminates and returns the clustering solution obtained in the previous iteration, satisfying objective (b).

Figure 6.10A shows a simulated 2-D point cloud generated by adding to a low uniform point distribution two rectangular areas of increased probability density. Figure 6.10B shows Affinity Propagation clustering results using maximum exemplar similarity $T_e = 0.2$ and no outlier detection. Of the four clusters produced by this solution, two consist mostly of outlier points. Figure 6.10C shows the clustering solution obtained using outlier detection with $T_o = 0.2$ and $T_e = 0.2$. Here, the two high-density areas are separated into distinct clusters and other points are assigned to a third ‘background’ cluster.

Table 6.1. Anatomical locations, Brodmann areas, and nearby clusters associated with each ERSP domain.

ERSP Domain	Nearby Clusters	Anatomical Area(s)	Brodmann Area(s)
1	11, 14	(Dominated by eye-artifact ICs)	N/A
2	12, 15	R Middle Occipital Gyrus (0.36) L Middle Occipital Gyrus (0.26) R Inferior Occipital Gyrus (0.09) L Inferior Occipital Gyrus (0.08) R Superior Occipital Gyrus (0.05) R Lingual Gyrus (0.04) R Inferior Temporal Gyrus (0.03) R Angular Gyrus (0.02) R Middle Temporal Gyrus (0.02)	BA 18 (0.34) Secondary visual (V2) BA 19 (0.34) Associative visual (V3) BA 37 (0.11) BA 39 (0.06) BA 17 (0.06), Primary visual (V1)

Table 6.1., continued.

ERSP Domain	Nearby Clusters	Anatomical Area(s)	Brodmann Area(s)
3	1	L Superior Occipital Gyrus (0.19) L Cuneus (0.16) L Middle Occipital Gyrus (0.15) R Cuneus (0.12) R Superior Occipital Gyrus (0.10) L Superior Parietal Gyrus (0.06) L Lingual Gyrus (0.04) L Precuneus (0.03) L Superior Temporal Gyrus (0.02) R Middle Occipital Gyrus (0.02) R Superior Temporal Gyrus (0.02) R Lingual Gyrus (0.02)	BA 18 (0.33) Secondary visual (V2) BA 19 (0.15) Associative visual (V3) BA 31 (0.13) BA 17 (0.12) Primary visual (V1) BA 7 (0.06) Somatosensory Association

Table 6.1., continued.

ERSP Domain	Nearby Clusters	Anatomical Area(s)	Brodmann Area(s)
4	4	L Superior Parietal Gyrus (0.27) L Postcentral Gyrus (0.27) L Supramarginal Gyrus (0.22) L Angular Gyrus (0.12) L Precentral Gyrus (0.10)	BA 40 (0.37) Spatial / Semantic Processing BA 7 (0.12) Somatosensory Association BA 3 (0.11) Primary Somatosensory BA 2 (0.10) Primary Somatosensory BA 4 (0.09) Primary Motor BA 39 (0.06)

Table 6.2. MPA performance scores for simulation results with a voxel significance p-value threshold of 0.05 and varying noise levels.

Mean MPA Performance Score (std)	Cohen's kappa Ratio (kappa, max possible)	Domain Dipole Noise Amplitude	Mean Domain Dipole SNR (std)	Extra Dipole Noise Amplitude	Projected Gaussian std. deviation (mm)
0.82 (0.21)	0.82 (0.63, .78)	0	1	0.2	12
0.85 (0.20)	0.84 (0.62,0.73)	0	1	0.2	14
0.81 (0.19)	0.78 (0.63, 0.8)	0	1	0.2	10
0.93 (0.11)	0.9 (0.5, 0.56)	0.2	0.88 (0.09)	0.2	12
0.93 (0.10)	0.93 (0.47,0.51)	0.2	0.88 (0.09)	0.2	14
0.89 (0.16)	0.84 (0.51,0.61)	0.2	0.88 (0.09)	0.2	10

Chapter 7

Subject Space Analysis

7.1 Introduction

A primary question of interest in multi-subject data analysis is the distribution of the inferred population-level EEG dynamics across individual subjects, i.e. which subjects display patterns that are (or are not) similar to the calculated subject average for a certain IC cluster or IC measure domain, and what subject sub-groups and outliers may be so identified from the data. Mathematically, this may be described as the study of geometrical or topological features of a *subject space* of relationships between brain-localized IC measures that cannot be well fit as a collection of identical subject data plus added multivariate Gaussian noise.

7.2 Methods

In the measure projection framework, comparing subject EEG dynamics is possible by calculating the projected measure (e.g., the ERSP or vector of ERSPs over conditions) associated with each subject (and/or recording session) within one or more brain regions of interest (ROIs). To obtain a similarity estimate over a given ROI for

each subject pair, first the two projected measures at each ROI location are compared (e.g., by correlation or mutual information) to obtain a similarity value at that location. These values are then combined (e.g. averaged) across the ROI and defined as the ROI measure similarity for that subject pair. A subject space is then built by comparing all possible subject pairs and representing the results as a similarity matrix:

$$S_{ij} = \sum_{x=1}^n p(x)f(M_i(x), M_j(x)) = E\{f(M_i(x), M_j(x))\} \quad (5)$$

S_{ij} : Similarity of the measure vector for subjects i and j across the ROI

x : Brain location

n : Number of brain locations

$p(x)$: ROI membership probability of voxel x

f : Similarity function (e.g., correlation or mutual information)

$M_i(x)$: Projected measure vector of subject i

It is possible to investigate relationships between subjects or session variables (e.g. group identities, age...) and this similarity matrix using statistical methods. For example, to look for group effects, the average similarity across subject pairs both belonging to a certain subject sub-group may be calculated and compared to the average similarities of subject pairs whose members are known to belong to different subject sub-groups. Bootstrap permutations across the associations between subjects

and groups can then establish the statistical significance of any difference between the two mean similarity values (or any other similarity value statistic).

7.3 Results and Discussion

Here we investigate the effect of subject identity on the EEG dynamics captured in different recording sessions in the RSVP study described in Chapter 6. For most subjects training and test sessions were collected several days or weeks apart. Each session was analyzed using a separate ICA decomposition, producing different IC equivalent dipole locations and associated EEG measures.

Figure 7.1 shows the relationship between the measure projected ERSP and dipole density for all recording sessions in different ROIs. Figure 7.1A shows the subject-space constructed by comparing dipole densities and visualized by two-dimensional multidimensional scaling (MDS, implemented in Matlab Statistics Toolbox). The similarity function in this plot was defined as the inner product of normalized (summing to unity) session dipole densities. Lines connect sessions for the same subject.

Visual inspection of Figure 7.1A suggests that the average dipole density distribution similarity between sessions belonging to the same subject is higher than average similarity between sessions from different subjects. We verified this by calculating the ratio between average similarity values for same-subject and different-subject session pairs (1.37) and performing a one-tailed statistical significance test by

performing 200,000 random permutations (without substitution) of subject identities in the similarity matrix, which gave a probability of the null hypothesis (no relation of dipole density to subject identity) of $p < 0.0012$. This shows that the locations of the retrieved IC equivalent dipole locations were more similar across sessions within subjects than across subjects.

Figure 7.1B shows the subject space for measure projected ERSPs over all brain locations. Here we may also observe similarity between sessions for the same subject. Using the same statistical procedure as above, the ratio of average similarity between session pairs from the same subject to other pairs was 1.94 with $p < 0.004$. Two sessions belonging to Subject 25 stand out in this figure as potential outliers (as they are far from the mean measure projected ERSP). In fact, the (reasons unknown) dissimilarity of the data from the two sessions of this subject was sufficient that, unlike for the other subjects, a Target detection brain-computer interface (BCI) model trained on one session could not accurately detect Target responses in the other session: the cross-session classification area under the ROC curve for this subject, as described in [48], was 0.56 (at chance level), while the median area under the ROC curve for all subjects was 0.88.

In Figure 7.1C we focused subject-space analysis on ERSP Domain 2 ROI (see Figure 6.7). The measure projected ERSP to this region was compared across sessions. In addition to two sessions from Subject 25, a session from Subject 24 appears to have different ERSP patterns in regards to Target and Nontarget conditions. Further

investigation indicated that Subject 24 was not associated with any dipoles near (occipital) ERSP Domain 2. Both mean ratios and their significance were similar to Figure 7.1B (ratio = 1.94 with $p < 0.004$)

We then built a probabilistic frontal ROI using the LPBA40 probabilistic atlas [52] and compared measure projected session ERSPs in frontal areas (Figure 7.1D). This plot looks markedly different from Figure 7.1C, indicating that the subject similarity space may vary for different brain regions. This ROI was also associated with significantly higher similarity between same-subject sessions (ratio = 2.46, $p < 0.0093$).

7.4 Figures

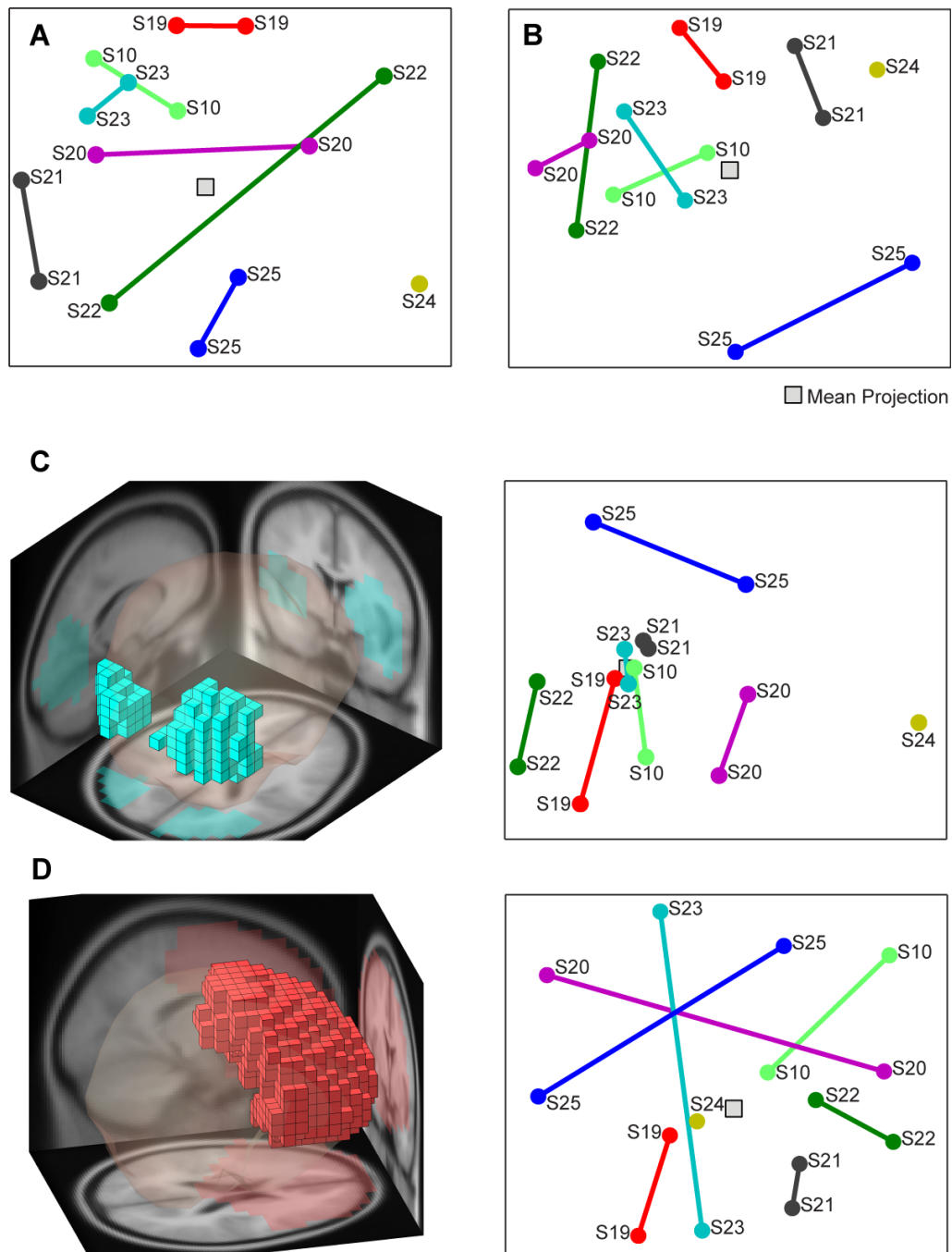


Figure 7.1. (A and B, C and D right) Subject space visualizations using 2-D multi-dimensional scaling (S12 = Subject 12; solid lines connect sessions from the same subject) applied to (A) differences in session dipole density, (B) differences in measure projected ERSPs (all brain locations), (C) measure projected ERSPs associated with ERSP Domain 2 (light blue), (D) measure projected ERSPs in frontal brain (red).

Chapter 8

Classification feature analysis of oscillatory EEG dynamics accompanying auditory/visual attention switching

8.1 Introduction

Here we investigate a novel application of machine learning to electroencephalographic (EEG) data with two purposes: First, we present a decoding model [73, 99] for non-stationary event-related oscillatory EEG brain dynamics – used here to classify, for a given single trial of data, whether the participant switched attention from an auditory stimulus stream to a concurrent visual stream or vice versa. Second, we image the brain EEG processes captured by this model in 3d cortical space and illustrate in a cross-subject group analysis a range of connections to the fMRI attention reorientation literature. These two goals are complementary: In the first case

we train a decoding model from recorded data and study its predictive performance, while in the second we elucidate the structure of the learned model itself.

We first introduce a mathematical formulation, *Regularized Spatio-Spectral Dynamics* (RSSD), which yields to a novel general-purpose machine learning and brain imaging method producing models that explain or predict an abstract cognitive state variable (or condition) in terms of distributed non-stationary EEG space/time/frequency dynamics. The main strength of the RSSD method is that it captures the relevant details of highly complex joint oscillatory dynamics in an interpretable source-space representation, which is the unique solution of a single convex optimization problem. For brain imaging meaningful subject group-level analysis is also desirable – therefore we employ a recently proposed EEG model aggregation method, Measure Projection Analysis (MPA), for spatial co-registration and cross-subject statistical estimation of cortical source dynamic patterns described in Chapter 6 (also see [45]).

We applied these methods to EEG data from a multimodal attention-switching task [61] for which we expected to have invoked well-defined event-related changes in oscillatory dynamics, a task in which subjects were repeatedly cued to reorient their attention from a stream of visual stimuli to a concurrent stream of auditory stimuli and then back again, with similar stimulus density and motor responses in both directions. Our dual objective here was 1) to correctly classify the direction of the cued audiovisual attention switch without knowing the type of the cue, and 2) to generate

and interpret 3-D maps at both the single-subject and population levels of the source-level spectral power shift clues most strongly contributing to successful classification.

We chose to use power spectral dynamics occurring relative to the attention shift cues because alpha band spectral power in both visual and auditory cortical regions is sensitive to degree of modal attention, with withdrawal of attention associated with ‘alpha flooding’ and focusing of attention, with ‘alpha blocking’ [100]. Thus, we expected informative switch-related spectral shifts to include alpha band power changes in these expected directions. Previous functional imaging results suggested a set of cortical regions in which we might also expect to see EEG spectral shifts during attention shifting [101-108]. Using EEG rather than fMRI BOLD data also allowed us to examine the detailed time course of these shifts in the affected cortical areas. Finally, we wanted to determine whether informative features also occurred in other spectral bands, and if so in which frequency bands and cortical areas?

8.2 Methods

8.2.1 Experimental Task

The study comprised data from 31 healthy adult subjects (pooled from two age groups of 20-40 years and 60-90 years, respectively) of both genders. Thirty-two channels of EEG data sampled at 250 Hz at 16-bit resolution were recorded from each participant using an SA Instrumentation amplifier via custom software. Stimuli

were presented in blocks of 264 stimuli, each 160-sec block including 12 bimodal “Hear” and 12 “Look” attention-switch cues inserted among 120 randomly interleaved task stimuli in each modality (see Figure 8.1). This design was originally created to allow evaluation of attention effects on Nontarget stimulus event-related potentials (ERPs) (Townsend et al., 2003). In the “Attention Shift condition” studied here, the Switch cues would cue the participant to shift their attention to either the auditory or visual modality stimuli so as to prepare to produce a manual button response to target stimuli only in the newly attended modality. On average, Switch cues occurred once every 6.6 sec and were followed on average by 10 +/- 3 stimuli in each modality before the next Switch cue.

Target and Nontarget stimuli in each of two modalities (auditory and visual) were presented one at a time in random order with stimulus onset asynchronies (SOAs, onset-to-onset) between 200 ms and 800 ms in each modality (i.e., with a 100-400 ms multimodal SOA). The auditory stimuli were 100-ms, 550-Hz (Target) and 500-Hz (Nontarget) sine-wave tones, amplitude-modulated at 5 Hz. In all task conditions, Targets occurred with a within-modality probability of 20%. The tones were played over two loudspeakers placed beside a 21-inch computer monitor situated at eye level 1.5 m in front of the subject At the subject’s head, tone loudness was 63 dB SPL (sound pressure level). The visual stimuli displayed on the computer monitor were single light-blue (Target) and dark-blue (Nontarget) 8.4-cm² filled squares subtending 3.3 deg of visual angle.

Temporally interspersed among the Target and Nontarget stimuli were Switch cues, bimodal (auditory and visual) stimuli 200-ms in duration conveying the instructions to “Look” for or “Hear” the next Target respectively. Visual Switch cues consisted of a bright-orange capitalized word presented at central fixation; the simultaneous binaural presentation of the same word was spoken in the voice of a naïve male English-speaker at the same volume as the auditory stimuli.

8.2.2 Data Analysis

In the first stage, we trained an RSSD predictive model for each participant from the continuous data of the participant’s recording session with its two groups of (HEAR/LOOK) Switch cue event markers. The resulting models $\{M_s\}$ were parametric representations of the relationship between EEG and marker class for each subject. Next, we estimated the predictive performance of the models (estimated percent correct classifications) using five-fold block-wise cross-validation.

In a second-stage analysis, the resulting models were subjected to group-level comparison using measure projection analysis (MPA). In MPA, source-level model features are spatially co-registered/aligned in a common brain space and group-levels statistics are calculated for a 3-D voxel grid in this space. The resulting per-voxel measures (here time-frequency weight maps) were segregated into brain-space domains associated with similar sets of features across subjects. Domain-centroid

(‘informative feature’) weight maps were then computed and plotted for visual inspection and comparison with the brain-imaging attention literature.

8.2.3 Regularized Spatial-Spectral Dynamics (RSSD)

The RSSD method is an alternative to methods such as, for example, Common Spatial Patterns (CSP) or the discriminative framework for neuroimaging recently proposed by Tomioka and Mueller [109], an early inspiration for this method. The core of RSSD is a convex optimization that jointly optimizes the weights of a generalized linear model parameterized in space, time, and frequency. Thanks to the convex formulation, the resulting model is the globally optimal solution for the given assumptions. The weights are optimized based on a collection of observed data trials (X_t), each parameterized in the same manner, plus an associated “class label” or target value y_t . Here y was binary, from the set $\{-1, +1\}$ corresponding to the two Switch cues {LOOK, HEAR}. Note, however, that binary classification is not an inherent restriction of the method since its underlying generalized linear model (GLM) can be set up to perform various types of regression, including logistic, multinomial, Poisson, or linear by choice of an appropriate link function.

8.2.4 Data Preprocessing for RSSD

After the raw continuous EEG recording was segmented into a collection of multi-channel epochs identically time-locked to the two classes of markers, the

epoched data were transformed into a space x time x frequency representation. This could in principle be accomplished using a multitude of techniques, the most straightforward being to use the individual scalp channel signals as the spatial basis and a short-time Fourier transform (STFT) approach for deriving a latency-by-frequency matrix for each channel and epoch. Unfortunately, EEG channels measure highly correlated signals, each of which is a linear mixture of all the electrical activity of the brain, conveyed to each scalp electrode channel by volume conduction and linearly summed. Since the point-spread function of any electrical source in the brain (for EEG, predominantly in cortex) includes nearly the whole scalp, dramatically better RSSD results may be achieved by first spatially filtering the data, i.e., remapping the scalp channel signals to a linearly transformed representation that more closely resembles the set of resolvable, functionally distinct cortical source activities.

A technique often used to perform such spatial transformation is blind source separation, in particular Independent Component Analysis (ICA). These methods make use only of statistical properties of the data. Beamforming is often used for finding functionally distinct signals as well, but it ideally requires accurately co-registered electrical forward models of each participant's head based on an MRI scan; these were not available here. Methods such as sparse signal recovery may also be applicable but also require accurate forward electrical head models. Useful spatial filters might also be learned using supervised nonlinear methods that make use of the classifying label information. However, with most existing nonlinear methods it is

rather difficult to separately identify and compare the spatiotemporal data features that most highly contribute to the classification. Thus, we chose to use an ICA approach to spatially separate the channel data into spatially and functionally distinct signals.

8.2.5 Adaptive Mixture ICA

Here, we used an advanced ICA decomposition approach, Adaptive Mixture ICA (AMICA; [58, 59]), to compute a type of overcomplete spatial decomposition of the data. AMICA is a generalization of the traditional ICA model into a mixture of multiple “sub-models” such that each data point is associated with one sub-model and each sub-model explains a part of the data. Similarly to the well-known Gaussian mixture model for clustering, both the “cluster” (i.e., sub-model) membership for each data point and the parameters of each of the models, including its unmixing matrix and adaptive probability density functions (pdfs) of the sources are all learned simultaneously in an expectation-maximization fashion. After training, the component data points are maximally temporally independent within their respective model. Here we decomposed the data using 3 AMICA models and for the sake of simplicity take the resulting $3 \times 32 = 96$ components as an overcomplete dictionary of spatial filters.

AMICA is purely data driven and requires no auxiliary information. However, pre-processing to remove low-frequency drifts and non-stereotypical artifacts is necessary for the decomposition to find spatially localizable component processes. Here we used automated artifact rejection tools to thus ‘clean’ the data before

submitting it to AMICA, using a pipeline and parameters similar to the ‘seated’ setting in the BCILAB toolbox 1.0 [110, 111]. Full details will be deferred to a subsequent paper. In summary, the data were first high-pass filtered by a FIR filter with a transition band between 0.5 and 1 Hz, then a set of 1-second time windows was chosen for removal using a quantile threshold on the windowed signal power (calculated per channel and pooled so as to decouple the measure from channel artifacts). Finally, a set of channels were chosen for removal using a quantile threshold on mutual correlation between channels (calculated on a window-by-window basis and pooled in order to be robust in the presence of temporally localized artifacts).

Once the spatial decomposition $C \in R^x \times Y$ was derived, it was applied to each multi-channel epoch to yield new multi-channel epochs in the overcomplete, spatially-transformed component space. The time/frequency decomposition of each resulting component signal was performed using a form of continuous Morlet wavelet transform to obtain estimates of amplitude at 48 latencies between -2000 ms to 3000 ms following Switch cue presentations across 50 log-spaced frequencies between 2.5 Hz and 50 Hz. The number of wavelet cycles depended on frequency and linearly increased from 0.5 cycles at 2.5 Hz to 3 cycles at 50 Hz.

8.2.6 Regularization

A generalized linear model (GLM) with the logistic link function was used in RSSD,

$$q_{\Theta}(Y = y | \mathcal{X}) = \frac{1}{1 + e^{-y f_{\Theta}(\mathcal{X})}}, (y \in \{-1, +1\}).$$

With each sample observation \mathcal{X}_t now represented as a [space \times time \times frequency] multi-array of (96 \times 48 \times 50 dimensions), RSSD optimization was performed by solving the following optimization problem:

$$\min_{\Theta} \quad \frac{1}{T} \sum_t \log \left(1 + e^{-y_t f_{\Theta}(\mathcal{X}_t)} \right) + \lambda \sum_{p=1}^n \sum_{k=1}^{\text{rank}(\Theta_p)} \sigma_k(\Theta_p),$$

Where $\Theta = (\Theta_1, \Theta_2, \dots, \Theta_n, b)$ are the time-frequency weights for n ICA components, \mathcal{X}_t is the tensor of time-frequency features for n components for trial t, and $f_{\Theta}(\mathcal{X}) = \sum_{p=1}^n \langle \mathcal{X}_p, \Theta_p \rangle + b$ is a linear predictor function with $\langle ., . \rangle$ denoting the inner product between matrices.

This can be viewed as a logistic regression that predicts the class label from the observed data using a generalized linear mapping. Notably, the number of parameters to be estimated in this model is larger than 300k, while the number of data trials available here was on the order of 100. Thus, some strong prior assumptions shaping the character of the RSSD solution are necessary to obtain a high-quality solution.

Here, we assumed: 1) Only a sparse set of independent component activities were relevant for classification (groupwise sparsity), an assumption justified by the

fact that these components are (model-wise) statistically independent. 2) The time/frequency measures useful for classification concern a relatively small number of latent oscillatory processes, each characterized by a characteristic frequency profile F and an associated modulation time course T .

These two assumptions can be collapsed into a single regularization term, the sum of the trace norms for each component weight map. The trace norm penalty is a convex surrogate for the rank of a matrix and implements the assumption that a weight map should be the sum of relatively few rank-one matrices (here latent time/frequency process weights) [112]. The sum over components acts as a groupwise L1 norm over component weights, minimizing the total number of component processes contributing to the classifier.

A potential flaw of the convex relaxation is that the norm treats regions in which relevant oscillatory processes overlap in time and frequency slightly differently from regions in which they do not overlap (since the sum of their spectrograms is not generally equal to the spectrogram of their sum). Fortunately, each independent component tends to contain only a small set of such independent time/frequency processes, leaving little opportunity for such sub-optimal behavior.

8.2.7 Spatial source restriction

It is also possible to factor into RSSD additional ‘Region Of Interest’ (ROI) anatomical, spectral, or temporal priors into the RSSD solution. By Green’s theorem, concurrent activity across a cortical patch, producing a coherent far-field signal on the scalp that is a maximally independent of the far-field signals of other sources, must have a scalp projection pattern that matches that of an equivalent current dipole, a vanishingly small battery-like source element located near the ‘center of gravity’ of the originating cortical source patch [113]. Applied to sufficient multi-channel data, AMICA finds a relatively large number of components whose scalp projections can be fit well by an equivalent current dipole [28].

To obtain the results we present here, we employed a soft probabilistic restriction to components whose best-fit equivalent dipole was located within of the cerebrum according to the Talairach atlas [70], assuming an average location error of 7mm, and where the residual variance of the fit was below 15%. This approach is implemented in an automated processing pipeline that we have made available as open source software [114]. Here, a fraction of components accounting for scalp channel activity produced by eye movements were not eliminated by this prior and were removed manually before performing the group measure projection analysis (described below).

8.2.8 Optimization and performance estimation

The optimization problem has a regularization parameter, λ in (1), found by cross-validation. We performed a 5x5-fold nested cross-validation to optimize its value over the range 2^8 to 2^{-5} in decrements of $x2^{-0.25}$. The outer cross-validation served to obtain an estimate of the overall predictive performance of the models. Since no statistic that informs the model may include the testing data, to obtain realistic performance estimates both the artifact rejection and the AMICA decomposition had to be computed separately in each fold of the outer validation loop. This nested evaluation procedure is implemented in the BCILAB package [110].

8.2.9 Measure Projection Analysis

The RSSD method produces predictive models that consist of a collection of S spatial filters W_c – one per independent component – and corresponding filter inverses P_c which can be viewed as forward projections of the filtered signal back onto the sensors. We then tried to find spatial regions in which RSSD time-frequency weight maps for component processes with nearby equivalent dipoles were more similar to each other across participants than could be expected by chance. To achieve this, we performed statistical significance testing on the pair-wise similarity of these RSSP maps in each spatial neighborhood. To model the spatial uncertainty from dipole localization as well as expected functional and anatomical differences across subjects, we first represented each of these dipoles by a truncated Gaussian density probability cloud with 12-mm standard deviation. We then calculated a similarity matrix between

RSSD time-frequency weight maps by applying this equation to their pairwise Pearson correlations:

$$\text{Mutual Information} = \frac{1}{2} \text{ sign (correlation)} \log_2 \left(\frac{1}{1 - \text{correlation}^2} \right) \text{ (bits / sample)} \quad (2)$$

We then defined a measure of similarity $C(y)$ in local neighborhood of each point $y \in V$ in the MNI brain space V using (3):

$$C(y) = E\{S(y)\} = \frac{\sum_{i=1}^n \sum_{j=1, j \neq i}^n P_i(y) P_j(y) S_{i,j}}{\sum_{i=1}^n \sum_{j=1, j \neq i}^n P_i(y) P_j(y)} \quad (3)$$

Here, $P_i(y)$ is the probability of RSSD equivalent dipole i being at location $y \in V$ and $S_{i,j}$ is the degree of similarity between importance maps associated with dipoles i and j . Convergence $C(y)$ is the expected value of similarity at location $y \in V$ assuming that the joint probability of each dipole pair i and j being located at $y \in V$ can be written (factorized based on the component independence assumption) as $P_i(y)P_j(y)$.

Calculated convergence $C(y)$ is a scalar and is larger for areas in which the IC dipole importance maps are homogeneous (similar). The probability of making an error of Type I may be obtained for each brain location by comparing $C(y)$ to a

distribution of surrogate convergence values $C'(y), i=1, \dots, k$ constructed from k randomized surrogates. Each surrogate convergence value is obtained by destroying the association between dipoles and their measure vectors by randomly selecting, with substitution, n surrogate measure vectors $M'_i, i=1, \dots, n$ and associating them with dipoles $D_i, i=1, \dots, n$. The surrogate similarity matrix $S'_{i,j}$ is obtained by calculating similarities between these surrogate measure vectors.

By repeating the process above k times, a distribution of surrogate convergence values $C'_i(y), i=1, \dots, k$ at each brain location $y \in V$ is obtained and the significance of convergence $C(y)$ is obtained by comparing it to the right tail of this null distribution. This p-value is equal to the proportion of surrogate $C'(y)$ values higher than the actual convergence value $C(y)$

$$p\text{-value}\{C(y)\} = \frac{\#\{i : C'_i(y) > C(y); i \in 1, \dots, k\}}{k}. \quad (4)$$

We then selected brain locations with $p < 0.002$ and calculated the expected, or *Projected*, value of the importance map at these $y \in V$ locations using the formula below:

$$E\{M(y)\} = \langle M(y) \rangle = \frac{\sum_{i=1}^n P_i(y) M_i}{\sum_{i=1}^n P_i(y)} \quad (5)$$

Where $M(y)$ is the vector of importance map projected to location $y \in V$. To simplify the analysis we then segmented these projected values into *domains*, each exhibiting similar importance maps, in a way that the centroid of each domain becomes less similar than Pearson correlation < 0.9 to any other domain (this was achieved by performing a modified version of Affinity Propagation clustering [reference] on pairwise correlation similarity of importance maps associated with significant brain locations).

8.3 Results

8.3.1 RSSD results

Figure 8.2 depicts the most highly-weighted RSSD data features for a participant for whom estimated classification performance was 86.4% correct. Scalp maps show forward projections the 12 most highly-weighted components. For each component, the method produces an ‘importance map’ of weights over latencies and frequencies time locked to the switch cue. Because the RSSD is a generalized linear model and trained to predict +1 for data corresponding to HEAR→LOOK trials and -1 for data LOOK→HEAR trials, the resulting importance maps can be viewed as analogous to the contrast formed by the subtraction of HEAR→LOOK trials (switch to visual) minus LOOK→HEAR trials (switch to auditory). The difference is that here, a multivariate rescaling (similar in effect to z-scoring) is performed, and a low-rank and group-wise sparse prior is employed.

The highest-weighted features in the model depicted in Figure 8.2 (A, B) weight a marked decrease in the amplitude of narrow alpha-band oscillations centered about 900 ms after Switch cue onsets. In about 90% of subjects a similar feature was associated with one or more posterior components. This decrease implies that in HEAR→LOOK trials, following the switch to visual attention power of the alpha band oscillation was decreased, as expected (whereas inversely, following LOOK→HEAR Switch cues, alpha band activity increased).

The timing of this transition is quite clearly defined by the alpha band features and differs between the occipital and the parietal components (C, F, H). Some other occipital components are weighted less strongly, possibly as a result of the component-wise sparsity assumption rather than because of their smaller extent, but show the same directional effect (I, J).

One of the bilateral parietal components (G), however, shows the opposite pattern, with a clear, brief suppression of alpha power following the Switch cue, followed by an alpha rebound. The top right component (D) is a right temporal source that exhibits post-switch alpha flooding at two closely spaced alpha band frequencies following HEAR→LOOK cues (implying corresponding alpha blocking following LOOK→HEAR cues), consistent with a source in auditory cortex [115]. Similar features were highly weighted in a fraction of subjects (20-30%).

Component E weights a decrease in low-frequency activity following HEAD→LOOK cues, likely reflecting a suppression of blinks or vertical eye movements following switches to visual attention. This effect was highly weighted in several subjects.

Another phenomenon, expressed in nearly every subject, was an amplification of low-frequency occipital component activities (here, B and G) following HEAR→LOOK Switch cues; this might in some part reflect attention-related increase in the amplitude of visual stimulus-evoked potentials following the switch to visual attention.

While the largest average attention-shift effects in the participant model of Figure 8.2 are clearly in occipital and parietal cortices, some temporal lobe features were also highly weighted for a subset of subjects, whereas lateral frontal and frontal-midline component features were less consistently selected. However, about half of the participant models included some form of frontal theta band effect time-locked to subsets of the underlying audio/visual/cue stimuli (for example, Figure 8.3A and E), some of which (here, A) were harmonic to a prominent alpha band feature. A smaller fraction included frontal beta band features (Figure 8.3E). Highly-weighted switch-related changes in frontal alpha power did not appear in these participant models.

8.3.2 Measure Projection Analysis

Figure 8.4 shows seven Measure Projection Analysis (Chapter 6) domains created from component equivalent dipole locations and RSSD maps across the 31 participants. We used 12 mm Gaussian std. for dipole densities and the projected measure from significant voxels with $p < 0.01$ were clustered using Affinity Propagation algorithm with maximum exemplar similarity of 0.8 correlation. Table 8.1 contains different anatomical locations associated with domains.

8.4 Discussion

The single-participant results show some rather consistent and expected patterns, namely the alpha suppression in switch-to-visual conditions and corresponding alpha flooding in the periods before the switch. One of the less expected effects that was however replicated in at least 25% of subjects is an occipital alpha suppression around the time of the cue perception followed by a subsequent rebound. We believe that this depends on an inter-individually different strategy, namely whether subjects are watching for the cue to appear and subsequently withdraw attentional resources for a period of time, or whether they are listening for the cue (note that cues are bimodally presented), or whether they rely mostly on anticipation to predict and respond to the cue (since the cue timing is roughly predictable). The relatively rare occurrence of auditory cortex components could be explained by the relatively weak signal emitted from this area, combined with the relatively low difficulty of the task, which conceivably does not achieve maximum

alpha modulation. Systematic differences in frontal theta are among the least expected effects, yet expressed quite frequently upon closer inspection (although not very consistently). The near-complete absence of frontal alpha modulation could be attributed to the relative functional invariance of these areas under the changes in sensory modality investigated here.

8.5 Conclusion

The work presented here is the fusion of two new brain imaging methods that are both general by themselves yet synergize with each other as shown. The RSSD method was created to help bridge the gap between traditional techniques from the EEG-based Brain-Computer Interfacing (BCI) or Cognitive State Assessment (CSA) fields and modern machine learning aided brain imaging. BCI/CSA are still dominated by algorithms that frequently require heuristics for time window and/or frequency band selection – limitations that can now be overcome by use of large-scale optimization and sufficiently good prior assumptions. Machine learning aided brain imaging on the other hand is still in its very infancy, especially when applied to EEG data, which is still plagued by the reputation of being a low-resolution measure – in part due to the relatively low-end analysis approaches that have been applied in the past; again, this is a limitation that can be overcome as has been demonstrated here as well as in other recent work.

8.6 Acknowledgements

Chapter 8, in full is currently being prepared for submission for publication of the material. C. Kothe, N. Bigdely-Shamlo, M. Westerfield, J. Townsend, S. Makeig. The dissertation author was the secondary investigator and author of this paper.

8.7 Figures

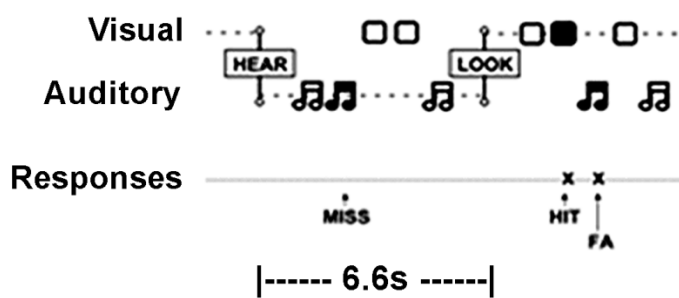


Figure 8.1. Time line of the task. The dotted line indicates the currently attended modality, and its changes in response to audiovisual 'HEAR' and 'LOOK' cues.

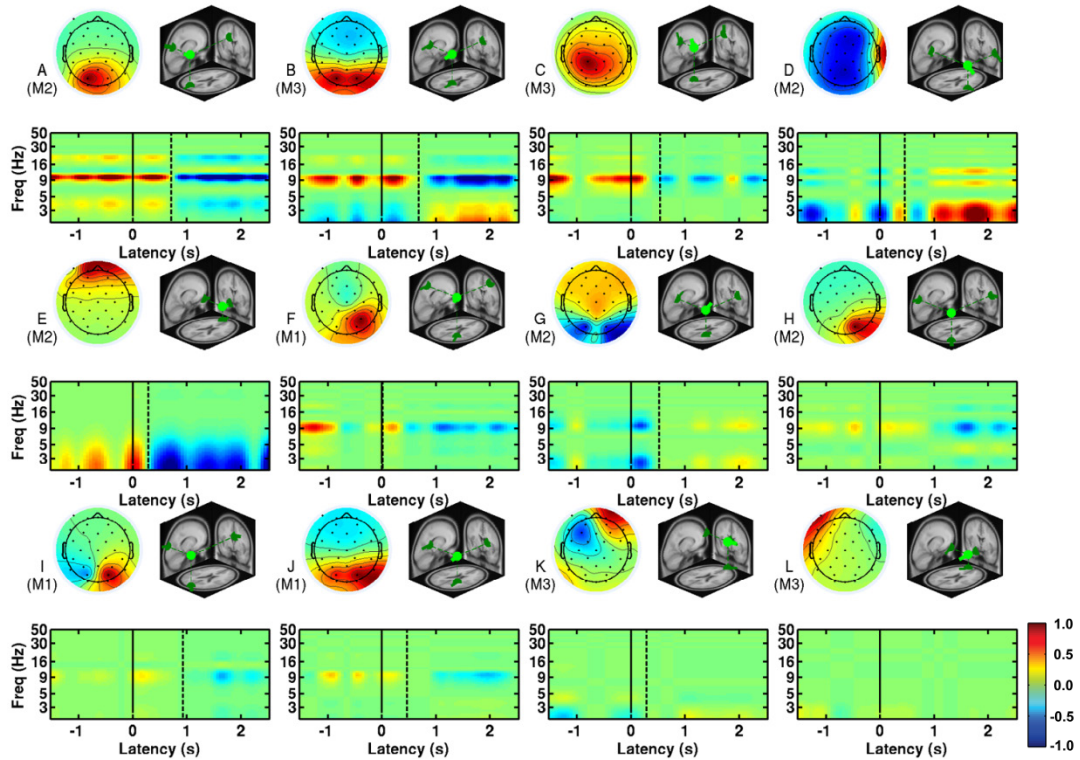


Figure 8.2. Best-classifying component scalp maps and their time/frequency weights, learned using RSSD for one participant, exhibit a variety of attention switch-related time/frequency effects across at least 12 maximally independent EEG components. The model from which each component originated is indicated in brackets. Scalp maps show the normalized scalp distribution of the forward projection of the component signal (non-contributing time/frequency points are shown in green). Time/frequency plots here show the relative weighting of time/frequency regions across latencies time-locked to the HEAR or LOOK cues which were presented at 0 ms (solid vertical line). Components are sorted by decreasing maximum absolute weight (in English reading order). The positively weighted direction is HEAR→LOOK; thus, switching attention to the visual stream was predominantly associated, as expected, with blocking of narrow-band alpha (circa 10-Hz) oscillations in posterior cortical processes (dashed vertical lines), as well as with spectral changes in other frequency bands.

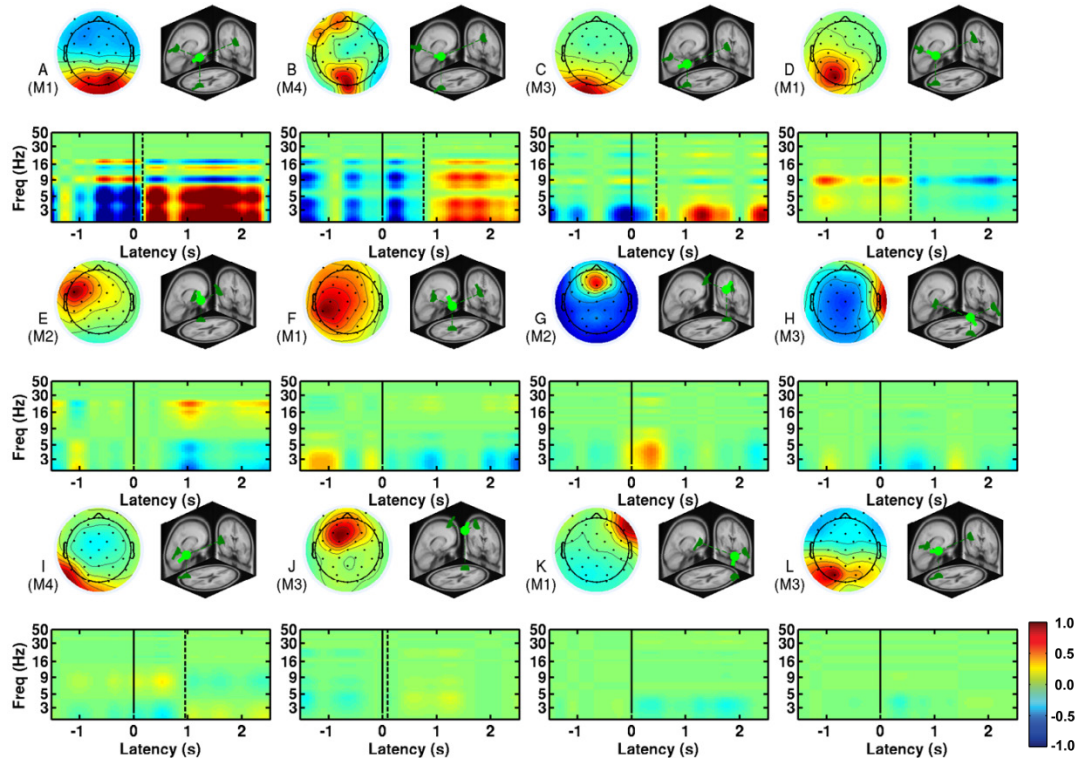


Figure 8.3. Frontal source features were highly weighted in many though not in all subjects. For example, in this participant the highly-weighted features included frontal midline theta bursts (G), as well as beta bursts (E) aside from expected occipital and parietal alpha effects (A,B,D).

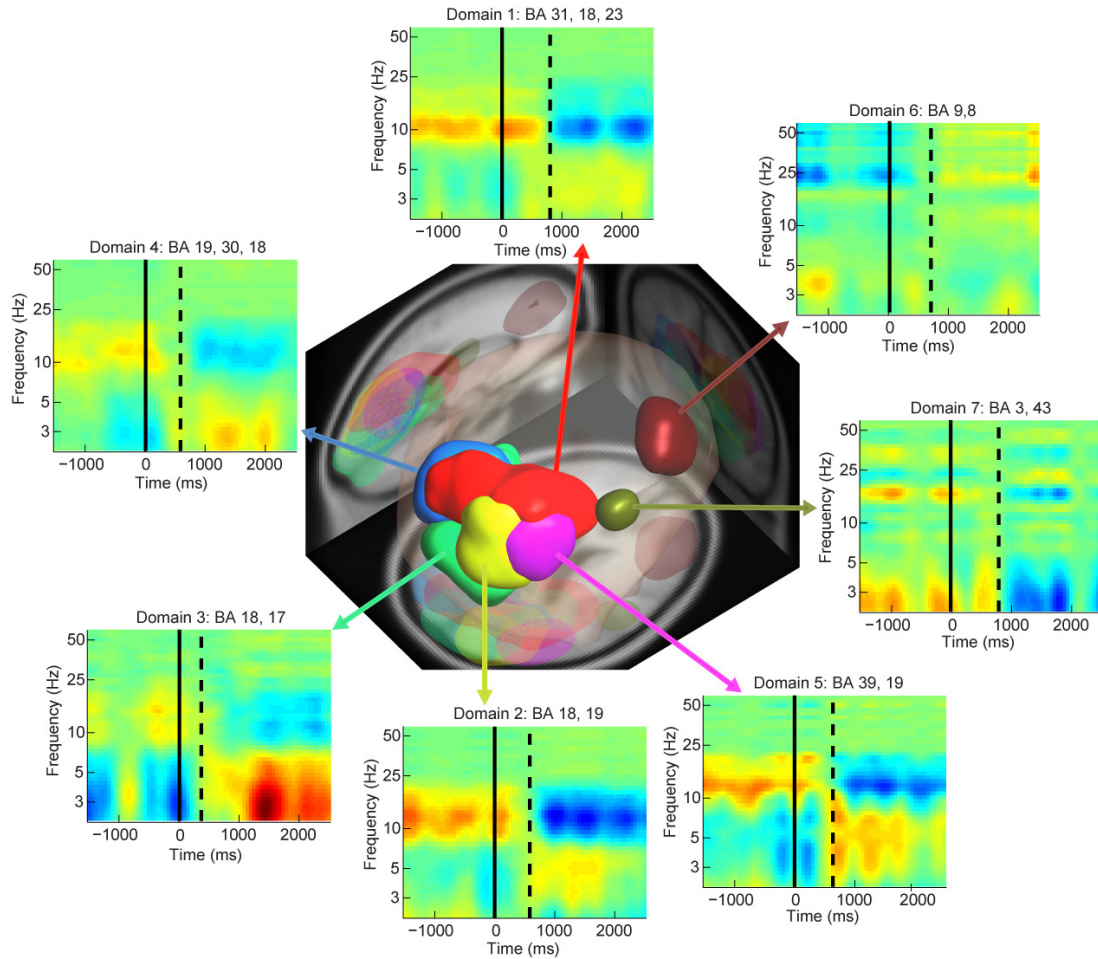


Figure 8.4. Spatial distributions and exemplar voxel time-frequency weight maps for seven domains learned by affinity propagation from MPA of the component equivalent dipole locations and RSSD maps across the 31 participants.

Table 8.1. Anatomical locations associated with domains in Figure 8.4.

Domain	Anatomical Area(s)	Brodmann Area(s)
1	R Superior Parietal Gyrus (0.26) L Precuneus (0.10) L Superior Parietal Gyrus (0.10) R Precuneus (0.09) L Superior Occipital Gyrus (0.09) R Angular Gyrus (0.08) L Cuneus (0.07)	BA 31 (0.39) BA 18 (0.13), Secondary visual (V2) BA 23 (0.13) BA 30 (0.11) BA 7 (0.09), Somatosensory Association
2	R Middle Occipital Gyrus (0.45) R Superior Occipital Gyrus (0.24) R Lingual Gyrus (0.19)	BA 18 (0.36), Secondary visual (V2) BA 19 (0.20), Associative visual (V3) BA 30 (0.17) BA 31 (0.13) BA 17 (0.09), Primary visual (V1)
3	R Inferior Occipital Gyrus (0.23) L Lingual Gyrus (0.18) Cerebellum (0.14), R Lingual Gyrus (0.12), R Middle Occipital Gyrus (0.10)	BA 18 (0.47), Secondary visual (V2) BA 17 (0.22), Primary visual (V1) BA 19 (0.13), Associative visual (V3) BA 30 (0.08)

Table 8.1., continued.

Domain	Anatomical Area(s)	Brodmann Area(s)
5	R Middle Occipital Gyrus (0.51)	BA 39 (0.43)
	R Angular Gyrus (0.31)	BA 19 (0.22), Associative visual (V3)
	R Middle Temporal Gyrus (0.11)	BA 37 (0.19) BA 22 (0.14), Auditory processing
6	R Middle Frontal Gyrus (0.92)	BA 9 (0.59)
	R Inferior Frontal Gyrus (0.06)	BA 8 (0.24), Includes Frontal eye fields and Lateral and medial supplementary motor area (SMA) BA 10 (0.12)
7	R Postcentral Gyrus (0.65)	BA 3 (0.30), Primary Somatosensory
	R Supramarginal Gyrus (0.32)	BA 43 (0.21), Subcentralis BA 4 (0.15), Primary Motor
		BA 40 (0.15), Spatial and Semantic Processing
		BA 13 (0.08), Inferior Insula
		BA 2 (0.07), Primary Somatosensory

Chapter 9

Network Projection

9.1 Introduction

Analysis of functional brain network dynamics has become an important topic in Cognitive Science and EEG analysis [116]. Functional connectivity is related to the correlations in activity (e.g. EEG, fMRI) between brain regions and is inherently symmetrical. In contrast, Effective connectivity relates to causal dependencies between brain regions during information processing and is inherently asymmetrical.

Various measures such as correlation, coherence, Granger Causality [117, 118], Partial directed coherence [119] and Generalized partial directed coherence [120], have been proposed to investigate functional and effective connectivity. These measure may be applied either to EEG channel data or EEG source derived from a source separation method such as ICA [121]. Using EEG source activities for functional or effective connectivity is more meaningful and is shown to results in less false positives [122].

Group-level analysis of EEG source connectivity is a relatively recent topic. In contrast to EEG source measures such as ERP and ERSP that are associated with a

single cortical source, connectivity measures are associated with a *pair* of cortical sources. This complicates their analysis with methods such as simple clustering. Each EEG group-level connectivity analysis algorithm is devised to work with a subset of source estimation and connectivity estimation approaches, taking into account the limitations and underlying assumptions of each approach. For example, group-level analysis of “lagged phase synchronization” index [123, 124] works in conjunction with eLoreta [123] and several method exists in DCM framework [125, 126] to perform group-level connectivity analysis [127, 128].

In [129], Thompson el al. introduced a method based Bayesian clustering for analyzing effective connectivity for a group of subjects based on EEG equivalent dipole sources obtained from ICA scalp maps. The method was applicable to 1-D features such as time-varying dDTF [11, 12] measure in a single frequency band. Here we propose Network Projection Analysis (NPA), a generalization of Measure Projection Analysis (MPA) to pairs of brain dipolar sources for group-level analysis of EEG connectivity. NPA is applicable to connectivity measures with arbitrary dimensions (e.g. 2-D time-frequency dDTF).

9.2 Methods

Network Projection Analysis (NPA) is based on the same concepts, assumptions and mathematical framework as MPA (see chapter [chapter number needed], also see [130, 131] for a precursor to NPA). The two main differences

between NPA and MPA are (a) projected entities in NPA are network connectivity measures that are assigned to *ordered pairs* of brain sources, where in MPA projected entities are measures associated with single brain sources, (b) NPA projects into ordered pairs of anatomically selected brain regions (ROIs, e.g. anterior cingulated to left orbitofrontal) while MPA projects into individual brain areas or voxels. Because of this NPA does not require the domain creation step employed in MPA.

For a number of measure vectors $M_i, i = 1..N$, e.g. dDTF, each associated with a ordered pair of ICs from the same subject, $D_j: IC_a \rightarrow IC_b, j = 1..N$, , the projected measure $\langle M(y_k) \rangle$ for a directed pair of ROIs, $y_k: ROI_g \rightarrow ROI_h, k = 1..Q$ is defined as

$$\langle M(y_k) \rangle = \frac{\sum_{i=1}^N P_i(y_k) M_i}{\sum_{i=1}^N P_i(y_k)} \quad (1)$$

where $P_i, 1 = 1..N$ is the probability that IC_a of $D_j: IC_a \rightarrow IC_b$ is located inside ROI_g of $y_k: ROI_g \rightarrow ROI_h$ and IC_b is located inside ROI_h . Assuming these two probabilities to be independent, P_i can be calculated as

$$P_i = p(IC_a \text{ is located in } ROI_g) p(IC_b \text{ is located in } ROI_h). \quad (2)$$

Figure 9.1 shows a sample ordered ROI pair (from left superior frontal region to right precentral area) and the highest contributing ordered dipole pairs to it (dipole

pairs with the largest P_i). Dark arrows show the direction of the contributing dipole pairs.

If we follow the truncated Gaussian dipole probability density assumption used in MPA (see Chapter 6), each of these probabilities can be numerically calculated by summing up Gaussian probability densities for each IC at locations associated with each ROI.

The *measure convergence* quantity, $C(y)$, indicates the expected value of similarity S between measures M_i projected into directed ROI pair y_k :

$$C(y_k) = \frac{\sum_{i=1}^N \sum_{j=1, j \neq i}^N P_i(y_k) P_j(y_k) S_{i,j}}{\sum_{i=1}^N \sum_{j=1, j \neq i}^N P_i(y_k) P_j(y_k)}. \quad (3)$$

In this equation $S_{i,j}$ is the similarity (e.g. correlation, mutual information) between measures M_i and M_j . We seek directed ROI pairs where the value of convergence, $C(y_k)$, is larger than what could be obtained by chance. The significance of his value may be calculated, in a manner similar to MPA (equation A.3 in Chapter 6), by comparing $C(y_k)$ to a distribution of L surrogate converge values $C_v(y_k), v = 1..L$:

$$p-value(C(y_k)) = \frac{\#\{v : C_v(y_k) > C(y_k); v \in 1..L\}}{L}. \quad (4)$$

After p-values are calculated for each directed ROI pair, they may be corrected for multiple comparisons across Q pairs and only ROI pairs with a significant measure convergence (e.g. $p < 0.05$ after FDR correction) selected for further analysis. Since $C(y)$ is a scalar value and often has a much lower dimension than measure value $M(y)$, the multiple comparison problem is more manageable when dealing with convergence values.

9.3 Results

Graph-normalized Direct Directed Transfer Function (dDTF) [11, 12], a frequency-domain measure of multivariate Granger-causal relationships, time-locked to correct and incorrect responses from 128-channel (256 Hz) EEG data collected from 24 subjects (29 sessions) performing a visual letter two-back task with auditory feedback [132, 133] (see Figure 9.2 for more information about the experimental paradigm), was kindly provided us by Tim Mullen (same data used in [129]). Using SIFT toolbox [111, 131], time-varying dDTF was estimated on independent components (ICs) using a sliding-window vector autoregressive (VAR) model with a 500 ms window length and 30 ms step size producing 80 time points. The dDTF was integrated over the theta band (3-7 Hz) and modeled as a smooth function of time via a penalized B-spline [129].

Before ICA calculation data had gone through zero-phase FIR high-pass filtering at 1 Hz and ICA was calculated using Infomax algorithm [20] and response-

locked data (-2 to 2 seconds) were subjected to Infomax Independent Component Analysis (ICA). A single (or dual symmetric) equivalent dipole model was then fit to each independent component (IC) using EEGLAB's DIPFIT2 function. ICs corresponding to artifacts such as eye blinks and muscle activity, and those with a poor dipole fit ($> 15\%$ residual scalpmap variance after dipole model fitting, or lying outside brain volume) were excluded from the analysis.

The data consisted of 3055 ordered IC-pairs, corresponding to 257 total equivalent dipoles, and each associated with 80 dDTF values from -750 to 1700 ms. We first calculated the probability that each of these dipoles is located in an ROI from AAL atlas [134] assuming a truncated Gaussian probability density model with 12 mm std. with truncation at 3 std. The probability that each ordered pair of dipoles is located in each ordered pair of ROIs was then calculated by equation (2).

Figure 9.3 shows total ordered dipole pair density in each ordered ROI pair. Relatively few ROI pairs contain the majority of this density. In fact 51% of total dipole pair density is concentrated in the top 10% ROI pairs.

For NPA results for an ROI pair to be meaningful, a large enough number of subjects should have dipole pairs that contribute to the pair. Hence for subsequent analysis we selected a subset of ROIs to which the majority of subjects have each contributed at least 0.02 ordered dipole pairs. We then calculated the NPA convergence significance for the 199 selected ROIs using equation (4).

Figure 9.4 shows the ROI-pairs with significant ($p < 0.05$, FDR corrected) effective time-varying theta band (5-7 Hz) connectivity calculated with dDTF. Gray background indicates connectivity between sources inside the same ROI. Red traces highlights time period where dDTF value is significantly higher than -750 to -500 ms , relative to subject response, baseline (z -score > 3).

9.4 Discussion

The dDTF values in our analysis were time-locked to subject incorrect responses. For this class of paradigms, it is often assumed that in the majority of trials subjects become aware of their error during or shortly after the response. In this experiment there is also an auditory feedback provided about 240 ms after the response. Our results in Figure 9.4 point to the causal involvement of Medial Cingulate Cortex (MCC) in error processing. This is in agreement with functional imaging studies results that find negative affect, pain and cognitive control activate anterior midcingulate cortex (aMCC) and anatomical evidence that suggests aMCC is a hub that connects reinforcement-related information (e.g. errors) to motor areas associated with expressing affects and executing goal-directed behavior [135]. Figure 9.4 in fact shows a significant causal influence from MCC (labeled as Cingulum Mid. L & R) to supplementary motor areas. The same connectivity pattern for MCC was also found in [129] by applying Bayesian spatiotemporal model to the exact same data (see Figure 9.5).

Here we showed a method for group-level analysis of effective connectivity networks associated with EEG sources obtained by ICA and dipole localization. To our knowledge the only other method that works on networks of dipolar sources is the Bayesian spatiotemporal method [129]. In this method a dimensionality reduction step has to be applied to the connectivity measure in order to facilitate Bayesian estimation of model parameters. In comparison, NPA does not require any dimensionality reduction and is able to handle connectivity measures with arbitrary dimensions. This is because in NPA, as in MPA, significance calculation is performed in the similarity ('kernel') space.

A future direction for NPA is to be used in the EEG Search Engine proposed in chapter [chapter number needed] to allow discovery of connectivity patterns and networks similar to a given query pattern. This can be achieved by using NPA and extend the MPA-based similarity estimation method proposed in that chapter to networks of brain ROIs.

9.5 Figures

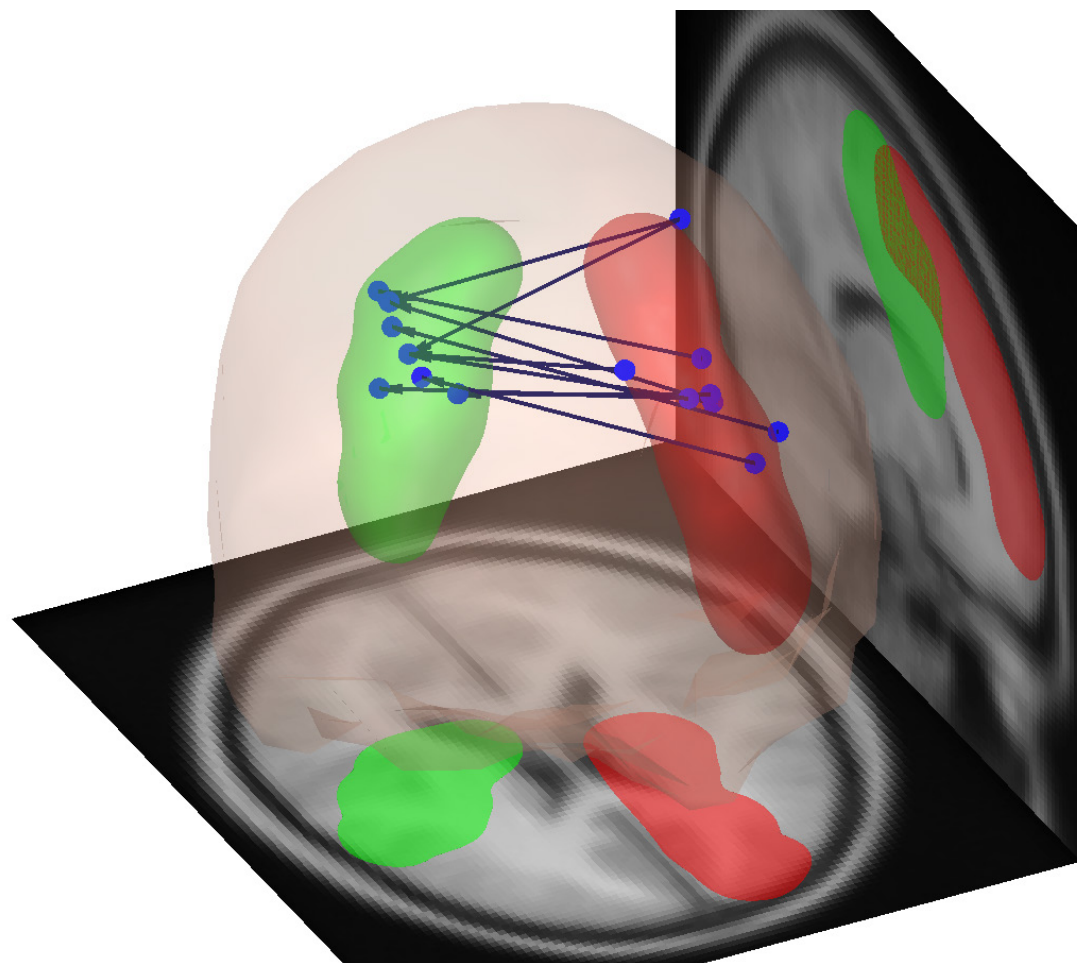
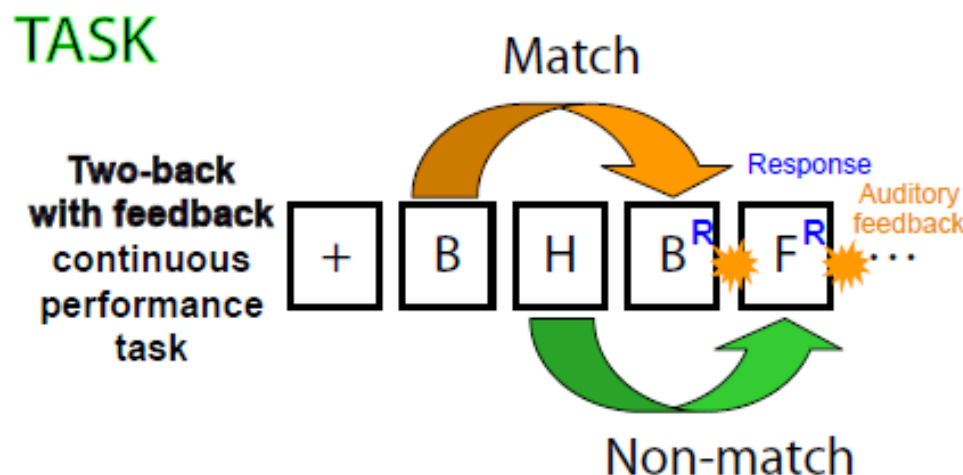


Figure 9.1. Sample ordered ROI pair (from left superior frontal region to right precentral area) and the highest contributing ordered dipole pairs to it. Dark arrows show the direction of the contributing dipole pairs.



Subjects were presented sequential single letters whose durations varied based on subject performance (SOA ~ 1.5 s). Beginning with the third letter, subjects responded to each letter, specifying with a right or left thumb press whether the current letter was the same as the one presented two before. An auditory feedback signal at letter offset informed the subject of whether their answer was correct or wrong. After 850 ms, the next letter was presented. Correct responses added 1 cent, and incorrect or failures to respond deducted 1 cent from the subject's performance reward. Following 20 percent of correct responses, a different feedback tone signaled a larger (5 cent) 'bonus.' Similarly, following 10 percent of incorrect responses another tone signaled a larger (5 cent) 'penalty.' In 6 percent of trials, a 'neutral' feedback signal gave no performance feedback.

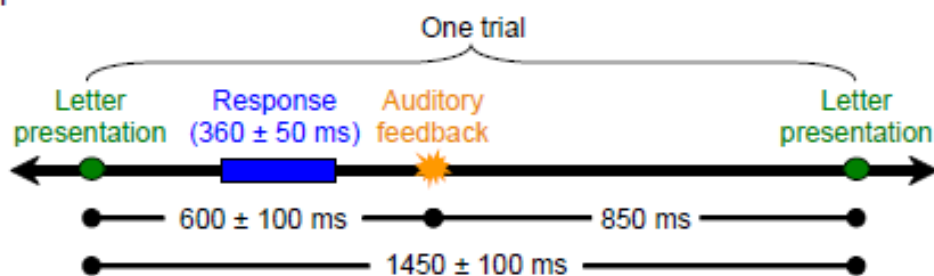


Figure 9.2. A schematic and description of two-back experiment paradigm, reproduced from [133].

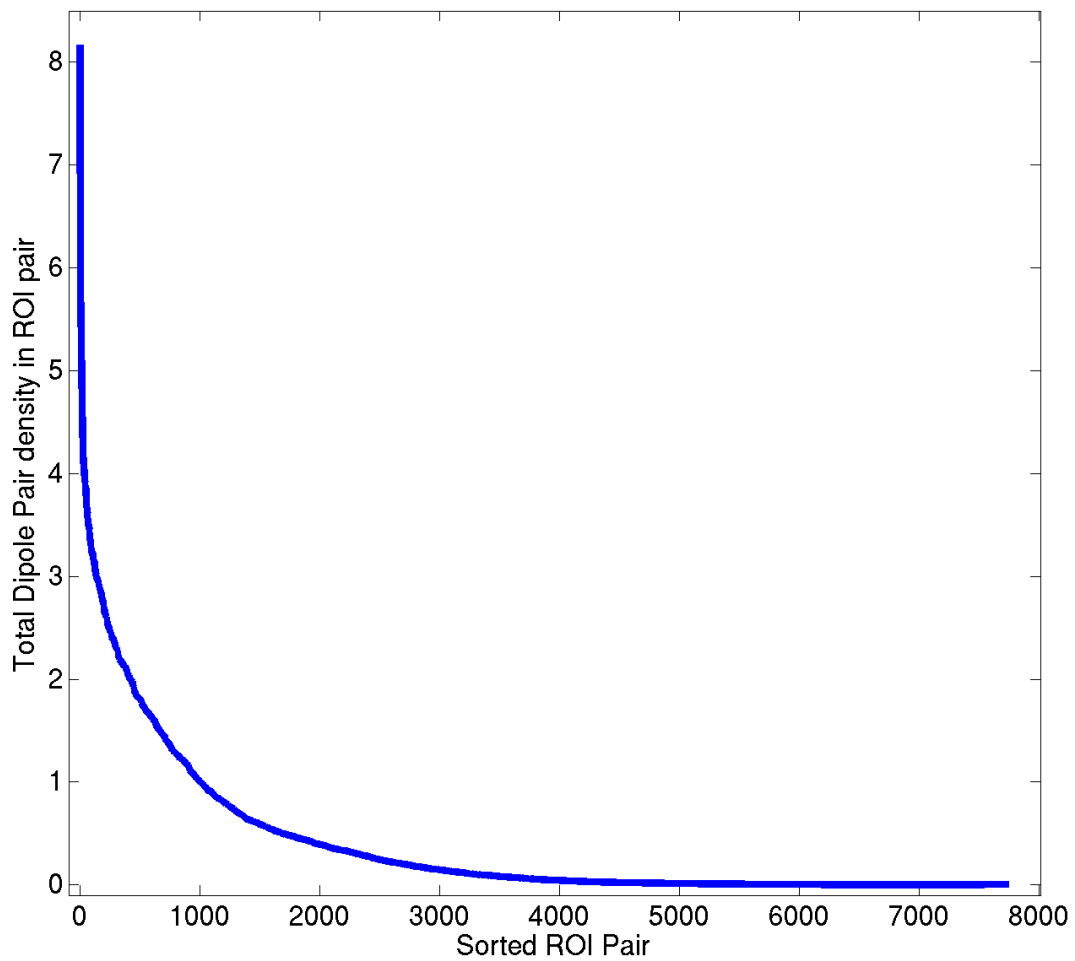


Figure 9.3. Total ordered dipole pair density in each ordered ROI pair. Relatively few ROI pairs contain the majority of the density.

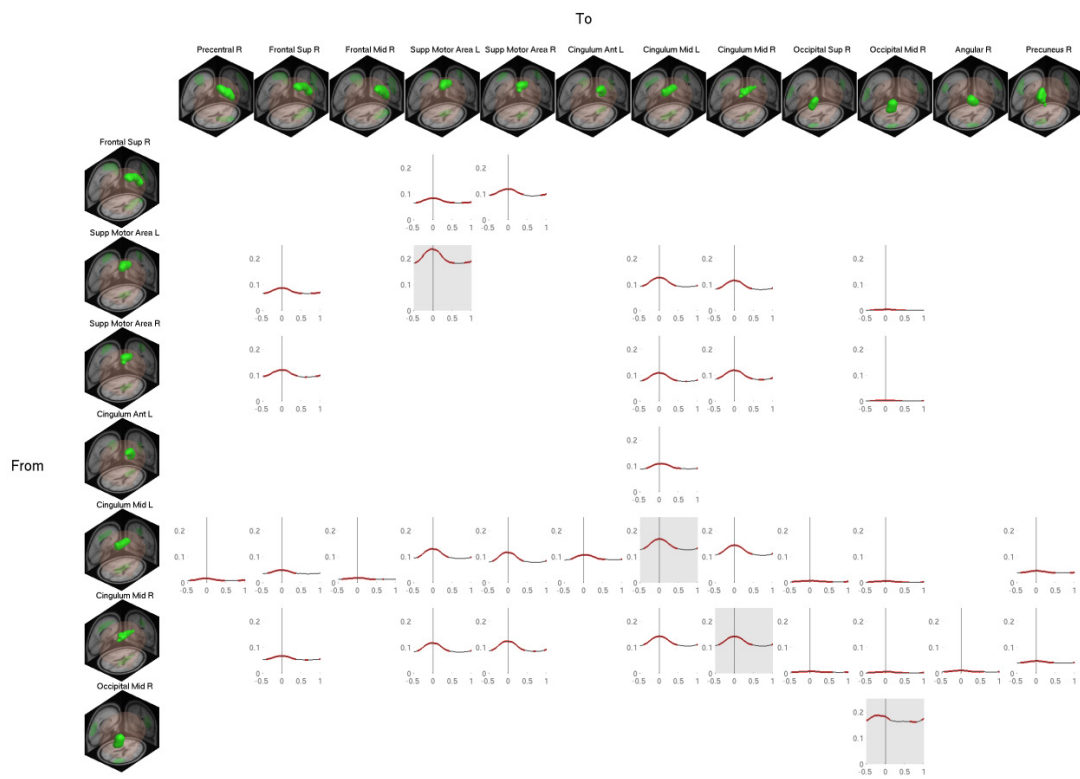


Figure 9.4. ROI-pairs with significant ($p < 0.05$, FDR corrected) effective time-varying theta band (5-7 Hz) connectivity calculated with dDTF. Gray background indicates connectivity between sources inside the same ROI.

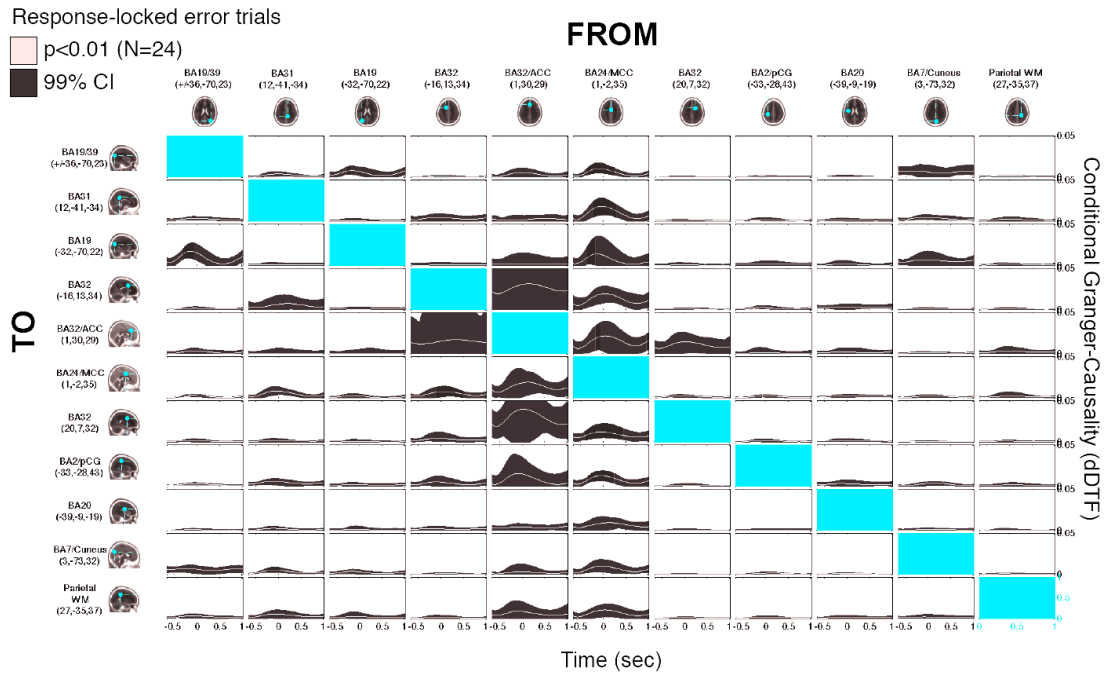


Figure 9.5. Reproduced from [129]: “Time-varying theta-band (3-7 Hz) dDTF group-level inferences with 99% confidence intervals. Mean source locations with Talairach coordinates and anatomical designations (Talairach Daemon) are shown on the marginals. Translucent regions indicate time intervals that deviate significantly from the [-750 to -500] ms baseline ($p < 0.01$, uncorrected).”

Chapter 10

Optimal Low pass Filtering

10.1 Introduction

Event-Related Potentials, or ERPs, are calculated by averaging time-locked channel or independent component (IC) activations for a number of trials. Since the number of trials being averaged is limited, the average still contains some noise. A number of methods have been proposed to ‘de-noise’ ERP data. These include weighted averaging [136], multi-channel noise subspace removal [137], sorted averaging [138], point-wise median [139] and wavelet-based de-noising [140].

A simple way to reduce ERP noise is to apply a low-pass filter. It is common practice to low-pass ERPs at around 20 Hz [141-143]. Here we introduce a method to find the optimal low-pass filter frequency, evaluate its performance and see how it can improve Measure Projection Analysis of multi-subject ERP data.

10.2 Methods

Based on the Scientific Method [144], scientific models should be compared based on their predictive power. An 'EEG model' hence should predict the EEG patterns that will be observed at each brain area associated with an experimental event or state. A function that has a number of trial EEG activations (from channels or ICs) as its input and outputs a pattern that predicts (estimates) an unseen EEG trial is an example of an EEG predicitve mode. One choice for this function, F_1 , for trial data $D_{1..N}$ is the average:

$$F_1(D_{1..N}, [\dots]) = F_1(D_{1..N}) = \overline{D_{1..N}} \quad (1)$$

But there may be functions (models) that offer a better predictive power and hence favored by the Scientific Method. A simple example of such a function is 'optimal low-pass':

$$F_2(D_{1..N}, [\dots]) = F_2(D_{1..N}) = \text{Low-pass filter}(\overline{D_{1..N}}, f) \quad (2)$$

where $f = \arg \max(\sum_{i=1}^N ROV(f, i))$ and

$$ROV(f, i) = 1 - \frac{\left\| D_i - (\text{Low-pass filter}(\frac{\sum_{j=1..N, j \neq i} D_j}{N-1}, f)) \right\|_2^2}{\|D_i\|_2^2}. \quad (3)$$

This equation refers to leave-one-out cross-validation in order to find the low-pass frequency threshold that maximizes the sum of reduction of variance ratios (ROVs) across trials. Here the ratio is used since the absolute reduction of variance value (the numerator in equation 3) is more sensitive to outlier trials with unusually high amplitudes.

10.3 Results

We used the single trial data from one session of the RSVP experiment described in [48] (the same study analyzed in Chapter 6), time locked to the onset of visual target detection. Figure 10.1 shows leave-one-out cross-validation ROV values at different frequencies for three ICs. For each IC there is a clear pick at a certain frequency. Notice how the two mirror-image ICs have their peak ROV at the same 7 Hz frequency. Figure 10.2 shows the original (unfiltered) ERP (thin black) and optimal low-passed filtered ERP (thicker magenta) for one of these ICs.

We performed 500 Monte-Carlo 20-Fold cross-validations (using 'Mcreps', 500, 'Kfold', 20 in Matlab crossval() function) on 30 ICs with highest signal variance in the whole experiment. On each fold the optimal low-pass frequency was calculated by performing a leave-one-out nested cross-validation on the training data and the ROV was calculated on the unseen (test) data. Figure 10.3 shows the ROV results in comparison often-used 20 Hz low-pass filtering of ERP. It shows that 29 of these 30 ICs have a significantly better test ROV than 20 Hz low-pass (error bars depicting one

std. of test ROV were plotted but due to their small size they cannot be seen in the figure).

Figure 10.4 shows the optimal low-pass frequencies for the first 30 ICs of the session (x axis) and the final percent reduction of variance (ROV) after optimal filtering. Negative ROV for an IC indicates that its ERP does not have predictive value for unseen trials. Interestingly, for most ICs in this experiment the optimal low-pass frequency was under 8 Hz, significantly lower than the often-used 20 Hz low-pass. Also, eye-related and noise ICs were assigned an optimal frequency lower than 3 Hz, in effect eliminating their (noise) ERP.

Since noisy ERPs look more dissimilar to each other, the presence of ERP noise has an impact on convergence values and their significance calculated with measure projection analysis (MPA). We investigated this effect by performing MPA separately on 20-Hz low-passed and optimal low-passed ERPs from the RSVP study. Figure 10.5 shows brain locations for these two conditions with ERP convergence significance $p < 0.05$ (FDR corrected). MPA using optimal low-pass ERPs, shown in Figure 10.5 bottom leads to 345% more significant locations compared to MPA results with 20-Hz low-passed ERPs.

Figure 10.6 shows areas with significant ($p < 0.05$, FDR corrected) ERSP convergence in green and areas with significant ERP convergence in red for 20-Hz low-passed (top) and optimal low-passed (bottom). You can see that there is a considerable overlap between brain areas that are associated with significant ERP and

ERSP patterns across subjects. Also, ERP results with optimal low-pass had three times more overlap with ERSP areas (236 significant voxels overlapped compared to 78 voxels for 20-Hz low-passed ERP results), suggesting that using optimal low-pass filtering produces less false negatives.

10.4 Discussion

Our results emphasize the importance of eliminating noise from ERPs before performing MPA. Optimal low-pass filtering is simple way to achieve this goal by eliminating high-frequency noise.

10.5 Acknowledgements

This research was sponsored by the Army Research Laboratory and was accomplished under Cooperative Agreement Number W911NF-10-2-0022, by NIH grant 1R01MH084819-03, and by a gift from The Swartz Foundation (Old Field NY). The views and the conclusions contained in this document are those of the authors and should not be interpreted as representing the official policies, either expressed or implied, of the Army Research Laboratory or the U.S Government. The U.S Government is authorized to reproduce and distribute reprints for Government purposes notwithstanding any copyright notation herein.

10.6 Figures

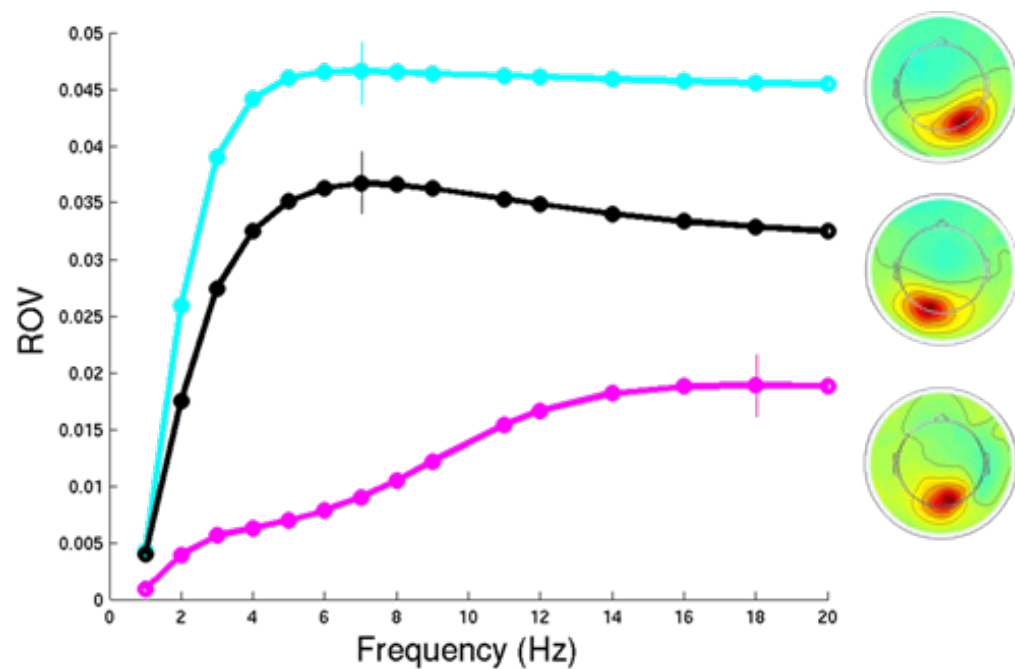


Figure 10.1. Sum of leave-one-out cross-validation ROVs at different low-pass frequencies for three ICs.

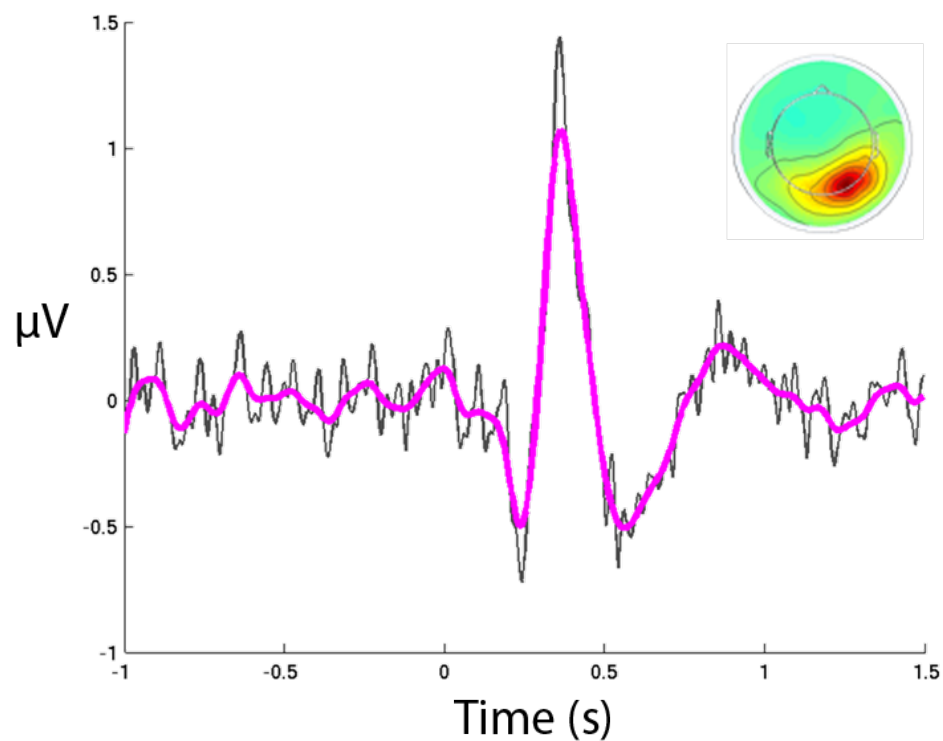


Figure 10.2. Original ERP (thin black) and optimal low-passed filtered ERP (at 7 Hz, thicker magenta) for an IC from the RSVP experiment.

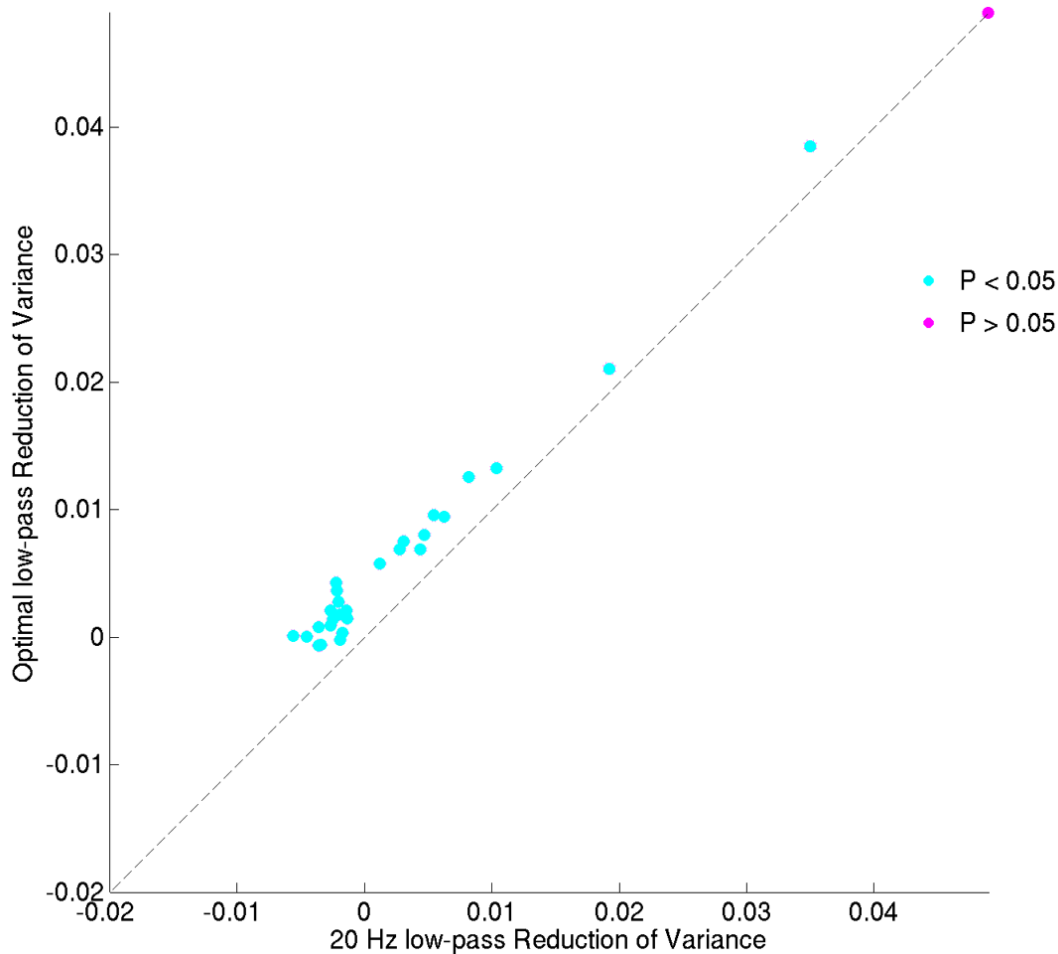


Figure 10.3. ROV comparison between optimal and 20 Hz low-pass filtering of ERPs from the top 30 ICs with highest total signal variance in the whole experiment using 500 Monte-Carlo 20-Fold cross-validations. Error bars depicting one std. of test ROV were plotted but due to their small size they cannot be seen in the figure.

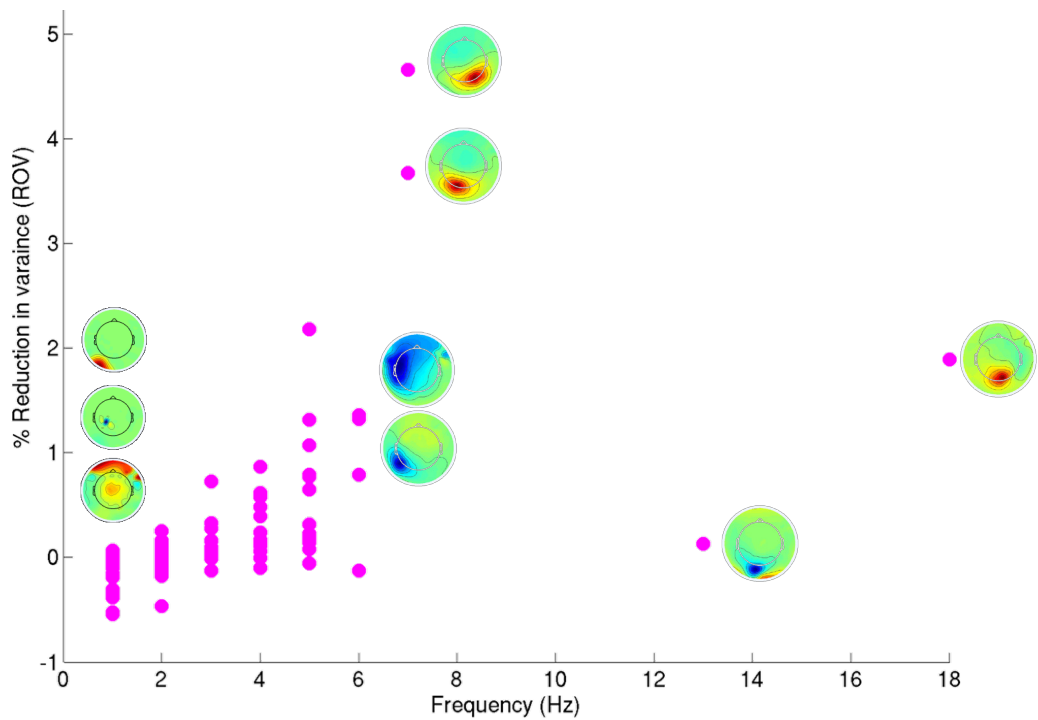


Figure 10.4. Optimal low-pass frequencies for the top 30 high variance 30 ICs (x axis) and the final percent reduction of variance (ROV) after optimal filtering. Negative ROV for an IC indicates that its ERP does not have predictive value for unseen trials.

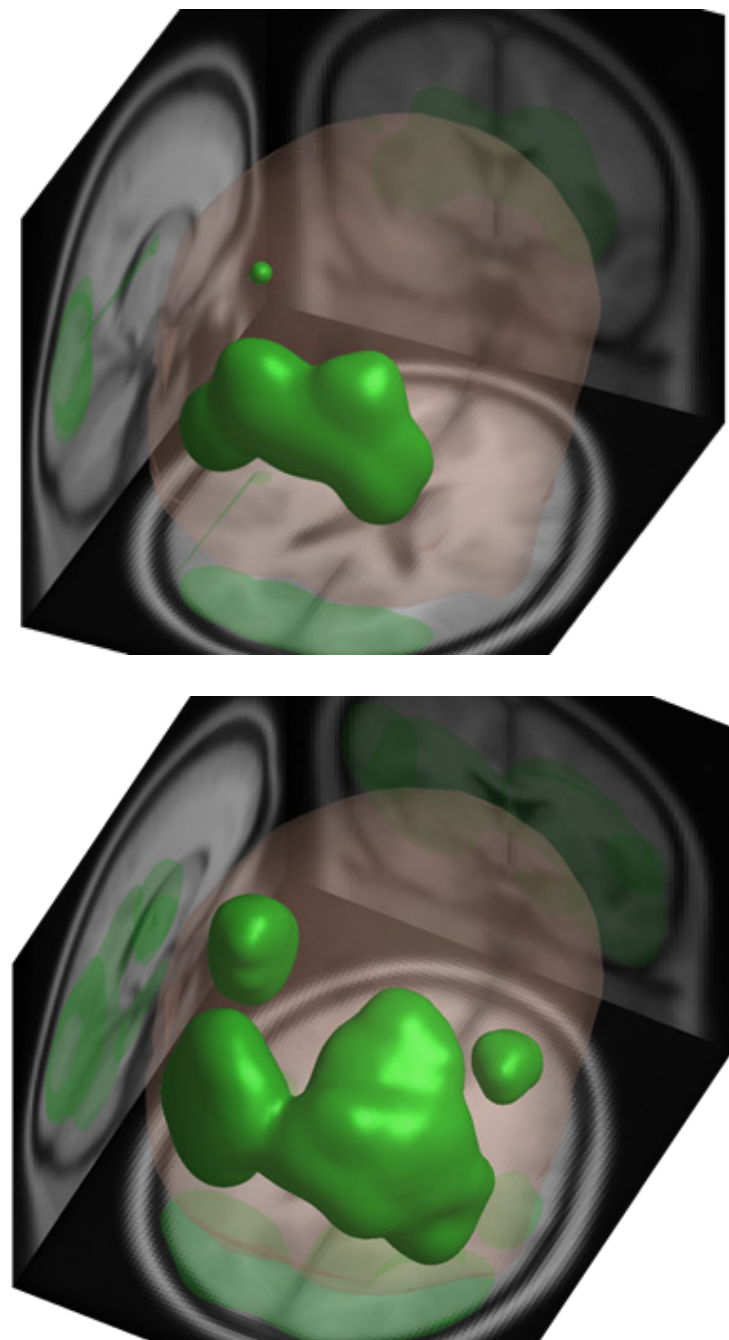


Figure 10.5. (top) Areas with significant ($p < 0.05$, FDR corrected) MPA convergence values using ERPs low-passed at 20-Hz. (bottom) Areas with significant ($p < 0.05$, FDR corrected) MPA convergence values using optimally low-passed ERPs.

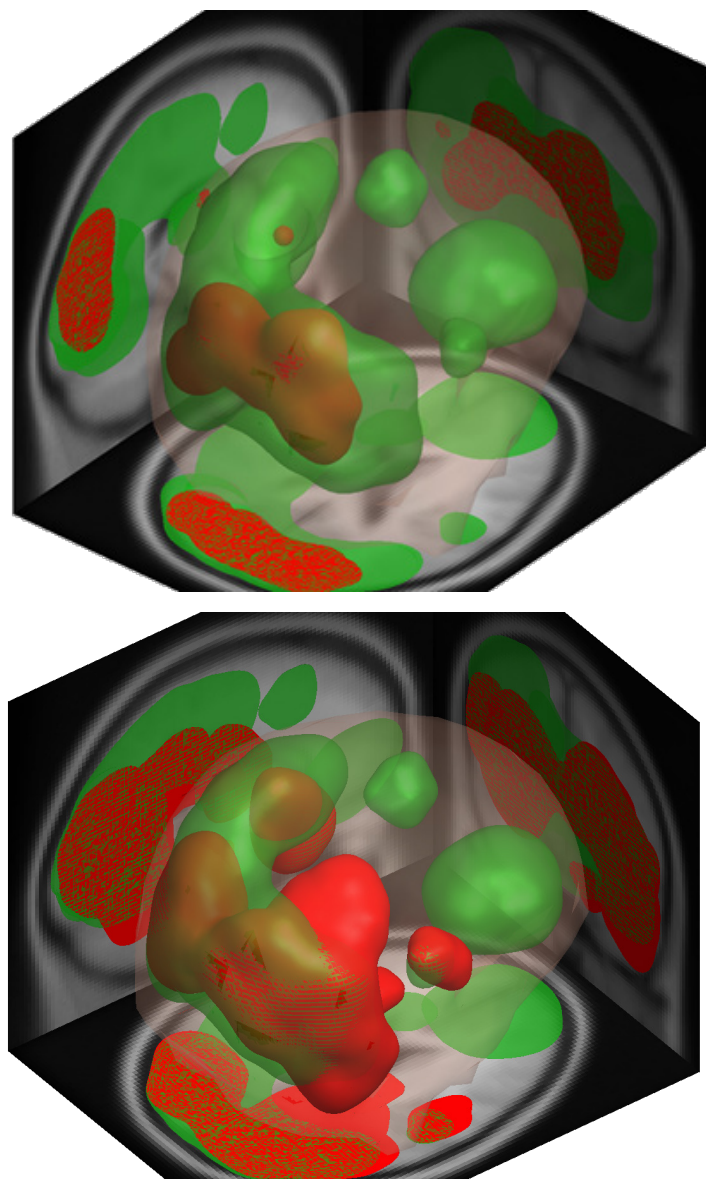


Figure 10.6. Areas with significant ($p < 0.05$, FDR corrected) ERSP convergence in green and areas with significant ERP convergence in red for 20-Hz low-passed (top) and optimal low-passed (bottom).

Chapter 11

Collaborative Averaging

11.1 Introduction

In the previous chapter we saw that a function $F(D)$ of data samples $D_{1..N}$ can predictor an unseen sample D_{N+1} better than the average of available samples $\overline{D_{1..N}}$. In this chapter we extend this notion and demonstrate how data from other subjects performing the same cognitive task may be used to better predict new single trial data from a new subject.

11.2 Methods

Most results in EEG analysis are based on the assumption that subjects have similar (although not identical) EEG dynamics, hence we may use the data from other subjects to construct a predictive function:

$$F(D_{1..N}, [...]) = F(D_{1..N}^{self}, [D_{1..M}^{other1}, D_{1..Q}^{other2}, ...]). \quad (1)$$

We can use the average pattern of all other subjects in the same brain area and combine it linearly with the pattern from the subject:

$$F(D_{1..N}^{self}, [D_{1..M}^{other1}, D_{1..Q}^{other2}, \dots]) = F(D_{1..N}^{self}, \overline{D_{1..M}^{other1}, D_{1..Q}^{other2}, \dots}). \quad (2)$$

The average pattern from all other subjects at a particular brain location can be obtained from Measure Projection:

$$\overline{D_{1..M}^{other1}, D_{1..Q}^{other2}, \dots, D_{1..N}^{otherZ}} = \frac{\sum_{i=1}^M p_i \overline{d_i}}{\sum_{i=1}^M p_i} \quad (3)$$

where d_i is an equivalent dipole associated with an IC from $D^{other1..otherZ}$ and p_i is the dipole density of this source at the location of the IC associated with data D^{self} . We can use the average pattern of all other subjects in the same brain area and combine it linearly with the pattern from the subject:

$$F_1(D_{1..N}^{self}, \overline{D_{1..M}^{other1}, D_{1..Q}^{other2}, \dots}) = \alpha \overline{D_{1..N}^{self}} + (1 - \alpha) \overline{D_{1..M}^{other1}, D_{1..Q}^{other2}, \dots} \quad (4)$$

where

$$\alpha = \arg \max \left(\sum_{i=1}^N ROV(\alpha, i) \right), \quad 0 < \alpha \leq 1$$

$$ROV(\alpha, i) = 1 - \frac{\left\| D_i - \left(\alpha \frac{\sum_{j=1..N, j \neq i} D_j}{N-1} + (1 - \alpha) \overline{D_{1..M}^{other1}, D_{1..Q}^{other2}, \dots} \right) \right\|_2^2}{\|D_i\|_2^2}. \quad (5)$$

Alternatively, instead of using the average of all other subjects, we can use a weighted linear combination of patterns from other subjects and the new subject at the same brain area:

$$F_2(D_{1..N}^{self}, \overline{D_{1..M}^{other1}}, \overline{D_{1..Q}^{other2}}, \dots) = \alpha_1 \overline{D_{1..N}^{self}} + \alpha_2 \overline{D_{1..M}^{other1}} + \dots + \alpha_Z \overline{D_{1..M}^{otherZ}} \quad (6)$$

where

$$\vec{\alpha} = \arg \max \left(\sum_{i=1}^N ROV(\vec{\alpha}, i) \right), \quad 0 < \sum_{i=1}^Z \alpha_i \leq 1$$

$$ROV(\vec{\alpha}, i) = 1 - \frac{\left\| D_i - \left(\alpha_1 \frac{\sum_{j=1..N, j \neq i} D_j}{N-1} + \alpha_2 \overline{D_{1..M}^{other1}} + \dots + \alpha_Z \overline{D_{1..M}^{otherZ}} \right) \right\|_2^2}{\|D_i\|_2^2}. \quad (7)$$

One way to solve this problem is by performing a grid search over α_i values. The other way to solve it is to use convex solver, such as CVX Matlab toolbox [145]. This is because equation (7) is the sum of quadratic functions of $\vec{\alpha}$ and hence convex in this variable. Compared to grid search, this approach offers faster and more accurate results. It also enables scaling the individually-weighted collaborative approach to large number of subjects since grid search quickly becomes infeasible as the volume of search space grows exponentially with the number of weights to be calculated.

11.3 Results

We selected a sample IC from a session of the RSVP experiment described in [48] (the same study analyzed in the previous chapter), time locked to the onset of visual target detection. Figure 10.1 shows the scalp map and the equivalent dipole location associated with this IC. We then optimally low-passed all the ERPs in the study with the method described in Chapter 10 and used measure projection to calculate the expected (projected) ERP at the location of the selected IC from other sessions of the study.

Figure 11.2 shows the optimally low-passed ERP of the sample IC (at 7 Hz) in red and the projected ERP from all other study sessions, scaled to have the same polarity and L-2 norm, in green. You can see that they are quite similar to one another.

To find out if using collaborative averaging formula (2) can lead to a better results we selected subsets of trials with varying length from the total of 118 single trials of the selected IC and found the optimal (maximum ROV) weight for combining the average of ERPs of other sessions with the average of trials from each subset. The optimal weight was calculated by grid search on 11 uniformly distributed α values between 0 and 1 (see equation 4). The average of ERPs of other sessions used here was normalized to have the same polarity (positive inner product) and L-2 norm as the average of trial subset.

Figure 11.3 shows correlations between the average ERP from all (118) trials and ERPs calculated by averaging (red) and collaborative averaging (green) subsets of varying sizes of single trials. We randomly selected trial subsets for 200 iterations (permutations without substitution). Error bars showing one std. are plotted but are too small to observe. For subsets with 30 trials or less there is a marked improvement in terms of correlation with the ERP using all the trials. Figure 11.4 shows percent ROV improvement using collaborative averaging compared to regular averaging for different number of trials. Not only this value is over 100% for subsets with less than 30 trials, but also collaborative averaging resulted in about 2% ROV improvement is ROV when using all the 118 trials, suggesting that collaborative averaging could be useful even when a large number of trials are available.

Figure 11.5 shows how many more trials, compared to using collaborative averaging, are needed to achieve the same level of correlation with the ERP calculated from all 118 trials. As you can see in this figure, using collaborative averaging in some cases may result in an ERP improvement equivalent to having 6 times more single trials.

Figure 11.6 shows the optimal weight for the average of other subjects, $1 - \alpha$ in equation (4), obtained by collaborative averaging for different number of trials. It shows that when the number of trials is low, e.g. less than 25, collaborative averaging weights the pattern from other subjects more than the pattern from the subject herself as the pattern from others is more reliable than subject ERP. Another interesting

observation is that even for large number of trials (e.g. 118) collaborative filtering is still using 20% of average pattern from other subjects.

We then tried the individually-weighted collaborative filtering method on the same sample IC data. In order to reduce the number of weight values to be estimated (and prevent overfitting) we calculated a single ERP for combined sessions of each of other subjects (6 other subjects , 14 sessions) with measure projection. We then weighted the six resulting ERP patterns separately and found the weight vector that maximized leave-one-out cross-validation ROV. For each of the subjects, six weight values uniformly distributed between 0 and 1 were searched, resulting in $6^6=46656$ total possible weight combination for all subjects.

Figure 11.7 shows target ERP of the select IC from all trials (gray), the first 30 trials (blue) and collaborative averaging using the first 30 trials of the subject and individually weighted patterns from other subjects. The green rectangle highlights a period where the ERP from 30 trials contains extraneous peaks that are corrected when using collaborative averaging.

Figure 11.8 shows correlations between the average ERP from all (118) trials and ERPs calculated by averaging (black), collaborative averaging using the average ERPs of other sessions (red) and collaborative averaging with each subject weighted separately (green). Statistics are for 7800 random permutations (without substitution) and error bars show 1 std. For this sample IC, when the number of trials was 30 or less, weighting subjects individually resulted in a better correlation with the average

ERP from all trials ($p < 4.3 * 10^{-21}$ from paired t -test) compared to either collaborative averaging using the mean of other subjects or regular ERP averaging.

Figure 11.9 shows cross-validation reduction of variance (ROV) values for different numbers of trials and different pattern estimation methods. CVX convex optimization toolbox [145] was used for performing collaborative averaging method in this figure . For number of trials less than 118, the individually weighted collaborative ERP resulted in a better ROV than the Average collaborative ERP method, and both did better than regular ERP method (paired t -test $p<0.01$). For 11 trials, Average collaborative ERP method performs similarly to the regular ERP ($p=0.11$), while Individually Collaborative method performs better than both ($p<0.01$).

Figure 11.10 shows cross-validation reduction of variance (ROV) values for another IC and different numbers of trials and three pattern estimation methods. For number of trials equal or less than 80, both collaborative ERP resulted in a better ROV than the regular ERP method (paired t -test $p < 0.05$).

11.4 Discussion

We showed how a more predictive ERP pattern for a source may be learned by using Measure Projection Analysis to combine ERP patterns from other subjects estimated at the location of the source. Since the underlying assumptions are the same, our results are likely to generalize to other EEG measures such as ERSP and ITC and also to BCI classifier patterns.

When the number of trials is low, using this collaborative approach can provide significant improvements in estimation of EEG dynamics. In the case of BCIs this could result in better classification accuracy and shorter training/calibration time, as shown with other collaborative BCI learning methods [2, 146, 147]. In EEG analysis this could enable investigating events with lower number of occurrences. However, statistical methods need to be adjusted in order to enable the calculation of significance values for data learned through collaborative filtering. We also showed that in some cases (Figure 11.9), the collaborative approach can result in statistically significant improvements even when a relatively large number of trials (here 118) are available.

Here we only considered using data from other subjects in the same experiment, but the same principles still apply to using data from subjects in *other experiments* during similar cognitive events and states. This offers an exciting prospect of combining data across a large number of partially overlapping experimental paradigms. In [HED chapter number here] we propose a tagging scheme, based on popular cognitive ontologies, that enables the discovery of similar events from other experiments.

The use of convex optimization for collaborative pattern estimation also enables employing various regularization methods, such as L-1, L-2, and trace norm penalties to prevent over-fitting. An alternative method to prevent over-fitting is to

apply subject weights indirectly and through functions that relate differences in subject variables, such as age, gender... to weights:

$$\alpha_i = \sum_{j=1..P} w_j G_j(q_j^{self} - q_j^i) \quad (8)$$

here α_i is the collaborative weight for subject i , P the number of different subject variables of interest (e.g. age, gender, years of experience) q_j and G_j is a ‘transfer’ function of the difference between the subject at hand and subject i in quantity q_j .

G_j may be chosen to be a simple linear function of the difference in the quantity of interest, possibly with some additional weighting:

$$G_j(q_j^{self} - q_j^i) = \beta_j \|(q_j^{self} - q_j^i)\|. \quad (9)$$

Another appropriate form of G_j , for dealing with quantities where some saturation is expected (e.g. age), is the logistic transfer function:

$$G_j(q_j^{self} - q_j^i) = \frac{1}{1 + e^{-\beta_j \|(q_j^{self} - q_j^i)\|}}. \quad (10)$$

In both cases the new set of weight parameters β_i may be learned by cross-validation.

11.5 Acknowledgements

This research was sponsored by the Army Research Laboratory and was accomplished under Cooperative Agreement Number W911NF-10-2-0022, by NIH grant 1R01MH084819-03, and by a gift from The Swartz Foundation (Old Field NY). The views and the conclusions contained in this document are those of the authors and should not be interpreted as representing the official policies, either expressed or implied, of the Army Research Laboratory or the U.S Government. The U.S Government is authorized to reproduce and distribute reprints for Government purposes notwithstanding any copyright notation herein.

11.6 Figures

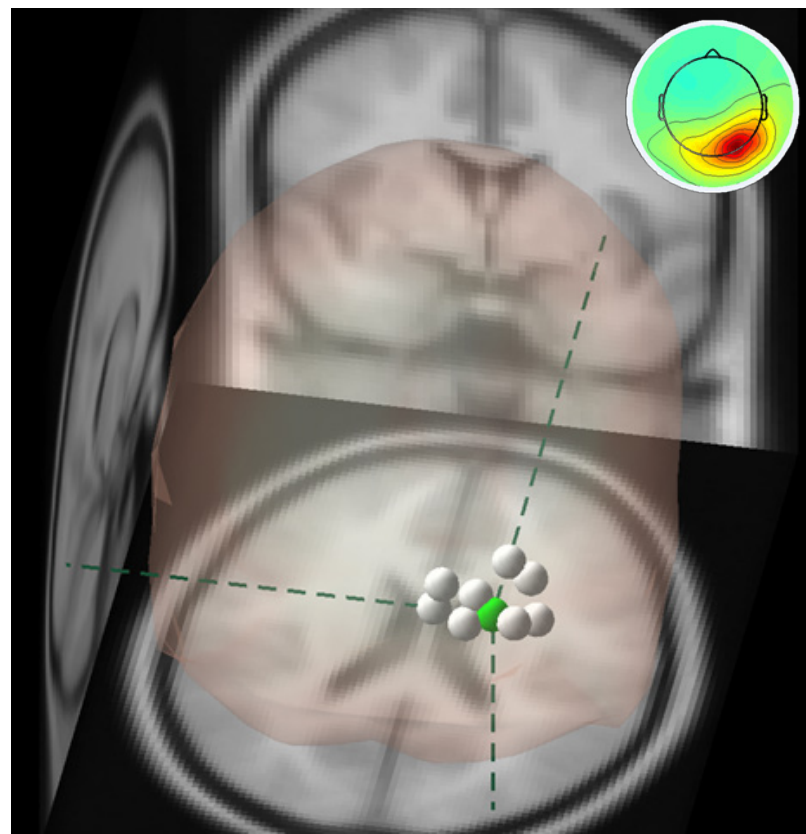


Figure 11.1. sample IC and its equivalent dipole in the right occipital region.

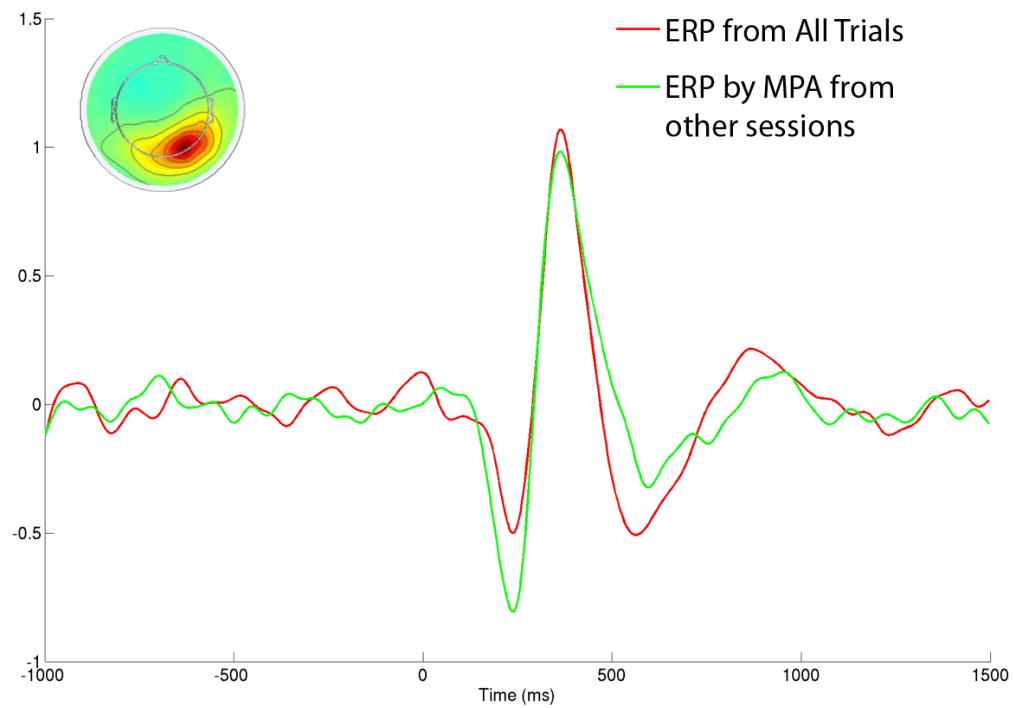


Figure 11.2. Optimally low-passed ERP of the sample IC in red and the projected ERP from all other study sessions, scaled to equal L-2 norm, in green.

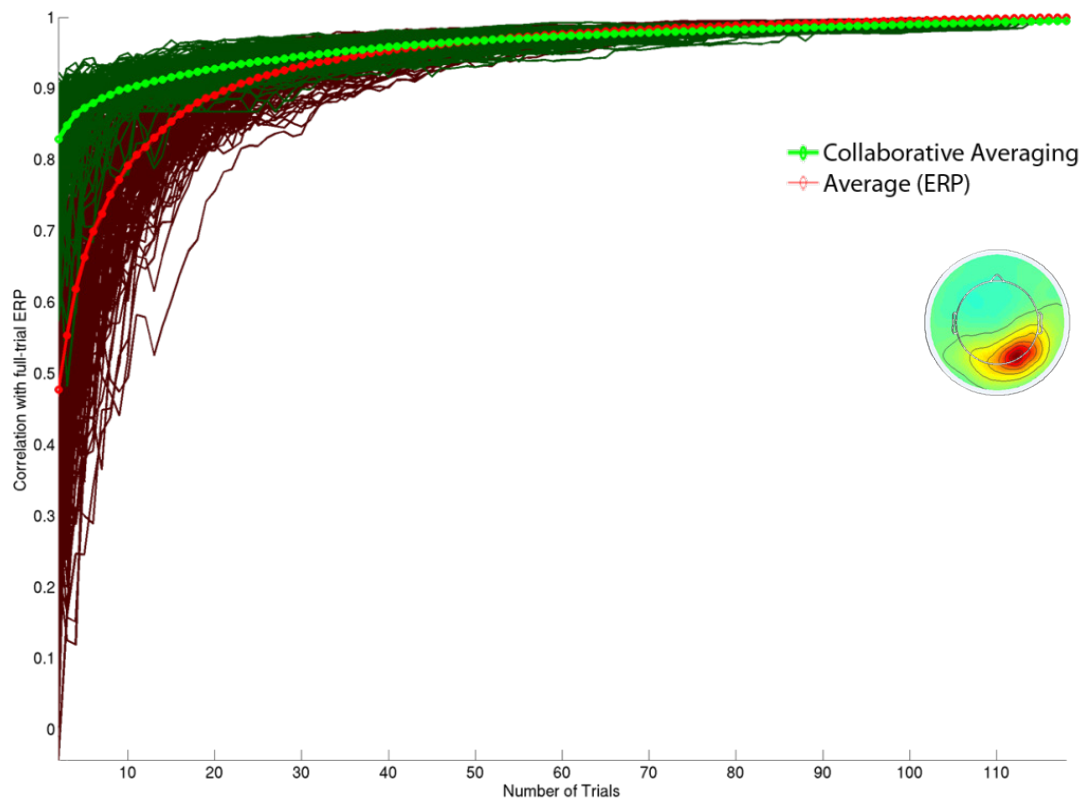


Figure 11.3. Correlations between the average ERP from all (118) trials and ERPs calculated by averaging (red) and collaborative averaging (green) using the average ERPs of other sessions. Error bars showing 1 std. are plotted but are too small to see. Dark traces show results for sample iterations.

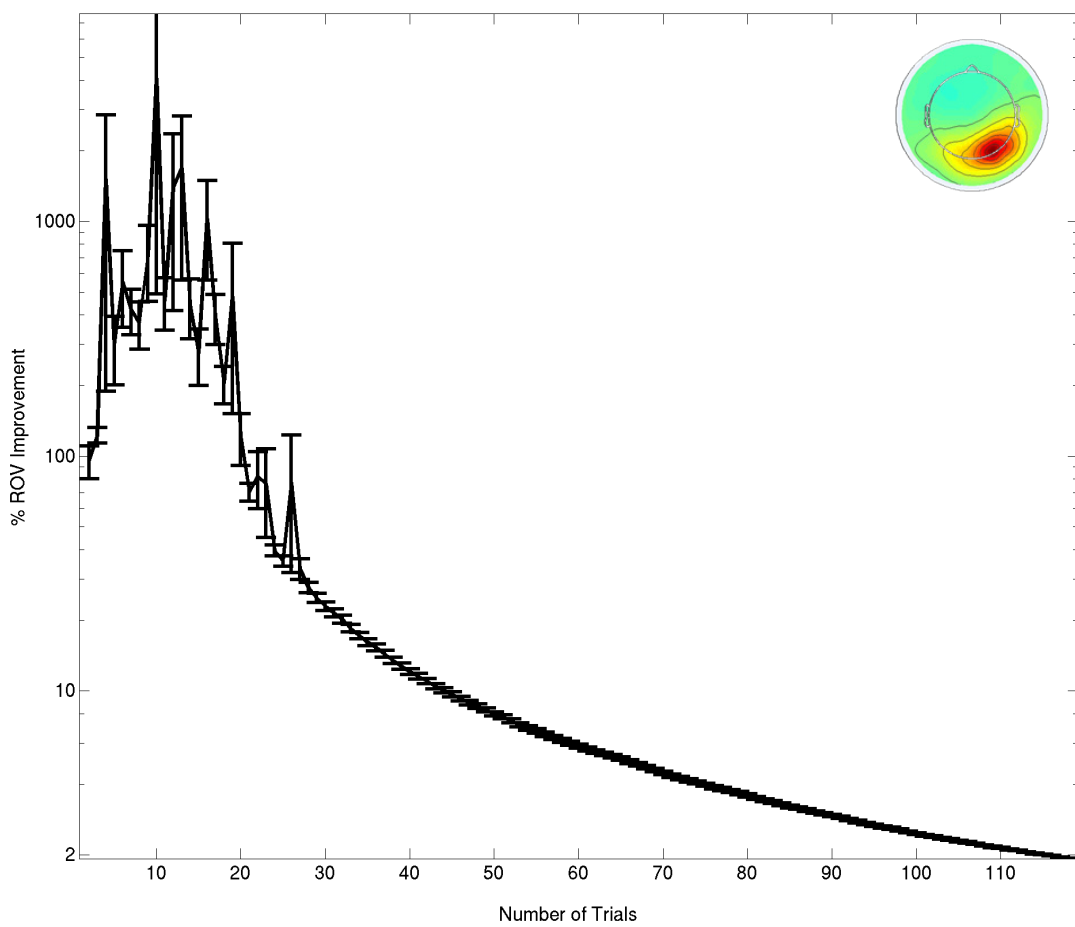


Figure 11.4. Percent ROV improvement using collaborative averaging compared to regular averaging for different number of trials.

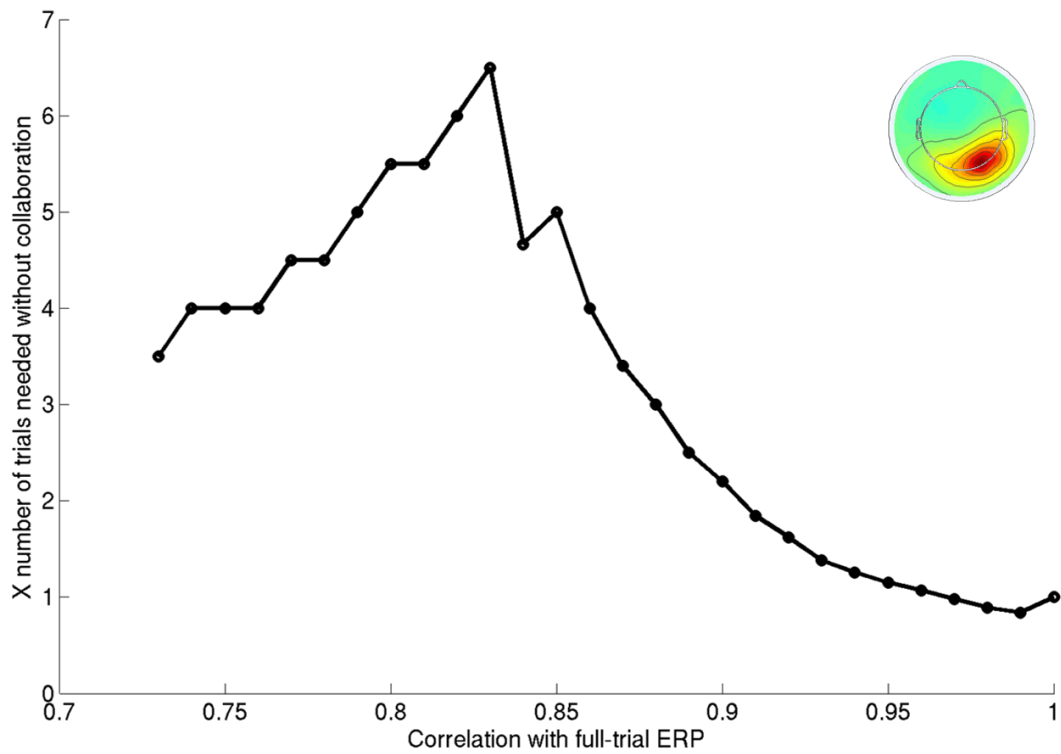


Figure 11.5. Shows how many more trials, compared to using collaborative averaging, are needed to achieve the same level of correlation with the ERP calculated from all 118 trials.

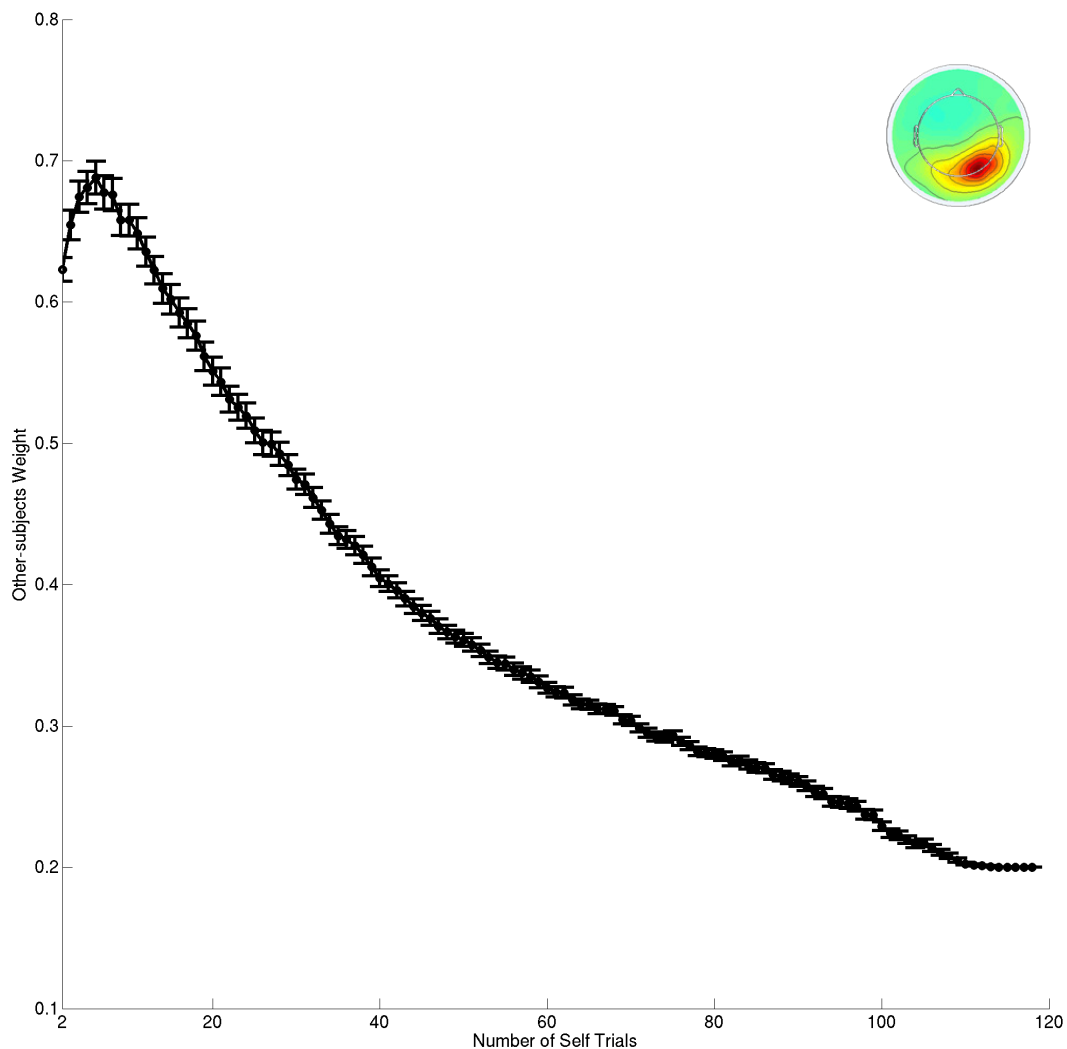


Figure 11.6. Optimal weight for the average of other subjects, obtained by collaborative averaging for different number of trials.

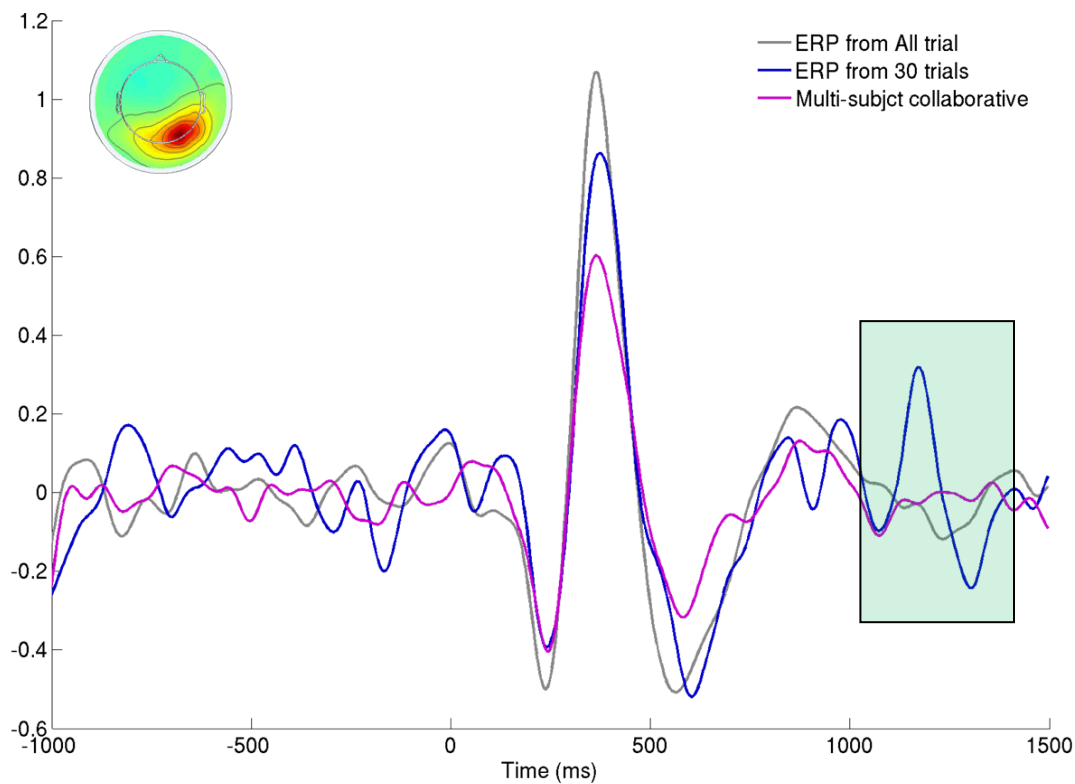


Figure 11.7. Target ERP of the select IC from all trials (gray), the first 30 trials (blue) and collaborative averaging using the first 30 trials of the subject and individually weighted patterns from other subjects. The green rectangle highlights a period where the ERP from 30 trials contains extraneous peaks that are corrected when using collaborative averaging.

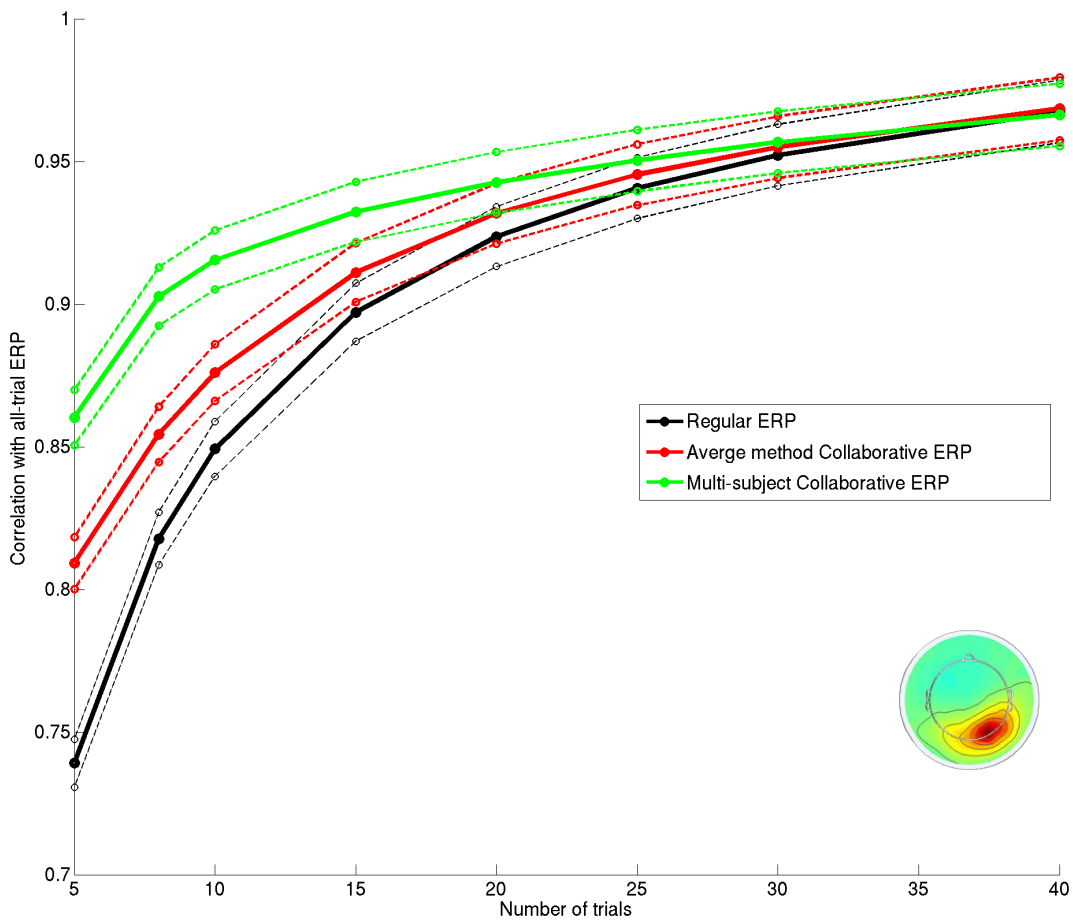


Figure 11.8. Correlations between the average ERP from all (118) trials and ERPs from a subset of trials calculated by regular averaging (black), collaborative averaging using the average ERPs of other sessions (red) and collaborative averaging with each subject weighted separately (green). Statistics are for 7800 random permutations (without substitution). Dotted lines show 1 standard deviation after.

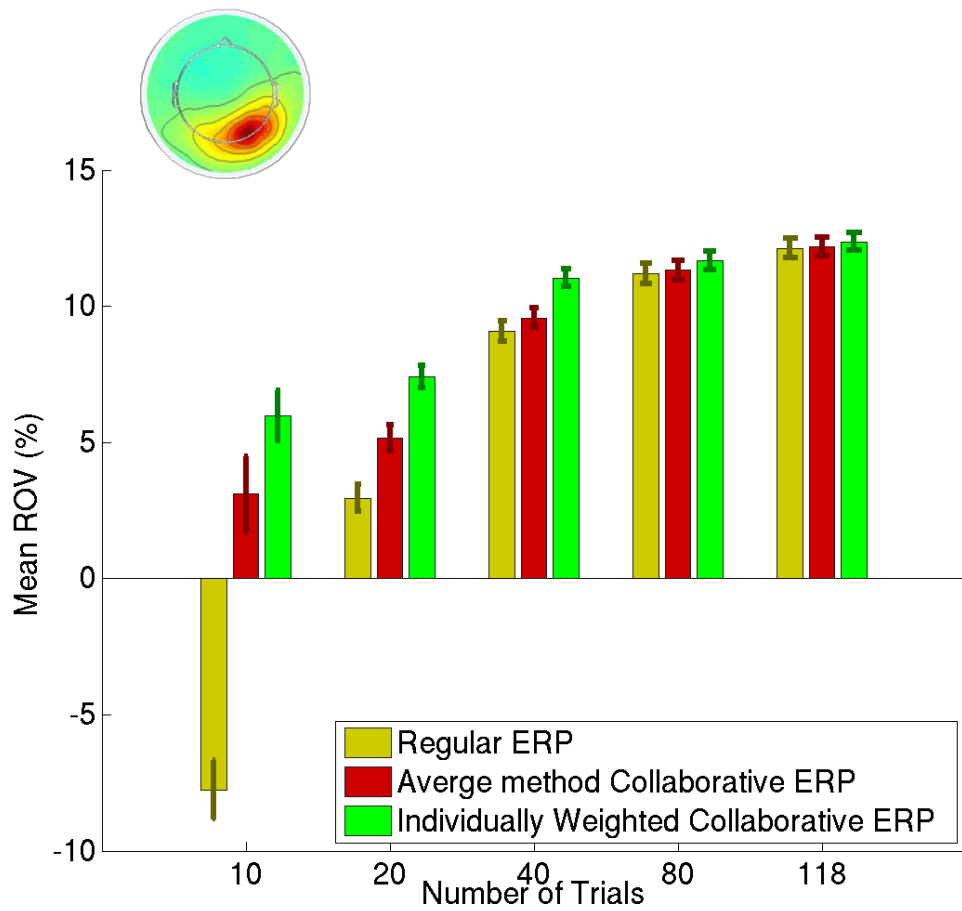


Figure 11.9. Cross-validation reduction of variance (ROV) values for different numbers of trials and different pattern estimation methods. For number of trials less than 118, the individually weighted collaborative ERP resulted in a better ROV than the Average collaborative ERP method, and both did better than regular ERP method (paired t -test $p < 0.01$). For 11 trials, Average collaborative ERP method performs similarly to the regular ERP ($p = 0.11$), while Individually Collaborative method performs better than both ($p < 0.01$).

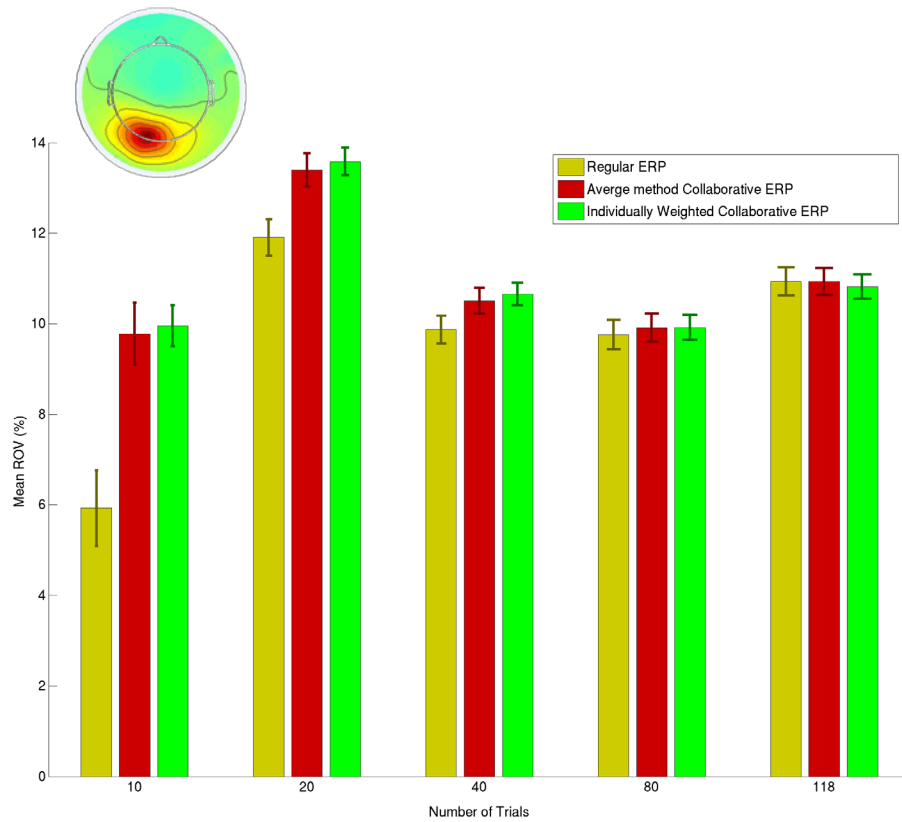


Figure 11.10. Cross-validation reduction of variance (ROV) values for different numbers of trials and different pattern estimation methods. For number of trials equal or less than 80, both collaborative ERP resulted in a better ROV than the regular ERP method (paired t -test $p < 0.05$).

Chapter 12

Comparison of Averaging and Regression Techniques for Estimating Event Related Potentials

12.1 Abstract

The traditional method of estimating an Event Related Potential (ERP) is to take the average of signal epochs time locked to a set of similar experimental events. This averaging method is useful as long as the experimental procedure can sufficiently isolate the brain or non-brain process of interest. However, if responses from multiple cognitive processes, time locked to multiple classes of closely spaced events, overlap in time with varying inter-event intervals, averaging will most likely fail to identify the individual response time courses. For this situation, we study estimation of responses to all recorded events in an experiment by a single model using standard linear regression (the rERP technique). Applied to data collected during a Rapid Serial Visual Presentation (RSVP) task, our analysis shows: (1) The rERP technique accounts for more variance in the data than averaging when individual event responses

are highly overlapping; (2) the variance accounted for by the estimates is concentrated into a fewer ICA components than raw EEG channel signals.

12.2 Introduction

The Event Related Potential (ERP) averaging method for electroencephalographic (EEG) data [148] is one way to gain insight into how specific cognitive processes are related to brain electrical activity. Traditionally, the way of increasing the signal to noise ratio (SNR) of an ERP estimate is to average epochs time-locked to a stimulus class of interest. This technique places severe restrictions on the experimental protocol: only a small number of stimulus categories can be used, stimulus events must be well separated in time and all other cognitive processes must be held constant. Violating the latter conditions will cause the ERP to be estimated sub-optimally. Here we study using multiple regression as a way to overcome this limitation, extending the work of N. J. Smith [149]. In [150], Hinrichs et al. have suggested a highly similar approach for deconvolving fMRI responses. [151, 152] have suggested using separate regression models for each individual latency, such as massive univariate general linear analyses. [153] has proposed using Generalized Additive Models (GAMs). In [149], Smith offers a unified conceptual framework for ERP regression and shows how these different techniques relate to averaging for the purposes of ERP estimation.

We continue this discussion by applying linear regression and averaging to a real EEG dataset and exhaustively comparing the results of the two approaches. The goal is to make clear that in practice, regression can offer a significant performance increase compared to averaging. Indeed, as EEG experiments become more sophisticated, with many (intermittent or continuous) processes being monitored simultaneously, averaging ceases to be an effective option. Independent Component Analysis (ICA) [154] has become a popular and often effective method for separating EEG sources [21, 155]. Thus, we also compared how regression and averaging compare with one another in both ICA component activations (ICs) and EEG channels.

12.3 Background

12.3.1 A Problem With Averaging

If events in an experiment occur sufficiently close in time to one another, the EEG brain responses to these events will overlap. Taking an average of these event time-locked epochs will produce a summed and/or blurred ERP estimate.

12.3.2 Data

The experiment is fully described in [156]. 127-channel EEG data were collected during a Rapid Serial Visual Presentation (RSVP) task involving satellite picture presentation. The subject was shown bursts of 49 satellite images in 4.1 seconds (12/s.). In 60% of the bursts, a (flying airplane) target feature was randomly

added to one image. At each burst end, the participant indicated by button press whether or not that burst contained the target feature. During training, they were told whether they were correct or not.

There were nine recorded event types in the experiment, listed by (*event-code*) *event-description*: (1) non-target stimulus, (2) target stimulus, (4) “no targets” button press, (5) “one target” button press, (6) trial block start, (16) trial start, (32) “correct” feedback given, (64) “incorrect” feedback shown, and (129) image burst start.

12.4 Methods

We calculated ERP estimates for a seven subject/12 session study across nine different events using averaging and linear regression with Ordinary Least Squares (OLS). This analysis was repeated for all 127 channels of EEG data and again for all 127 ICs, derived by extended Infomax ICA [157]. We used five-fold cross-validation to obtain our performance figures: the ERPs were calculated with training data and validated on test data [158].

12.4.1 Preprocessing

First, we addressed the issue of outliers and artifacts. We identified outlier data portions by two methods: Low Probability and Mutual Information Reduction (MIR). For the probability method we first whitened the data and performed a rank transform to obtain a two-tailed significance value for each sample. We then found

200 ms windows where the average log significance over all the sphered dimensions and time-frames was higher than 2.1 and marked them as outliers. For the MIR method, we first calculated the mutual information reduction index [28] in 2s windows with 80% overlap using the sphering matrix. Then we found regions with MIR Z score of lower than -1.5 and marked them as outliers. We discarded events occurring during or near outlier periods. Out of 23,477 events, 1,654 were identified as contaminated and discarded. The data were highpass filtered (-3 dB at 1 Hz) to reduce DC bias.

All ERPs were estimated using the same maximum length, heuristically set for this analysis at 1 second (256 samples), from -125 ms to 875 ms around each event. This defined 256 variables per event. For nine event types, each regression or averaging model thus contained 2304 ERP parameters for each EEG channel or IC.

12.4.2 Regression Framework

First we looked at the case of only one event type, E_I , producing an ERP response β_I . The observed signal (IC or channel) y is then a linear transformation of β_I plus a Gaussian noise term, $\varepsilon \sim N(\theta, \sigma I)$.

$$\beta_I = [\beta_{I1} \ \beta_{I2} \dots \ \beta_{IN}]^T \quad (1)$$

$$y = A_I \beta_I + \varepsilon \quad (2)$$

We position y and β_I as a column vectors of length M (the length of the data) and N ($= 256$) respectively. A_I is the $M \times N$ matrix of *predictors*, x_{mn} , constructed from latency recordings. x_{mn} has a value of 1 when the n^{th} sample of ERP β_I is predicted to occur at latency m .

If we want to estimate the response to more than one event type, we stack the β_n in a column vector, and concatenate their corresponding A_n along the second dimension

$$A = [A_1 \ A_2 \ \dots \ A_n] \quad (3)$$

$$\beta = [(\beta_1)^T \ (\beta_2)^T \ \dots \ (\beta_n)^T]^T \quad (4)$$

and subsequently

$$y = A\beta + \varepsilon \quad (5)$$

with least squares solution

$$\beta_{\text{reg}} = (A^T A)^{-1} A^T y \approx \beta \quad (6)$$

12.4.3 Performance Metrics

We subtract the ERP estimates from the original signal to obtain a residual noise signal. The difference between the variance (power) of the original signal and the variance of the noise signal represents the variance accounted for by that ERP. We

use this Reduction of Variance (ROV), as our metric, with higher ROV corresponding to better performance.

$$ROV \equiv (P_{Data} - P_{Noise}) \quad (7)$$

The reason for using ROV instead of Signal to Noise Ratio (SNR)

$$SNR \equiv P_{Signal} / P_{Noise} \quad (8)$$

is that we aren't especially interested in maximizing the size of the ERP estimate (the "signal" in this case). ROV measures to what extent the estimate accounts for overall variance in the data.

For each event type in the experiment, we computed the ROV for averaging by extracting each epoch (y_i) and subtracting the averaged ERP estimate β_{av} from it.

$$\varepsilon^{av}_i = y_i - \beta_{av} \quad (9)$$

$$ROV_{av} = \langle var[y_i] - var[\varepsilon^{av}_i] \rangle \quad (10)$$

where the mean is taken across all the events of that type. For regression, we computed a signal estimate

$$y^{reg} = \mathbf{A}\beta_{reg} \quad (11)$$

then, extracted each epoch from the estimated signal (y^{reg}_i) and the original signal (y_i).

$$\varepsilon^{reg}_i = y_i - \bar{y}^{reg}_i \quad (12)$$

$$ROV_{reg} = \langle var[y_i] - var[\varepsilon^{reg}_i] \rangle \quad (13)$$

We use normalized estimates from (14) to identify which channels/ICs have the highest ROV percentage.

$$ROV' = ROV / var[y_i] \quad (14)$$

ROV' of the top 20 channels/ICs from each dataset are averaged to obtain the final estimates for each event type. For significance testing we applied a two-sample t -test ($p < 0.01$) to the cross-validation folds of all twelve datasets.

12.5 Results

12.5.1 ERP Estimates (Figure 2)

Due to the 83-ms stimulus onset asynchrony, simple average responses to non-target type 1 events had significant confound from overlapping responses. As shown in *Figure 2*, the averaged estimate does not reflect the ERP associated with a single non-target frame (*Figure 1* shows graphically how this occurs). In this case, regression recovered a plausible visual response to each non-target stimulus event. Event type 6 did not usually occur near any other experiment events. Here, as expected, regression and averaging gave similar results.

12.5.2 Performance as Measured by ROV (Figure 3)

Event type 1 (Figure 3, top panel) shows the most significant difference between the two methods for both ICs and channels. For the most frequent event type 1, regression has the advantage for both channel and IC measures. Compare the difference in the regression versus the average ERP (SSR) estimates in Figure 2 (top panel). The averaging method clearly did not estimate ERP for this event type. For the other event types, which are less affected by overlap, the two methods performed similarly.

(1) Comparing IC and channel results, we notice a peak of ROV in the first 2-3 ICs for each stimulus type. Since ICs are thought to typically represent the synchronous field activity across a single cortical patch [159], broadly projected to the scalp electrodes by volume conduction, we may expect the regression result to show higher ROV for a smaller number of ICs than scalp channels. The ROV for channels is indeed distributed across a larger number of channels. This is expected, since EEG signals at scalp electrodes that are physically close are highly correlated [155].

(2) Normalized ROV is quite low across the board: no more than 12% of the variance in any channel or component signal is accounted for by either method, and usually much less. This is consistent with the frequent observation that most EEG signal variance is not produced by time and phase locked responses to external events.

12.6 Discussion

As demonstrated in [149], OLS regression can be thought of as a natural extension of ERP averaging that can be applied in a larger range of experimental conditions. Algebraically, OLS reduces to averaging when there is no overlap between experimental responses (e.g. *Figure 2*, bottom panel).

Our ROV analysis showed that regression is capable of explaining more variance in experimental data than averaging. This overall comparison is limited in the sense that it cannot tell us whether a certain *portion* of an ERP waveform is best represented by either method. In other words, whether or not a specific peak in a response is better estimated by averaging or regression cannot be decided from this analysis alone. The potential benefit of regression is only clear when considering an ERP as a whole and should depend on its degree of overlap with responses to other experimental events.

Possible extensions: Since OLS is the simplest estimator beyond averaging, the predictive performance of our model might be expected to increase by utilizing more modern techniques. A problem with estimating EEG parameters by OLS is that artifacts can drastically affect its L2-norm error function. The Least Absolute Deviations (LAD) [160] technique instead relies on an L1-norm error function and thereby may provide a more robust estimator. The performance of the model is also highly sensitive to its number of parameters. Introducing regularization on the ERP parameters would be a reasonable way to control for this effect and discourage overfitting.

12.7 Conclusion

When overlapping evoked responses are produced by experimental events that are closely spaced in time, multiple stimulus events may contribute to any given average event-related potential (ERP) feature. Some additional assumption is necessary to properly segregate this variance. The regression (rERP) technique assumes that ERPs to distinct events sum linearly. In all other ways, the rERP and ERP measures are identical. Yet, as we show here, the rERP approach can account for more total data variance. This shows that the rERP assumption is a viable one for analyzing data from rich and complex EEG data-sets.

Chapter 12, in full, is a reprint of the material as it appears in M. D. Burns, N. Bigdely-Shamlo, N. J. Smith, K. Kreutz-Delgado, S. Makeig, "Comparison of averaging and regression techniques for estimating Event Related Potentials," Engineering in Medicine and Biology Society (EMBC), 2013 35th Annual International Conference of the IEEE , vol., no., pp.1680,1683, 3-7 July 2013 doi: 10.1109/EMBC.2013.6609841. The dissertation author was the secondary investigator and author of this paper.

12.8 Figures

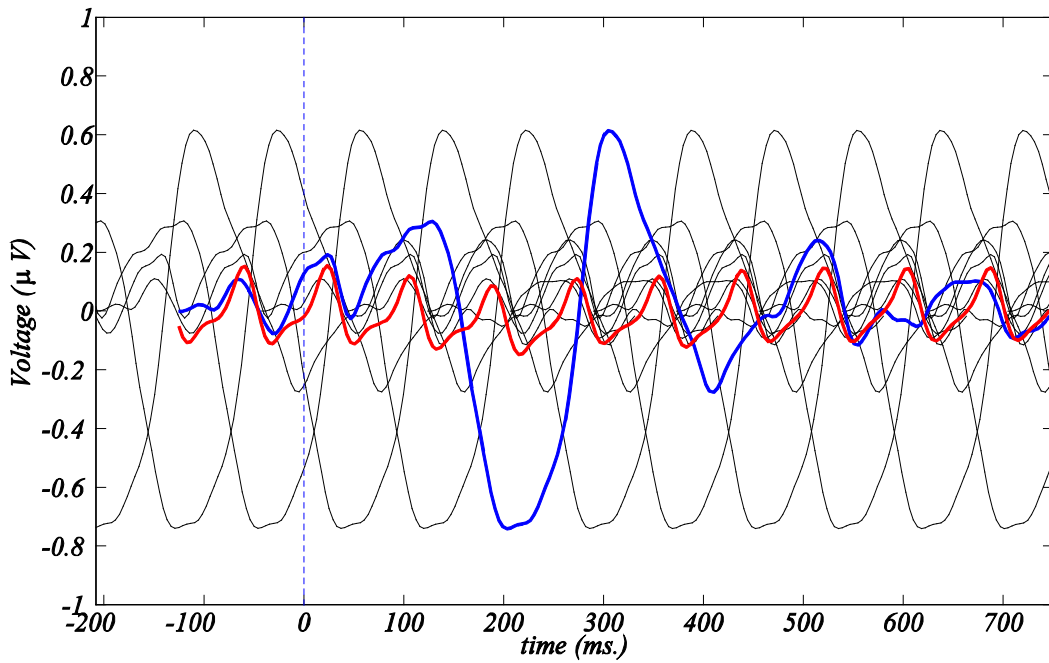


Figure 12.1. Illustrating how averaging can produce an incorrect ERP estimate in the presence of overlapping activity due to closely spaced cognitive events. The latency window is a typical EEG epoch in a 12/s rapid serial visual presentation (RSVP) experiment. An ERP of interest (blue), is produced following each visual stimulus every 83 ms (black). These ERPs combine additively, giving a misleading (red) averaged Steady State Response (SSR) ERP estimate. Regression considers all the experimental events in a single additive model, taking into account this overlap.

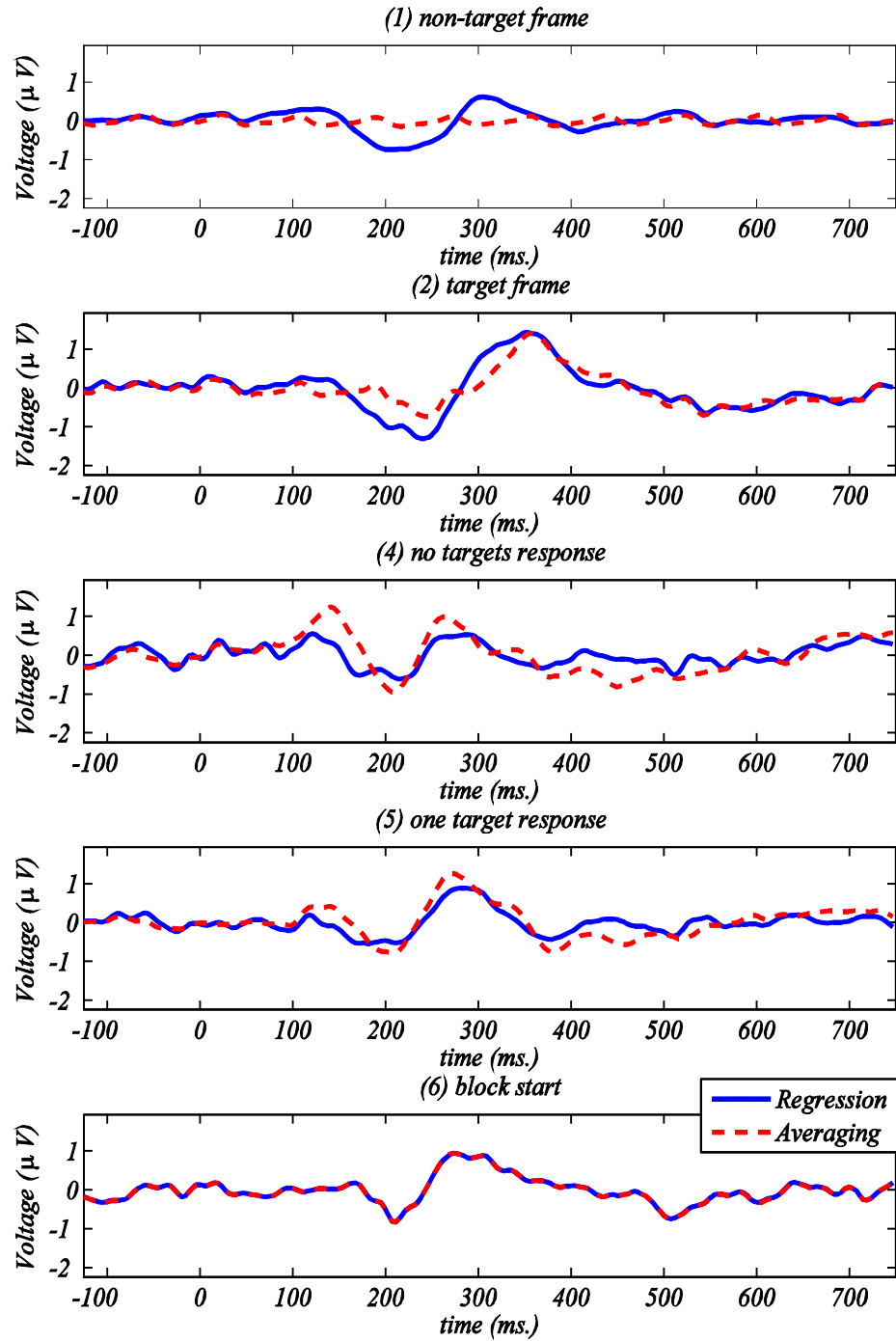


Figure 12.2. Comparison of ERP estimates by averaging (red) and regression (blue) for five event types. ROV was statistically higher for regression in event type 1. Estimates are for a lateral occipital IC.

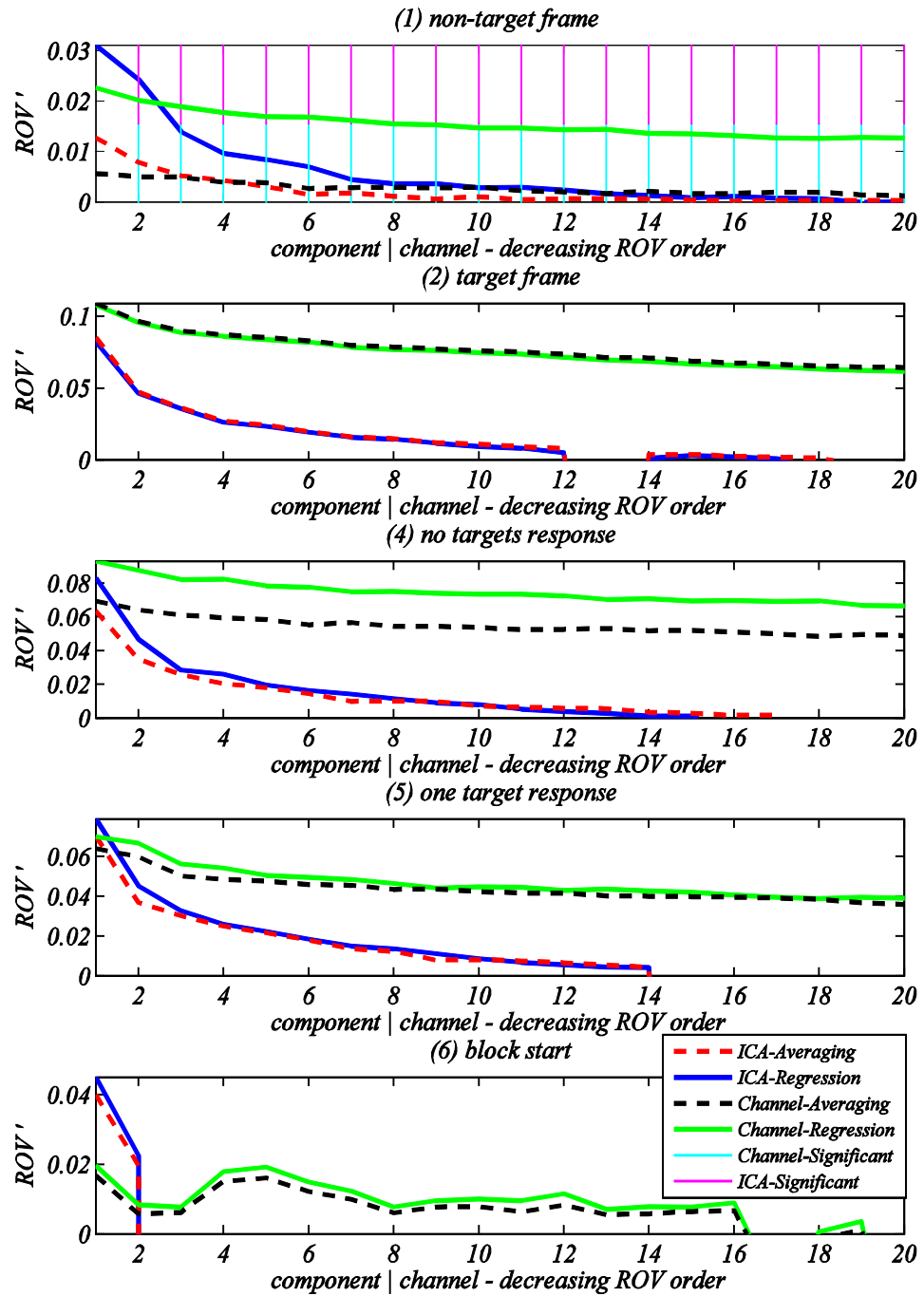


Figure 12.3. Comparison between averaging and regression ROV for EEG channels and ICA components. The components and channels are sorted and plotted in normalized ROV form.

Chapter 13 Hierarchical Event

Descriptor (HED) Tags for Analysis of

Event-Related EEG Studies

13.1 Abstract

Data from well-designed EEG experiments should find uses beyond initial reports, even when study authors cannot anticipate how it may contribute to future analyses. Several ontologies have been proposed for describing events in cognitive experiments to make data available for re-use and meta-analysis, but none are widely used. One reason for this is that the tools needed to make use of these ontologies are complex, placing a significant burden on experimenters while not providing any immediate reward for their efforts. Here we propose an extensible, user-friendly experiment event tagging method built on the BrainMap and CogPO ontologies and similar to the object tagging style used extensively on the Web. Hierarchical Event Descriptor (HED) tags, a hierarchy of standard and extended descriptors for EEG experimental events, provide a uniform human- and machine-readable interface facilitating use of an underlying event-description ontology during EEG data acquisition, analysis, and sharing. HED tags may be used to mark and annotate all known events in an experimental session. We describe an available real-time EEG

experiment control and recording system that uses HED tags for annotation, transmission and storage of detailed information about events in EEG experiments.

13.2 Introduction

The current period in the history of science has been called the era of Big Data collection and analysis. Annotated data can be highly useful to meta-analysis. Hence there have been several efforts to standardize terminologies used to describe cognitive paradigms by developing formal database ontologies (e.g., Nemo [161], BrainMap [13], CogPO [162], and NeroLex [163]), but currently none of these is often used to describe EEG events in publications. We believe key hindrances are:

- *Complexity of appearance and difficulty of use:* Although formal ontologies developed in the OWL format [164] are elegant and can be readily processed by computers, their apparent complexity discourages human casual use. Tools to interact with and make use of such ontologies are complicated, and using them may require learning a large number of detailed concepts, standards, and file formats.
- *Lack of immediate reward for use:* Most neurophysiological database tools do not provide clear and immediate benefits to researchers who perform the work required to donate their data to the resource – i.e., they give little or no tangible reward to make researchers feel it worthwhile to undertake the work of annotating and uploading data for (their own and/or others') further use.

13.3 Hierarchical Event Descriptors

To address problem (1) above, we have adopted a popular object tagging style used extensively on the Web (for example, for image tags on Flickr.com and video tags on YouTube.com). *Hierarchical Event Descriptor (HED)* tags are a hierarchy of standard and extended descriptors for EEG experiment events. The HED system includes a base set of hierarchically organized descriptor tags, in part adapted from the BrainMap and CogPO ontologies [13, 162], that can be used to describe many types of EEG experiment events in a uniform (though easily extensible) human- and machine-readable manner. The main contribution of the HED tagging system is to offer a user-friendly interface for use of the underlying event description ontology in EEG acquisition and analysis workflows.

Another goal of HED tagging is to support EEG data analysis and meta-analysis by enabling automated discovery of appropriate statistical designs in complex EEG studies including many types of known events. Using HED tags could provide an immediate reward to researchers by simplifying and automating their analysis workflow, thus addressing (2) above.

The hierarchical structure of the HED tags makes it easy to search through variations of the same type of event across studies (enabling EEG data meta-analyses), while preserving the unique details of each event type. For example, an event marking the presentation of a visual feedback stimulus in EEG Study A may present a red

circle to the participant on a black screen background, while in Study B the visual feedback stimulus is a blue rectangle on a white screen background. In HED syntax, these event types can be described by two HED strings (collections of comma-separated HED tags) as follows:

In Study A:

- Stimulus/Feedback,
- Stimulus/Visual/Uniform Color/Red,
- Stimulus/Visual/Shape/Ellipse/Circle/Height/2-deg,
- Stimulus/Visual/Shape/Ellipse/Circle/Width/2-deg,
- Stimulus/Visual/Background/Uniform Color/Black

In Study B:

- Stimulus/Feedback,
- Stimulus/Visual/ Uniform Color/Blue,
- Stimulus/Visual/Shape/Rectangle/Height/2-deg,
- Stimulus/Visual/Shape/Rectangle/Width/3-deg,
- Stimulus/Visual/Background/Uniform Color/White

These descriptors explicitly capture both salient commonalities across and differences between the two event types. If the feedback events were accompanied by an auditory beep (500 Hz, 25-dB), the following tags might be added:

- Stimulus/Auditory/Loudness/25-dB,
- Stimulus/Auditory/Tone/500-Hz,
- Stimulus/Auditory/Tone/Ramp Up/10-ms,
- Stimulus/Auditory/Tone/Ramp Down/10-ms

While higher levels of the HED hierarchy are intended to be fixed (i.e., revised infrequently with discrete versioning based on community feedback), lower levels may be extended without restriction to describe any event type to any desired level of

detail. For example, the tag *Stimulus/Visual/Shape/Ellipse/Circle* may be extended by adding */Filled* at the end to provide more information about the circle.

In addition to describing delivered stimuli, HED tags can also describe subject actions (e.g., button presses, swipes, saccades, etc.), subject and task states (e.g., drowsy, attend visual, etc.), and combinations of these (e.g., feedback tones produced in immediate response to button presses by a drowsy subject). Since HED tags can be easily interpreted by computer applications, HED tagging can facilitate search and inference of event-related EEG dynamics across multiple studies, when and where available. Also, HED tags organize events from a study into a logical hierarchy so they can be more easily analyzed. For example, several event subtypes may be aggregated into a more general event type that can then be compared to other event types.

13.3.1 Example Tagging for RSVP

Here we explain the use of HED tags to describe events in a sample Rapid Serial Visual Presentation (RSVP) study of target recognition in satellite imagery [48] using HED 1.31 specification available in Appendix I (in section 13.8, for the latest HED specification see [165]). Each recording session of this experiment comprised of 504 4.9-s image bursts of 49 oval image clips from a large satellite image of London presented at a rate of 12/s. Some (60%) of these bursts contained one image in which a target white airplane shape was introduced at a random position and orientation. Following each burst, subjects were asked to press one of two buttons to indicate

whether or not they had detected a target airplane in any burst image clip. Figure 13.1 shows a time line of each RSVP burst. For further details see [48].

Now we use HED tags to form HED strings describing events (from left to right) in Figure 13.1. Display of a silver fixation cross on a gray background:

- Stimulus/Visual/Shape/Cross,
- Stimulus/Visual/Uniform Color/Silver,
- Stimulus/Visual/Achromatic,
- Stimulus/Visual/Screen Location/Center,
- Stimulus/Visual/Background/Uniform Color/Gray,
- Stimulus/Visual/Fixation Point,
- Stimulus/Instruction/Fixate

Non-Target image presentation event:

- Stimulus/Visual/Achromatic,
- Stimulus/Expected/Non-Target

Target image presentation event:

- Stimulus/Visual/Achromatic,
- Stimulus/Target

Presentation of visual cue asking the participant whether (s)he has detected a target airplane image ('0 or 1?'):

- Stimulus/Visual/Language,
- Stimulus/Instruction/Count,
- Stimulus/Visual/Uniform Color/White,
- Stimulus/Visual/Achromatic,
- Stimulus/Visual/Background/Uniform Color/Black

Participant answers the question by pressing one of two buttons (here, to indicate a response of '1') with his/her right hand:

- Response/Button Press,
- Response/Hand/Right Hand/Index Finger,
- Response/Count/1

Presentation of visual feedback ('Correct' or 'Incorrect') cue in training trials:

Stimulus/Visual/Language/Word/Noun,
 Stimulus/Visual/Language/Latin/English,
 Stimulus/Feedback/Correct, (or /Incorrect)
 Stimulus/Visual/Uniform Color/White,
 Stimulus/Visual/Achromatic,
 Stimulus/Visual/Background/Uniform Color/Black

Finally, we specify the paradigm as:

Paradigm/Rapid Serial Visual Presentation/Visual Target Detection Paradigm,
 Paradigm/Oddball discrimination paradigm/Visual oddball paradigm

13.3.2 HED Grammar

HED tags consist of a series of identifiers separated by the forward slash '/' character. A HED identifier may contain any characters except the characters '/' (forward slash), ',' (comma), ';' (semicolon), and '\"' (quotes). To use these reserved characters in a HED identifier, the HED identifier may be wrapped in a pair of double-quote ("") characters. To use the quote character inside a quoted HED, use '\"' (backslash double-quote).

Sometimes an event may be associated with more than one stimulus or response – for example when a red circle is presented on screen left and, at the same moment a blue rectangle is displayed on screen right. In such cases, parentheses can be used to group together HED tags associated with each stimulus. In this example:

(Stimulus/Visual/Shape/Ellipse/Circle, Stimulus/Visual/Uniform Color/Red,
 Stimulus/Visual/Screen Location/Left),

 (Stimulus/Visual/Shape/Ellipse/Rectangle, Stimulus/Visual/Uniform
 Color/Blue, Stimulus/Visual/Screen Location/Right)

13.4 HED Tools and Resources

MATLAB (The Mathworks, Inc.) tools for basic HED tag operations, such as validation, auto-completion and comparisons between pairs of HED tags and strings have been developed and are available at [165].

13.4.1 Community HED Tagging

Community tagging tools (described in a parallel submission [166]) have been developed that allow users to tag events based on their types and other attributes. These tools allow users to create HED tag overlays that can be easily edited to allow retagging. The tools include a HED database with usage counts, so that a group of users can collaborate to develop new tags. These tools can be called from the MATLAB command line or from the EEGLAB [21] menu.

13.4.2 Real-time HED Tagging of Experimental Conditions

Most EEG acquisition hardware only provides a single time series channel for recording the (integer-coded) type of experimental event, associated with the concurrent EEG data frame. This limits the number of distinct events that can be recorded and makes it necessary to associate the data with a table that maps these ‘event type’ indices to their human-readable descriptions.

However, a current trend in cognitive neuroscience is towards performing more naturalistic and less constrained experiments, for example experiments in which

participants play games in ambulatory settings. Because of the multiplicative interactions of behavioral and contextual dimensions of interest in these experiments, the number of potential event types can be quite large and can hardly be captured by a one-dimensional (often 1- or 2-byte) event number channel. Even when it is possible to sacrifice encoding experiment details and only use a single channel for recording this information, the resulting mapping table could become quite large and difficult to maintain and use for statistical analyses.

An alternative approach is for the experiment control and data recording software to use HED tags to fully encode all aspects of interest for each instance of an experimental event, directly sending the resulting HED strings, in real time, to the data acquisition system. These strings will then be recorded synchronous to the recorded EEG data.

We (C. Kothe *et al.*) have developed, tested, and now use in practice a real-time interactive experiment control and data recording system that implements this approach using HED strings for event description. The system consists of the Simulation and Neuroscience Application Platform (SNAP) for real-time experimental control [167], the lab streaming layer (LSL) framework for synchronous multimodal data transfer [168], and the Extensible Data Format (XDF) file format for data storage [169].

SNAP is a python-based experiment control framework that can send HED strings to LSL, a (C++-coded) real-time data collection and distribution system, to be

recorded with acquired EEG data (in our laboratory from standard Biosemi EEG hardware) in an XDF file format capable of synchronously recording multi-channel, multi-stream data that is heterogeneous in both type and sampling rate. Figure 13.2 Figure 2 shows the links between components of this system.

13.4.3 Extended Use of HED Tags for Study Meta-Data

We have also developed a companion XML-based specification, called the *EEG Study Schema* (ESS) to hold all the information necessary to analyze an EEG study, e.g. subject gender, handedness, age and group associations, task and paradigm description, etc. in a format that is both machine and human readable. To achieve this goal, ESS relies on HED descriptions of experimental events and tasks that are embedded in an ESS XML document. When ESS XML files are viewed in current web browsers (e.g., FireFox) they are automatically formatted as readable reports using a provided XSLT style sheet. For more information about ESS see [170].

Using the ESS/HED system we have documented 18 laboratory studies comprising 388 data recording sessions. Five of these studies are publicly available at our online EEG study repository HeadIT [171]. Figure 13.3 shows a hierarchical representation of HED-tagged event types from all 18 studies (most event types typically being in common to all study sessions). Values in parentheses show the number of unique event types from all studies that match the HED tag associated with each level of the hierarchy.

13.5 Discussion

A future direction is to make formal connections between HED tags and ontological terms defined in Neurolex [163]. Another extension is to classify the type of relationship between HED child nodes and their parents ('is-a' for event subtypes such as Ellipse/Circle, versus 'has-a' for properties like Shape/Color). This should enable more complete automated statistical analysis of brain dynamics associated with HED-specified cognitive events and states. Finally, tools that immediately reward researchers for annotating and uploading their data, by returning useful information to them about it, may generate the researcher interest needed to amass a sufficient quantity of data to allow large scale EEG data mining for a range of purposes.

13.6 Acknowledgements

This research was sponsored by the Army Research Laboratory and was accomplished under Cooperative Agreement Number W911NF-10-2-0022, by NIH grant 1R01MH084819-03, and by a gift from The Swartz Foundation (Old Field NY). The views and the conclusions contained in this document are those of the authors and should not be interpreted as representing the official policies, either expressed or implied, of the Army Research Laboratory or the U.S Government. The U.S Government is authorized to reproduce and distribute reprints for Government purposes notwithstanding any copyright notation herein.

Chapter 13, in full, is a reprint of the material as has been submitted for publication and will appear in N. Bigdely-Shamlo, K. Kreutz-Delgado, K. Robbins, M. Miyakoshi, M. Westerfield, T. Bel-Bahar, C. Kothe, J. Hsi, and S. Makeig, "Hierarchical Event Descriptor (HED) Tags for Analysis of Event-Related EEG Studies," IEEE GlobalSIP, Austin, TX, 2013. The dissertation author was the primary investigator and author of this paper.

13.7 Figures

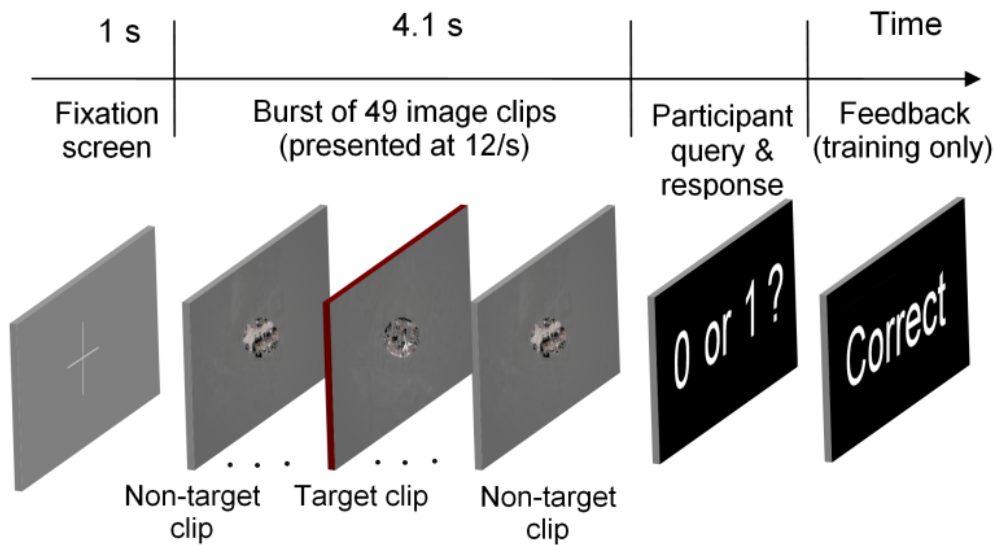


Figure 13.1. Trial schematic for an RSVP experiment [6].

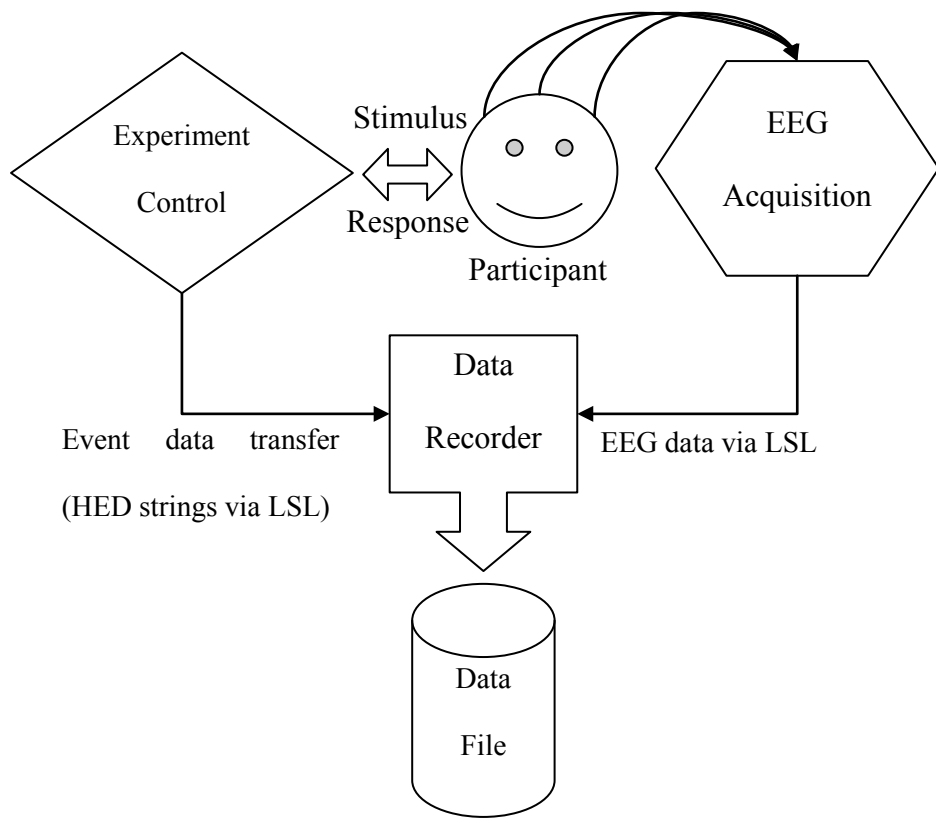


Figure 13.2. A system for real-time HED tagging and synchronous recording of EEG data and events. LSL tools including drivers for many types of input devices are available at [168].

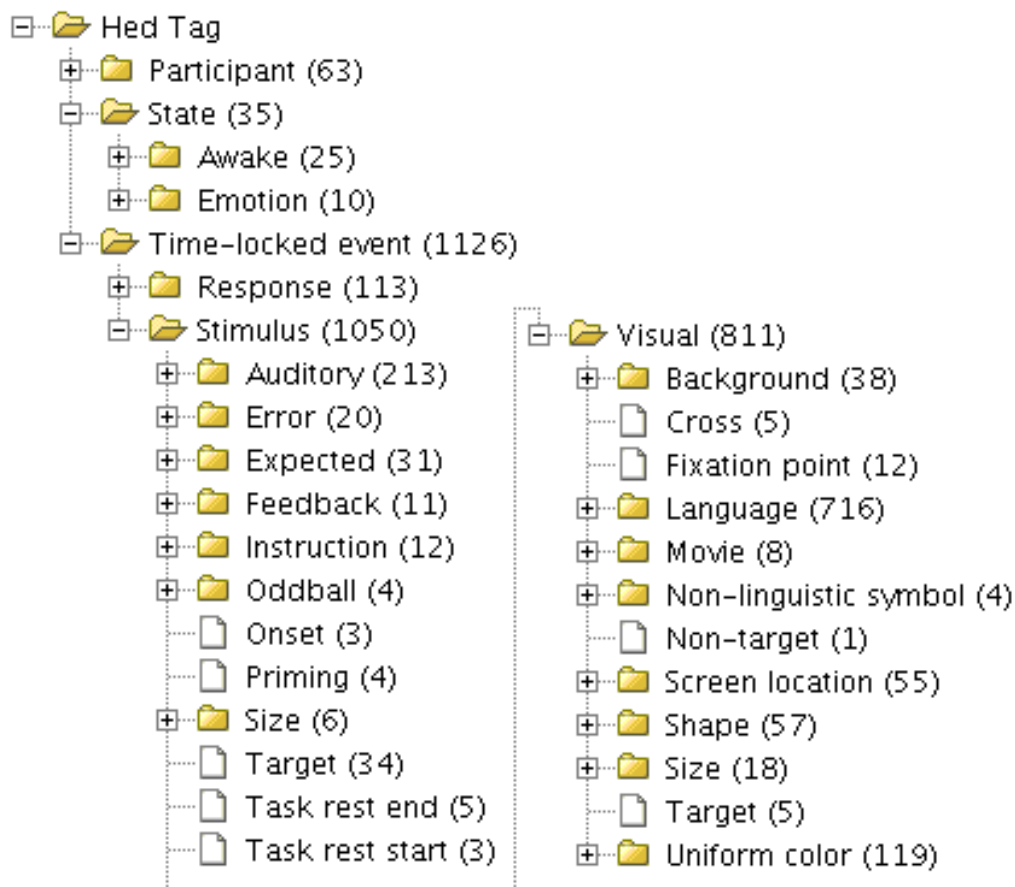


Figure 13.3. Hierarchical representation of HED-tagged event types from 18 archived studies. Values in parentheses show the number of unique event types, across all studies, that match the HED tag associated with each level of the hierarchy.

13.8 Appendix I, HED Node Hierarchy (1.31)

13.8.1 Time-Locked Event [default]

- Stimulus [input from outside world, exogenous]
 - Visual
 - Fixation Point
 - Shape
 - Ellipse
 - Circle
 - Rectangle
 - Square
 - Frame
 - Star
 - Triangle
 - Gabor Patch
 - Cross [by default a vertical-horizontal cross, for rotated add /rotated/ tag]
 - Rotated
 - # [in degrees]
 - Luminance
 - Size
 - # [in candela, e.g 25 cd]
 - # [in degrees, e.g 5 deg]
 - Checkerboard
 - Uniform Color
 - Aqua [these are CSS 3 basic color names, available in Color Names table at the end of this appendix]
 - Black
 - Blue
 - Fuchsia
 - Gray
 - Green
 - Lime
 - Maroon
 - Navy
 - Olive
 - Purple
 - Red
 - Silver
 - Teal
 - White
 - Yellow

- Red
 - # [R value of RGB, between 0 and 1]
- Blue
 - # [B value of RGB, between 0 and 1]
- Green
 - # [G value of RGB, between 0 and 1]
- Hue
 - # [H value of HSV, between 0 and 1]
- Saturation
 - # [S value of HSV, between 0 and 1]
- Value
 - # [V value of HSV, between 0 and 1]

Achromatic [gray, is only in black, white or between]

- # [white intensity between 0 and 1]

Screen Location [if centered at a screen location, not all over the screen]

- Center
- Top
- Bottom
- Left
- Right
- Upper Left
- Lower Left
- Upper Right
- Lower Right
- Angle [clockwise angle]
- Center Displacement
 - # [displacement from screen center, in any direction, in degrees]

Up-down Separated [stimuli presented both at the top and the bottom of fovea]

- # [separation in degrees]

Bilateral [for bilateral visual field stimulus presentations]

- # [separation in degrees]

Foveal [presented exactly where the subject is now looking]

Peripheral [presented where the subject is not directly looking]

Clock Face

- # [hour:min]

3D Object

Abstract Pattern

Non-Linguistic Symbol

- Meaningful
- Not Meaningful
- Newly Learned Meaning

Braille Character

Face

- Whole face with hair
- Whole face without hair

- Cut-out
- Parts only
 - Nose
 - Lips
 - Chin
 - Eyes
 - Eye
- Movie
 - Motion
 - In 3D Space
 - Body
 - Point Light
 - Motion Capture
 - Video
 - Animation
 - Outline
 - On Screen

Social [e.g., mother-child interaction, videotaped or animated by a triangle and a square]

Down [e.g. /2 deg]

Up

Horizontal

• Right [e.g. /3 deg]

Oblique

• Clock Face

◦ # (e.g., 4:30)

Flickering

• Checkerboard

• Dots

• Steady State [fixed stimulus onset asynchrony]

• # (flicker rate in Hz)

[Note: above, also need/could use starting position on screen, end position, velocity in deg/s, etc.]

- Film Clip [any clip from a commercial film, TV,...]

False Font

Food

Fractal

LED

Random Dot

Language

- Asian

◦ Chinese

- Japanese
- Latin
 - English
 - German
 - French
- [allow extension here for other language families]
- Character
 - Digit
 - Pseudo-character [alphabet-like but not really]
 - Letter [Authograph, valid letters including numbers, e.g. A, B, 5...,]
- Word
 - Noun
 - Proper [a proper noun, refers to a unique entity, such as London, Jupiter, ...]
 - Common [refers to a class of entities (cities, planets, persons, corporations), or non-unique instances of a certain class (a city, another planet, these persons, our corporation)].
 - Verb
 - Adjective
 - Pseudoword
 - # [number of words]
- Sentence
 - Full
 - Partial
 - # [number of sentences]
 - Paragraph
 - # [number of paragraphs]
 - Story

Natural Scene

Drawing [e.g. cartoons]

- Line Drawing

Picture

IAPS [International Affective Picture System]

Bistable [this could be either abstract line drawings or object illustrations]

Background

- Uniform Color
 - Aqua [these are CSS 3 basic color names, available in Appendix 1]
 - Black
 - Blue
 - Fuchsia
 - Gray
 - Green

- Lime
- Maroon,
- Navy
- Olive
- Purple
- Red
- Silver
- Teal
- White
- Yellow
- Red
 - # [R value of RGB, between 0 and 1]
- Blue
 - # [B value of RGB, between 0 and 1]
- Green
 - # [G value of RGB, between 0 and 1]
- Hue
 - # [H value of HSV, between 0 and 1]
- Saturation
 - # [S value of HSV, between 0 and 1]
- Value
 - # [V value of HSV, between 0 and 1]

Auditory

Reward [e.g., trumpets!]

- Cash Register
- Ding
- [extend here]

Warning

- Fire Alarm
- [extend here]

Nameable [could be described by a word]

Loudness

- # [in dB]

Music

Chord Sequence

Click

- ABR [Auditory Brainstem Response]

Noise

- White
- Colored [not white, 1/f, spectrum]

Syllable

Tone

- # [in Hz]
- Ramp Up
- Ramp Down
- [extend here]

Nonverbal Vocal Sound

Nonvocal Sound

Language

- Word
 - Name
 - Noun
 - Verb
 - Adjective
 - Pseudoword
 - # [number of words]
- Sentence
 - Full
 - Partial
 - # [number of sentences]
 - Paragraph
 - # [number of paragraphs]
 - Story
- [extend with language names here]

Animal Voice

Real world sounds [people, machines, etc..]

Emotional sounds

File

- [file name or quoted path name]

Direction

- Azimuth
 - # [relative azimuth of the sound, preferably in degrees, clockwise]
- Elevation
 - # [relative elevation of the sound, preferably in degrees]
- Left
- Front
- Right
- Back

TMS

With SPGS [SPGS = spatial position guiding system]

Without SPGS [SPGS = spatial position guiding system]

Tactile

Vibration

Acupuncture

Eye Puff

Pain

Heat

Cold

Pressure

Electric Shock

- Laser-evoked
- Taste
- Smell
- Target [something the subject is looking for is detected]
- Oddball [unexpected, infrequent]
 - One Stimulus [see [http://dx.doi.org/10.1016/0167-8760\(96\)00030-X](http://dx.doi.org/10.1016/0167-8760(96)00030-X)]
 - Two Stimuli [see [http://dx.doi.org/10.1016/0167-8760\(96\)00030-X](http://dx.doi.org/10.1016/0167-8760(96)00030-X)]
 - Three Stimuli [see [http://dx.doi.org/10.1016/0167-8760\(96\)00030-X](http://dx.doi.org/10.1016/0167-8760(96)00030-X)]
- Silent counting
- Button pressing for target
- Button pressing for all
- # [Probability, between 0 and 1]
- Novel [Genuine once or so per experiment event]
- Expected [of low information value]
- Standard
- Distractor
- Non-Target
- Feedback
 - Correct [confirm, something went well, last action was correct]
 - Incorrect
 - Expected [feedback was expected, for example they were often correct and they are again correct]
 - Unexpected [feedback was unexpected, for example they were often correct and they are again correct]
 - On Accuracy [feedback was provided by evaluating their accuracy]
 - On Reaction Time [feedback was provided by evaluating their reaction time]
 - To Self [default]
 - To Other [observed feedback to another person, typically in a social paradigm]
 - Deterministic [should have a fixed relationship to what happened before]
 - Stochastic [non-deterministic, it does not have fixed relationship with what has happened before in the experiment]
- Reward
 - Low
 - Medium
 - High
 - # [monetary values in some currency, for example \$1, or the ratio of the reward to the maximum possible (3 of max 10 becomes 0.3), or x Points]
- Penalty
 - Low
 - Medium
 - High
 - # [absolute monetary values in some currency, for example \$1, or the ratio of the reward to the maximum possible (3 of max 10 becomes 0.3), or x Points]
- Error

Self Originated	
Other Originated	
	<ul style="list-style-type: none"> • Human • Non-human
Expected	
Unexpected	
	Planned [the error feedback was given regardless of the validity of subject response, e.g. in a yoked design]
Threat	
To Self	
To others	<ul style="list-style-type: none"> • Close
	Task Rest Start [stop doing the task and rest, or just rest if the task has not yet begun]
	Task Rest End [stop resting and prepare for or start performing the task]
	Presented action of another person [e.g., saw someone pick up something]
Priming	
Semantic	
Motoric	
Emotional	
Perceptual	
Instruction	
Attend	
Fixate	
Recall	
Generate	
Repeat	
Breath-Hold	
Imagine	
Rest	
Count	
Move	<ul style="list-style-type: none"> • Natural/Constrained • Walk • Breathe • Move upper torso • Move lower torso • Move whole body
Speak	
Sing	
Detect	
Name	
Smile	
Discriminate	
Read	
Track	

Encode

Eye-Blink Inhibition

Subliminal

unmasked

Masked

- Forward
- Backward

Supraliminal [by default this is what assumed about each stimulus]

Liminal [at the 75%/25% perception threshold]

Onset [it is assumed by default that a stimulus event

marks the onset of the stimulus]

- Offset [vs. Onset]
- Congruence
 - Congruent
 - Incongruent
 - Semantic [semantic similarity]
 - Temporal Synchrony
 - Synchronous
 - Asynchronous

- Response [self-initiated action, can be extended]

- Button Press
 - Touch Screen
 - Keyboard
 - Mouse
- Button Hold [press and keep pressed]
- Hand
 - Right
 - Left
 - Finger
 - Tap [when there is nothing to be pressed, like tapping on a chair surface to follow a rhythm]
 - Lift

Leg

Right

Left

Walk

- Start Stride
- Peak stride
- End Stride

Speech

Head

Turn

Torso

Turn
 Movement
 Onset Velocity
 Peak Velocity
 Offset Velocity
 Onset Acceleration
 Peak Acceleration
 Offset Acceleration
 Onset Jerk
 Peak Jerk
 Offset Jerk
 Turn [change in direction of movement]
 Follow
 Lead
 Point
 Object [to an object]
 Direction [to a direction]
 Eye
 Saccade

- Start
- Middle
- End

 Fixation
 Blink
 Close [and keep closed for $>\sim 0.1$ s]
 Open [and keep open for $>\sim 0.1$ s]

13.8.2 State

- Emotion
 - Awe
 - Frustration
 - Joy
 - Anger
 - Happiness
 - Sadness
 - Love
 - Fear
 - Compassion
 - Jealousy
 - Contentment
 - Grief

- Relief
 - Excitement
 - Disgust
 - Negative Valence
 - # (a number between 0 and 1)
 - Positive Valence
 - # (a number between 0 and 1)
 - Awake
 - Task-relevant
 - Task-irrelevant
 - Induced
 - Sense of Community
 - Sense of Social Justice
 - Stress Level
 - # (a number between 0 and 1)
- Task Load
- # (a number between 0 and 1)
- Emotion
- Awe
 - Frustration
 - Joy
 - Anger
 - Happiness
 - Sadness
 - Love
 - Fear
 - Compassion
 - Jealousy
 - Contentment
 - Grief
 - Relief
 - Excitement
 - Disgust
 - Negative Valence
 - # (a number between 0 and 1)
 - Positive Valence
 - # (a number between 0 and 1)

Under time pressure

Response Window

Competitive [subject is competing against an opponent, for example when the faster respondent wins]

Social Interaction [social]

pseudo [instructed so but actually not, the other person may not exist in real world, e.g. be a computer program agent]

Passive [not engaged in any particular task]

Attention

Top-down
 Bottom-up
 Covert
 Overt
 Implicit
 Explicit
 automatic
 Orienting
 Alerting
 Control
 Divided
 Focused
 Sustained [being alert]
 Auditory
 Visual
 Tactile
 To a Location [Spatial]

- Right
- Left
- Top
- Bottom
- Center

 Low Conscious
 Sleep
 Drunk
 Anesthesia
 Locked-in
 Coma
 Vegetative
 Brain-Death

13.8.3 Participant

[for identifying different participants in social, multi-person experiments]

- Role [The role of the participant associated with the event, e.g. viewer, follower, leader, is placed at a lower level, e.g. Participant/Role/Leader)
- ID [subject may swap their roles during the experiment but still need to be each identified by a unique ID, which may or may not be numeric. For example all stimuli presented to a particular participant is tagged as: Participant/ID/Player 1].

13.8.4 Context

[describes the context of the whole experiment, also includes tags that are common across all events]

- [add common tags across all stimuli/ and/or responses here, e.g if all experiment events share /State/Drowsy, you can place it here instead of tagging each event individually]
- With Chin Rest
- Sitting
- Standing
- Prone [e.g. on a bed]
- Running
 - Treadmill
 - # Speed (meters per second)
- Walking
 - Treadmill
 - # Speed (meters per second)
-
- Indoors [default]
 - Clinic [recording in a clinical setting, e.g. in a hospital or doctor's office]
- Outdoors
- Motion platform [subject is on a motion platform, e.g. simulated car movements]
- Screen Distance
 - # [distance in meters from subject eyes to the presentation screen , e.g. 0.3 for 30 cm from subject eyes to the monitor]
- [extend here]

13.8.5 Experiment Control

[information about states and events of the software program that controls the experiment]

- Sequence
 - Permutation ID
 - # [permutation number/code used for permuted experiment parts]
 - Experiment Begins
 - Experiment Ends
 - Block Begins
 - # [block number]
 - Block Ends
 - # [block number]

- Trial Begins
 - # [trial number]
- Trial Ends
 - # [trial number]
- Pause Begins
- Pause Ends
- Task [task-specific events, such as moving a piece in a chess game]
 - Action
 - Correct
 - Incorrect [e.g., due to timeout]
 - Missed
 - Inappropriate
- Synchronization
 - Display Refresh
 - Trigger
 - Tag
 - [actual tag: string or integer]
- Status
 - Waiting For Input
 - Loading
 - Error
- Setup
 - Parameters
 - (experiment parameters in some (quoted) string)

13.8.6 Custom

This node can be used to organize events in an alternative (parallel) hierarchy: you can define your custom tags and hierarchies without any restriction under this node. These tags will still be matched to each other, for example */Custom/Dance/Waltz* is considered a subtype of */Custom/Dance*.

Example: */Initial Score/#* [monetary values in some currency, for example \$1, or the ratio of the reward to the maximum possible (3 of max 10 becomes 0.3), or x Points]

13.8.7 Paradigm

- Action imitation task
- Action observation paradigm
- Action observation task
- Acupuncture task
- Adult attachment interview
- Alternating runs paradigm
- Animal naming task
- Antisaccade-prosaccade task
- Attention networks test
- Attentional blink task
- Audio-visual target-detection task
- Autism diagnostic observation schedule
- Ax-cpt task
- Backward digit span task
- Backward masking
- Balloon analogue risk task (BART)
- Behavioral investment allocation strategy (BIAS)
- Behavioral rating inventory of executive function
- Benton facial recognition test
- Birmingham object recognition battery
- Block design test
- Block tapping test
- Boston naming test
- Braille reading task
- Breath-holding
- Breathhold paradigm
- Brixton spatial anticipation test
- California verbal learning test
- California verbal learning test-ii
- Cambridge face memory test
- Cambridge gambling task
- Cambridge neuropsychological test automated battery
- Catbat task
- Category fluency test
- Cattell culture fair intelligence test
- Chewing-swallowing
- Chimeric animal stroop task
- Choice reaction time task
- Choice task between risky and non-risky options
- Classical conditioning
- Clinical evaluation of language fundamentals-3
- Color trails test
- Color-discrimination task
- Color-word stroop task
- Complex span test
- Conditional stop signal task

- Conditioning paradigm
 - Behavioral conditioning paradigm
 - Classical conditioning paradigm
- Continuous performance task
- Continuous recognition paradigm
- Counting stroop task
- Counting-calculation
- Cued explicit recognition
- Cups task
- Deception task
- Deductive reasoning paradigm
- Deductive reasoning task
- Delayed discounting task
- Delayed match to sample task
- Delayed nonmatch to sample task
- Delayed recall test
- Delayed response task
 - Delayed matching to sample paradigm
 - Sternberg paradigm
- Devils task
- Dichotic listening task
- Digit cancellation task
- Digit span task
- Digit-symbol coding test
- Directed forgetting task
- Divided auditory attention
- Divided auditory attention paradigm
- Doors and people test
- Dot pattern expectancy task
- Drawing (Cognitive Atlas Term)
- Drawing paradigm
- Dual-task paradigm
- Early social communications scales
- Eating paradigm
- Eating-drinking
- Embedded figures test
- Emotional regulation task
- Encoding paradigm
- Encoding task
- Episodic recall
- Episodic recall paradigm
- Eriksen flanker task
- Extradimensional shift task
- Eye Saccade paradigm
 - Anti saccade paradigm
 - Simple saccade paradigm

- Face monitor-discrimination
- Face n-back task
- Fagerstrom test for nicotine dependence (Cognitive Atlas Term)
- Film viewing
- Finger tapping task
- Fixation task
- Flashing checkerboard
- Flexion-extension
- Forward digit span task
- Free word list recall
- Glasgow coma scale
- Go-no-go task
- Grasping task
- Gray oral reading test - 4
- Haptic illusion task
- Hayling sentence completion test
- Heat sensitization-adaptation
- Heat stimulation
- Hooper visual organization test
- Imagined movement
- Imagined objects-scenes
- Immediate recall test
- Inductive reasoning aptitude
- International affective picture system
- Intradimensional shift task
- Ishihara plates for color blindness
- Isometric force
- Item recognition paradigm
 - Serial item recognition paradigm
- Item recognition task
- Kanizsa figures
- Keep-track task
- Letter comparison
- Letter fluency test
- Letter n-back task
- Letter naming task
- Letter number sequencing
- Lexical decision task
- Listening span task
- Macauthur communicative development inventory
- Matching familiar figures test
- Matching pennies game
- Maudsley obsessive compulsive inventory
- Mechanical stimulation
- Memory span test
- Mental rotation task

- Micturition task
- Mini mental state examination (Cognitive Atlas Term)
- Mirror tracing test
- Mismatch negativity paradigm
- Mixed gambles task
- Modified erikson scale of communication attitudes
- Morris water maze
- Motor sequencing task
- Music comprehension-production
- N-back task
- Naming (Covert)
- Naming (Overt)
- Nine-hole peg test
- Non-choice task to study expected value and uncertainty
- Non-painful electrical stimulation
- Non-painful thermal stimulation
- Nonword repetition task
- Object alternation task
- Object-discrimination task
- Oculomotor delayed response
- Oddball discrimination paradigm
 - Auditory oddball paradigm
 - Visual oddball paradigm
- Oddball task
- Olfactory monitor-discrimination
- Operation span task
- Orthographic discrimination
- Paced auditory serial addition test
- Pain monitor-discrimination task
- Paired associate learning
- Paired associate recall
- Pantomime task
- Parrott scale
- Passive listening
- Passive viewing
- Pattern comparison
- Phonological discrimination
- Picture naming task
- Picture set test
- Picture-word stroop task
- Pitch monitor-discrimination
- Pointing
- Porteus maze test
- Positive and negative affect scale
- Posner cueing task
- Probabilistic classification task

- Probabilistic gambling task
- Probabilistic reversal learning
- Pseudoword naming task
- Pursuit rotor task
- Pyramids and palm trees task
- Rapid automatized naming test
- Rapid serial object transformation
- Reading (Covert)
- Reading (Overt)
- Reading paradigm
 - Covert braille reading paradigm
 - Covert visual reading paradigm
- Reading span task
- Recitation-repetition (Covert)
- Recitation-repetition (Overt)
- Remember-know task
- Response mapping task
- Rest
- Retrieval-induced forgetting task
- Reversal learning task
- Reward task
- Rey auditory verbal learning task
- Rey-ostereith complex figure test
- Reynell developmental language scales
- Rhyme verification task
- Risky gains task
- Rivermead behavioural memory test
- [extend here]

13.8.8 Label

- [a short label for the event. For example /Label/Accept Button. Please note that the information under this tag will not be used in the analysis and is provided solely for the convenience in referring to events in the context of a single study.]

13.8.9 Description

- [A detailed description of the event as text, can be used to complement information encoded in other HED tags. Please note that information under this

tag would be unusable by computers and analysis software and should not be used as the main method for describing events (use HED tags other than Description and Label to explain events in a machine-understandable manner)]

13.8.10 Group ID

- [a string that uniquely identifies a group of related events, e.g. events that describe visual and auditory stimulus onsets and offsets of a particular bird may all be tagged with /Group ID/Bird #54]

13.8.11 HED

- # [HED specification version number: normally there is no need to specify the version number in the HED string since it will be matched by default to the most recent compliant version, but this tag can be used to specify the exact HED version the HED string was based on.]

13.8.12 Restrictions on HED Identifier Names

A HED identifier may contain any characters except for the characters ‘/’ (forward slash), ‘,’ (comma), ‘;’ (semicolon), and “” (quotes). In order to use these characters in a HED identifier the HED identifier may be wrapped by a pair of double-quote (“”) characters. In order to use the quote character inside a quoted HED identifier the two-character escape sequence ‘\\’ (backslash double-quote) shall be used. This is the only escape sequence recognized by the HED grammar. The following is a list of valid example HED identifiers:

MyIdentifier

My-Id<en>ti:fier

“My/Identifier”

“My\”Identifier”

13.8.13 Color Names

	Color name	Hex rgb	Decimal
black	black	#000000	0,0,0
silver	silver	#C0C0C0	192,192,192
gray	gray	#808080	128,128,128
white	white	#FFFFFF	255,255,255
maroon	maroon	#800000	128,0,0
red	red	#FF0000	255,0,0
purple	purple	#800080	128,0,128
fuchsia	fuchsia	#FF00FF	255,0,255
green	green	#008000	0,128,0
lime	lime	#00FF00	0,255,0
olive	olive	#808000	128,128,0
yellow	yellow	#FFFF00	255,255,0
navy	navy	#000080	0,0,128
blue	blue	#0000FF	0,0,255
teal	teal	#008080	0,128,128
aqua	aqua	#00FFFF	0,255,255

Chapter 14

Towards an EEG Search Engine

14.1 Abstract

The current EEG analysis-publication workflow mostly documents qualitative descriptions of event-related EEG dynamics. This makes it difficult to look for comparable results in the literature since search options are limited to textual descriptions and/or similar-appearing results depicted in the paper figures. We demonstrate a method for quantitative comparison of source-resolved results (e.g., ERPs, ERSPs) across different EEG studies. Our proposed *source-resolved EEG measure search engine* receives search queries composed of event-related EEG measures, each associated with an estimated brain source location to be compared using Measure Projection Analysis (MPA) to all records in the search engine database accumulated by automated data analysis workflows applied to data of multiple studies. A similarity-ranked list of events from other studies that have elicited similar EEG dynamics in nearby source-locations is then returned to the user along with their experiment and event metadata. We performed a search query using this method through 52 event-related ERSP measures from four studies for Left Precentral Gyrus source measures similar to an input ERSP pattern associated with RSVP target

detection, obtaining results consistent with the EEG literature and giving information about the interpretation of the phenomenon of interest not possible to infer from the single input study.

14.2 Introduction

The current EEG analysis→publication workflow is mostly based on qualitative descriptions of EEG dynamic events (e.g., “a 3-8 µV positivity at 350 ms or theta burst near 800 ms over frontocentral scalp”). Such descriptions make it difficult to look for comparable results in the literature. For example, if a researcher finds some event-related feature in their data, s/he must perform a tedious text search through an ever-increasing number of published papers for comparable text descriptions and/or similar-appearing measures depicted in the paper figures. It is not yet possible to quantitatively compare source-resolved results from different EEG studies.

Also, no single study is ever large enough to account for all the variability originating from subject group differences (age, gender, etc.), and each experimental event-type explores only a subset of associated circumstances. For example, every study of EEG dynamics involving subject ‘error’ awareness includes at most a few types of ‘error’ conditions. Quantitative comparison of EEG dynamics associated with a much larger collection of ‘error’-recognition conditions across many EEG studies could give much useful information for scientific interpretation of new single-study results.

Here we propose a method for building a *Source-resolved EEG Measure Search* engine built on an EEG measure database that would receive search queries composed of event-related EEG measures each associated with a brain source location estimate, and optionally a machine-readable description of the time-locked events (e.g. HED tags [172, 173]) and/or, an anatomical brain region of interest (ROI). This query information would then be compared to all the same-measure-type records in the search engine database accumulated from previous automated data analysis workflows applied to other study data and potentially other search queries. A similarity-ranked list of the most related-measure and source-location pairs (events that have elicited similar EEG dynamics in similar source-locations) from other studies will then be returned to the user along with their metadata (including pointers to any relevant publications). Figure 14.1 shows a flowchart of the proposed search operation.

14.3 Methods

The first step of the search operation is to transform the query data into the (time/space/frequency/...) coordinate systems of the database. For instance, we use here the spatial coordinate system of the MNI (Montreal Neurological Institute [68]) template brain. Next, a mapping that assigns a similarity index (or equivalently a distance measure) to each database entry for some given query data is invoked.

In our implementation we achieve this by first applying the Measure Projection Analysis (MPA) method [45] to interpolate all source measures associated with each

database item (subject, session or study data associated with a single event), originally assigned to discrete and sparse spatial locations, over a dense standardized 3-D grid of spatial brain-space voxels. The result is a common spatial representation of source-resolved EEG measures. MPA amounts to first convolving a 3-D spatial Gaussian kernel (whose standard deviation represents expected uncertainties in localization error and subject head model error) with the entered source locations to produce a source density value at each 3-D brain grid location and then calculating source density weighted average of nearby source measures at each brain voxel. Finally, the similarity of between the query EEG measures and stored measures is calculated by aggregating their similarities across all voxels in the region of interest (ROI) specified in the query.

To calculate the similarity between two search items, each associated with a set of n equivalent dipoles $D_i(y), i=1,..,n$ located at brain locations $y_i \in ROI \subset R^3$ and their associated measure vectors (e.g. vectorized ERSP) $\overrightarrow{M}_i, i=1,..,n$, we first calculate the expected, or *projected*, value for the measure vector for each item at location $y_i \in ROI$ from

$$E\{\overrightarrow{M}(y)\} = \left\langle \overrightarrow{M}(y) \right\rangle = \frac{\sum_{i=1}^n P_i(y) \overrightarrow{M}_i}{\sum_{i=1}^n P_i(y)}. \quad (1)$$

Here $P_j(y) = TN(y; \hat{x}_j, \sigma^2 \cdot I, t)$ where TN is a normalized, truncated (at $t\sigma$, here $t=3$) Gaussian distribution with standard deviation σ and \hat{x}_j is the estimated location of dipole D_j . We then compare projected measure vectors $\overrightarrow{M_i^1}$ and $\overrightarrow{M_i^2}$ of the two items at each voxel $y_k \in ROI, k = 1, \dots, m$ and average these values over query-specified ROI locations (m voxels) to obtain a final similarity value between the two search items with

$$\text{Similarity} = \frac{\sum_{k=1}^m F(\text{Correlation}(\overrightarrow{M_k^1}, \overrightarrow{M_k^2}))}{m}, \quad (2)$$

where

$$F(c) = \text{Fisher's Z}(c) = \frac{1}{2} \ln \frac{1+c}{1-c}. \quad (3)$$

Figure 14.2 gives a flow chart of the measure comparison process between two conditions measures, and potentially from different studies, using Measure Projection.

14.4 Results

We implemented the EEG measure search algorithm described above in MATLAB (Mathworks, Inc.) and applied it to grand mean (across-subjects) event-related time/frequency ERSP (event-related spectral perturbation) measures for 52 study event types within four EEG studies:

1. Target detection task during rapid serial visual presentation (RSVP) without immediate button press feedback [48].
2. A two-back Continuous Performance task with auditory feedback in which subjects have to indicate, by button press, whether the current letter presented on the screen is the same as the letter presented two letters earlier [174].
3. A visual response task in an EEG study on the domain-generality of visual self-representation. Domain-general self-representation was operationally defined as the self-relevance common to one's own Face and Cup [175].
4. An inter-modal audiovisual task in which subjects either switched attention upon receiving audiovisual cues, or ignored the cues and continued to focus on the interleaved audio or visual stimulus stream, responding to occasional target stimuli with button presses [176].

We used the ERSP associated with target presentation in the RSVP study as the search event and compared it to event-related source-resolved dynamics for the remaining 51 event types within a Left Precentral Gyrus region of interest. A 3-D Gaussian with 12-mm standard deviation was used in measure projection of the other 51 ERSPs. The brain volume was segmented into 3,908 voxels in a cubic grid with 8-mm voxel spacing. Figure 14.3 (top) shows the ERSP pattern and ROI used as the input search query and Figure 14.3 (bottom) three most-similar results based on the computed event-related measure similarities.

14.5 Discussion

The first three results, shown in Figure 14.3 (bottom), have a quite similar ERSP pattern in Left Precentral Gyrus and are all associated with target detection, although derived from another study (Attention Shift [176]). In both the input condition and the top three matching results the participant was instructed to press a button with their right hand after detecting the target, which associated as expected from the literature with the prominent mu rhythm blocking beginning at 400 ms, in or near the right hand somatomotor area in the Left Precentral Gyrus. Identifying this factor common to the matching condition strengthens the implication that the EEG dynamics here represent dynamics relating to purposive hand movements. Given a much larger database of source-resolved study measures, further study or more formal analysis of commonalities in the matching condition descriptors might give further insights into the functional role of this cortical area and of the captured EEG dynamics.

To our knowledge this is the first demonstration of EEG source pattern search across different studies. A future direction is to create an EEG search engine with much larger database of source-resolved EEG dynamics, each tagged with a machine readable description of associated cognitive events or state, e.g. using Hierarchical Event Descriptor (HED) tags [172, 173] and subject information (age, gender...), e.g. using EEG Study Schema (ESS) [170]. This information can be added to the search query and used to refine the results. Such a large database of source EEG patterns, accompanied with task and subject information, could be built over an existing raw EEG archive such as HeadIT [171] and have applications beyond EEG search. For

example it may enable the creation of more accurate BCI models by providing neuroscience-informed priors to be used in BCI machine learning algorithms.

Another future direction is to integrate the abovementioned search engine into widely-used EEG analysis software, e.g. EEGLAB [21, 177], and to present relevant search results to researchers during their analysis so as to facilitate better interpretation of patterns present in their data.

14.6 Acknowledgements

This research was sponsored by the Army Research Laboratory under Cooperative Agreement Number W911NF-10-2-0022 and by NIMH grant 1R01-MH084819-03. The views and the conclusions contained in this document are those of the authors and should not be interpreted as representing the official policies, either expressed or implied, of the Army Research Laboratory or the U.S Government. The U.S Government is authorized to reproduce and distribute reprints for Government purposes notwithstanding any copyright notation herein.

Chapter 14 , in full, is a reprint of the material as has been submitted for publication and will appear in N. Bigdely-Shamlo, K. Kreutz-Delgado, C. Kothe, S. Makeig, "Towards an EEG Search Engine," IEEE GlobalSIP Conference, Austin, TX, 2013. The dissertation author was the primary investigator and author of this paper.

14.7 Figures

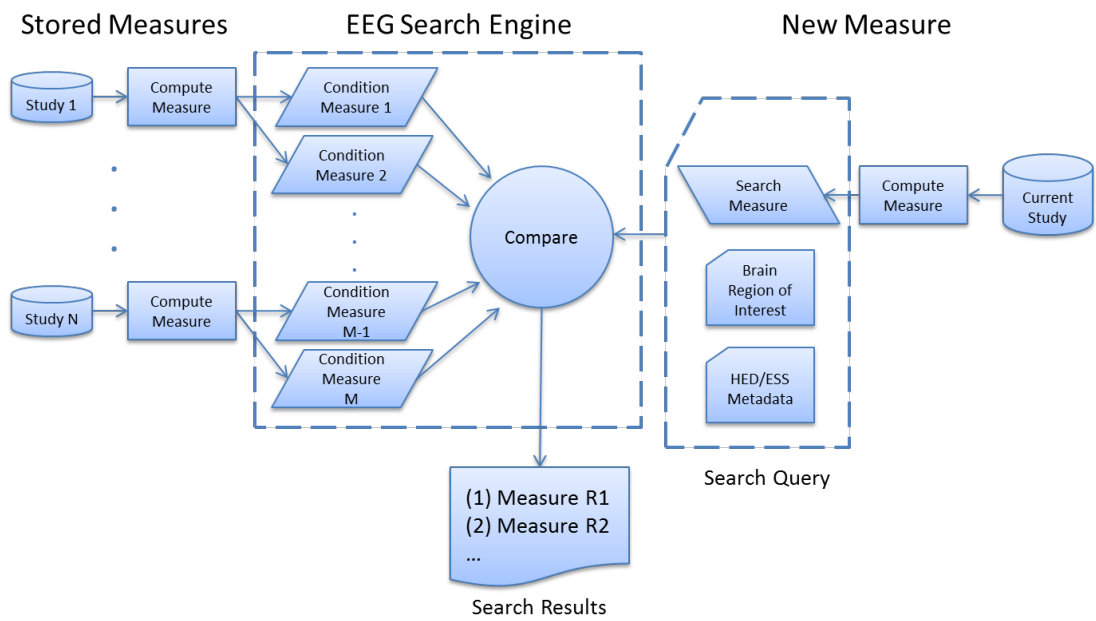


Figure 14.1. Flowchart of the proposed HeadIT Measure Search Engine.

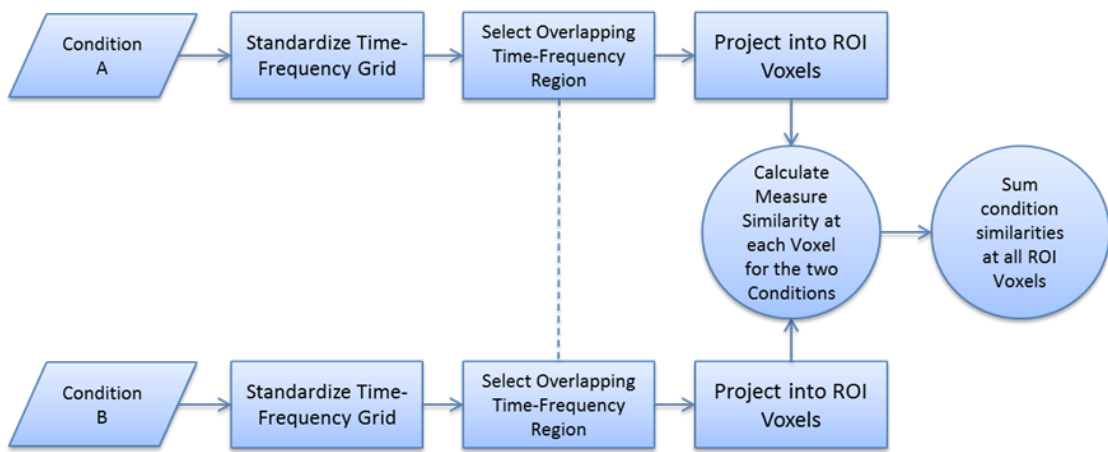
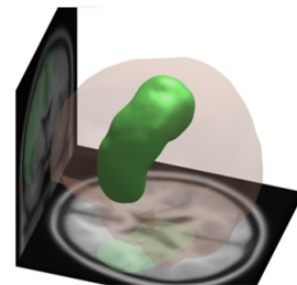
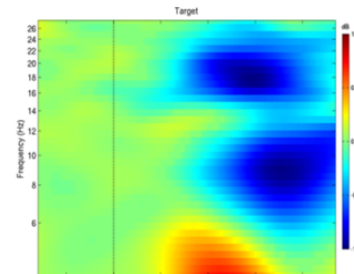


Figure 14.2. Flowchart of event-related measure comparison using measure projection.

Input Search Condition (Target in an RSVP task):



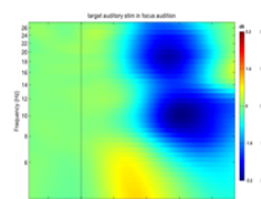
Region of Interest



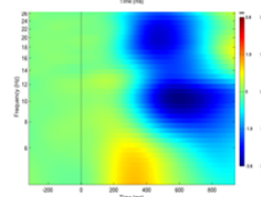
Target Condition ERSP

Top 3 Search Result Conditions (from the total 51):

1. Auditory Target Response during the Auditory Focus condition



2. Visual Target Response during the Visual Focus condition



3. Visual Target Response during the switch from Auditory to Vision Focus condition

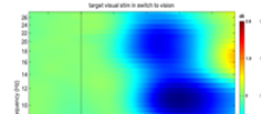


Figure 14.3. (top) input query, and (bottom) top-ranked ERSP measure search results

References

- [1] F. Lotte and G. Cuntai, "Regularizing Common Spatial Patterns to Improve BCI Designs: Unified Theory and New Algorithms," *Biomedical Engineering, IEEE Transactions on*, vol. 58, pp. 355-362, 2011.
- [2] M. Alamgir, M. Grosse-Wentrup, and Y. Altun, "Multi-task learning for Brain-Computer Interfaces," 2009.
- [3] S. Fazli, C. Grozea, M. Danoczy, B. Blankertz, F. Popescu, and K.-r. Müller, "Subject independent EEG-based BCI decoding," in *Advances in Neural Information Processing Systems*, 2009, pp. 513-521.
- [4] M. Krauledat, M. Tangermann, B. Blankertz, and K.-R. Müller, "Towards zero training for brain-computer interfacing," *PloS one*, vol. 3, p. e2967, 2008.
- [5] R. D. Pascual-Marqui, C. M. Michel, and D. Lehmann, "Low resolution electromagnetic tomography: a new method for localizing electrical activity in the brain," *International journal of psychophysiology : official journal of the International Organization of Psychophysiology*, vol. 18, pp. 49-65, Oct 1994.
- [6] R. Pascual-Marqui, M. Esslen, K. Kochi, and D. Lehmann, "Functional imaging with low-resolution brain electromagnetic tomography (LORETA): a review," *Methods and findings in experimental and clinical pharmacology*, vol. 24, pp. 91-95, 2002.
- [7] R. Pascual-Marqui, "Standardized low-resolution brain electromagnetic tomography (sLORETA): technical details," *Methods Find Exp Clin Pharmacol*, vol. 24, pp. 5-12, 2002.
- [8] R. D. Pascual-Marqui, A. D. Pascual-Montano, D. Lehmann, K. Kochi, M. Esslen, L. Jancke, P. Anderer, B. Saletu, H. Tanaka, and K. Hirata, "Exact low resolution brain electromagnetic tomography (eLORETA)," *NeuroImage*, vol. 31, 2006.
- [9] T. Limpiti, B. D. Van Veen, and R. T. Wakai, "Cortical patch basis model for spatially extended neural activity," *Biomedical Engineering, IEEE Transactions on*, vol. 53, pp. 1740-1754, 2006.
- [10] Z. A. Acar, G. Worrell, and S. Makeig, "Patch-basis electrocortical source imaging in epilepsy," in *Engineering in Medicine and Biology Society, 2009. EMBC 2009. Annual International Conference of the IEEE*, 2009, pp. 2930-2933.

- [11] A. Korzeniewska, M. Mańczak, M. Kamiński, K. J. Blinowska, and S. Kasicki, "Determination of information flow direction among brain structures by a modified directed transfer function (dDTF) method," *Journal of Neuroscience Methods*, vol. 125, pp. 195-207, 2003.
- [12] A. Korzeniewska, C. M. Crainiceanu, R. Kuś, P. J. Franaszczuk, and N. E. Crone, "Dynamics of event-related causality in brain electrical activity," *Human brain mapping*, vol. 29, pp. 1170-1192, 2008.
- [13] P. T. Fox, A. R. Laird, S. P. Fox, P. M. Fox, A. M. Uecker, M. Crank, S. F. Koenig, and J. L. Lancaster, "BrainMap taxonomy of experimental design: description and evaluation," *Human brain mapping*, vol. 25, pp. 185-98, May 2005.
- [14] A. R. Laird, J. L. Lancaster, and P. T. Fox, "BrainMap: the social evolution of a human brain mapping database," *Neuroinformatics*, vol. 3, pp. 65-78, 2005.
- [15] A. R. Laird, S. B. Eickhoff, F. Kurth, P. M. Fox, A. M. Uecker, J. A. Turner, J. L. Robinson, J. L. Lancaster, and P. T. Fox, "ALE Meta-Analysis Workflows Via the Brainmap Database: Progress Towards A Probabilistic Functional Brain Atlas," *Frontiers in neuroinformatics*, vol. 3, p. 23, 2009.
- [16] A. R. Laird, S. B. Eickhoff, P. M. Fox, A. M. Uecker, K. L. Ray, J. J. Saenz, Jr., D. R. McKay, D. Bzdok, R. W. Laird, J. L. Robinson, J. A. Turner, P. E. Turkeltaub, J. L. Lancaster, and P. T. Fox, "The BrainMap strategy for standardization, sharing, and meta-analysis of neuroimaging data," *BMC research notes*, vol. 4, p. 349, 2011.
- [17] T. Yarkoni, R. Poldrack, T. Nichols, D. Van Essen, and T. Wager, "NeuroSynth: a new platform for large-scale automated synthesis of human functional neuroimaging data," in *Front. Neuroinform. Conference Abstract: 4th INCF Congress of Neuroinformatics. doi: 10.3389/conf.fninf*, 2011.
- [18] D. C. Van Essen, "Surface-based approaches to spatial localization and registration in primate cerebral cortex," *NeuroImage*, vol. 23, pp. S97-S107, 2004.
- [19] Available: <http://neuro.debian.net/survey/2011/results.html>
- [20] A. J. Bell and T. J. Sejnowski, "An Information Maximization Approach to Blind Separation and Blind Deconvolution," *Neural Computation*, vol. 7, pp. 1129-1159, Nov 1995.

- [21] A. Delorme and S. Makeig, "EEGLAB: an open source toolbox for analysis of single-trial EEG dynamics including independent component analysis," *Journal of Neuroscience Methods*, vol. 134, pp. 9-21, Mar 15 2004.
- [22] S. Makeig, A. J. Bell, T. P. Jung, and T. Sejnowski, "Independent component analysis of electroencephalographic data," *Advances in Neural Information Processing Systems*, vol. 8, pp. 145-151 1996.
- [23] S. Makeig, T. P. Jung, A. J. Bell, D. Ghahremani, and T. J. Sejnowski, "Blind separation of auditory event-related brain responses into independent components," *Proceedings of the National Academy of Sciences of the United States of America*, vol. 94, pp. 10979-10984, Sep 30 1997.
- [24] T. W. Lee, M. Girolami, and T. J. Sejnowski, "Independent component analysis using an extended infomax algorithm for mixed subgaussian and supergaussian sources," *Neural Computation*, vol. 11, pp. 417-441, Feb 15 1999.
- [25] T. P. Jung, S. Makeig, M. J. McKeown, A. J. Bell, T. W. Lee, and T. J. Sejnowski, "Imaging brain dynamics using independent component analysis," *Proceedings of the Ieee*, vol. 89, pp. 1107-1122, Jul 2001.
- [26] S. Makeig, M. Westerfield, T. P. Jung, S. Enghoff, J. Townsend, E. Courchesne, and T. J. Sejnowski, "Dynamic brain sources of visual evoked responses," *Science*, vol. 295, pp. 690-694, Jan 25 2002.
- [27] P. L. Nunez and R. Srinivasan, *Electric fields of the brain : the neurophysics of EEG*, 2nd ed. Oxford ; New York: Oxford University Press, 2006.
- [28] A. Delorme, J. Palmer, J. Onton, R. Oostenveld, and S. Makeig, "Independent EEG sources are dipolar," *PloS one*, vol. 7, p. e30135, 2012.
- [29] M. Scherg, "Fundamentals of dipole source potential analysis," in *Auditory evoked magnetic fields and electric potentials*, F. Grandori, M. Hoke, and G. L. Romani, Eds., ed Basel ; New York: Karger, 1990, pp. 40-69.
- [30] Z. A. Acar and S. Makeig, "Neuroelectromagnetic Forward Head Modeling Toolbox," *Journal of Neuroscience Methods*, vol. 190, pp. 258-270, Jul 15 2010.
- [31] C. W. Pleydell-pearce, "DC potential correlates of attention and cognitive load," *Cognitive Neuropsychology*, vol. 11, pp. 149-166, 1994/04/01 1994.

- [32] T. Mullen. *CleanLine Plugin for EEGLAB*. Available: <https://bitbucket.org/tmullen/cleanline>
- [33] T. Mullen, C. Kothe, Y. M. Chi, A. Ojeda, T. Kerth, S. Makeig, G. Cauwenberghs, and T. P. Jung, "Real-time modeling and 3D visualization of source dynamics and connectivity using wearable EEG," *Conference proceedings : ... Annual International Conference of the IEEE Engineering in Medicine and Biology Society. IEEE Engineering in Medicine and Biology Society. Conference*, vol. 2013, pp. 2184-2187, Jul 2013.
- [34] A. Delorme and S. Makeig, "EEG changes accompanying learned regulation of 12-Hz EEG activity," *IEEE Trans Neural Syst Rehabil Eng*, vol. 11, pp. 133-7, Jun 2003.
- [35] P. Comon, "Independent component analysis, A new concept?," *Signal Processing*, vol. 36, pp. 287-314, 1994.
- [36] T. Eichele, V. D. Calhoun, and S. Debener, "Mining EEG-fMRI using independent component analysis," *International Journal of Psychophysiology*, vol. 73, pp. 53-61, Jul 2009.
- [37] N. Kovacevic and A. R. McIntosh, "Groupwise independent component decomposition of EEG data and partial least square analysis," *NeuroImage*, vol. 35, pp. 1103-1112, Apr 15 2007.
- [38] V. D. Calhoun, J. Liu, and T. Adali, "A review of group ICA for fMRI data and ICA for joint inference of imaging, genetic, and ERP data," *NeuroImage*, vol. 45, pp. S163-S172, Mar 2009.
- [39] M. Congedo, R. E. John, D. De Ridder, and L. Prichep, "Group independent component analysis of resting state EEG in large normative samples," *International journal of psychophysiology : official journal of the International Organization of Psychophysiology*, vol. 78, pp. 89-99, Nov 2010.
- [40] J. H. Lee, T. W. Lee, F. A. Jolesz, and S. S. Yoo, "Independent vector analysis (IVA): multivariate approach for fMRI group study," *NeuroImage*, vol. 40, pp. 86-109, 2008.
- [41] Y. O. Li, T. Adali, W. Wang, and V. D. Calhoun, "Joint Blind Source Separation by Multi-set Canonical Correlation Analysis," *IEEE transactions on signal processing : a publication of the IEEE Signal Processing Society*, vol. 57, pp. 3918-3929, Oct 1 2009.

- [42] R. Phlypo, "Jacobi iterations for Canonical Dependence Analysis," *Signal Processing*, vol. 93, pp. 185-197, 2013.
- [43] X. L. Li, T. Adali, and M. Anderson, "Joint blind source separation by generalized joint diagonalization of cumulant matrices," *Signal Processing*, vol. 91, pp. 2314-2322, Oct 2011.
- [44] J. Via, M. Anderson, X.-L. Li, and T. Adali, "Joint blind source separation from second-order statistics: Necessary and sufficient identifiability conditions," in *Acoustics, Speech and Signal Processing (ICASSP), 2011 IEEE International Conference on*, 2011, pp. 2520-2523.
- [45] N. Bigdely-Shamlo, T. Mullen, K. Kreutz-Delgado, and S. Makeig, "Measure projection analysis: a probabilistic approach to EEG source comparison and multi-subject inference," *NeuroImage*, vol. 72, pp. 287-303, May 15 2013.
- [46] S. Makeig and T. P. Jung, "Changes in alertness are a principal component of variance in the EEG spectrum," *Neuroreport*, vol. 7, pp. 213-6, Dec 29 1995.
- [47] S. P. Boyd and L. Vandenberghe, *Convex optimization*. Cambridge, UK ; New York: Cambridge University Press, 2004.
- [48] N. Bigdely-Shamlo, A. Vankov, R. R. Ramirez, and S. Makeig, "Brain Activity-Based Image Classification From Rapid Serial Visual Presentation," *IEEE Transactions on Neural Systems and Rehabilitation Engineering*, vol. 16, pp. 432-441, Oct 2008.
- [49] H. H. Yoon, S. M. Malone, S. J. Burwell, E. M. Bernat, and W. G. Iacono, "Association between P3 event-related potential amplitude and externalizing disorders: A time-domain and time-frequency investigation of 29-year-old adults," *Psychophysiology*, 2013.
- [50] W. G. Iacono, S. R. Carlson, S. M. Malone, and M. McGue, "P3 event-related potential amplitude and the risk for disinhibitory disorders in adolescent boys," *Archives of general psychiatry*, vol. 59, pp. 750-7, Aug 2002.
- [51] H. Begleiter, B. Porjesz, B. Bihari, and B. Kissin, "Event-Related Brain Potentials in Boys at Risk for Alcoholism," *Science*, vol. 225, pp. 1493-1496, 1984.
- [52] D. W. Shattuck, M. Mirza, V. Adisetiyo, C. Hojatkashani, G. Salamon, K. L. Narr, R. A. Poldrack, R. M. Bilder, and A. W. Toga, "Construction of a 3D

- probabilistic atlas of human cortical structures," *NeuroImage*, vol. 39, pp. 1064-1080, Feb 1 2008.
- [53] C. Bledowski, D. Prvulovic, K. Hoechstetter, M. Scherg, M. Wibral, R. Goebel, and D. E. Linden, "Localizing P300 generators in visual target and distractor processing: a combined event-related potential and functional magnetic resonance imaging study," *The Journal of neuroscience*, vol. 24, pp. 9353-9360, 2004.
 - [54] A. D. Gerson, L. C. Parra, and P. Sajda, "Cortical origins of response time variability during rapid discrimination of visual objects," *NeuroImage*, vol. 28, pp. 342-53, Nov 1 2005.
 - [55] F. C. Viola, J. Thorne, B. Edmonds, T. Schneider, T. Eichele, and S. Debener, "Semi-automatic identification of independent components representing EEG artifact," *Clinical Neurophysiology*, vol. 120, pp. 868-877, May 2009.
 - [56] T. P. Jung, S. Makeig, M. Westerfield, J. Townsend, E. Courchesne, and T. J. Sejnowski, "Removal of eye activity artifacts from visual event-related potentials in normal and clinical subjects," *Clinical neurophysiology : official journal of the International Federation of Clinical Neurophysiology*, vol. 111, pp. 1745-58, Oct 2000.
 - [57] A. Mognon, J. Jovicich, L. Bruzzone, and M. Buiatti, "ADJUST: An automatic EEG artifact detector based on the joint use of spatial and temporal features," *Psychophysiology*, vol. 48, pp. 229-240, Feb 2011.
 - [58] J. Palmer, K. Kreutz-Delgado, and S. Makeig, "Super-Gaussian mixture source model for ICA," *Independent Component Analysis and Blind Signal Separation*, pp. 854-861, 2006.
 - [59] J. Palmer, S. Makeig, K. Delgado, and B. Rao, "Newton method for the ICA mixture model," in *Acoustics, Speech and Signal Processing, 2008. ICASSP 2008. IEEE International Conference on*, 2008, pp. 1805-1808.
 - [60] A. Delorme, T. Mullen, C. Kothe, Z. Akalin Acar, N. Bigdely-Shamlo, A. Vankov, and S. Makeig, "EEGLAB, SIFT, NFT, BCILAB, and ERICA: new tools for advanced EEG processing," *Computational Intelligence and Neuroscience*, vol. 2011, 2011.
 - [61] R. Čeponienė, M. Westerfield, M. Torki, and J. Townsend, "Modality-specificity of sensory aging in vision and audition: Evidence from event-related potentials," *Brain research*, vol. 1215, pp. 53-68, 2008.

- [62] B. J. Frey and D. Dueck, "Clustering by passing messages between data points," *Science*, vol. 315, pp. 972-976, Feb 16 2007.
- [63] J. P. Egan, *Signal detection theory and ROC-analysis*. New York: Academic Press, 1975.
- [64] *Measure Projection Toolbox*. Available: <http://www.sccn.ucsd.edu/wiki/MPT>
- [65] J. onton and S. Makeig, "Spatial dependence of EEG independent component source distributions on task demands.," presented at the Human Brain Mapping, Toronto, Ontario, Canada, 2005.
- [66] P. J. Basser and C. Pierpaoli, "Microstructural and physiological features of tissues elucidated by quantitative-diffusion-tensor MRI," *Journal of magnetic resonance. Series B*, vol. 111, pp. 209-19, Jun 1996.
- [67] M. X. Huang, J. J. Shih, R. R. Lee, D. L. Harrington, R. J. Thoma, M. P. Weisend, F. Hanlon, K. M. Paulson, T. Li, K. Martin, G. A. Miller, and J. M. Canive, "Commonalities and Differences Among Vectorized Beamformers in Electromagnetic Source Imaging," *Brain Topography*, vol. 16, pp. 139-158, 2004/03/01 2004.
- [68] A. C. Evans, D. L. Collins, S. R. Mills, E. D. Brown, R. L. Kelly, and T. M. Peters, "3D statistical neuroanatomical models from 305 MRI volumes," in *Nuclear Science Symposium and Medical Imaging Conference, 1993., 1993 IEEE Conference Record.*, 1993, pp. 1813-1817 vol.3.
- [69] Y. Benjamini and Y. Hochberg, "Controlling the False Discovery Rate - a Practical and Powerful Approach to Multiple Testing," *Journal of the Royal Statistical Society Series B-Methodological*, vol. 57, pp. 289-300, 1995.
- [70] J. L. Lancaster, M. G. Woldorff, L. M. Parsons, M. Liotti, E. S. Freitas, L. Rainey, P. V. Kochunov, D. Nickerson, S. A. Mikiten, and P. T. Fox, "Automated Talairach Atlas labels for functional brain mapping," *Human Brain Mapping*, vol. 10, pp. 120-131, Jul 2000.
- [71] M. H. Rosenbloom, J. D. Schmahmann, and B. H. Price, "The functional neuroanatomy of decision-making," *The Journal of neuropsychiatry and clinical neurosciences*, vol. 24, pp. 266-77, Summer 2012.
- [72] R. Oostenveld, P. Fries, E. Maris, and J. M. Schoffelen, "FieldTrip: Open source software for advanced analysis of MEG, EEG, and invasive

- electrophysiological data," *Comput Intell Neurosci*, vol. 2011, p. 156869, 2011.
- [73] K. J. Friston, *Statistical parametric mapping : the analysis of functional brain images*, 1st ed. Amsterdam ; Boston: Elsevier/Academic Press, 2007.
 - [74] A. Cichocki and S. i. Amari, *Adaptive blind signal and image processing : learning algorithms and applications*. Chichester ; New York: J. Wiley, 2002.
 - [75] S. Makeig, "Auditory Event-Related Dynamics of the Eeg Spectrum and Effects of Exposure to Tones," *Electroencephalography and Clinical Neurophysiology*, vol. 86, pp. 283-293, Apr 1993.
 - [76] T. W. Picton, S. Bentin, P. Berg, E. Donchin, S. A. Hillyard, R. Johnson, G. A. Miller, W. Ritter, D. S. Ruchkin, M. D. Rugg, and M. J. Taylor, "Guidelines for using human event-related potentials to study cognition: Recording standards and publication criteria," *Psychophysiology*, vol. 37, pp. 127-152, Mar 2000.
 - [77] S. J. Kiebel and K. J. Friston, "Statistical parametric mapping for event-related potentials: I. Generic considerations," *NeuroImage*, vol. 22, pp. 492-502, Jun 2004.
 - [78] J. Onton, M. Westerfield, J. Townsend, and S. Makeig, "Imaging human EEG dynamics using independent component analysis," *Neuroscience and Biobehavioral Reviews*, vol. 30, pp. 808-822, 2006.
 - [79] J. Onton and S. Makeig, "Information-based modeling of event-related brain dynamics," *Event-Related Dynamics of Brain Oscillations*, vol. 159, pp. 99-120, 2006.
 - [80] S. Spadone, F. de Pasquale, D. Mantini, and S. Della Penna, "A K-means multivariate approach for clustering independent components from magnetoencephalographic data," *NeuroImage*, 2012 2012.
 - [81] G. A. Darbellay and I. Vajda, "Estimation of the information by an adaptive partitioning of the observation space," *Ieee Transactions on Information Theory*, vol. 45, pp. 1315-1321, May 1999.
 - [82] K. Brodmann, "Vergleichende Lokalisationslehre der Grosshirnrinde," *ihren Prinzipien dargestellt auf Grund des Zellenbaues*, 1909.

- [83] V. L. Marcar, T. Loenneker, A. Straessle, S. Jaggy, K. Kucian, and E. Martin, "An fMRI study of the cerebral macro network involved in 'cue invariant' form perception and how it is influenced by stimulus complexity," *NeuroImage*, vol. 23, pp. 947-55, Nov 2004.
- [84] R. F. Dougherty, V. M. Koch, A. A. Brewer, B. Fischer, J. Modersitzki, and B. A. Wandell, "Visual field representations and locations of visual areas V1/2/3 in human visual cortex," *Journal of Vision*, vol. 3, pp. 586-598, 2003.
- [85] I. J. Deary, E. Simonotto, M. Meyer, A. Marshall, I. Marshall, N. Goddard, and J. M. Wardlaw, "The functional anatomy of inspection time: an event-related fMRI study," *NeuroImage*, vol. 22, pp. 1466-79, Aug 2004.
- [86] M. G. Philiastides and P. Sajda, "EEG-informed fMRI reveals spatiotemporal characteristics of perceptual decision making," *J Neurosci*, vol. 27, pp. 13082-91, Nov 28 2007.
- [87] S. Makeig, A. Delorme, M. Westerfield, T. P. Jung, J. Townsend, E. Courchesne, and T. J. Sejnowski, "Electroencephalographic brain dynamics following manually responded visual targets," *Plos Biology*, vol. 2, pp. 747-762, Jun 2004.
- [88] J. Cohen, "A Coefficient of Agreement for Nominal Scales," *Educational and Psychological Measurement*, vol. 20, pp. 37-46, 1960.
- [89] R. Heller, D. Stanley, D. Yekutieli, N. Rubin, and Y. Benjamini, "Cluster-based analysis of fMRI data," *NeuroImage*, vol. 33, pp. 599-608, 2006.
- [90] V. D. Calhoun, T. Adali, G. D. Pearlson, and J. J. Pekar, "A method for making group inferences from functional MRI data using independent component analysis," *Human Brain Mapping*, vol. 14, pp. 140-151, Nov 2001.
- [91] V. J. Schmithorst and S. K. Holland, "Comparison of three methods for generating group statistical inferences from independent component analysis of functional magnetic resonance imaging data," *Journal of Magnetic Resonance Imaging*, vol. 19, pp. 365-368, Mar 2004.
- [92] C. F. Beckmann and S. M. Smith, "Tensorial extensions of independent component analysis for multisubject fMRI analysis," *NeuroImage*, vol. 25, pp. 294-311, Mar 2005.
- [93] F. Esposito, T. Scarabino, A. Hyvarinen, J. Himberg, E. Formisano, S. Comani, G. Tedeschi, R. Goebel, E. Seifritz, and F. Di Salle, "Independent

- component analysis of fMRI group studies by self-organizing clustering," *NeuroImage*, vol. 25, pp. 193-205, Mar 2005.
- [94] M. Moosmann, T. Eichele, H. Nordby, K. Hugdahl, and V. D. Calhoun, "Joint independent component analysis for simultaneous EEG-fMRI: Principle and simulation," *International Journal of Psychophysiology*, vol. 67, pp. 212-221, Mar 2008.
 - [95] S. Rachakonda, T. Eichele, and V. Calhoun. (2011). *Group ICA of EEG Toolbox (EEGIFT) Walk Through* Available: http://icatb.sourceforge.net/gift/v1.0c_EEGIFT_Walk_Through.pdf
 - [96] A. Hyvarinen, "Testing the ICA mixing matrix based on inter-subject or inter-session consistency," *NeuroImage*, vol. 58, pp. 122-136, Sep 1 2011.
 - [97] E. Maris and R. Oostenveld, "Nonparametric statistical testing of EEG- and MEG-data," *Journal of Neuroscience Methods*, vol. 164, pp. 177-90, Aug 15 2007.
 - [98] K. J. Worsley, J. E. Taylor, F. Tomaiuolo, and J. Lerch, "Unified univariate and multivariate random field theory," *NeuroImage*, vol. 23 Suppl 1, pp. S189-95, 2004.
 - [99] K. Friston, C. Chu, J. Mourão-Miranda, O. Hulme, G. Rees, W. Penny, and J. Ashburner, "Bayesian decoding of brain images," *NeuroImage*, vol. 39, pp. 181-205, 2008.
 - [100] M. S. Worden, J. J. Foxe, N. Wang, and G. V. Simpson, "Anticipatory biasing of visuospatial attention indexed by retinotopically specific alpha-band electroencephalography increases over occipital cortex," *The Journal of neuroscience : the official journal of the Society for Neuroscience*, vol. 20, p. RC63, Mar 15 2000.
 - [101] M. Corbetta, F. M. Miezin, S. Dobmeyer, G. L. Shulman, and S. E. Petersen, "Attentional modulation of neural processing of shape, color, and velocity in humans," *Science*, vol. 248, pp. 1556-1559, 1990.
 - [102] M. Corbetta, F. M. Miezin, S. Dobmeyer, G. L. Shulman, and S. E. Petersen, "Selective and divided attention during visual discriminations of shape, color, and speed: functional anatomy by positron emission tomography," *The Journal of neuroscience*, vol. 11, pp. 2383-2402, 1991.

- [103] M. Corbetta, F. M. Miezin, G. L. Shulman, and S. E. Petersen, "A PET study of visuospatial attention," *The Journal of neuroscience*, vol. 13, pp. 1202-1226, 1993.
- [104] M. Corbetta, G. L. Shulman, F. M. Miezin, and S. E. Petersen, "Superior parietal cortex activation during spatial attention shifts and visual feature conjunction," *Science*, vol. 270, pp. 802-805, 1995.
- [105] M. Corbetta, "Frontoparietal cortical networks for directing attention and the eye to visual locations: Identical, independent, or overlapping neural systems?," *Proceedings of the National Academy of Sciences*, vol. 95, pp. 831-838, 1998.
- [106] M. Corbetta, E. Akbudak, T. E. Conturo, A. Z. Snyder, J. M. Ollinger, H. A. Drury, M. R. Linenweber, S. E. Petersen, M. E. Raichle, and D. C. Van Essen, "A common network of functional areas for attention and eye movements," *Neuron*, vol. 21, pp. 761-773, 1998.
- [107] M. Corbetta and G. L. Shulman, "Control of goal-directed and stimulus-driven attention in the brain," *Nature reviews neuroscience*, vol. 3, pp. 201-215, 2002.
- [108] M. D. Fox, M. Corbetta, A. Z. Snyder, J. L. Vincent, and M. E. Raichle, "Spontaneous neuronal activity distinguishes human dorsal and ventral attention systems," *Proceedings of the National Academy of Sciences*, vol. 103, pp. 10046-10051, 2006.
- [109] R. Tomioka and K. R. Muller, "A regularized discriminative framework for EEG analysis with application to brain-computer interface," *NeuroImage*, vol. 49, pp. 415-432, Jan 1 2010.
- [110] C. A. Kothe and S. Makeig, "BCILAB: a platform for brain-computer interface development," *Journal of Neural Engineering*, vol. 10, p. 056014, Oct 2013.
- [111] A. Delorme, T. Mullen, C. Kothe, Z. Akalin Acar, N. Bigdely-Shamlo, A. Vankov, and S. Makeig, "EEGLAB, SIFT, NFT, BCILAB, and ERICA: new tools for advanced EEG processing," *Computational intelligence and neuroscience*, vol. 2011, p. 130714, 2011.
- [112] T. K. Pong, P. Tseng, S. Ji, and J. Ye, "Trace norm regularization: reformulations, algorithms, and multi-task learning," *SIAM Journal on Optimization*, vol. 20, pp. 3465-3489, 2010.

- [113] M. Scherg and D. Von Cramon, "Evoked dipole source potentials of the human auditory cortex," *Electroencephalography and Clinical Neurophysiology/Evoked Potentials Section*, vol. 65, pp. 344-360, 1986.
- [114] *BCILAB Software*. Available: <https://github.com/sccn/BCILAB/archive/master.zip>
- [115] J. O. Pickles, in *An introduction to the physiology of hearing*, Fourth edition. ed Bingley, UK: Emerald Group Publishing Limited, 2012, pp. 215–217.
- [116] L. Lee, L. M. Harrison, and A. Mechelli, "A report of the functional connectivity workshop, Dusseldorf 2002," *NeuroImage*, vol. 19, pp. 457-465, 2003.
- [117] S. L. Bressler and A. K. Seth, "Wiener-Granger causality: a well established methodology," *NeuroImage*, vol. 58, pp. 323-9, Sep 15 2011.
- [118] C. W. J. Granger, "Investigating Causal Relations by Econometric Models and Cross-Spectral Methods," *Econometrica*, vol. 37, pp. 414-&, 1969.
- [119] L. A. Baccalá and K. Sameshima, "Partial directed coherence: a new concept in neural structure determination," *Biological cybernetics*, vol. 84, pp. 463-474, 2001.
- [120] L. Baccalá, "Generalized partial directed coherence," in *Digital Signal Processing, 2007 15th International Conference on*, 2007, pp. 163-166.
- [121] G. Gomez-Herrero, M. Atienza, K. Egiazarian, and J. L. Cantero, "Measuring directional coupling between EEG sources," *NeuroImage*, vol. 43, pp. 497-508, 2008.
- [122] J. M. Schoffelen and J. Gross, "Source connectivity analysis with MEG and EEG," *Human brain mapping*, vol. 30, pp. 1857-65, Jun 2009.
- [123] R. D. Pascual-Marqui, D. Lehmann, M. Koukkou, K. Kochi, P. Anderer, B. Saletu, H. Tanaka, K. Hirata, E. R. John, and L. Prichep, "Assessing interactions in the brain with exact low-resolution electromagnetic tomography," *Philosophical Transactions of the Royal Society A: Mathematical, Physical and Engineering Sciences*, vol. 369, pp. 3768-3784, 2011.

- [124] R. D. Pascual-Marqui, "Instantaneous and lagged measurements of linear and nonlinear dependence between groups of multivariate time series: frequency decomposition," *arXiv preprint arXiv:0711.1455*, 2007.
- [125] K. Stephan, L. Harrison, S. Kiebel, O. David, W. Penny, and K. Friston, "Dynamic causal models of neural system dynamics: current state and future extensions," *Journal of Biosciences*, vol. 32, pp. 129-144, 2007/01/01 2007.
- [126] J. M. Schoffelen and J. Gross, "Source connectivity analysis with MEG and EEG," *Human brain mapping*, vol. 30, pp. 1857-1865, 2009.
- [127] T. Bitan, J. R. Booth, J. Choy, D. D. Burman, D. R. Gitelman, and M. M. Mesulam, "Shifts of effective connectivity within a language network during rhyming and spelling," *Journal of Neuroscience*, vol. 25, pp. 5397-5403, Jun 1 2005.
- [128] A. P. R. Smith, K. E. Stephan, M. D. Rugg, and R. J. Dolan, "Task and Content Modulate Amygdala-Hippocampal Connectivity in Emotional Retrieval," *Neuron*, vol. 49, pp. 631-638, 2006.
- [129] W. Thompson, T. Mullen, and S. Makeig, "A Bayesian spatiotemporal model for multi-subject EEG source dynamics and effective connectivity," in *XI International Conference on Cognitive Neuroscience (ICON XI)*, Mallorca, Spain, 2011.
- [130] T. Mullen, J. Onton, A. Delorme, W. Thompson, and S. Makeig, "Analysis and visualization of theta-band information flow dynamics in an ERN-producing task," in *Human Brain Mapping*, Barcelona, Spain, 2010.
- [131] T. Mullen. (2010). *The Source Information Flow Toolbox (SIFT): An Electrophysiological Information Flow Toolbox for EEGLAB. Theoretical Handbook and User Manual*. Available: www.sccn.ucsd.edu/wiki/SIFT
- [132] J. Onton and S. Makeig, "Information-based modeling of event-related brain dynamics," in *Progress in Brain Research*. vol. Volume 159, N. Christa and K. Wolfgang, Eds., ed: Elsevier, 2006, pp. 99-120.
- [133] N. Swann, J. Onton, and M. S., "Single-Trial EEG changes associated with specific behavioral contexts in a Two-Back Task," in *Society for Neuroscience*, San Diego, CA, 2007.
- [134] N. Tzourio-Mazoyer, B. Landau, D. Papathanassiou, F. Crivello, O. Etard, N. Delcroix, B. Mazoyer, and M. Joliot, "Automated anatomical labeling of

- activations in SPM using a macroscopic anatomical parcellation of the MNI MRI single-subject brain," *NeuroImage*, vol. 15, pp. 273-89, Jan 2002.
- [135] A. J. Shackman, T. V. Salomons, H. A. Slagter, A. S. Fox, J. J. Winter, and R. J. Davidson, "The integration of negative affect, pain and cognitive control in the cingulate cortex," *Nature reviews. Neuroscience*, vol. 12, pp. 154-67, Mar 2011.
 - [136] M. Hoke, B. Ross, R. Wickesberg, and B. Lütkenhöner, "Weighted averaging — theory and application to electric response audiometry," *Electroencephalography and Clinical Neurophysiology*, vol. 57, pp. 484-489, 1984.
 - [137] A. Ivannikov, I. Kalyakin, J. Hääläinen, P. H. T. Leppänen, T. Ristaniemi, H. Lyytinen, and T. Kärkkäinen, "ERP denoising in multichannel EEG data using contrasts between signal and noise subspaces," *Journal of Neuroscience Methods*, vol. 180, pp. 340-351, 2009.
 - [138] R. v. S. Müller, Hellmut, "Sorted averaging-principle and application to auditory brainstem responses," *Scandinavian Audiology*, vol. 28, pp. 145-149, 1999.
 - [139] H. Yabe, F. Saito, and Y. Fukushima, "Median method for detecting endogenous event-related brain potentials," *Electroencephalography and Clinical Neurophysiology*, vol. 87, pp. 403-407, 1993.
 - [140] R. Q. Quiroga and H. Garcia, "Single-trial event-related potentials with wavelet denoising," *Clinical Neurophysiology*, vol. 114, pp. 376-390, 2003.
 - [141] M. Miyakoshi, M. Nomura, and H. Ohira, "An ERP study on self-relevant object recognition," *Brain and cognition*, vol. 63, pp. 182-189, 2007.
 - [142] J. Kayser and C. E. Tenke, "Principal components analysis of Laplacian waveforms as a generic method for identifying ERP generator patterns: II. Adequacy of low-density estimates," *Clinical Neurophysiology*, vol. 117, pp. 369-380, 2006.
 - [143] G. A. Rousselet, "Does Filtering Preclude Us from Studying ERP Time-Courses?," *Frontiers in Psychology*, vol. 3, 2012.
 - [144] P. Godfrey-Smith, "Theory and reality : an introduction to the philosophy of science," in *Science and its conceptual foundations*, ed. Chicago: University of Chicago Press, 2003, p. 236.

- [145] I. CVX Research. (2012). *CVX: Matlab Software for Disciplined Convex Programming, version 2.0 beta.*
- [146] D. Devlaminck, B. Wyns, M. Grosse-Wentrup, G. Otte, and P. Santens, "Multisubject learning for common spatial patterns in motor-imagery BCI," *Computational intelligence and neuroscience*, vol. 2011, p. 8, 2011.
- [147] D. Wu, B. J. Lance, and T. D. Parsons, "Collaborative Filtering for Brain-Computer Interaction Using Transfer Learning and Active Class Selection," *PloS one*, vol. 8, p. e56624, 2013.
- [148] S. J. Luck, *An introduction to the event-related potential technique*, 2005.
- [149] N. J. Smith. (2011). *Scaling up psycholinguistics*. Available: <http://wwwlib.umi.com/cr/fullcit?p3472953>
- [150] H. Hinrichs, M. Scholz, C. Tempelmann, M. G. Woldorff, A. M. Dale, and H. J. Heinze, "Deconvolution of event-related fMRI responses in fast-rate experimental designs: tracking amplitude variations," *Journal of Cognitive Neuroscience*, vol. 12, pp. 76-89, 2000.
- [151] O. Hauk, M. Davis, M. Ford, F. Pulvermller, and W. Marslen-Wilson, "The time course of visual word recognition as revealed by linear regression analysis of ERP data," *Neuroimage*, vol. 30, pp. 1383-1400, 2006.
- [152] C. R. Pernet, N. Chauveau, C. Gaspar, and G. A. Rousselet, "Limo EEG: a toolbox for hierarchical linear modeling of electroencephalographic data," *Computational intelligence and neuroscience*, vol. 2011, p. 3, 2011.
- [153] P. Hendrix, W. Tabak, R. Schreuder, and R. Baayen, "nd, Electrophysiological effects in language production: a picture naming study using generalized additive modeling," ed: preparation, 2009.
- [154] A. Hyvärinen and E. Oja, "Independent component analysis: algorithms and applications," *Neural networks*, vol. 13, pp. 411-430, 2000.
- [155] S. Makeig, A. J. Bell, T. P. Jung, and T. J. Sejnowski, "Independent component analysis of electroencephalographic data," *Advances in neural information processing systems*, pp. 145-151, 1996.
- [156] N. Bigdely-Shamlo, A. Vankov, R. R. Ramirez, and S. Makeig, "Brain activity-based image classification from rapid serial visual presentation,"

- Neural Systems and Rehabilitation Engineering, IEEE Transactions on*, vol. 16, pp. 432-441, 2008.
- [157] S. Makeig, T. P. Jung, A. J. Bell, D. Ghahremani, and T. J. Sejnowski, "Blind separation of auditory event-related brain responses into independent components," *Proceedings of the National Academy of Sciences*, vol. 94, pp. 10979-10984, 1997.
 - [158] P. Burman, "A comparative study of ordinary cross-validation, v-fold cross-validation and the repeated learning-testing methods," *Biometrika*, vol. 76, pp. 503-514, 1989.
 - [159] S. Makeig, M. Westerfield, T. P. Jung, S. Enghoff, J. Townsend, E. Courchesne, and T. Sejnowski, "Dynamic brain sources of visual evoked responses," *Science*, vol. 295, pp. 690-694, 2002.
 - [160] P. Bloomfield and W. L. Steiger, *Least absolute deviations: theory, applications, and algorithms*: Birkhäuser Boston, 1983.
 - [161] *Neural Electro Magnetic Ontologies (NEMO)*. Available: <http://nemo.nic.uoregon.edu/>
 - [162] *Cognitive Paradigm Ontology (CogPO)*. Available: http://wiki.cogpo.org/index.php?title=Main_Page
 - [163] *The Neuroscience Lexicon*. Available: http://neurolex.org/wiki/Behavioral_Paradigm_Hierarchy
 - [164] *OWL 2 Web Ontology Language Document Overview*. Available: <http://www.w3.org/TR/owl2-overview/>
 - [165] *HeadIT tools*. Available: <http://sccn.ucsd.edu/wiki/HED>
 - [166] Rognon, R. Strautman, J. Lauren, N. Bigdely-Shamlo, S. Makeig, T. Johnson, and K. Robbins, "CTAGGER: Semi-structured community tagging for annotation and data-mining in event-rich contexts " presented at the IEEE GlobalSIP, San Antonio, TX, 2013.
 - [167] *Simulation and Neuroscience Application Platform (SNAP)*. Available: <https://github.com/sccn/SNAP>
 - [168] *Lab Streaming Layer (LSL)*. Available: <https://code.google.com/p/labstreaminglayer/>

- [169] *Extensible Data Format (XDF)*. Available: <https://code.google.com/p/xdf/>
- [170] *EEG Study Schema (ESS)*. Available: <http://sccn.ucsd.edu/wiki/ESS>
- [171] *Human Electrophysiology, Anatomic Data, and Integrated Tools (HeadIT)*. Available: <http://headit.org/>
- [172] *Hierarchical Event Descriptor (HED) Tags*. Available: <http://sccn.ucsd.edu/wiki/HED>
- [173] N. Bigdely-Shamlo, K. Kreutz-Delgado, K. Robbins, M. Miyakoshi, M. Westerfield, T. Bel-Bahar, C. Kothe, J. Hsi, and S. Makeig, "Hierarchical Event Descriptor (HED) Tags for Analysis of Event-Related EEG Studies," presented at the IEEE GlobalSIP, Austin, TX (submitted), 2013.
- [174] T. Mullen, J. Onton, A. Delorme, and S. Makeig, "Analysis and visualization of theta-band information flow dynamics in an ERN-producing task," presented at the Human Brain Mapping, Barcelona, Spain, June 2010.
- [175] M. Miyakoshi, N. Kanayama, T. Iidaka, and H. Ohira, "EEG evidence of face-specific visual self-representation," *NeuroImage*, vol. 50, pp. 1666-75, May 1 2010.
- [176] R. Ceponiene, M. Westerfield, M. Torki, and J. Townsend, "Modality-specificity of sensory aging in vision and audition: evidence from event-related potentials," *Brain research*, vol. 1215, pp. 53-68, Jun 18 2008.
- [177] A. Delorme, T. Mullen, C. Kothe, N. Bigdely-Shamlo, Z. Akalin, A. V. Acar, and S. Makeig, "EEGLAB, MPT, NetSIFT, NFT, BCILAB, and ERICA: New tools for advanced EEG/MEG processing," *Computational intelligence and Neuroscience*, 2011.